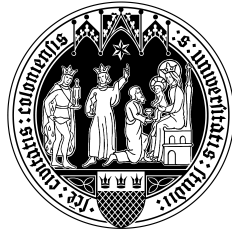


**Spectroscopic studies on AGNs  
and  
High angular resolution in the NIR:  
The construction of an imaging beam  
combiner for the LBT**

INAUGURAL-DISSERTATION

zur  
Erlangung des Doktorgrades  
der Mathematisch-Naturwissenschaftlichen Fakultät  
der Universität zu Köln



vorgelegt von

**Evangelia Tremou**  
aus Trikala, Griechenland

Köln 2011

Berichterstatter: Prof. Dr. J. Anton Zensus  
Prof. Dr. Andreas Eckart

Tag der letzten mündlichen Prüfung: 04. April 2011

*To my soul mate N.P.*



# Abstract

The current thesis is divided into two projects. The first part deals with studies on active galaxies hosting an Active Galactic Nucleus (AGN). Specifically, an optical spectroscopic study of a nearby ( $z < 0.06$ ) volume - limited sample of Low - Luminosity Quasi - Stellar Objects (LLQSOs) has been carried out. The sample has been drawn from the Hamburg/ESO QSO survey (HES), which has a well-defined flux limit of  $B_j < 17.3$ . The aim of the present project is to characterize the excitation degree of the sample, distinguish between possible star forming and Seyfert activity and to investigate the spectral characteristics of the sample.

The spectroscopic data were analyzed and emission lines were fitted using a routine, which employs Levenberg - Marquardt least square minimization. The same analysis was also applied for some additional archival data from the 6 Degree Field Galaxy Survey (6DFGS). The objects of the LLQSOs sample are classified according to the classical optical diagnostic diagrams, based on optical emission lines close in wavelength, avoiding almost any impact of reddening. The diagrams provide a diagnosis of the ionizing source within a galaxy, hence activity between H II, LINERs (Low Ionization Nuclear Emission-line Region), and Seyfert galaxies can be clearly distinguished. The classification of all members of the LLQSOs sample is shown in chapter 3. The broadness of the emission lines, cases with double components and the electron density are also analyzed.

The comparison of the diagnostic diagrams between the two data sets (HES and 6DFGS) results in different classifications of most of the sources. This is due to the different spectroscopic techniques applied in the two data sets during the observations, and is sketched in chapter 4. Several galaxies at a variety of cosmological distances, with elliptical and circular morphologies, were simulated. In these simulations, different instruments (different spectroscopic techniques, i.e. slit, fiber) were applied to the galaxies, in order to study the instrumental effect (aperture effect). The impact of the aperture effect in local and high redshift universe is discussed in detail.

The second project of the thesis focuses on the construction of an image beam combiner for the Large Binocular Telescope (LBT). The LINC - NIRVANA instrument will be operating in the near - infrared (1 - 2.4  $\mu\text{m}$ ) and will provide a high angular resolution ( $\sim 9$  mas at 1.25  $\mu\text{m}$ ) over a wide field of view ( $\sim 100$  arcsec at 1.25  $\mu\text{m}$ ). A fundamental component of the instrument, the Fringe and Flexure Tracking System (FFTS) is responsible to ensure a complete and time-stable wavefront correction at the position of the science detector. This will allow for long integration times at interferometric angular resolutions. A historical overview and our current achievements are also discussed in chapter 5.

Laboratory tests of specific parts of the FFTS are presented in chapter 6. Especially, the subparts of the Detector Positioning Unit (DPU), which has to be moved with respect to an altitude - azimuth mounting under vacuum conditions, are characterized. The tilting

of the instrument as a function of elevation results in a flexure of the system that has to be corrected by an algorithm.

# Zusammenfassung

Die vorliegende Arbeit unterteilt sich in zwei Bereiche. Der erste Teil beschäftigt sich mit Galaxien, die einen Aktiven Galaktischen Nukleus (AGN) besitzen. Hierzu wird eine volumenlimitierte Stichprobe von optische selektierten Low-Luminosity Quasi-Stellar Objects (LLQSOs) benutzt. Diese basiert auf dem Hamburg/ESO QSO Survey (HES) und besitzt eine wohldefinierte Flussbegrenzung von  $B_j < 17.3$ . Ziel ist es, die Anregungsbedingungen der Linienstrahlung und die relative Bedeutung von Sternentstehungs- und Seyfert-Aktivität für diese Stichprobe zu untersuchen.

Die Analyse der spektroskopischen Daten fokussiert sich dabei auf die Anpassung von Emissionslinien mittels Levenberg - Marquardt Minimierung der kleinsten Quadrate. Zusätzlich wurden Archivdaten des 6 Degree Field Galaxy Survey (6dFGS) für einen Teil der Quellen der Stichprobe untersucht. Die LLQSOs werden entsprechend der klassischen optischen Diagnostik klassifiziert, die auf Flussverhältnissen von benachbarten Emissionlinien beruht. Dies minimiert den Einfluss von Rötung auf die Bestimmung der Linienflüsse. Diese Diagnostik erlaubt eine Unterscheidung von H II, LINERs (Low Ionization Nuclear Emission-line Region), and Seyfert Galaxien, d.h. der dominierenden Quellen der ionisierenden Strahlung. Die Ergebnisse für die vorliegende Stichprobe werden in Kap. 3 präsentiert.

Für den Großteil der Stichprobe, für den sowohl HES als auch 6DFGS Daten vorliegen, ergibt die Analyse eine unterschiedlich Klassifikation. Dies liegt in den unterschiedlichen Beobachtungstechniken begründet und wird im Kap. 4 untersucht. Hierzu wurden Galaxien unterschiedlicher (elliptischer und zirkulrer) Morphologie und bei verschiedenen kosmologischen Abständen als Funktion der instrumentellen Apertur, d.h. Schlitz- vs. Faserspektrograph, simuliert. Der Einfluss der Apertur auf die Beobachtung im nahen und hochrotverschobenen Universum wird im Detail diskutiert.

Der zweite Teil der Arbeit handelt von der Konstruktion von LINC-NIRVANA, der abbildenden Strahlvereiner Kamera für das Large Binocular Telescope (LBT). Das Instrument arbeitet im Nahinfraroten (von  $1.0\text{-}2.4\mu\text{m}$ ) und liefert hohe räumliche Auflösung ( $\sim 9\text{ mas}$  at  $1.25\mu\text{m}$ ) über ein großes Gesichtsfeld ( $\sim 100\text{ arcsec}$  at  $1.25\mu\text{m}$ ). Eine wichtige Komponente des Instruments ist das Fringe and Flexure Tracking System (FFTS), das eine phasenkohärente Strahlvereinerung (d.h. bei interferometrischer Winkelauflösung) über lange Integrationszeiten an der Position des wissenschaftlichen Detektors ermöglicht.

In Kap. 6 werden Labortests von spezifischen Komponenten des FFTS präsentiert. Im Speziellen wird die Detektorpositionierungseinheit (Detector Positioning Unit kurz DPU) charakterisiert. Diese bewegt sich unter Vakuumbedingungen in der Fokalebene des Instruments entsprechend der Alt-Azimuth Aufhängung des Teleskops. Das Kippen des Instruments als Funktion der Elevation bedingt Verspannungen innerhalb des Systems, die bei der Bewegung des FFTS Detektors in der Fokalebene berücksichtigt werden müssen.





# Contents

<b>1</b>	<b>Motivation and Thesis Outline</b>	<b>1</b>
1.1	Galaxy evolution and interaction . . . . .	1
1.2	Quest for High Angular Resolution . . . . .	4
1.3	Outline of the current Thesis . . . . .	6
<b>2</b>	<b>AGN properties and Optical Spectroscopy</b>	<b>9</b>
2.1	Host galaxies and their Active Galactic Nuclei . . . . .	9
2.1.1	The Unification model . . . . .	11
2.2	Optical spectroscopy . . . . .	13
2.2.1	Techniques . . . . .	14
2.2.2	Emission Lines of extragalactic objects . . . . .	17
2.3	Sorting out Active Galactic Nuclei . . . . .	20
<b>3</b>	<b>Optical spectroscopic studies on the Low Luminosity Quasi Stellar Objects sample</b>	<b>25</b>
3.1	The nearby low luminosity QSO sample . . . . .	25
3.2	Observations and Data Reduction . . . . .	28
3.2.1	Hamburg/ESO Survey Observations . . . . .	28
3.2.2	6 Degree Field Galaxy Survey . . . . .	30
3.3	Data Analysis . . . . .	34
3.4	Results and Discussion . . . . .	36
3.4.1	Classification using the BPT diagrams . . . . .	37
3.4.2	Analysis of the broad component . . . . .	40
3.4.3	Electron density analysis . . . . .	46
3.5	Concluding Remarks . . . . .	46
<b>4</b>	<b>Simulating the Aperture Effect</b>	<b>49</b>
4.1	Motivation . . . . .	49
4.1.1	Previous Investigations . . . . .	50
4.2	Studies on the Aperture Effect . . . . .	52
4.2.1	Nearby galaxies at high redshifts . . . . .	53
4.2.2	Software algorithm for the simulations . . . . .	57
4.2.3	The aperture effect in the local universe . . . . .	59
4.2.4	Aperture effect at high redshift: Cosmological implications . . . . .	63
4.3	Concluding Remarks . . . . .	66

<b>5</b>	<b>Optical/Infrared Interferometry - LINC NIRVANA</b>	<b>69</b>
5.1	Interferometry retrospection . . . . .	69
5.1.1	Adaptive Optics . . . . .	71
5.1.2	Multi-Conjugate Adaptive Optics . . . . .	73
5.2	The Large Binocular Telescope . . . . .	74
5.2.1	The LBT Instruments . . . . .	74
5.3	The LINC-NIRVANA Instrument . . . . .	76
5.3.1	Principle of operation . . . . .	78
5.4	The Fringe and Flexure Tracking System . . . . .	78
<b>6</b>	<b>Laboratory Tests of FFTS-DPU</b>	<b>81</b>
6.1	The Detector Positioning Unit . . . . .	81
6.2	Laboratory Tests of FFTS . . . . .	84
6.2.1	Temperature and heat transfer tests of the linear stages . . . . .	84
6.2.2	Tip-Tilt test . . . . .	86
6.2.3	Software . . . . .	89
6.2.4	DPU Repeatability and Flexure . . . . .	90
6.3	Concluding Remarks . . . . .	94
6.3.1	Outlook through High Angular Resolution Interferometry . . . . .	94
<b>A</b>	<b>Appendix</b>	<b>97</b>
A.1	The optical spectra of 6dFGS . . . . .	97
	<b>Bibliography</b>	<b>145</b>
	<b>List of Acronyms</b>	<b>153</b>
	<b>Acknowledgements</b>	<b>155</b>
	<b>Erklärung</b>	<b>157</b>
	<b>Lebenslauf</b>	<b>161</b>

# List of Figures

1.1	Artistic representation of the center of an AGN . . . . .	2
1.2	Projected gas density of the merger of two galaxies. . . . .	3
1.3	The transparency of the atmosphere at different wavelengths. . . . .	5
2.1	Microphotometer tracings in the nebula NGC 1068. . . . .	10
2.2	Schematic View of the Unification model of AGNs . . . . .	12
2.3	Instrumental profiles for a perfect spectroscope and an optically perfect but real spectroscope. . . . .	13
2.4	The basic components of a spectroscope . . . . .	14
2.5	An objective prism spectroscope . . . . .	15
2.6	Schematic view of an echelle grating and a cross disperser . . . . .	16
2.7	The main techniques for achieving integral field spectroscopy. . . . .	17
2.8	Ly $\alpha$ line in a distant galaxy . . . . .	18
2.9	The optical spectrum of the Seyfert 1 galaxy NGC 5548. . . . .	19
2.10	Classical optical diagnostic diagram, BPT . . . . .	21
2.11	The three BPT diagrams . . . . .	22
3.1	Effective area of the Hamburg/ESO survey as a function of the Galactic extinction corrected BJ magnitude. . . . .	26
3.2	Magnitude and redshift distribution of the nearby LLQSO sample . . . . .	27
3.3	The three ESO telescopes . . . . .	29
3.4	UK Schmidt Telescope and 6dF robotic positioner. . . . .	30
3.5	6dFGS sky coverage . . . . .	31
3.6	The optical spectrum of g0111097-472735 source observed by 6dFGS and fitting of Balmer lines. . . . .	34
3.7	The galaxy g1138510-232135 and its optical spectrum and the fitting of line OI $\lambda$ 6300Å. . . . .	35
3.8	The entire spectrum of the galaxy g2234409-370644 and the fitting of line SII $\lambda$ 6717Å and $\lambda$ 6731Å . . . . .	36
3.9	Classification diagram of HES . . . . .	37
3.10	Classification diagrams of 6dFGS . . . . .	38
3.11	Classification diagrams of cross-matching sources of 6dFGS and HES . . . .	40
3.12	Distribution of H $\alpha$ and H $\beta$ broad component of HES. . . . .	42
3.13	Distribution of H $\alpha$ and H $\beta$ broad component of 6dFGS. . . . .	43
3.14	The source HE0236-3101. Fitting of lines H $\alpha$ $\lambda$ 6562Å and NII, H $\beta$ $\lambda$ 4861Å and OIII. . . . .	44
3.15	The source HE0203m0031. Fitting of Balmer lines. . . . .	45

4.1	The comparison of the optical spectrum profile of the source HE0212-0059.	49
4.2	The difference in classification of the source HE0212-0059 which was observed with different with instruments (HES and 6dFGS. . . . .	50
4.3	Galaxy simulated with slit and fibre . . . . .	53
4.4	Linear scale size of the galaxies as a function of redshift. . . . .	55
4.5	Galaxy in redshift $z=1$ and $z=7$ produced by simulations . . . . .	57
4.6	Simulating a galaxy with slit 2", fibre 6.7" and fibre 3" . . . . .	58
4.7	First case: The classification diagram of a simulated local galaxy ( $z = 0.02$ ). . . . .	59
4.8	Second case: The classification diagram of a simulated local galaxy ( $z = 0.02$ ). . . . .	60
4.9	Third case: The classification diagram of a simulated local galaxy ( $z = 0.02$ ). . . . .	62
4.10	Fourth case: The classification diagram of a simulated local galaxy ( $z = 0.02$ ). . . . .	62
4.11	The classification diagrams for high redshift objects $0.1 \leq z \leq 7$ , circular symmetry. . . . .	65
4.12	The classification diagrams for high redshift objects $0.1 \leq z \leq 7$ , observed with long slit spectroscopy. . . . .	66
5.1	Optics originally used by Labeyrie, Stachnik and Gezari for speckle interferometry. . . . .	70
5.2	Gemini North Laser Guide Star from Canada France Hawaii Telescope, credit:Gemini Observatory . . . . .	71
5.3	Adaptive Optics system. . . . .	72
5.4	Multi-Conjugate Adaptive Optics . . . . .	73
5.5	The Large Binocular Telescope. . . . .	75
5.6	Instruments location on the LBT . . . . .	76
5.7	The LINC NIRVANA Instrument . . . . .	77
5.8	The FFTS and the main subparts . . . . .	79
6.1	The X, Y, Z linear stages . . . . .	81
6.2	The rotation of the field . . . . .	83
6.3	The set up of the temperature test. . . . .	85
6.4	Results of the temperature measurements. . . . .	86
6.5	The Tip - Tilt test set up . . . . .	87
6.6	KGM 182 Heidenhain interferometric grid plate. . . . .	87
6.7	The forth and back movement of X and Y stages with constant velocity under 0, 45 and 90 degrees of elevation. . . . .	88
6.8	The flexure of X and Y stage. . . . .	89
6.9	Screen shot of Dr. Greenthumb graphical interface. . . . .	90
6.10	The repeatability of the X and Y stage. . . . .	92
6.11	The precision of X linear stage movement. . . . .	93
6.12	The motor error distribution of the X micro positioning stage. . . . .	94
6.13	The motor error distribution of the Y micro positioning stage. . . . .	94
A.1	The source g0023554-180251. . . . .	97
A.2	The source g0025013-452955. . . . .	98
A.3	The source g0039159-511702. . . . .	99

---

A.4	The source g0042369-104922.	100
A.5	The source g0047413-212927.	101
A.6	The source g0053544-240437.	102
A.7	The source g0111097-472735.	103
A.8	The source g0111143-161555.	104
A.9	The source g0129067-073830.	105
A.10	The source g0151419-361116.	106
A.11	The source g0206160-001729.	107
A.12	The source g0214336-004600.	108
A.13	The source g0226257-282059.	109
A.14	The source g0230055-085953.	110
A.15	The source g0111097-472735.	111
A.16	The source g0234378-084716.	112
A.17	The source g0256027-162916.	113
A.18	The source g0259305-242254.	114
A.19	The source g0333078-135433.	115
A.20	The source g0334245-151340.	116
A.21	The source g0345032-264820.	117
A.22	The source g0351417-402759.	118
A.23	The source g0400407-370506.	119
A.24	The source g0401462-383320.	120
A.25	The source g0405017-371115.	121
A.26	The source g0414527-075540.	122
A.27	The source g0431371-024124.	123
A.28	The source g0436223-102234.	124
A.29	The source g0450251-035903.	125
A.30	The source g0609175-560658.	126
A.31	The source g0856178-013807.	127
A.32	The source g0952191-013644.	128
A.33	The source g1014207-041841.	129
A.34	The source g1031573-184633.	130
A.35	The source g1110480-283004.	131
A.36	The source g1138510-232135.	132
A.37	The source g1251324-141316.	133
A.38	The source g1313058-110742.	134
A.39	The source g1331138-252410.	135
A.40	The source g1332391-102853.	136
A.41	The source g1349193-301834.	137
A.42	The source g1356367-193145.	138
A.43	The source g2130499-020814.	139
A.44	The source g2207450-323502.	140
A.45	The source g2214420-384823.	141
A.46	The source g2234409-370644.	142
A.47	The source g2309192-322958.	143
A.48	The source g2340321-263319.	144



# List of Tables

3.1	Main Characteristics of the LLQSOs sample. . . . .	33
3.2	Statistics of the sample . . . . .	39
3.3	Statistics of the cross-matching sources. . . . .	40
3.4	Electron density. . . . .	46
4.1	Angular diameter sizes of the simulated galaxies. . . . .	56
4.2	First Case: The emission line contribution on each region of the galaxy. . .	59
4.3	Second Case: The emission line contribution on each region of the galaxy. .	61
4.4	Third Case: The emission line contribution on each region of the galaxy. .	62
4.5	Fourth Case: The emission line contribution on each region of the galaxy. .	63
5.1	Main characteristics and status of the LBT Instruments . . . . .	76
6.1	The high level requirements of the FFFTS component. . . . .	82
6.2	The main characteristics of the 3 micro positioning stages. . . . .	82
6.3	The main characteristics of KGM 182 Heidenhain grid plate. . . . .	88





# 1. Motivation and Thesis Outline

*The first chapter is an introductory one and its scope is to explain the motivation that stands behind the studies of the present thesis following in the next sections. Since the thesis consists of two main parts, an introduction is given for both of them (AGN and high angular resolution studies using an upcoming instrument).*

## 1.1 Galaxy evolution and interaction

An Active Galactic Nucleus (AGN) is an object in the center of a galaxy whose spectrum cannot be explained just by starlight. It produces enormous luminosities arising from very compact volumes. The light emitted by the nucleus equals (Seyfert activity) or even exceeds (Quasi Stellar Object, QSO) the total emission of the rest of the galaxy (host galaxy). The physics behind the AGN are still not completely understood, but the most current accepted model includes a super massive black hole in the center surrounded by a small ( $< 1$  pc) accretion disc which is responsible for the huge amount of radiation we observe (Rees 1984; Magorrian et al. 1998). The accretion disc extends to the outer regions, forming a torus (1 to a few tens parsecs) that surrounds the entire AGN. As the matter falls into the central hole, some of it will escape from the disk forming jets. The inner clouds of the host galaxy form the Broad Line Region (BLR) as the gas rotates faster closer to the black hole and the Doppler effect widens the emission lines of these clouds. The outer clouds form the narrow line region (NRL), which can extend for a few kpc (see Figure 1.1). The radiation from AGN is generally associated with gas accretion onto a Super Massive Black Hole (SMBH) located at the center of the host galaxy. The tight correlation between the black hole mass and the stellar velocity dispersion (Gebhardt et al. 2000) and the mass of the surrounding bulge (Häring & Rix 2004) suggests a co-evolution of the central black hole and its host galaxy.

Over the last decades observations of spiral galaxies point towards a hierarchy of mechanisms that all combine to transport the gas from the large kpc scales down to the inner pc scales. Additionally, fueling mechanisms triggered by the galactic environment, such as minor mergers and tidal interactions, might play a prominent role. Even less known are the processes responsible for fueling the innermost regions: secondary or inner bars were first proposed (Shlosman et al. 1989; Knapen 2005) to bridge the last few 100 pc, but more recent other mechanisms, such as  $m=1$  modes (Emsellem 2001), warped gas disks (Schinnerer et al. 2000) and/or gas density waves (Englmaier & Shlosman 2000; Martini et al. 2003; Maciejewski 2004) have been suggested to be equally or more important.

The unified model of AGNs tells us that massive and super massive black holes underlie the behaviors of almost all types of AGNs (Kormendy & Richstone 1995; Tremaine

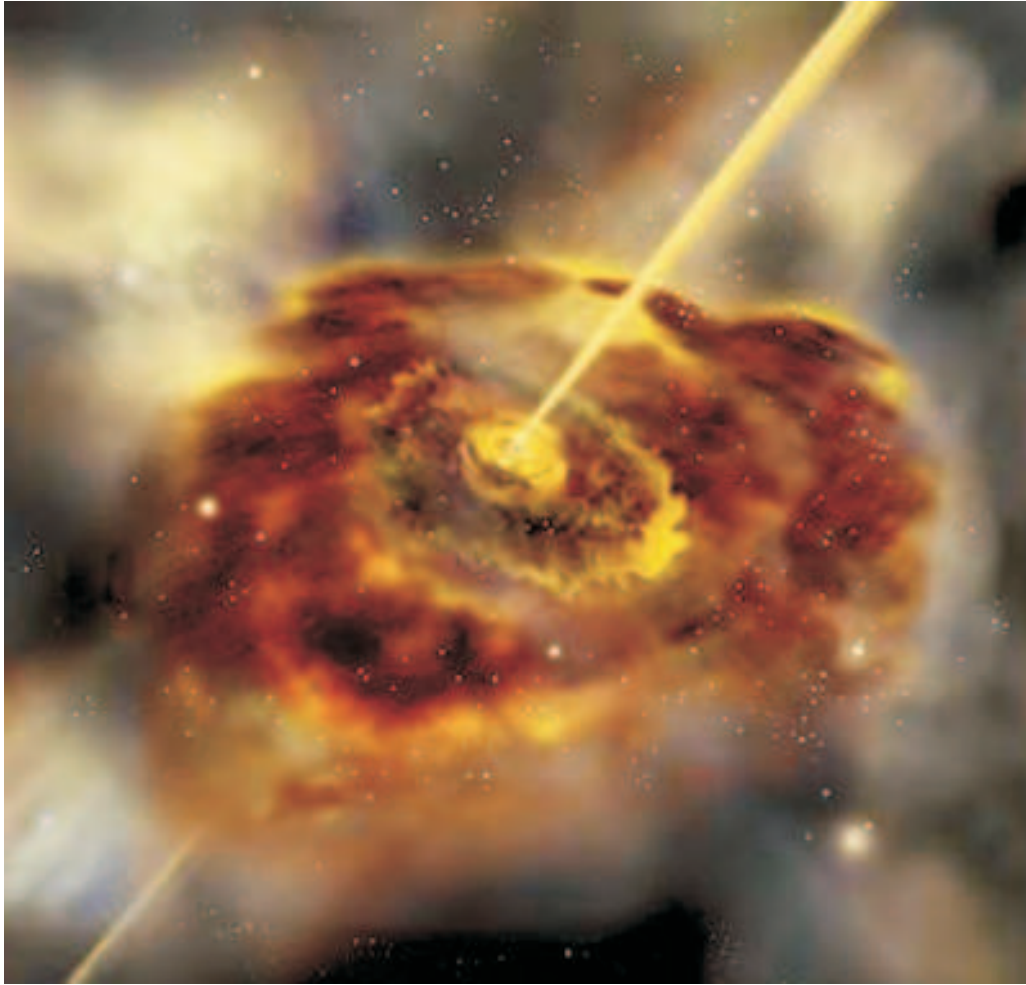


Figure 1.1: Artistic representation of the center of an AGN. Credit: Sonoma State University, NASA E/PO, Aurore Simonnet, <http://epo.sonoma.edu>

et al. 2002; Yu & Tremaine 2002). The first necessity in developing a theory of AGN evolution is thus to understand how such black holes originate. The fact that the earliest known QSOs and quasars were in existence just a few hundred million years after the Big Bang, constrains severely the fact that SMBHs must form very quickly by galactic time standards. The most popular suggestion is that super-massive black holes are born directly from the collapse of super-massive stars, which they have themselves been created from collapsing gas and dust clouds. The model of massive black hole formation via collisions within dense clusters is supported by the correlation between the masses of the central objects and those of the bulges of the host galaxies. The black holes are found to have masses between 0.2% and 1% of the mass of the bulge. The bulge in the case of an elliptical galaxy is the galaxy itself, for a spiral galaxy it is the galaxy's nucleus.

Further growth of the central black holes can occur if material from the outer parts of the host galaxy finds its way down into the central regions. Collisions between galaxies can drive to an increase of the black hole mass. Such collisions send fuel down towards the central black hole (see Figure 1.2), but also if both galaxies have central black holes, it can lead to a large increase in the black holes mass as those two black holes collide and merge.

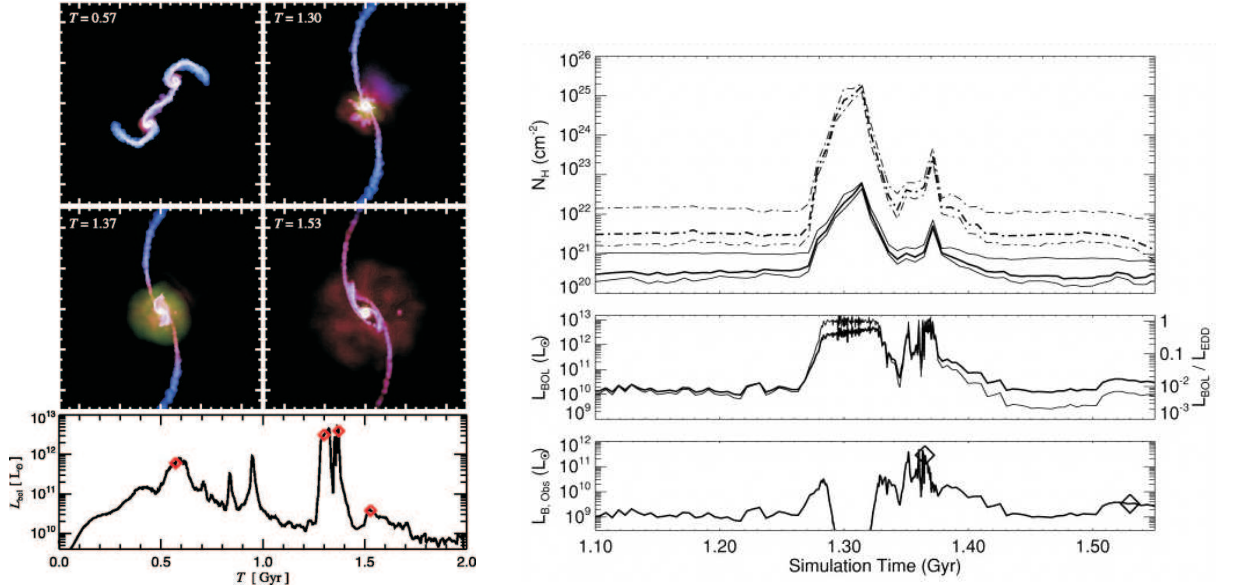


Figure 1.2: Left Panels: Projected gas density of the merger of two galaxies shown in boxes of 140 kpc in side, color-coded by temperature (blue to red, upper panels). The bolometric luminosity of the central black hole(s) is shown in the lower panel, with diamonds marking the times shown above. Bolometric luminosities prior to the merger are the sum of the two individual black hole luminosities. Right Panels. Top: Thick contours plot the median column density  $N_H$  as a function of the simulation time, with thin contours at 25 % and 75 % inclusion levels. Solid contours represent the density of the 'hot-phase' inter stellar medium (ISM), and dashed contours represent the total simulation density. Right Panels. Middle: Bolometric luminosity of the black hole,  $L_{bol} = \epsilon \dot{M} c^2$  (thick line) and ratio of bolometric to Eddington luminosity,  $l \equiv L_{bol}/L_{Edd}$  (thin line). Right Panels. Bottom: Observed B-band luminosity calculated given the median hot-phase ISM density. Diamonds mark times shown in the right panel (Hopkins et al. 2005).

The starburst galaxies comprise a transient phase since they must have been some other type of galaxy before their starburst event and will go on to revert to some other type of galaxy after the starburst is over. The cores of starburst galaxies are not that active and starburst regions can occur within an AGN. In most of them there are signs of undergoing or of having undergone an encounter with another galaxy, and it is the disturbance to the gas and dust clouds arising from the tides induced during that encounter that lead to the outbursts of star formation. Star-formation rates in starburst galaxies can be up to several thousand solar masses per year. After the outburst, the galaxy is likely present a highly disturbed appearance for some time before eventually settling down towards an elliptical form. Interactions involving two large spiral galaxies can produce the most violent starbursts. Though spiral galaxy collisions arise probably the most luminous starburst galaxies ULIRGs (ultra luminous infrared galaxy). ULIRGs contain huge amounts of dust, therefore they emit most of their energy in far - infrared domain.

Great efforts have been made to understand the evolution scenarios of ULIRGs by previous studies depending either on their activity or their morphology. First, Sanders et al. (1988a) postulated that all ULIRGs develop into QSOs, which are hidden by dust. The idea behind this scenario is that a cold ULIRG passes through the warm ULIRG<sup>1</sup> stage and finally formulates a QSO. A different evolutionary merging scenario for ULIRGs was

<sup>1</sup>Warm ULIRGs are defined the systems with IRAS (Infrared Astronomical Satellite) colors  $f_{25}/f_{60} > 0.2$  (Sanders et al. 1988b), while cold ULIRGs show IRAS colors  $f_{25}/f_{60} < 0.2$

proposed by Colina et al. (2001), which was based on the mass of the objects involved in the interaction. Concerning to this scenario, the merger of two intermediate mass ( $0.5L_* < L < L_*$ ) galaxies results a warm ULIRG or a low luminosity QSO (Chapter 3). The advance phase of the merger of low mass galaxies is a cold ULIRG, while the merge of massive ( $< L_*$ ) galaxies produce high luminosity QSOs.

Based on the morphology of the observed ULIRGs, a different model has been proposed (i.e Kormendy & Sanders (1992); Genzel et al. (2001)). The last phase of this scenario is an elliptical galaxy which has been formed by the merger of two galaxies.

## 1.2 Quest for High Angular Resolution

The progress in astronomy is strongly dependent on the instrumentation breakthroughs. The performance of any telescope and its ability to image celestial objects is limited by a fundamental optical phenomenon called Fraunhofer diffraction. The spatial or angular resolution of every telescope (circular diameter,  $D$ ) is correlated by its power to distinguish the angular distance between two astronomical objects. Assuming, perfect optical properties of the telescope and ideal circumstances, the angular resolution has a theoretical limit and is given by the Rayleigh criterion :

$$\sin\theta^2 = 1.22 \frac{\lambda}{D}, \quad (1.2.1)$$

which actually is the diameter of the observed object' s Airy disk and depends on the telescope' s diameter and on the wavelength (visible, infrared, X- rays) (see also Figure 1.3). In practice, this could be more realistic for space telescopes, such as Hubble Space Telescope (HST) and the Spitzer Space Telescope, in contrast to the ground based telescope facilities that have to face the problem of the earth' s atmospheric turbulence, the astronomical 'seeing'.

The light of a celestial object that travels through the turbulent layers of the atmosphere is collected from a telescope as a perturbed wavefront, because the gas density in the atmosphere is varying due to temperature and pressure inhomogeneities and with it the refraction index (Cox 2000). Its point spread function (PSF) is known as the 'seeing disk' and is approximately Gaussian distributed. A model about the nature of the wavefront perturbations was introduced by Kolmogorov (1941) and developed by Tatarskii (1971). The model considers pressure, temperature and density in the atmosphere, and the variation of wind velocities and directions. The results show that the refractive index structure function is being dependent not only on the altitude  $z$  but also on various geographical and seasonal conditions, such as geographical location and altitude of the telescope site, local environment of the telescope (i.e. the construction of the dome).

Considering that, a fundamental parameter,  $r_0$  defined by Fried (1966) to characterize spatial extent of the phase perturbations (see also section 5.1). The FWHM of the 'seeing disc' in combination with the Fried parameter results then : (Dierickx et al. 1988; Sarazin & Roddier 1990)

$$seeing = FWHM = 0.98 \frac{\lambda}{r_0}, \quad (1.2.2)$$

---

<sup>2</sup> $\theta$  is the angular resolution in radians. It is also called Dawes limit, which was introduced as the result of a long series of observations by W. R. Dawes (1799 - 1868), one of the nineteenth century's most skilled observers.

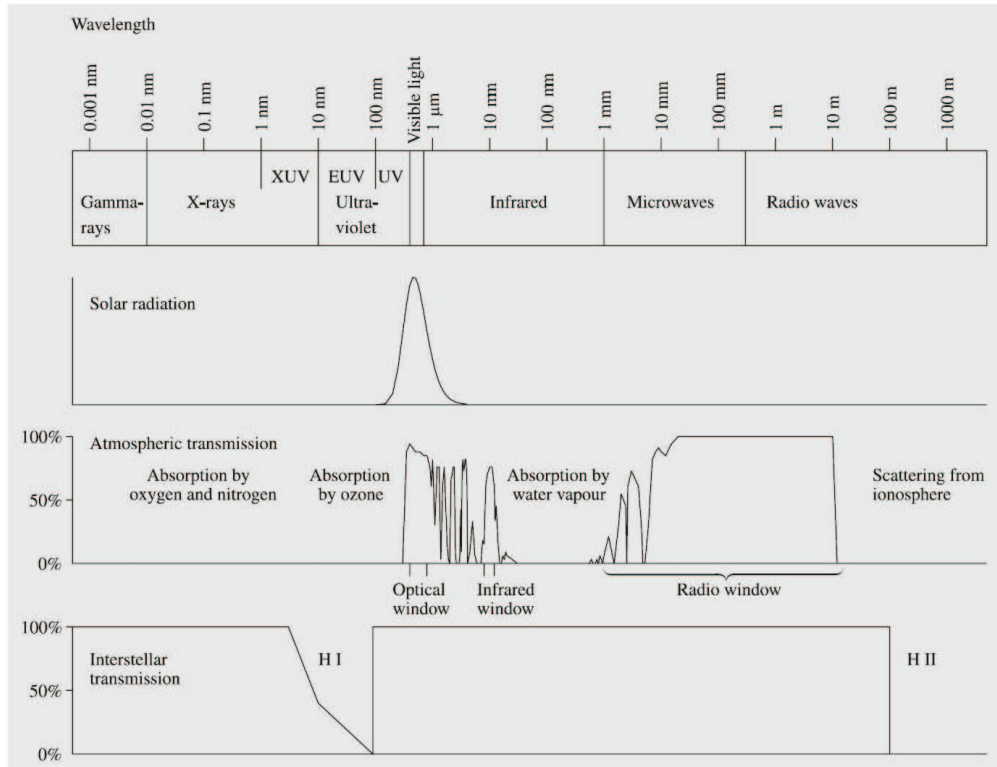


Figure 1.3: The transparency of the atmosphere at different wavelengths. 100% transmission means that all radiation reaches the surface of the Earth. The radiation is also absorbed by interstellar gas, as shown in the lowermost very schematic figure. The interstellar absorption also varies very much depending on the direction. Taken from [Karttunen et al. \(2007\)](#).

where it varies for the different ranges of wavelength,  $\lambda$ . Telescopes with diameters exceeding  $r_0$  are dominated by seeing. A typical value for  $r_0$  in the visible wavelength domain is  $\approx 10$  cm ([Buscher 1988](#)), corresponding to a size of the seeing disk of  $\approx 1.1$  arcsec.

The construction of the observatories in sites that are located on high altitude mountains far from cities with light pollution, and in areas with low humidity and suitable weather conditions, was the first step to overcome the limitations imposed by the atmospheric influence. However, the atmospheric effects still limit the performance of ground based telescopes, which exceed the aperture size of about 0.1 m in the visible and 0.6 m in the NIR ([Hardy 1998](#)).

Therefore, several efforts have been made to approach and come close to the theoretical resolving power of a telescope. The Speckle interferometry method was suggested by [Labeyrie \(1970\)](#), introducing the technique of short exposures times to 'freeze' the atmospheric turbulence. The short exposure images contain bright spots (speckles) and the high resolution image can be resulted by "shift and add" operation on the single frames. Nevertheless, in this technique the read out noise of the detector affects the each short time exposure and the desirable sensitivity is limited due to its short integration times (see also section 5.1).

On the other hand, Adaptive Optics (AO) systems (see also subsection 5.1.1) allow long integration times, exploiting the full sensitivity provided by the large aperture of the current generation of telescopes. The distorted wavefront from a point-source is measured with a wavefront sensor (WFS) and compensated by deformable mirrors (DM).

However, the most basic principles of optical (i.e. visual and infrared) interferometry were already formulated in 1868 by A. Fizeau, who proposed to place a mask with two holes in front of a telescope aperture. He suggested measuring the diameter of stars by finding the hole separation at which the formed interference pattern vanished. This technique was also applied successfully from other scientists (such as [Michelson \(1891\)](#); [Michelson & Pease \(1921\)](#)), but the first optical aperture synthesis images was obtained by [Buscher et al. \(1990\)](#), imaging the surface of Betelgeuse and [Baldwin et al. \(1996\)](#) imaging the binary star Capella.

Nowadays, long baseline stellar interferometers ( $> 100$  m) such as the VLT interferometer or the Keck interferometer can achieve high spatial resolution in the NIR (few mas). But since their optical designs do not support homothetic beam combination, their Field of View (FoV) is small. The Fizeau imaging interferometer LINC-NIRVANA at the Large Binocular Telescope will provide a better spatial resolution and sensitivity in comparison to the current interferometers<sup>3</sup>.

### 1.3 Outline of the current Thesis

The AGN dominates the brightness of a QSO host galaxy and therefore the studies on the parameters of the host galaxy is often a big query. The central few hundred parsec region of the host galaxy contains not only the AGN environment but may also contain massive circum nuclear starburst regions. During the last decade, great efforts have been made by astronomers to study the probable connection between the AGN and its host galaxy. For this reason, the high angular resolution is a key feature in order to separate possible starburst regions and the AGN components from the galaxy that hosts them.

With current AO systems we can achieve a resolution of 50 mas at 2  $\mu\text{m}$ , which corresponds to 100 pc angular diameter distance. With the interferometric near-infrared imaging camera for the LBT, LINC-NIRVANA, we will achieve 10pc, which is the torus of an AGN. The torus provides the viewing angle-dependent obscuration which is necessary to explain the apparent difference between type 1 and type 2 AGN. In type 2 AGN, the line of sight from the AGN to the observer passes through the torus. Therefore, the torus obscures the central accretion disk and broad-line region (BLR). In type 1 objects, the accretion disk and BLR are directly visible to the observer. The torus seems to play a fundamental role in providing the fuel to feed the central accretion disk and the black hole. It connects the outer most part of the accretion disk in the influence of the black hole to the inner galactic region on scales of up to several hundred parsecs.

In the course of my PhD thesis, I have used optical spectroscopic observations to study a nearby Low Luminosity Quasi Stellar Objects (LLQSOs) sample, that were defined by the known Hamburg/ESO survey. The sources were observed with different spectroscopic techniques, therefore the attempt to taxonomy the sample faced differences in classification of some individual galaxies. Simulations have been applied to study that effect which is commonly known as 'aperture effect'.

As a second distinct part of this 3 year course, I have also worked on the construction

---

<sup>3</sup>[Traub \(1986\)](#) set the golden rule of separated telescopes: 'As viewed from a point in the focal plane, beams from separated telescopes must be recombined so that they appear to be coming directly from a single large telescope which has been masked so as to reproduce exactly the ensemble of collecting telescopes'

of one fundamental part of the LINC NIRVANA instrument. In particular, I have tested a specific component which has to be moved with respect to an altitude - azimuth mounting under vacuum conditions. The tilting of the instrument under different elevations due to the mounting results in a flexure of the system that has to be corrected by an algorithm.

The following chapters of the thesis are structured as follows:

**Chapter 2:** The present knowledge about the AGN and the endeavors towards a unified model of AGN are sketched out. Techniques that are applied for spectroscopic observations and particularly focusing on the ones that our sample has been observed are described in detail. The significance of the emission lines of such objects is discussed in order to preface the following chapter.

**Chapter 3:** An overview of the sample that is used in the thesis is given as the first section, while the analysis is drawn in detail. The analysis was focused on some specific detectable optical spectral lines that have been used to clarify the excitation state of the sources, and their main characteristic spectral features.

**Chapter 4:** As a result of the investigation in chapter 3, strong differences in the optical spectra of some sources depending on the spectroscopic technique used, were found. The aperture effect due to the instruments is simulated and also compared to SDSS observations.

**Chapter 5:** The current knowledge about the great efforts on the interferometry and the approach to high spatial resolution is reported. The description of the Large Binocular Telescope, its LINC NIRVANA instrument, and the principle of operation of its components are specified as part of this chapter.

**Chapter 6:** This chapter is focused on the laboratory tests that have been designed and came out during this course of the thesis. In particular, the working order of the system under different elevations in vacuum conditions, and the characterization of some components are discussed.





## 2. AGN properties and Optical Spectroscopy

*The current chapter aims to give a historical overview of the astronomical objects studied in this thesis. Previous studies on the host galaxies along with their AGN and their physical properties (Binney & Merrifield 1998) are reported in the following sections. In particular, the discussion of AGN unification models (Padovani 1997; Antonucci 1993) comprises an important section of this chapter. One of the major scopes of this thesis is the study of the optical emission lines in extragalactic objects, therefore part of the present chapter is dedicated to the optical spectroscopic techniques in astronomy, as well as the properties of optical emission lines of extragalactic sources and their properties.*

### 2.1 Host galaxies and their Active Galactic Nuclei

In 1963, the discovery of quasi-stellar objects (QSOs or quasars) was a real milestone in the observational astronomy. Around 1960, in Jodrell Bank, a group of radio astronomers were interested in looking at the angular sizes of radio sources. Their first survey covered about 300 sources with average sizes of 30 arcsec. Statistically, most of the sources were in the range of 5 arcsec to a few arcmin. However, a small number of targets (around 10) were extremely small, with sizes of less than 1 arcsec. In particular, one of them (3C 48) was identified in the optical window of the spectrum and its shape was point-like. The strong emission lines in its spectrum seemed to be peculiar, and its light was variable (Matthews & Sandage 1963). The radio source structure appeared to have two components, one of them being a jet.

The jet strongly indicated that the source was not a simple star, but a much more violent system. After a symposium which took place in 1963 at Texas, this type of objects became known as 'quasi stellar objects' (QSOs) or 'quasars'. In the early years of their discovery, the term 'quasars' was linked to the 'radio-loud quasi-stellar' objects and the category 'radio-quiet quasi-stellar' sources was known for the QSOs. This distinction was related to the fact that the radio quiet QSOs were nearly invisible in the radio domain. Nowadays, the meaning for both quasars and QSOs is the same, due to the similar optical properties in both categories. The studies of Schmidt (1969) had driven the definition of some properties of QSOs. In summary, the QSOs are star-like objects (identified with a radio source, in the beginning) with variable light in large cosmological distances. They show large ultra violet (UV) flux and their spectra is characterized by broad emission

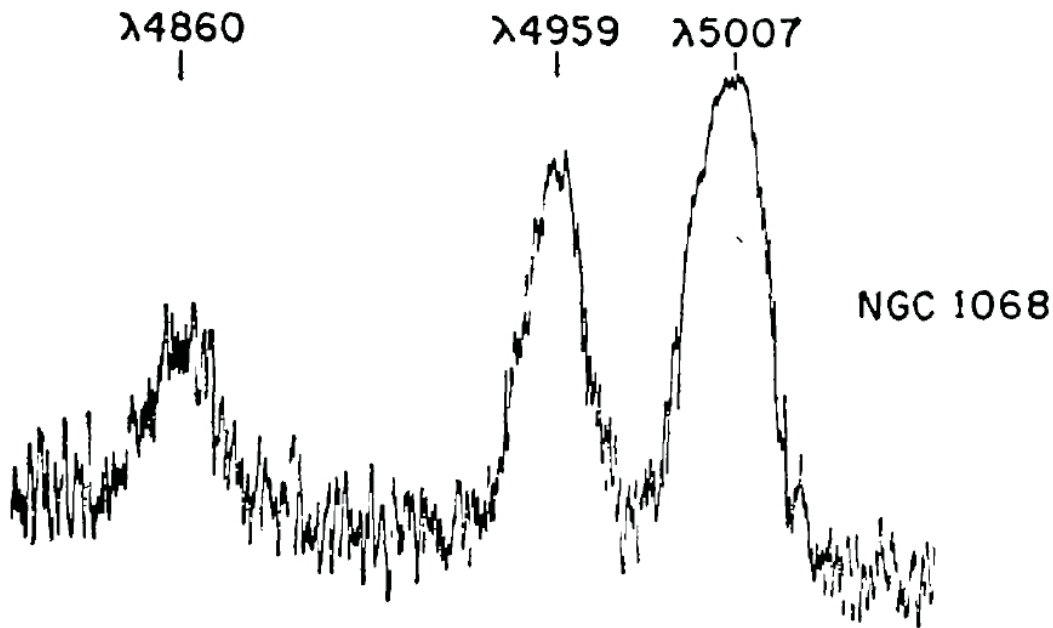


Figure 2.1: Microphotometer tracings of the emission lines  $\lambda$  4860  $H\beta$ , 4959 and 5007  $[O\text{III}]$  in the nebula NGC 1068 from Carl Seyfert, 1943, (Seyfert 1943).

lines, with absorption lines in some cases. The luminosity of their core can be thousand times more luminous than other galaxies.

QSOs are not the only objects that are part of the AGN family, they are the most luminous. AGNs are defined as compact regions in the centers of their host galaxies. They can be Seyfert, QSOs or Radio galaxies which differ in their luminosities and their spectral properties. AGN's spectra seems to be unlike to that one of stars and other galaxies, since it cannot be described in terms of blackbody emission. A unification model combining AGN types is described in next subsection 2.1.1.

Historically, Seyfert galaxies obtained their name by Carl Seyfert in 1943 (see Figure 2.1), who realized that several similar galaxies can form a class on themselves. However, the first time that an active galaxy (NGC 1068) was detected with strong broad emission lines in the optical window, was in 1908 by E.A Fath (Fath 1909).

Comparing to QSOs, Seyfert galaxies are lower luminous AGNs, and their host galaxy is clearly detectable and not outshone by the core, as it happens in QSOs. Seyfert galaxies have high surface brightness, and in the optical images they mainly appear to have spiral structure. Judging from the emission lines that these galaxies show, either narrow or broad or even both, they can be distinguished into two subcategories, Seyfert 1, and 2. Narrow emission lines are of the order of several hundred km/s. The spectrum of type 1 Seyfert includes both narrow and broad emission lines, in contrast to type 2 that they consist of only narrow emission lines. Intermediate classes such as Seyfert 1.5, 1.8 etc. were introduced based on a line width by Osterbrock (1981).

Giant elliptical galaxies with an active nucleus appear to be very bright in the radio domain. Radio galaxies are categorized in Broad Line Radio Galaxies (BLRGs) and in Narrow Line Radio Galaxies (NLRGs). BLRGs are the Seyfert type 1 and the NLRGs are Seyfert type 2, corresponding to the presence of broad emission lines and the absence

of them, respectively (Khachikian & Weedman 1974). Apart from the optical spectra classification, the radio sources are divided into two categories according to their radio morphology (Fanaroff & Riley 1974). Radio sources type Fanaroff-Riley Type I (FRI) have a very bright core and the surface brightness decreases outwards, in contrast to FR II that the surface brightness increases outwards.

Narrow lines profiles of AGN were identified by Heckman et al. (1980). This type of AGN show very low ionization nuclear emission-line region so called LINERs. LINERs are very common and they might be present in half of all the spiral galaxies. They can be distinguished from Seyfert galaxies and H II regions using some emission line flux ratios which are discussed in detail in the section 2.3.

Another interesting class of AGN are the BL Lac objects and the Optically Violent Variables (OVV). The first one took their name from the prototype source BL Lacertae. Both of them show short time-scale variations in contrast to other AGNs which are strong and rapid variable, but BL Lac objects miss the strong emission and absorption lines. The name blazars is commonly used for these two types of objects.

### 2.1.1 The Unification model

The name AGN includes a huge gamut of objects which have different appearance, but it is of high importance to indicate that there is not a real difference in their physical nature. Strong non-thermal emission in the core of the host galaxy is the common characteristic of AGNs.

The luminosity of some objects significantly larger than that of others, the presence or not of jets, and the anisotropic effects (i.e. different appearance depending on the objects orientation relative to the line of sight), are the three factors that support the different classification of these sources (Binney & Merrifield 1998). Keeping as reference the common characteristics of AGN members and their orientation to the observer, unified models have been proposed by scientists such as Antonucci (1993) and Urry & Padovani (1995). In principle, the unification of AGNs is an attempt to explain the diversity of observational properties in terms of a simple model (see Figure 2.2).

The basis of most unification models is that AGNs are not spherically symmetric and thus what you see depends on from where you look at them. The discovery of superluminal motion and the interpretation in terms of bulk relativistic motion of the emitter was what first made people realize that orientation in AGN was important. Rowan-Robinson (1977) work was one of the first efforts to unify Seyfert galaxies and radio sources. The disadvantage of this project was the lack of beaming consideration, which is the effect due to the relativistic motion of the AGN components. Nevertheless, a step forward for the importance of dust and IR emission came out from this research. Another important suggestion came from Scheuer & Readhead (1979); they proposed that radio-quiet quasars and flat spectrum radio-loud quasars constitute a single population assuming isotropic (extended) radio emission. However, some later observations with VLA and MERLIN (Orr & Browne 1982) had shown that low surface brightness extended structures are associated with sources that appear to be compact in less sensitive observations.

Antonucci (1993) and later Urry & Padovani (1995) summarized the simplest scheme (see Figure 2.2) that can be used to develop unifying models. The central engine is similar for any type of AGN and is believed that is Super Massive Black Hole (SMBH) in the center of the host galaxy, which is fed by an accretion disk. The Radio-quiet AGNs and

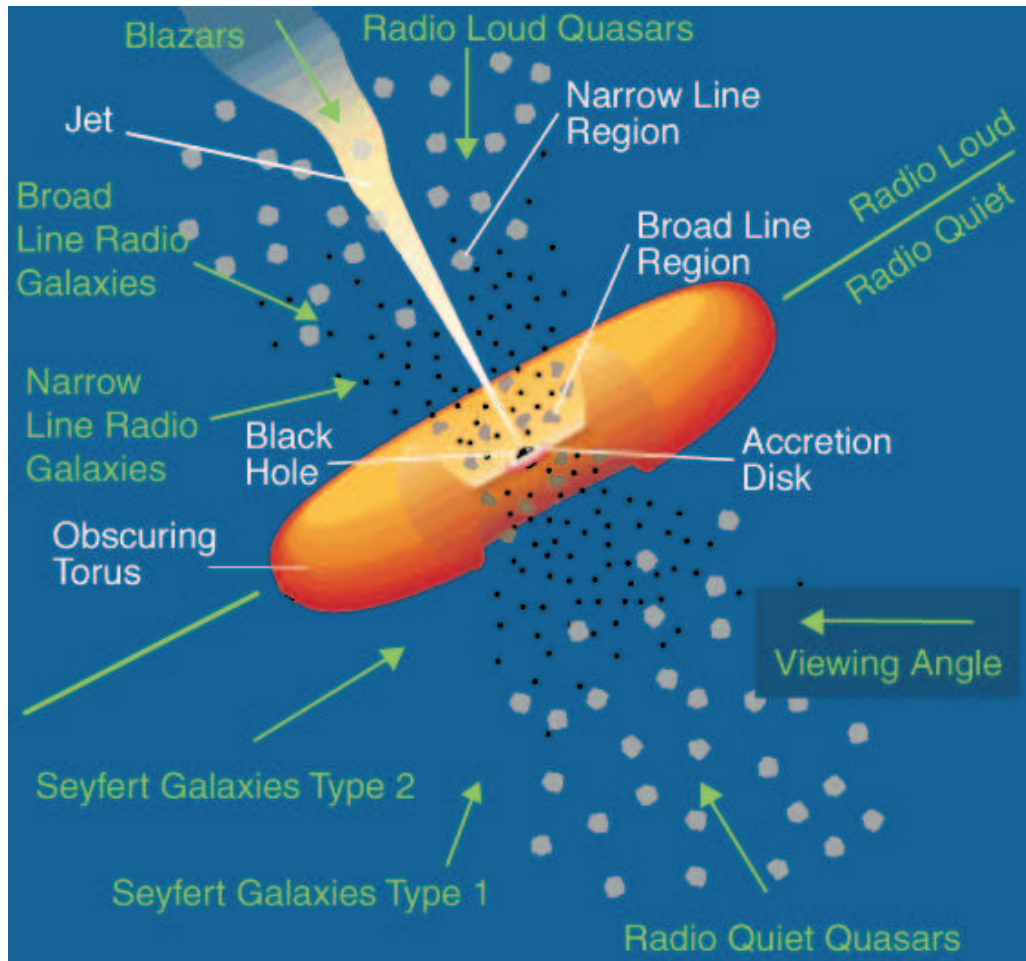


Figure 2.2: Schematic View of the Unification model of AGNs (Urry & Padovani 1995). A central massive black hole is surrounded by an accretion disk obscured by a torus. Depending on the viewing angle the AGN can be categorized in two major classes, the Radio Loud and the Radio Quiet Quasars. In the Radio Loud Quasars there is a contribution to their luminosity from the jet, which can be neglected in the Radio Quiet Quasars.

quasars have regions close to the nucleus that produce broad emission lines and continuum radiation. An opaque tori surrounds that region along the axis of which are located weak radio jets. When the torus is face-on to an observer, so that the line of sight reaches the nuclear region, the broad lines and the continuum are seen. Otherwise, only the narrow lines outside of the torus are visible directly. However, when the signal to noise ratio is high, radiation that is reflected into observer's direction because of the scattering by electrons producing polarization can be seen. In a few cases, twin jets of relativistic particles are present. When the axis of a radio-loud object is close to the line of sight, the observer can see a continuum with narrow and broad lines but also a one-sided jet. If it is too close to the line of the sight, then a beamed emission dominates and the object appears as a blazar.

## 2.2 Optical spectroscopy

Optical spectroscopy is a mean of studying the properties of physical objects based on measuring how an object emits and interacts with light. It can be used to measure attributes such as an object's chemical composition, temperature, and velocity. Since the optics is defined as the part of the electromagnetic spectrum that passes through the atmosphere, it involves visible, ultraviolet, or infrared light, alone or in combination, and is part of a larger group of spectroscopic techniques called electromagnetic spectroscopy. In the optical part of the spectrum the detectors operating are generally broad-band devices, sensitive to radiation over a wide range of wavelengths. Unlike to the shorter wavelengths, where the detectors response varies with the energy of the photon, the monochromatic signals cannot be observed directly (see Figure 2.3). A separate device called spectroscope, is required to separate out the radiation into its wavelength component before it is detected.

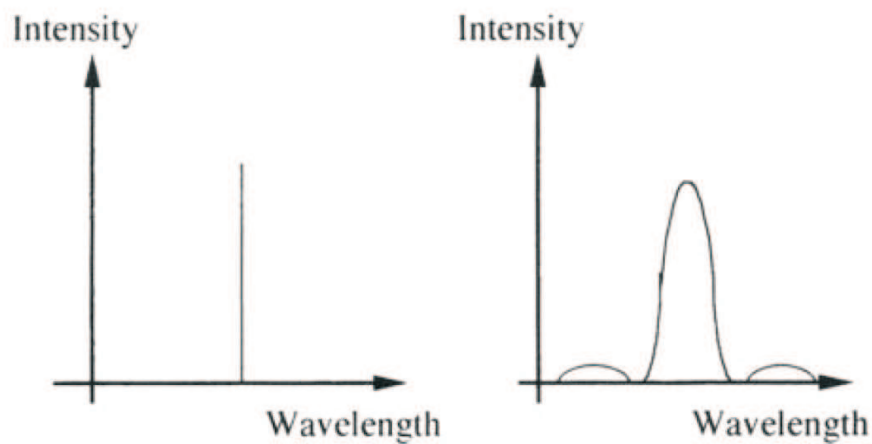


Figure 2.3: Instrumental profiles for a perfect spectroscope (left) and an optically perfect but real spectroscope (right). Figure from [Kitchin \(1996\)](#).

There are several processes whereby the radiation can be separated into its component wavelengths. The simplest is to use a range of filters placed before the detector to isolate particular regions of the spectrum. Traditionally, however, this method of studying the spectrum of an astronomical object is regarded as a separate subject from spectroscopy, and is called Photometry. A second method of obtaining a spectrum is based upon differential refraction and results in prism-based spectroscopes. The spectral resolution,  $R$ , is defined as

$$R = \frac{\lambda}{\Delta\lambda} \quad (2.2.1)$$

where  $\lambda$  is the operating wavelength and  $\Delta\lambda$  is the smallest wavelength interval that may be resolved.

However, most modern astronomical spectroscopes (see Figure 2.4) utilize interference effects in some way to produce the spectrum. The resulting devices which have found application in astronomy are Diffraction Gratings ([Hadden 1895](#)), Fabry-PCrot Etalons ([Babcock 1924](#); [Hernandez 1986](#)) and Fourier Transform Spectroscopes ([Ridgway & Hinkle 2010](#)).

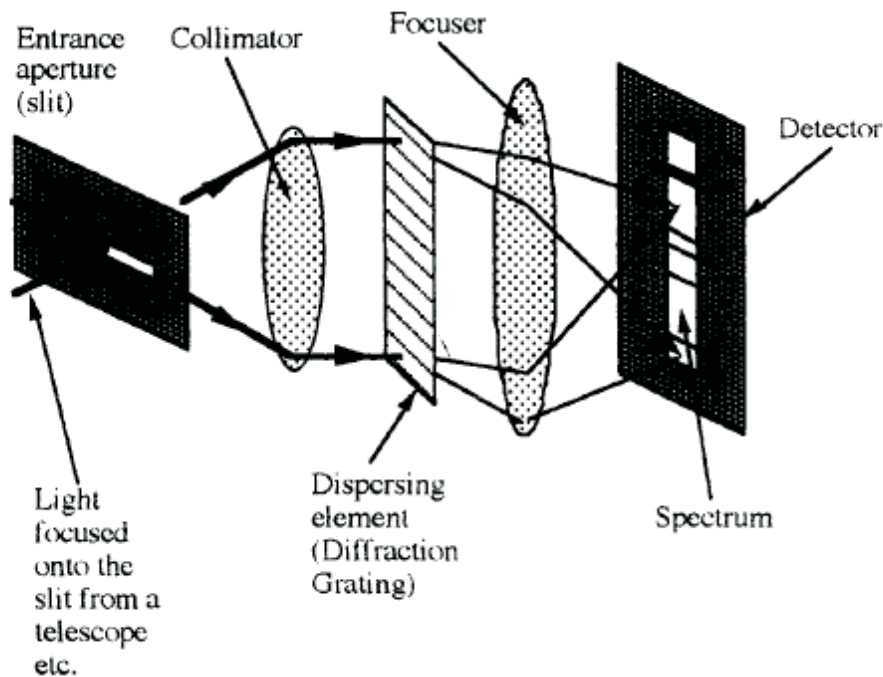


Figure 2.4: The basic components of a spectroscope. Polychromatic radiation (radiation of more than one wavelength) enters the monochromator through the entrance slit. The beam is collimated, and then strikes the dispersing element at an angle. The beam is split into its component wavelengths by the grating or prism. By moving the dispersing element or the exit slit, radiation of only a particular wavelength leaves the monochromator. Image credit : [Kitchin \(1996\)](#).

### 2.2.1 Techniques

The astronomical spectroscope must be as efficient as possible, because the sources are often very faint. The technique which aims to obtain spectroscopy of many of the objects within a telescope's field of view in a single exposure called Multi - object spectroscopy. A series of methods that are able to carry out such surveys are described in what follows.

**Slitless spectroscopy.** Instead of a spectrograph, a low dispersing element combined directly with the telescope can be used to collect the spectra of the brighter sources within a large field of view. For instance, an objective prism is placed in front of the telescope, which is often a Schmidt camera. The objective prism spectroscope (see Figure 2.5) is the simplest spectroscope in terms of design and its principle of operation, since it is just a large, low angle prism covering the whole aperture of the telescope. In this way every object on the image is represented by its spectrum. However, this method has serious disadvantages being the most important difficulty of finding radial velocities from the spectra because there is no comparison spectrum. The Crossley telescope is a 36-inch reflecting telescope located at Lick Observatory in California, USA and it utilizes a slitless spectrograph.

**Slitlet masks.** This method needs an initial image of the desirable sky region in order to define the location of the observable objects. Once the position of the sources is known small slits are milled in the corresponding locations in a metal plate. This plate is then substituted for the slit in a conventional spectrograph. Care must be taken that the spectra do not overlap; this usually limits the number of objects to 10 or so. Such

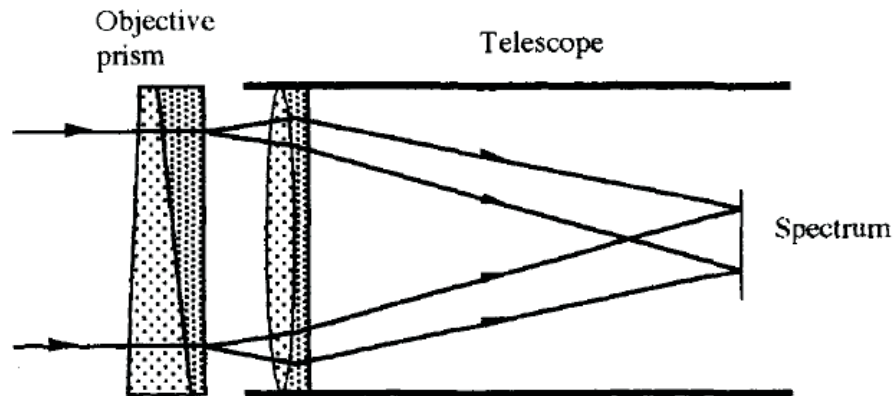


Figure 2.5: An objective prism spectroscope. Figure from [Kitchin \(1996\)](#).

systems have the advantage of good subtraction of the night sky, and very high efficiency. A slitlet mask is used with the ESO Faint Object Spectrograph and Camera (EFOSC2) instrument operated by ESO.

**Fiberfed spectroscopy.** In comparison with milling slitlets in a plate, this technique uses holes plugged with optical fibers. A spectrograph which is mounted on an optical bench receives the light transported via the fibers. At the spectrograph, the fibers are arrayed in a line, and act as the spectrograph slit. The faintest object that can be usefully observed is dependent upon how well one can calibrate the fiber to fiber transmissions, as separate fibers must be used to observe the night sky. A powerful fiber-fed spectrograph is placed at the MMT (Multiple Mirror Telescope) Observatory in Arizona, USA, named Hectospec ([Fabricant et al. 2005](#)).

**Echelle spectroscopy.** Echelle spectroscopy (see [Figure 2.6](#)) is a method of diffraction grating which is intended to be used in very high orders ( $n < 10$ ), resulting in very high resolving power. Echelle grating consists of a number of slits with widths close to the wavelength of the diffracted light like other types of diffraction grating. Normal spectrographs employ diffraction gratings that are intended to be used in low order ( $n = 1, 2, \text{ or } 3$ ), with colored glass filters used to prevent overlap of adjacent orders. An echelle uses a second dispersal element, usually another grating but sometimes a prism, at right angles to the first, in order to separate the successive spectral strips from each other. The VLT (Very Large Telescope) 8.2-m Unit Telescope utilizes an Ultraviolet and Visual Echelle Spectrograph (UVES), which is a high-resolution optical spectrograph located at the Nasmyth B focus of the telescope ([Dekker et al. 2000](#)).

**Coudé spectroscopy.** *Coudé* spectrographs are very stable, as they are located off the telescope, and the optics and gratings can be quite large since they do not need to be attached to the telescope. The use of echelles and fiberfed benchmounted spectrographs have largely replaced the *coudé* spectrograph; most modern telescopes are now built with altitude - azimuth mounts rather than equatorial mounts, leading to the further decline of *coudé* systems. The image from the telescope can often be brought into an area separate from the main observatory through an optical window. This area can then be temperature controlled to suit either the operators or the spectroscope (or both), reducing the problems due to temperature variations and improving observing conditions. *Coudé* and Nasmyth

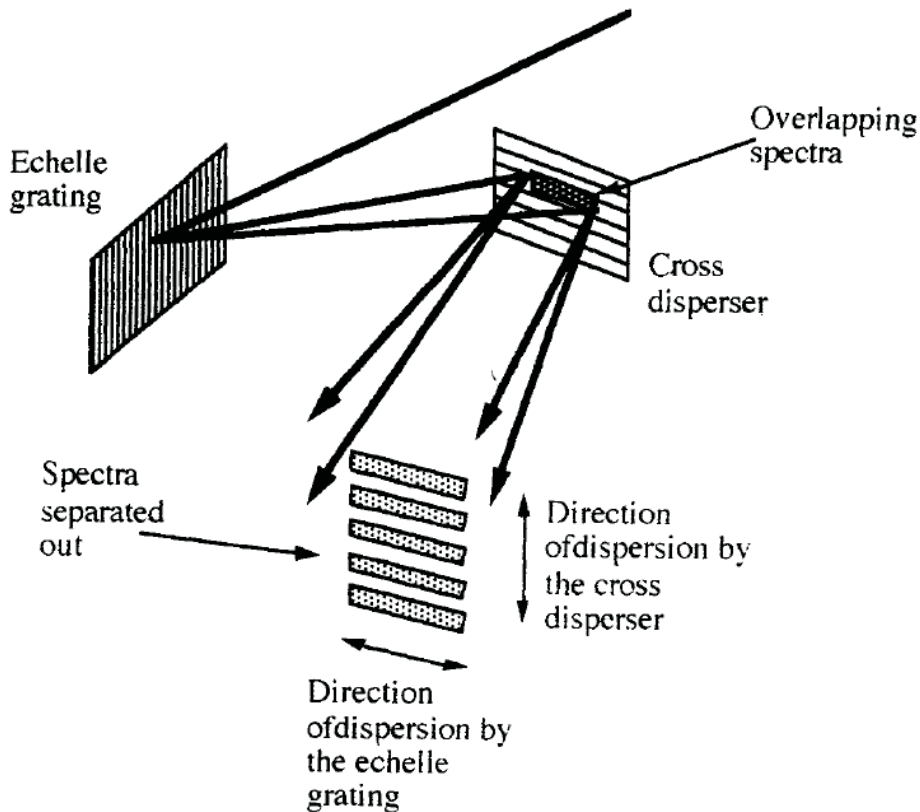


Figure 2.6: Schematic view of an echelle grating and a cross disperser. Figure from [Kitchin \(1996\)](#).

spectroscopes can thus be much larger, have higher dispersion and/or resolution, and be less robustly constructed than Cassegrain spectroscopes. The disadvantages of a *Coudé* or Nasmyth focus are that the image rotates as the telescope tracks the object across the sky, and that the focal ratio is usually very long.

**Integral field spectroscopy.** Integral field spectrographs are instruments which combine spectrographic and imaging capabilities, used to obtain spatially resolved spectra. The current technique allows to gather spectral information of the sky over a two-dimensional field of view. Hence the result is a data-cube, with axes of  $x$ ,  $y$  (or RA, Dec; the two spatial axes) and wavelength (velocity). An integral field spectrograph consists of two components: the spectrograph and an integral field unit (IFU). The 2D spatial plane is divided into a continuous array by the IFU in three main ways, lenslet array, fibers, and imager slicer (see Figure 2.7).

The most common technique in use the fibers (with or without lenslets) ([Allington-Smith et al. 1997](#)), where the light is transmitted via the fibers to a benchmounted spectrograph. Although the fibers are arrayed in a linear array at the spectrograph, their locations in the focal plane are known, and sophisticated data reduction techniques allows the astronomer to reconstruct a spectral image of the object. In the lenslet array technique ([Bacon et al. 1995](#)), the input image is split up by a microlens array, where the light from the observed object is concentrated into a small dot and dispersed by the spectrograph. When the input image is formed on a mirror that is segmented in thin horizontal



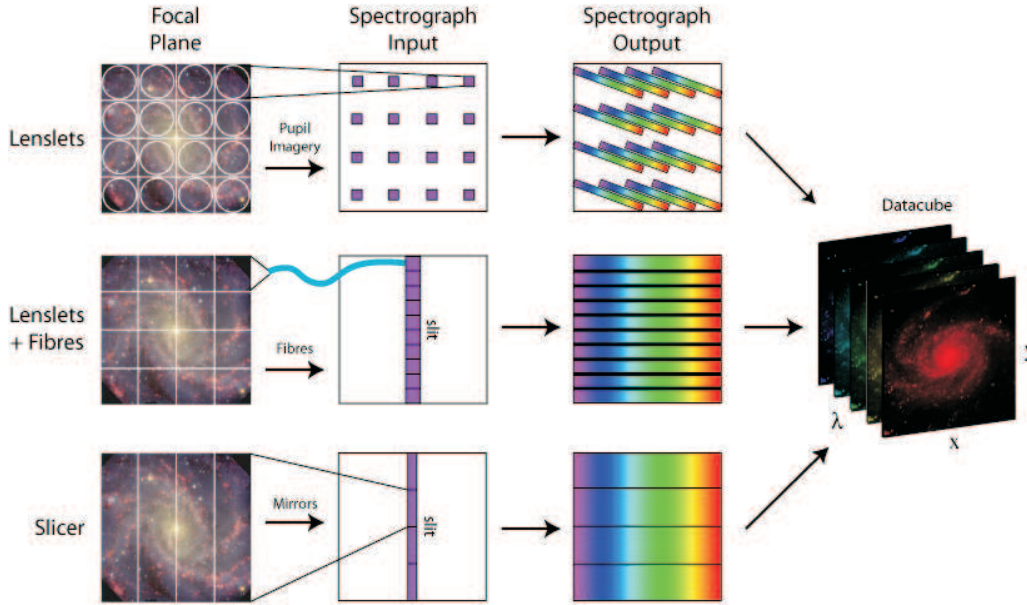


Figure 2.7: The main techniques for achieving integral field spectroscopy. Credit: M. Westmoquette, Figure from *Allington-Smith & Content (1998)*.

sections, sending each 'slice' in slightly different directions, the technique called 'imager slicer' (*Content 1997*). A second segmented mirror is arranged to reformat the slices so that, to form the slit of the spectrograph. NIFS is Near-Infrared Integral Field Spectrometer built by the Australian National University's Research School of Astronomy and Astrophysics utilized by Gemini observatory. The 4.2 William Herschel Telescope (WHT) located in Isaac Newton Group of Telescopes (ING), La Palma, Spain is an example of a telescope that utilizes two integral field spectrographs, the WHT SAURON using a lenslet array and the WHT INTEGRAL using fibers.

**Fourier transform spectroscopy.** Fourier transform spectroscopy, used particularly in the near infrared, employs an entirely different concept from the spectrographs described above. Instead of being dispersed in a spectrograph, the light of a wide band of wavelengths is passed through a Michelson interferometer with variable spacing of its two apertures. The resulting interferogram, which is an electronic record of the interference signal produced by the interferometer as the separation of the apertures is varied, is converted into a record of intensity versus wavelength by a computer, and is of extremely high spectral resolution.

### 2.2.2 Emission Lines of extragalactic objects

Extra-galactic objects are moving away from us, this leads to one of the main methods of estimating their cosmological distances,  $z$  (redshift), where  $z$  is defined by the equation :

$$z = \frac{\lambda_{obsv} - \lambda_{emit}}{\lambda_{emit}} \quad (2.2.2)$$

However, it also means that the observed spectra in the visual region wave was actually originated at shorter wavelengths. Therefore, for distant extra-galactic objects we may observe their rest - frame ultraviolet and far ultraviolet spectra via optical spectroscopy.

The Lyman- $\alpha$  line is often strong in emission, especially for active galaxies, quasars and similar objects. An efficient search for such objects may thus be made by using an objective prism on a Schmidt camera. There will be many thousands of spectra on such a plate, but the distant quasars etc will be easily picked out from the rest through the presence of the strong Ly $\alpha$  emission (see Figure 2.8). Cool gas clouds and galactic haloes along the line of sight to a distant object will result in many narrow absorption lines at lesser redshifts, also due to Ly $\alpha$ . These may sometimes be so numerous that they are referred to as the Ly $\alpha$  forest.

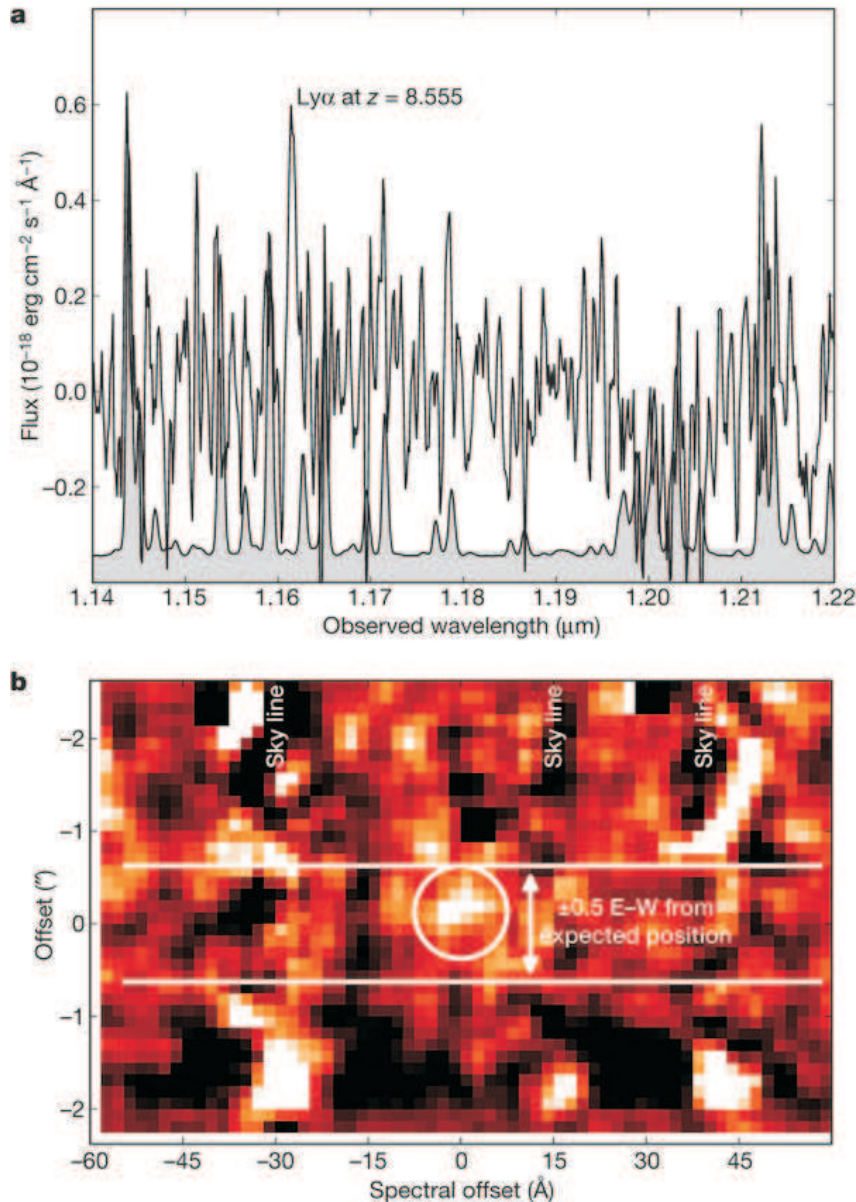


Figure 2.8: (a) The spectrum shows a faint emission line detected at  $6\sigma$  significance at a wavelength of  $11,615.6 \text{ \AA}$ , corresponding to a redshift  $z=8.5549 \pm 0.0020$  for Ly $\alpha$ , (b) The sky-subtracted two dimensional spectrum shows the projection of the spectrum along the spectral and right-ascension axes of the data cube (Lehnert et al. 2010).

On the contrary, the normally visible spectrum is observed for the nearer objects. Then, with many galaxies, the spectrum is just the total summary of the spectra of their

constituent stars and gas. Within the spectra of active galaxies, however, emission lines are frequently to be found, due to forbidden transitions. In quasars and Seyfert 1 galaxies, the allowed emission lines have velocity widths of 10000 km/s or so. The forbidden lines have widths of about 500 km/s and many of the lines arise from highly ionized states (see Figure 2.9). These kind of lines took their name due to their existence in the solar corona, therefore they are often called Coronal. In Seyfert 2 galaxies, all the lines are around 500 km/s in width, while in LINERS (Low Ionization Nuclear Emission Regions), the levels of ionization are much lower, as the acronym suggests.

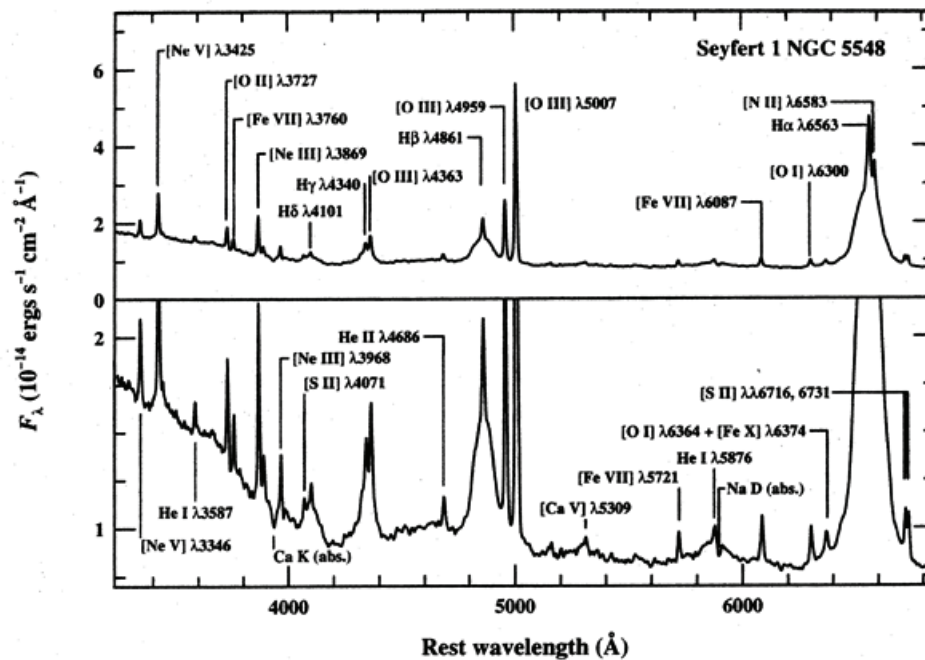


Figure 2.9: The optical spectrum of the Seyfert 1 galaxy NGC 5548. The prominent broad and narrow emission lines are labeled, as are strong absorption features of the host galaxy spectrum. The vertical scale is expanded in the lower panel to show the weaker features. The Full Width at Half Maximum (FWHM) of the broad components is about 5900 km/s, and the width of the narrow components is about 400 km/s. The strong rise shortward of 4000 Å is the long-wavelength end of the “small blue bump” feature which is a blend of Balmer continuum and [Fe II] line emission. This spectrum is the mean of several observations made during 1993 with the 3-m Shane Telescope and Kast spectrograph at the Lick Observatory. Data courtesy of A. V. Filippenko. Figure from Peterson (1997).

The emission lines of many active galaxies, including quasars, Seyferts, BL Lacs etc, vary on time scales of years or less, and in some cases the total luminosity may change as well. The active galaxies are often very strong emitters in the short wave and radio regions of the spectrum, with synchrotron radiation dominating in the latter. The overall spectrum of active galaxies is roughly constant in terms of energy per frequency decade, from the radio region to gamma rays. The nuclei of more normal galaxies, including our own, may have similar emissions on a smaller scale. The outer regions of galaxies generally have a roughly blackbody spectrum, peaking in the visible or near ultraviolet. Forbidden iron lines are an indicator of a starburst galaxy, and probably arise from the numerous supernovae occurring within them.

With the best of current instrumentation and techniques, slit spectra down to a visual magnitude of +23 are just about obtainable at a reasonable dispersion for emission line

objects in an exposure lasting all night. Since galaxies are often found in clusters, the various multi-object spectroscopes are frequently used to obtain many spectra simultaneously. In the nearer objects, H II regions and other hot nebulae can be highlighted by observing through a narrow band filter centered on one of their emission lines.

## 2.3 Sorting out Active Galactic Nuclei

The categorization of AGNs seems to be a complicated topic. The AGN phenomenon is concealed due to the lack of understanding the physics behind them. The one and only criterion for classifying the AGNs is the way that we observe them and not the fundamental differences between the various types. Various studies, depending on the selection criteria, morphology and line widths, have produced a variety of classification schemes. Spectroscopic studies have been proven to be a valuable tool for determining the main power source in active galaxies. A special research on the information contained in the relative intensities of the emission lines has been done by [Baldwin et al. \(1981\)](#). The main idea behind their classification scheme was to discriminate between the different excitation mechanisms operating on the line emitting gas.

The Active Galactic Nuclei (AGN) are believed to be supported by the gas accreted on to black holes at the centers of galaxies ([Shields 1978](#)). Depending on the level of the intensity of such activity (AGN), the galaxies can be categorized, comprising of quasi stellar objects (QSOs) at the high end down to Seyferts and Low-Ionization Nuclear Emission line Region (LINERs) ([Heckman et al. 1980](#)) at the low end (see [Figure 2.10](#)). LINERs appear to be the lowest luminosity AGN. Since the properties of a galaxy that hosts an AGN rely on the central source, considerations on the characteristics of its emission lines are required. According to [Koski \(1978\)](#) AGNs are photoionized by nonthermal or power-law continua, where [Dopita & Sutherland \(1995\)](#) postulated that fast shocks ([Heckman 1980](#); [Lípari et al. 2004](#)) may be responsible of some LINER activity. On the contrary Starburst galaxies are mainly ionized by hot stars ([Huchra 1977](#); [Filippenko & Terlevich 1992](#); [Shields 1992](#); [Maoz et al. 1998](#); [Barth & Shields 2000](#)). The line emitting gas in AGNs is photoionized by the central non-stellar continuum.

According to the standard unified model ([Antonucci 1993](#)), AGNs are divided into two main subcategories depending on the viewing angle of the central source and its continuum. Narrow permitted and forbidden emission lines (300-1000 km/s width) coming from the Narrow Line Region (NRL) and broad lines (2000-6000 km/s width) coming from the Broad Line Region (BLR) when it is viewed directly ([Veilleux & Osterbrock 1987a](#)). Some objects such as QSOs and Seyfert 1 galaxies show both types of lines. Seyfert 2 and LINERs show only narrow line emission. Actually, this makes AGN spectra differ from the spectra of most stars and many galaxies where lines are relatively weak and predominantly in absorption. LINERs are generally thought to be either photoionized by power-law continua ([Veilleux & Osterbrock 1987b](#)) or shock excited ([Dopita 1997](#); [Lutz et al. 1999](#)).

QSOs show strong optical continuum emission, X-ray continuum emission, and broad and narrow optical emission lines. The spectra of LINER, Seyfert and star forming galaxies, where the emission is powered by early type stars, cannot be distinguished from one other on the basis of any single flux ratio from any pair of lines ([Peterson 1997](#)), although some efforts have been made in this direction i.e [Stasińska et al. \(2006\)](#). The emission

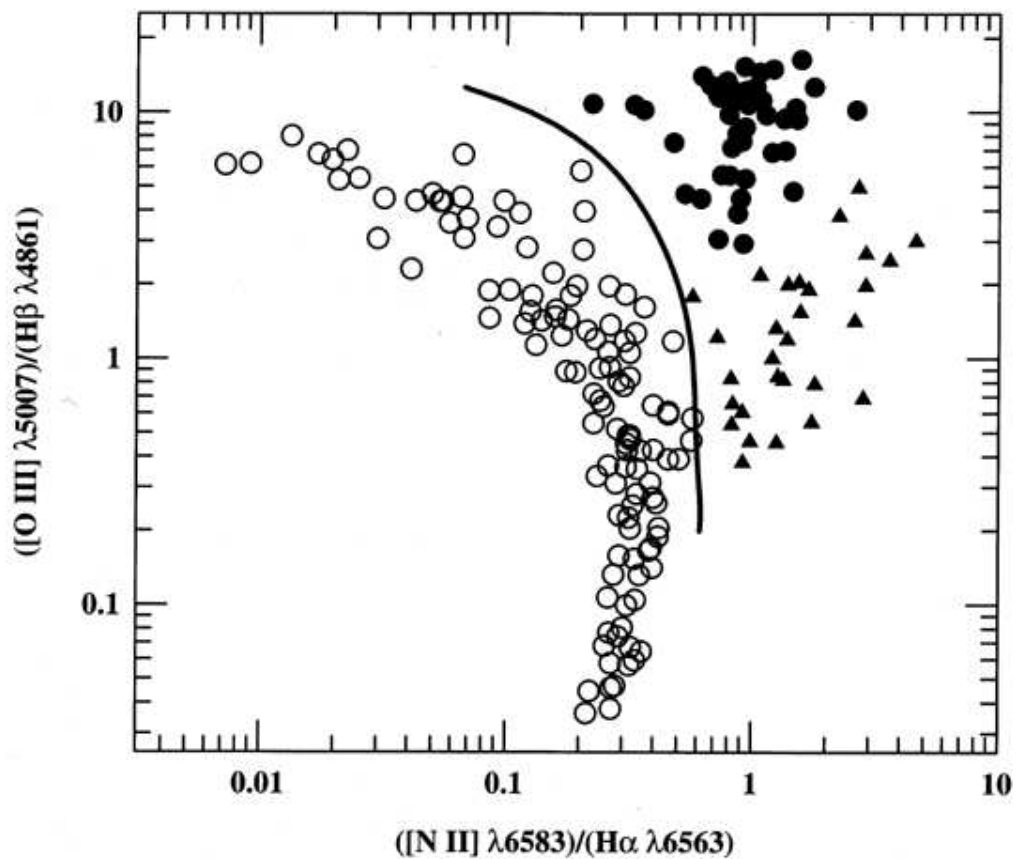


Figure 2.10: A diagnostic (or BPT) diagram for emission-line galaxies. The vertical axis is the  $[O\text{ III}] \lambda 5007 / H\beta \lambda 4861$  flux ratio and the horizontal axis is the  $[N\text{ II}] \lambda 6583 / H\alpha \lambda 6563$  flux ratio. Both ratios are based on lines close in wavelength and are therefore nearly reddening independent. The open circles are for  $H\text{ II}$  regions and similar sources that are clearly ionized by hot stars. The closed circles are narrow-line AGNs (Seyfert 2s and NLRGs) which are ionized by “harder” continua (i.e., with a greater fraction of high-energy photons, such as a power-law spectrum); the solid line is an empirical division between these two classes of object. The triangles represent LINERs, which can be distinguished from  $H\text{ II}$  regions by higher values of  $[N\text{ II}] \lambda 6583 / H\alpha$ , and from Seyfert galaxies by lower values of  $[O\text{ III}] \lambda 5007 / H\beta$ . Based on a similar diagram from Osterbrock (1989), p. 346. Figure courtesy of R. W. Pogge, based on data from (Veilleux & Osterbrock 1987a). Figure from Peterson (1997).

line flux ratios are sensitive to the shape of the ionizing continuum and the previous consideration can provide us a useful tool to investigate the ionizing source of LINERs, Seyferts and star forming galaxies associated with hot stars. Baldwin, Phillips and Terlevich (Baldwin et al. 1981), hereafter BPT, have shown that various types of objects with similar emission line spectra can be distinguished by considering the intensity ratios of two pairs of lines.

That can be represented in a ‘BPT’ diagram, which demonstrates how LINERs can be distinguished from normal  $H\text{ II}$  regions and Seyferts/QSOs on the basis of the  $[O\text{ III}] \lambda 5006.843\text{Å} / H\beta \lambda 4861\text{Å}$ ,  $[N\text{ II}] \lambda 6583.41\text{Å} / H\alpha \lambda 6562\text{Å}$ ,  $[S\text{ II}] \lambda \lambda 6716,6731\text{Å} / H\alpha \lambda 6562\text{Å}$ , and  $[O\text{ I}] \lambda 6300\text{Å} / H\alpha \lambda 6562\text{Å}$  flux ratios. This method was refined by Veilleux and Osterbrock (Veilleux & Osterbrock 1987a) who used flux ratios computed from two pairs lines which are close in wavelength, so that the systematic effects of reddening are minimized. They derived a semi empirical boundary line used to separate starbursts from

Seyferts with these diagrams. In their system the division between Seyferts and LINERs occurs at  $[O\text{III}]/H\beta = 3.0$ . [Ho et al. \(2003\)](#) stress, however, that this boundary has no strict physical significance. The ionization level of the NLR in large, homogeneous samples of AGNs spans a wide and apparently continuous range and there is no evidence for any clear transition between Seyferts and LINERs.

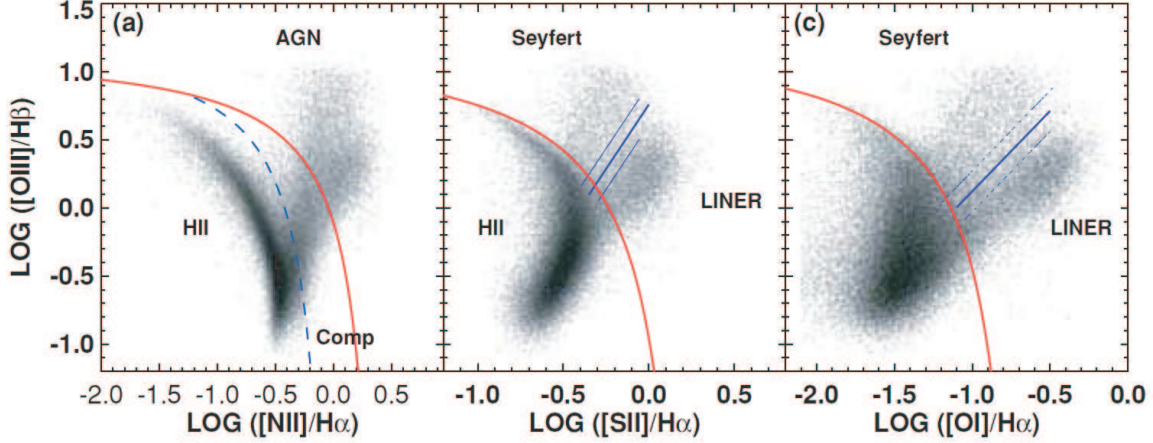


Figure 2.11: The three BPT diagrams showing our new scheme for classifying galaxies using emission-line ratios. The Ke01 extreme starburst classification line (red solid line), the Ka03 pure star formation line (blue dashed line), and the SeyfertLINER line (blue solid line) are used to separate galaxies into H II - region - like, Seyferts, LINERs, and composite H II AGN types. Adapted from [Kewley et al. \(2006\)](#).

A theoretical upper limit (Ke01) was defined by [Kewley et al. \(2001\)](#) to show the demarcation between starburst galaxies and AGN. They showed a new classification scheme, where a theoretical boundary lines which are used to classify Starbursts, Seyferts and LINERs. They used a combination of photoionization and stellar population synthesis models to place the upper limit on the location of star-forming models in the 'BPT' diagrams. An empirical line (Ka03) dividing pure star-forming galaxies from Seyfert and H II composite objects whose spectra contain significant contributions from both AGN and star formation added by [Kauffmann et al. \(2003\)](#). According to the new classification scheme (see Figure 2.11) the objects are defined as following:

**Star forming galaxies** lie below and to the left hand side of the Ka03 classification line in the  $[N\text{II}]/H\alpha$  and below and to the left hand side of the Ke01 in the  $[S\text{II}]/H\alpha$  diagrams:

$$\log([O\text{III}]/H\beta) < 0.61/[\log([N\text{II}]/H\alpha) - 0.05] + 1.3 \quad (2.3.1)$$

$$\log([O\text{III}]/H\beta) < 0.72/[\log([S\text{II}]/H\alpha) - 0.32] + 1.30 \quad (2.3.2)$$

and

$$\log([O\text{III}]/H\beta) < 0.73/[\log([O\text{I}]/H\alpha) + 0.59] + 1.33. \quad (2.3.3)$$

**Composite galaxies** lie between the two lines (Ka3 and Ke01) in the  $[N\text{II}]/H\alpha$

diagram:

$$\log([O\text{ III}]/H\beta) > 0.61/[\log([N\text{ II}]/H\alpha) - 0.05] + 1.3 \quad (2.3.4)$$

$$\log([O\text{ III}]/H\beta) < 0.61/[\log([N\text{ II}]/H\alpha) - 0.47] + 1.19. \quad (2.3.5)$$

**Seyfert galaxies** lie above the Ke01 line on the three diagnostic diagrams (Figure 2.11) and above the Seyfert - LINER line (blue solid) on the [S II] and [O I] diagrams:

$$\log([O\text{ III}]/H\beta) > 0.61/[\log([N\text{ II}]/H\alpha) - 0.47] + 1.19 \quad (2.3.6)$$

$$\log([O\text{ III}]/H\beta) > 0.72/[\log([S\text{ II}]/H\alpha) - 0.32] + 1.30 \quad (2.3.7)$$

$$\log([O\text{ III}]/H\beta) > 0.73/[\log([O\text{ I}]/H\alpha) + 0.59] + 1.33. \quad (2.3.8)$$

or

$$\log([O\text{ I}]/H\alpha) > -0.59 \quad (2.3.9)$$

and

$$\log([O\text{ III}]/H\beta) > 1.89/\log([S\text{ II}]/H\alpha) + 0.76 \quad (2.3.10)$$

$$\log([O\text{ III}]/H\beta) > 1.18/\log([O\text{ I}]/H\alpha) + 1.30. \quad (2.3.11)$$

**LINERs** lie above the Ke01 classification line on the three diagrams and below the Seyfert - LINER line on the [S II] and [O I] diagrams:

$$\log([O\text{ III}]/H\beta) > 0.61/[\log([N\text{ II}]/H\alpha) - 0.47] + 1.19 \quad (2.3.12)$$

$$\log([O\text{ III}]/H\beta) > 0.72/[\log([S\text{ II}]/H\alpha) - 0.32] + 1.30 \quad (2.3.13)$$

$$\log([O\text{ III}]/H\beta) < 1.89/\log([S\text{ II}]/H\alpha) + 0.76 \quad (2.3.14)$$

$$\log([O\text{ III}]/H\beta) > 0.73/[\log([O\text{ I}]/H\alpha) + 0.59] + 1.33 \quad (2.3.15)$$

or

$$\log([O\text{ I}]/H\alpha) > -0.59 \quad (2.3.16)$$

$$\log([O\text{ III}]/H\beta) < 1.18/\log([O\text{ I}]/H\alpha) + 1.30. \quad (2.3.17)$$

Nevertheless, there are some 'ambiguous' objects that classified as one type in some of the diagrams and as another type in the other diagrams. In the following chapter, we proceed with an optical spectroscopic analysis of some nearby objects and their classification according to their emission lines.





# 3. Optical spectroscopic studies on the Low Luminosity Quasi Stellar Objects sample

*The present chapter mainly focuses on the optical spectroscopic analysis of a sample of Low Luminosity Quasi Stellar Objects (LLQSOs) using two optical data sets. LLQSOs are key objects in the context of galaxy evolution. They may represent the transition population between luminous QSOs and less luminous local galaxies and Seyferts. The main aim of the present project is the global spectroscopic characterization of the LLQSOs sample. Specifically, we analyse the ionizing source of each galaxy in the sample and distinguish between different excitation mechanisms. Therefore, we perform line fitting of the most important emission lines relying on the BPT diagnostic diagrams, to compare the flux ratios of lines in low ionization species to those in high ionization ones. The analysis of the hydrogen recombination lines broad components and the electron density are presented, too.*

## 3.1 The nearby low luminosity QSO sample

The nearby Low Luminosity Quasi Stellar Objects LLQSOs sample has been drawn from the Hamburg/ESO survey (HES) (Wisotzki et al. 2000) which yields a well-defined, flux limited sample,  $B_J < 17.3$ . The Hamburg/ESO survey covers a large area on the sky, and the quasar candidate selection takes care to ensure that low redshift, low luminosity objects, i.e AGN with prominent host galaxies, are not systematically missed. It utilizes photographic objective prism plates taken with the ESO 1 m Schmidt telescope on La Silla. Plates in 380 different fields were obtained and subsequently digitized at Hamburg, followed by a fully automated extraction of the slitless spectra. In the case of the HES, the flux limit varies considerably between individual fields, mostly due to changes in the seeing and night-sky conditions, but also because of plate quality. Thus, each field maintains its own flux limit, always corresponding to the same limiting signal to noise ratio in the spectra. As long as redshift-dependent selection effects are neglected, the survey selection function is identical to the effective area of the survey, combining the 380 flux limits into single array that provides the total survey area as a function of magnitude. Figure 3.1 shows that the average extinction-corrected limiting magnitude of the HES is  $B_J < 17.3$ , but with a dispersion of 0.5 mag between individual fields. There is essentially no bright limit, with 3C 273 recovered as the brightest AGN in the sample.

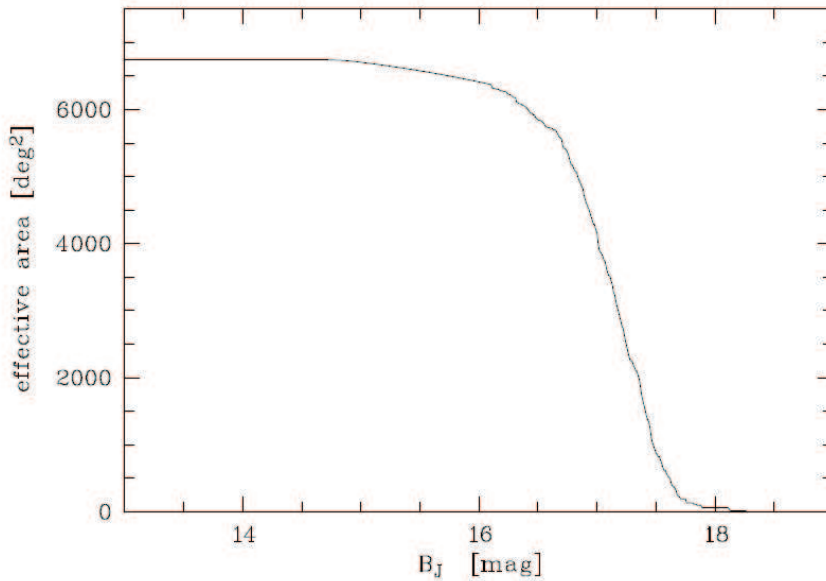


Figure 3.1: Effective area of the Hamburg/ESO survey as a function of the Galactic extinction corrected BJ magnitude (Schulze et al. 2009).

For each of the  $10^7$  objects extracted, spectral information at  $10\text{-}15 \text{ \AA}$  resolution in the range  $3200 \text{ \AA} < \lambda < 5200 \text{ \AA}$  is recorded. The extraction of spectra and the criteria to select AGN candidates contained a special treatment of extended sources, making the selection less sensitive to the masking of AGN by their host galaxies. In contrast to classical QSO selection, which tends to miss luminous AGN especially at low- $z$ , this property makes the HES unique among optical survey. In particular the main selection criteria that were used for the HES were the 'colors' and spectral feature detection. The first set of criteria mainly exploits continuum properties and can be, to a certain extent, related to traditional photometric colours. In this respect, the key criteria of HES was (i) the very relaxed UV excess selection criteria, equivalent to  $(U - B) < -0.18$ , (ii) the small errors of determining the UV excess in individual objects, and (iii) the high spectral resolution of the ESO objective prism spectra which ensures low stellar contamination without sacrifices in completeness. Full detailed description about the selection criteria can be found in Wisotzki et al. (2000).

Summarizing, the main scientific goals of the HES are to:

- Compile samples of high-redshift ( $1.5 < z < 3.2$ ), bright QSOs suited for high-resolution spectroscopy (e.g., for the ESO-VLT).
- Provide targets for ultraviolet spectroscopy with HST.
- Discover new gravitationally lensed systems.
- Construct large flux-limited and bias-free samples of bright low-redshift QSOs and Seyferts for host galaxy studies.
- Determine the local luminosity function of QSOs.
- Study the evolution of the most luminous part of the QSO population.

The (LLQSOs) sample consists of a subsample of the HES sources with small cosmological distance. Only objects with redshift  $z \leq 0.06$  (see Figure 3.2) were selected in order to ensure the observability of the diagnostic CO(2-0) rotation vibrational band head absorption line in the near infrared (NIR). This band is important for the stellar population analysis. This line is then still accessible in the K-band. The redshift limit was the only constraint for the targets to be chosen. With this criterion we end up with a volume limited sample of 99 LLQSOs, with absolute visible magnitudes just below the classical Seyfert / QSO demarcation.

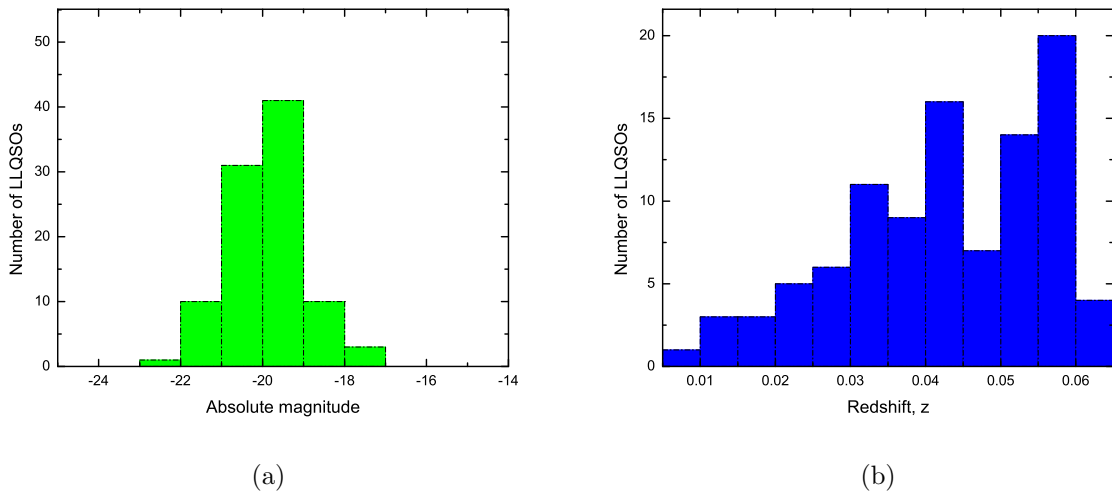


Figure 3.2: (a) Magnitude and (b) redshift distribution of the nearby LLQSO sample.

Previous CO(1-0) and HI studies (Bertram et al. 2007; König et al. 2009) show that the hosts of LLQSOs are rich in molecular/atomic gas ( $M_{H_2} \approx 5 \cdot 10^9 M_\odot$ ,  $M_{HI} \approx 10^{10} M_\odot$ ) and that their global star-forming properties are intermediate to those of local Seyfert and non-active galaxies, and higher- $z$  QSOs (e.g., PG QSOs) and ULIRGs. A recent work on the HE sample by Schulze et al. (2009) show that the evolution-corrected local luminosity function within  $-19 < M_{BJ} < -26$  is well described by a single power law of slope  $\alpha = -2.6$ , still significantly shallower than the  $z = 0$  extrapolation of the AGN luminosity function measured at higher redshifts. Furthermore, a very tight correlation between  $H\alpha$  luminosities and broad band absolute magnitudes  $M_{BJ}$  over the entire luminosity range of the sample, confirms that host galaxy contamination to the  $M_{BJ}$  magnitudes is not of high importance. Studies of the low-redshift active black hole population, residing in broad-line active galactic nuclei and black hole masses and Eddington ratios estimations (Schulze & Wisotzki 2010), show that the observed black hole masses cover a range  $10^6 - 2 \cdot 10^9 M_\odot$ , therefore lying in the category of SMBHs and the Eddington ratio is roughly confined between 0.01 - 1.

It is worthwhile to mention that no luminosity discrimination between QSOs and Seyfert 1 galaxies was applied by the Hamburg/ESO Survey. This has a direct implication on the absolute brightness distribution (see Figure 3.2b) of the LLQSO subsample. It clearly probes the low luminosity tail of the local quasar luminosity function (Koehler et al. 1997). All objects in the sample have absolute  $B_J$  magnitudes exceeding (i.e., dimmer

than) the traditional boundary  $M_B - 22$  mag between QSOs and Seyfert I galaxies. This boundary has no astrophysical motivation, as it was technologically induced at the time of its introduction (Schmidt & Green 1983). However, to respect the commonly used definition of the term QSO, the term low-luminosity QSO is used throughout the study for objects identified in QSO surveys that may be fainter than the traditional boundary magnitude. Not only the HES but also the PG Bright Quasar Survey provide low-luminosity QSOs in their samples.

## 3.2 Observations and Data Reduction

Optical spectroscopic observations for our sample were obtained from two surveys. The first data set used was the Hamburg/ESO survey from where optical spectrum from 89 sources were taken and the resolution was varied from  $\sim 8 \text{ \AA}$  to  $\sim 21 \text{ \AA}$ . Additionally, we retrieved spectroscopic observations ( $\sim 5 \text{ \AA}$ ) from the 6 Degree Field Galaxy survey (6DFGS) (Jones et al. 2004, 2009) for 59 out of the 99 targets of the nearby LLQSOs sample. Some of the most important characteristics of the LLQSO sample are presented in Table 3.1.

### 3.2.1 Hamburg/ESO Survey Observations

The HES sample observations were carried out with 3 ESO telescopes were used, the 3.6 m, the 2.2 m and the 1.54 m Danish telescope (see Figure 3.3). Long-slit low - resolution spectra of all candidates were obtained during five observational campaigns between 1990 and 2000. The telescopes are part of the La Silla Paranal Observatory which is located in the southern part of the Atacama desert in Chile and at an altitude of 2400 meters. The ESO 3.6 m telescope has a horseshoe/fork mounting, and an interchangeable top unit allowing the secondary mirror to be changed from a F/8 to a F/35 Cassegrain focus. The 2.2 m telescope has a fork mounted Ritchey-Chretien, and the Danish telescope has an off-axis mount and the optics are of a Ritchey-Chretien design (Ritchey 1928). Further details about the observatory and the telescopes can be found in their webpage (<http://www.eso.org/sci/facilities/lasilla/>).

The ESO Faint Object Spectrograph and Camera 2 (EFOSC2), the Boller and Chivens (B&C) spectrograph and the Danish Faint Object Spectrograph and Camera (DFOSC) are the instruments that were used for the spectroscopic observations. The EFOSC2 is a very versatile instrument for low resolution spectroscopy and imaging. The instrument has multi mode capability including normal/polarimetric imaging/spectroscopy (several submodes in each), multi-object spectroscopy and coronagraphy. The Boller & Chivens spectrograph has been equipped with a special dioptric camera to be used with the f/15 Cassegrain focus. The opto-mechanical configuration allows for a fixed angle between the incident and diffracted beam axis of the grating (configuration angle). The grating is mounted in an adjustable rotating cell that permits the choice of the central wavelength and spectral orders (grating angle). DFOSC is a focal reducer type spectrograph/camera similar in concept and in layout to ESO's EFOSC2. DFOSC consists of a collimator and a camera, between which are placed a filter and grism wheel. An aperture wheel is located at the telescope focus. All wheels have 8 positions. The instrument offers the possibility of changing between direct imaging and spectroscopy in less than a minute. The spectroscopic mode offers resolutions from about  $1\text{-}20 \text{ \AA}$  for a  $1''$  slit.

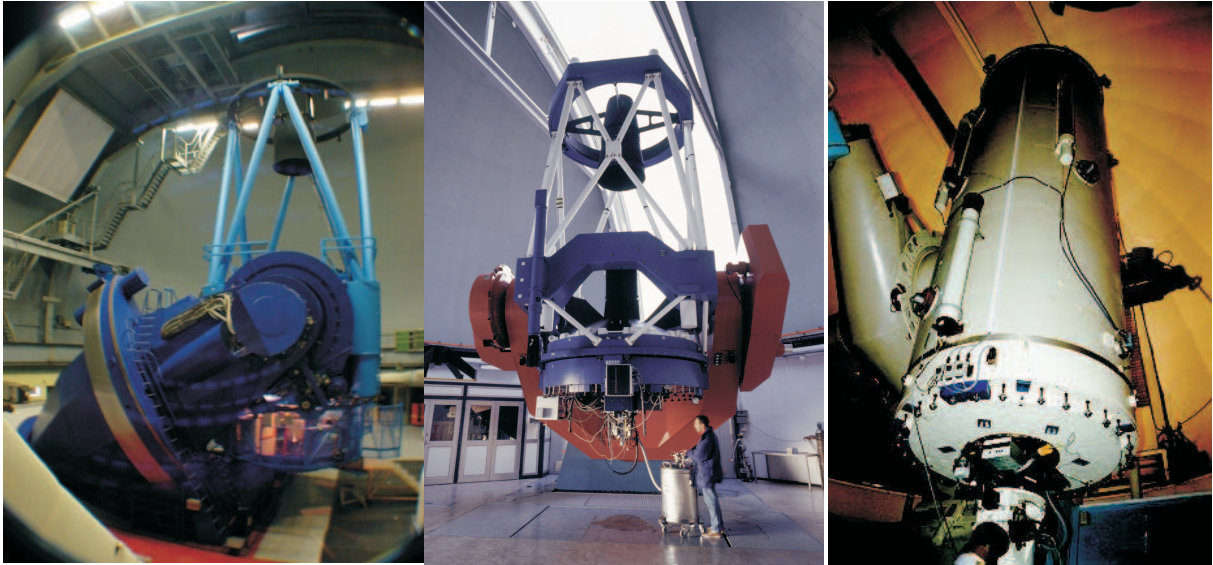


Figure 3.3: The three ESO telescopes located in La Silla Paranal Observatory. Right: The 3.6 m ESO telescope, Center: The 2.2 m ESO telescope, Left: The Danish telescope 1.54 m. Image credit : ESO.

At the two largest telescopes the exposure time was 5 minutes and at the 1.52 m telescope was between 10-30 minutes. To perform the relative flux calibration two or three spectrophotometric standard stars from Oke (1990) were used. Depending on the seeing, the slit width varied between  $1''.5$  and  $2''.5$ . The slit position angle was always East - West. The majority of the sources appear to have a morphology either of an ellipse or circle and only a few of them show spirals in their morphological type.

The data were fully reduced and calibrated at the moment of observations. Summarizing, the data reduction was performed under MIDAS (Banse et al. 1983; Grosbøl & Ponz 1990) and followed standard procedure (Llebaria & Martinis 1990). Arc spectra were taken at zenith position to determine the grism of grating dispersion relations; the zero point was adjusted in each spectrum using night sky emission lines. The spectra were optimally extracted with an algorithm similar to that of Horne (1986). In particular, leaving only the amplitudes as free parameters, the extraction procedure minimizes contamination from nearby sources, while at the same time the extraction windows (and subsequent photometry) are limited to apertures of the size of the seeing disk. Corrections for atmospheric extinction were applied by using a standard La Silla extinction curve (Burki et al. 1995). The flux calibration accuracy, monitored by the standard star spectra, is for many better than 20 %, but due to the narrow slit the data should not be considered spectrophotometric. However, no special effort to do spectrophotometry was made, the main purpose of the spectra being redshift and type confirmation. More information about the data reduction and the follow up spectroscopic observations can be found in Reimers et al. (1996).

### 3.2.2 6 Degree Field Galaxy Survey

The Six-Degree Field (6dF) multi-fibre spectrograph is an instrument able to record 150 simultaneous spectra over the 5.7 field of the UK Schmidt Telescope, UKST (Parker et al. 1998; Parker & Watson 2000; Saunders et al. 2001). It has been constructed by the Anglo-Australian Observatory (AAO) (see Figure 3.4).

6dF employs an  $r\vartheta$  robotic fibre positioner using fibre-placement technology where can place fibre buttons directly and accurately on the convex focal surface of the UKST, via a curved radial arm matched to the focal surface. This is coupled with a complete  $> 360^\circ$   $\vartheta$ -travel and with a pneumatically controlled fibre gripper traveling in the  $z$ -direction. Gripper positioning is honed (to  $< 10 \mu\text{m}$ ) using an in-built small CCD camera to permit centroid measurement from back-illuminated images of each fibre. Two identical field plate units are available, which allows one to be mounted on the telescope taking observations whilst the other is being configured by the 6dF robot. The size of the science fiber is  $6.7''$  ( $100\mu\text{m}$ ).

All 6dFGS data taken prior to 2002 October used 600V and 316R reflection gratings, covering  $4000 - 5600 \text{ \AA}$  and  $5500 - 8400 \text{ \AA}$ , respectively and signal-to-noise ratio  $\sim 10$  per pixel. The wavelength coverage is  $3900 - 5600 \text{ \AA}$  and  $5400 - 7500 \text{ \AA}$  and the grating and camera angles (and hence dimensionless resolutions) are identical. The observing strategy typically allows 35 survey fields to be observed on a clear night. Each field is observed with both V and R gratings that are later spliced to reconstruct a single spectrum from these two observations. Integrations were a minimum of 1 h for the V spectrum and 0.5 h for the R spectrum, although these times were increased in poor observing conditions.

The reduction of the spectra uses a modified version of 2DFDR package developed for the 2 Degree Field Galaxy Redshift Survey (Colless et al. 1999, 2007). All data are flux calibrated using 6dFGS observations of the standard stars Feige 110 and EG274. The same fixed average spectral transfer function is assumed. for each plate at all times. Differences in the transfer function between individual fibers are corrected for by the flat-fielding. The extracted spectra for each field are combined, usually weighted by S/N to cope with variable conditions. The reduced data can be retrieved by the online data base at <http://www-wfau.roe.ac.uk/6dFGS/>, which are publicly accessible. Further information and details about the instruments, the survey, the observations and the quality of the spectra can be found in the webpage above.

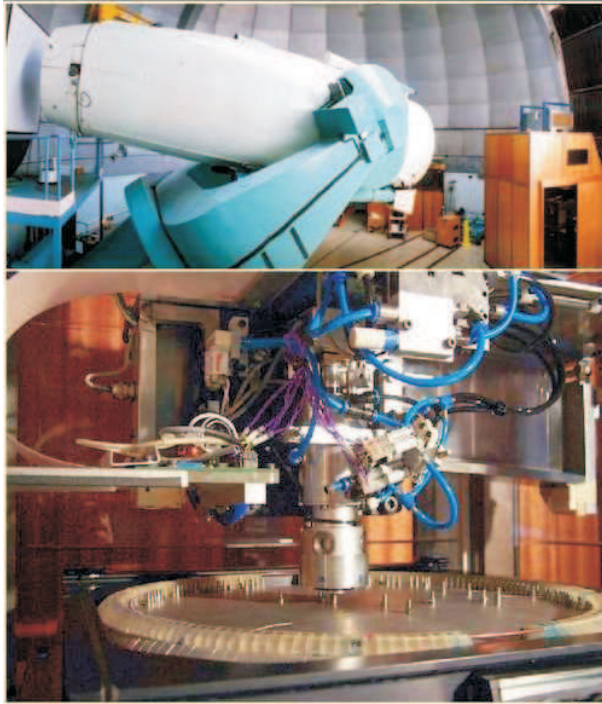


Figure 3.4: Upper: UK Schmidt Telescope and Lower: 6dF robotic positioner. Image credit: Anglo Australian Observatory (AAO).

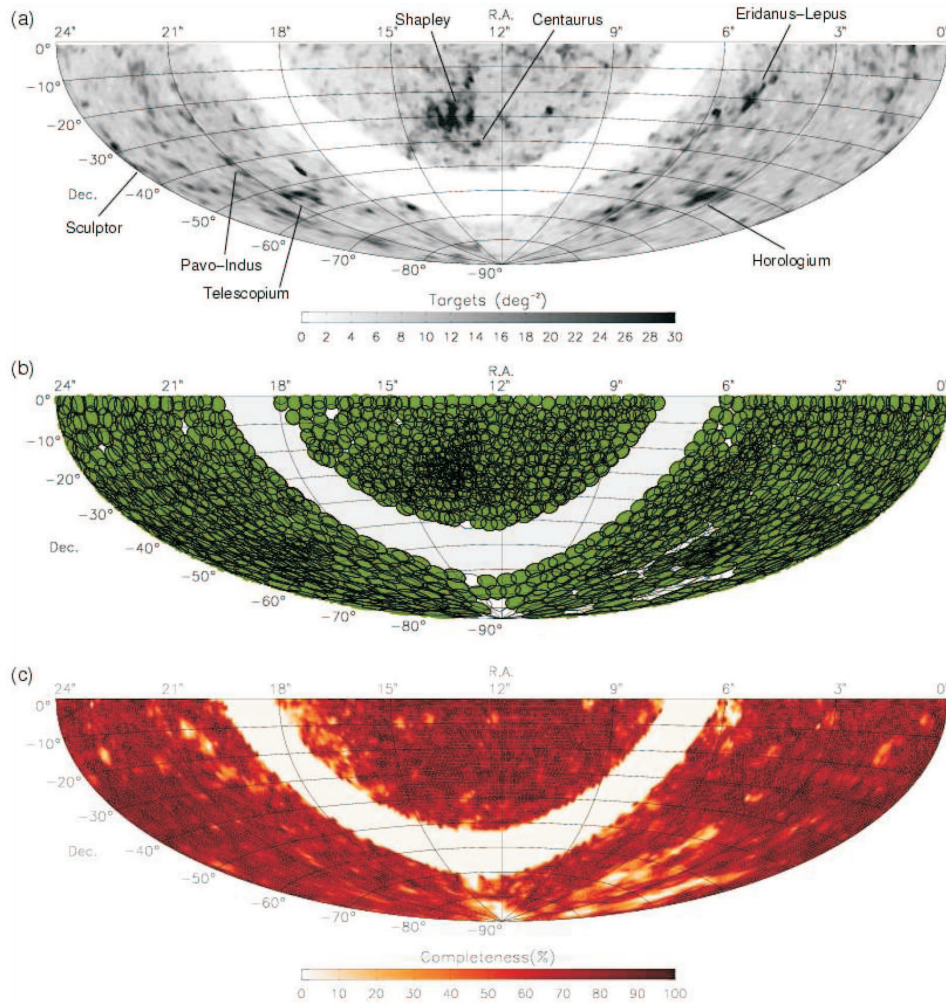


Figure 3.5: (a) Density of 6dFGS target sources (per square degree) on the sky; key supercluster overdensities are labelled. (b) Full 6dFGS field coverage (filled discs) and unobserved target fields (open circles). (c) Redshift completeness for  $K \leq 12.65$ . All panels show equal-area Aitoff projections Figure from Jones et al. (2009).

HE name	6dFGS name	ID <sup>1</sup>	RA	DEC	B-band	B-band	redshift
					Absolute magnitude	Blue magnitude	
HE0003-5023		1	1.42958	-50.1175	-20.3222	15.51	0.0334
HE0021-1810		2	5.915	-17.8978	-19.9870	16.9	0.0535
HE0021-1819	g0023554-180251	3	5.98292	-18.0483	-19.7443	17.13	0.0532
HE0022-4546	g0025013-452955	4	6.26125	-45.4947	-20.3000	16.69	0.056
HE0036-5133	g0039159-511702	5	9.815	-51.2836	-19.7930	15.71	0.0288
HE0038-0758		6	10.22167	-7.70042	-19.4879	17.42	0.054
HE0040-1105	g0042369-104922	7	10.65375	-10.8221	-18.8934	17.45	0.042
HE0045-2145	g0047413-212927	8			-19.5761	15.27	0.0214
HE0051-2420	g0053544-240437	9	13.48083	-24.0775	-19.6500	17.34	0.056
HE0103-3447		10	16.44458	-34.5307	-20.0200	17.01	0.057
HE0103-5842		11	16.32292	-58.4383	-19.1507	16.1	0.0257
HE0108-1631	g0111143-161555	12	17.81083	-16.2633	-20.6229	16.2	0.052
HE0108-4743	g0111097-472735	13	17.79333	-47.4619	-19.7601	15.33	0.0239
HE0111-1506	g0113499-145057	14	18.45833	-14.8449	-20.4730	16.38	0.0527
HE0114-0015		15	19.2675	0.00708	-19.7777	16.75	0.0456
HE0119-0118		16	20.49958	-1.03986	-20.9070	16.03	0.0547
HE0122-5137		17	21.25458	-51.3642	-19.8429	16.98	0.052
HE0125-1904		18	22.02875	-18.8104	-20.4361	15.96	0.043
HE0126-0753	g0129067-073830	19	22.28417	-7.64292	-20.0800	16.91	0.056
HE0149-3626	g0151419-361116	20	27.92458	-36.1871	-19.7788	16.06	0.0335
HE0150-0344		21			-19.6034	17.03	0.0478
HE0203-0031	g0206160-001729	22	31.56625	-0.29125	-21.0346	15.33	0.0424
HE0212-0059	g0214336-004600	23	33.64042	-0.76764	-20.5802	14.73	0.0264
HE0224-2834	g0226257-282059	24			-20.4048	16.76	0.0605
HE0227-0913	g0230055-085953	25	37.52292	-8.99764	-19.3001	14.96	0.0164
HE0232-0900	g0234378-084716	26	38.65834	-8.78722	-21.5461	14.85	0.043
HE0236-3101		27	39.68917	-30.8069	-21.4703	15.75	0.062
HE0236-5224		28	39.58292	-52.1922	-20.8180	15.68	0.045
HE0253-1641	g0256027-162916	29	44.00708	-16.4888	-19.5170	16.22	0.032
HE0257-2434	g0259305-242254	30	44.87792	-24.3804	-19.6864	16.25	0.035
HE0323-4204		31	51.26	-41.9072	-21.4593	15.61	0.058
HE0330-1404	g0333078-135433	32	53.28125	-13.9053	-19.7243	16.51	0.04
HE0332-1523	g0334245-151340	33	53.60209	-15.2238	-19.6264	16.31	0.035
HE0336-5545		34	54.53042	-55.5996	-19.8280	17.28	0.059
HE0342-2657	g0345032-264820	35	56.26834	-26.8068	-19.5293	17.54	0.058
HE0343-3943	g0345125-393429	36			-20.9013	15.5	0.0431
HE0345+0056		37	56.91125	1.09528	-20.7964	14.87	0.031
HE0349-4036	g0351417-402759	38	57.92208	-40.4675	-21.2371	15.84	0.0582
HE0351+0240		39	58.54208	2.82681	-18.5318	17.34	0.034
HE0358-3713	g0400407-370506	40			-19.6692	17.11	0.051
HE0359-3841	g0401462-383320	41			-19.7480	17.36	0.059
HE0403-3719	g0405017-371115	42	61.25458	-37.1861	-21.1175	15.84	0.0552
HE0412-0803	g0414527-075540	43	63.71583	-7.9225	-20.1338	15.98	0.0379
HE0429-0247	g0431371-024124	44	67.90375	-2.68792	-18.9595	17.33	0.041
HE0429-5343		45	67.66625	-53.6155	-19.6943	16.54	0.04
HE0433-1028	g0436223-102234	46	69.09292	-10.3739	-20.3580	15.61	0.0355
HE0433-1150		47			-19.4293	17.64	0.058
HE0436-4717		48	69.36083	-47.1885	-21.2658	15.6	0.053
HE0439-0832		49	70.47708	-8.44417	-19.9380	16.56	0.045
HE0444-0513		50	71.835	-5.13708	-19.8277	16.63	0.0442
HE0447-0404	g0450251-035903	51			-17.9872	16.92	0.022
HE0521-3630	g0522580-362731	52	80.74167	-36.4581	-20.3116	16.65	0.0553
HE0535-4224	g0537331-422230	53			-19.3464	16.59	0.035
HE0608-5606	g0609175-560658	54	92.32208	-56.1157	-18.9630	16.76	0.0318
HE0853-0126	g0856178-013807	55	134.0737	-1.63583	-20.3847	16.75	0.0597
HE0853+0102		56			-19.8329	16.99	0.052

Continued on next page

<sup>1</sup>ID number, useful for the nearby QSO sample database and the cross matching



HE0934+0119		57	144.2542	1.09681	-20.2180	16.53	0.0503
HE0949-0122	g0952191-013644	58	148.0796	-1.61083	-19.6136	15.05	0.0197
HE1011-0403	g1014207-041841	59	153.5821	-4.30694	-21.8326	15.26	0.0586
HE1013-1947		60	153.9863	-20.0386	-20.2670	16.67	0.0547
HE1017-0305		61	154.8871	-3.33736	-20.3483	16.35	0.0492
HE1029-1831	g1031573-184633	62	157.9858	-18.7746	-20.4665	15.79	0.0404
HE1107-0813		63			-21.0110	16.07	0.0583
HE1108-2813	g1110480-283004	64	167.6963	-28.5004	-20.3594	14.74	0.024
HE1126-0407		65			-22.2498	14.9	0.0601
HE1136-2304	g1138510-232135	66	174.7108	-23.3568	-17.9600	17.4	0.027
HE1143-1810		67	176.4187	-18.4546	-21.2286	14.57	0.0329
HE1237-0504		68	189.9150	-5.34319	-18.3741	14.42	0.0084
HE1248-1356	g1251324-141316	69			-16.9896	17	0.0145
HE1256-1805		70			-16.7626	17.15	0.014
HE1310-1051	g1313058-110742	71	198.2746	-11.1253	-19.7318	16.14	0.034
HE1319-3048	g1321582-310426	72	200.4917	-31.0704	-19.9280	16.56	0.0448
HE1328-2508	g1331138-252410	73	202.8067	-25.4017	-18.4764	16.8	0.026
HE1330-1013	g1332391-102853	74	203.1604	-10.4772	-18.7168	16.24	0.0225
HE1338-1423		75	205.3021	-14.6433	-20.8327	15.5	0.0418
HE1346-3003	g1349193-301834	76	207.3292	-30.3083	-19.2395	14.98	0.0161
HE1348-1758	g1351295-181347	77	207.8738	-18.2269	-17.9145	15.66	0.012
HE1353-1917	g1356367-193145	78	209.155	-19.5249	-18.8400	17.09	0.0349
HE1417-0909		79	215.0246	-9.38569	-19.5576	16.89	0.044
HE2112-5926		80			-35.7160	0	0.0317
HE2128-0221	g2130499-020814	81	322.7113	-2.13875	-19.2973	17.56	0.0528
HE2129-3356	g2132022-334254	82	323.0096	-33.7153	-20.2412	15.3	0.0293
HE2204-3249	g2207450-323502	83	331.9396	-32.5887	-20.8633	16.26	0.0594
HE2211-3903	g2214420-384823	84	333.6767	-38.8075	-20.5231	15.7	0.0398
HE2221-0221		85			-20.3600	16.67	0.057
HE2222-0026	g2224353-001104	86			-19.5032	17.57	0.0581
HE2231-3722	g2234409-370644	87	338.6696	-37.1139	-19.0161	17.38	0.043
HE2233+0124		88	338.9279	1.65833	-20.1961	16.81	0.0564
HE2236-3621		89	339.7758	-36.1007	-19.5060	17.64	0.06
HE2251-3316	g2253587-330014	90	343.4959	-33.0047	-19.7500	17.24	0.056
HE2254-3712	g2257390-365607	91	344.4138	-36.9354	-19.5097	16.61	0.038
HE2301-3517		92	346.1563	-35.0206	-18.5343	17.7	0.04
HE2302-0857		93	346.1825	-8.68514	-20.4403	16.16	0.0471
HE2306-3246	g2309192-322958	94	347.3304	-32.5010	-19.3229	17.5	0.052
HE2322-3843		95	351.3525	-38.4481	-20.4529	15.54	0.0359
HE2323-6122	g2326376-610602	96	351.6533	-61.1007	-20.7758	15.53	0.0413
HE2337-2649	g2340321-263319	97	355.1354	-26.5564	-19.7865	16.93	0.0496
HE2343-5235		98			-18.4364	17.5	0.035
HE2354-3044		99	359.3684	-30.4610	-19.8248	15.82	0.0307

Table 3.1: Main Characteristics of the LLQSOs sample.

### 3.3 Data Analysis

The analysis of the optical spectroscopic data which were obtained from the two data sets (HES and 6dFGS) was mainly focused on seven spectral emission lines:  $H\beta$   $\lambda$  4861Å,  $[O\text{ III}]$   $\lambda$  5006.843Å,  $[O\text{ I}]$   $\lambda$  6300Å,  $H\alpha$   $\lambda$  6562Å,  $[N\text{ II}]$   $\lambda$  6583.41Å,  $[S\text{ II}]$   $\lambda$  6717Å,  $[S\text{ II}]$   $\lambda$  6731Å. All lines are narrow, except for  $H\alpha$  and  $H\beta$ , that present both narrow and broad components. These lines were selected to classify the members of the sample using the BPT diagnostic diagrams (see section 3.4). Moreover, information about other characteristics of the spectra, such as sigma, velocity, number of line components etc can be extracted from these specific lines in order to enrich the studies of the nearby LLQSOs sample.

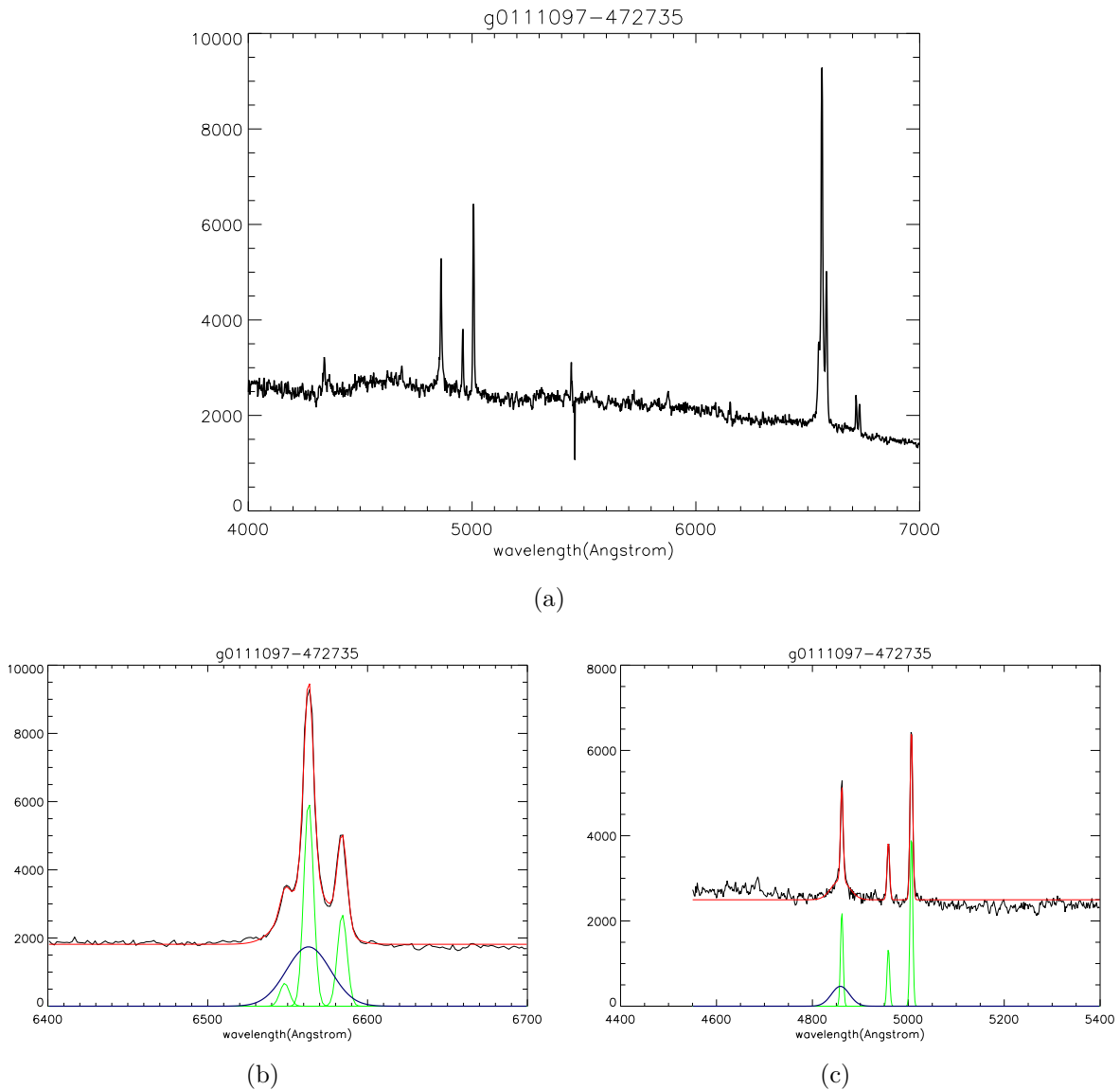


Figure 3.6: (a) The optical spectrum of g0111097-472735 source observed by 6dFGS, (b) Fitting of the lines  $H\alpha$   $\lambda$  6562Å and  $[N\text{ II}]$ , (c) Fitting of the lines  $H\beta$   $\lambda$  4861Å and  $[O\text{ III}]$ .

The MPFIT IDL software package (<http://www.physics.wisc.edu/craigm/idl/fitting.html>) was the fundamental tool which was used for the analysis. The routine performs Levenberg-

Marquardt least-squares minimization which provides a numerical solution to the problem of minimizing a function, generally nonlinear, over a space of parameters of the function.

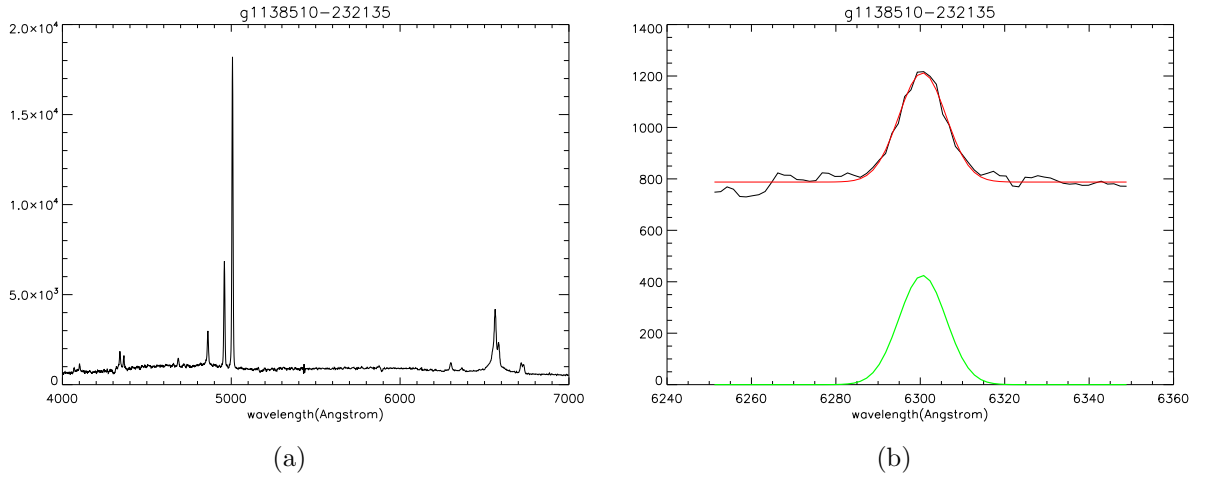


Figure 3.7: (a) Optical spectrum of the galaxy g1138510-232135 observed by 6dFGS and (b) Fitting of line [O I]  $\lambda$  6300Å.

The information provided by the fitting process is the continuum flux, the central wavelength, the Gaussian  $\sigma$  and the line flux. Because of the low resolution spectra from HES data, the fitting procedure was quite challenging. Due to the complexity of the spectral profiles, we had to set some constraints in order to achieve the best fitting. It is also well known that, under certain conditions, such as line blending, the fitting algorithms may derive different solutions. We therefore decided to apply some restrictions to constrain the results more reliably. The H $\beta$   $\lambda$  4861Å broad and narrow components, and the [O I]  $\lambda$  6300Å lines (see Figure 3.7) were individually fitted with a single component, with no particular constraint. We note that no H $\beta$   $\lambda$  4861Å (see Figure 3.6) in absorption was detected, and hence no correction was applied. The [O III]  $\lambda$  5006.843Å, [O III]  $\lambda$  4959Å, and H $\alpha$   $\lambda$  6562Å narrow and broad components and [N II]  $\lambda$  6583.41Å complexes were fitted with two and four Gaussian, respectively. The two [O III] lines, the H $\alpha$  narrow and the two [N II] components were assumed to have the same kinematics. We applied these conditions based on the assumption that these line complexes trace identically the ionized gas kinematics.

For fitting the [N II]  $\lambda$  6548Å, 6583.41Å (see Figure 3.6) doublet we left only the amplitude free. The relative positions were fixed, the intensity ratio was set to 3 (Osterbrock 1989; Ho et al. 1997), and the line width was fixed to the width of the narrow [O III] lines. The [O III]  $\lambda$  5006.843Å, [O III]  $\lambda$  4959Å lines were also fitted by a double Gaussian with the intensity ratio fixed to the theoretical value of  $\sim 3$  (Dimitrijević et al. 2007). The relative wavelengths of the doublet were fixed as well, but the position of the doublet relative to H $\beta$  was allowed to vary as a whole. For the [S II]  $\lambda$  6731Å, [S II]  $\lambda$  6717Å lines (see Figure 3.8), we assume only that they share the same kinematics, since their line ratio variations can be used to trace the electron density. With this set of constraints, each spectrum was fitted using a multi-Gaussian.

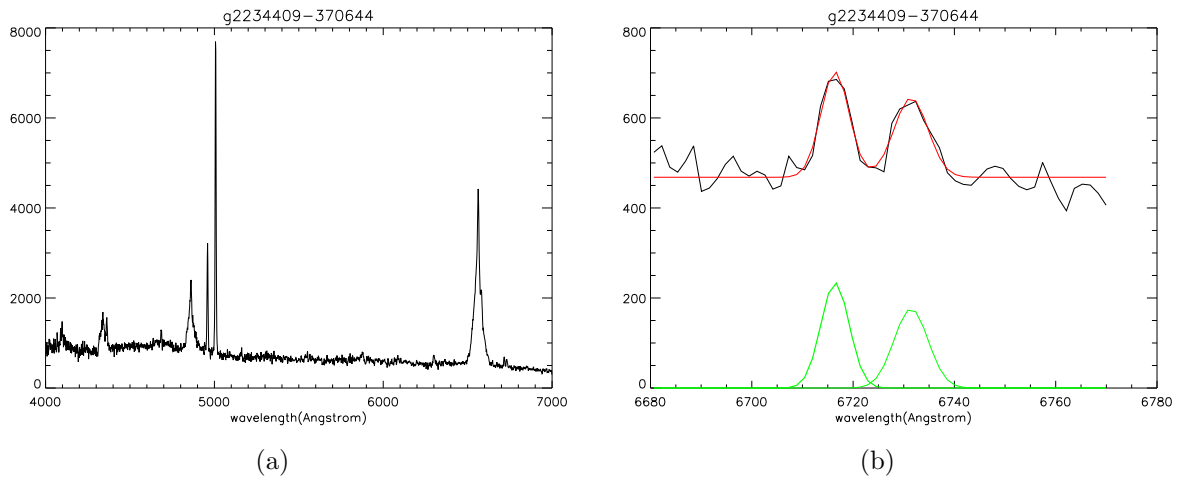


Figure 3.8: (a) The entire spectrum of the galaxy g2234409-370644 observed by 6dFGS and (b) the fitting of the lines [S II]  $\lambda$  6717Å and  $\lambda$  6731Å.

### 3.4 Results and Discussion

Baldwin et al. (1981) proposed the classification diagrams aka BPT diagrams. The main goal of that diagrams is to diagnose the ionizing source within a galaxy resulting the clear separation between the four common excitation mechanisms :

- photo-ionization by O and B stars,
- photo-ionization by a power-law continuum source,
- shock-wave heating and
- photo-ionization by hot O stars (planetary nebulae).

For both two data sets, using the information extracted from the fitting procedure, flux ratios [O III]/H $\beta$ , [N II]/H $\alpha$ , [II]/H $\alpha$ , and [O I]/H $\alpha$  are plotted in order to create the diagnostic BPT diagrams (see Figures 3.9 and 3.10). Hence, almost all members of the nearby LLQSOs sample can be distinguished from their ionization mechanisms. All four ratios are based on lines close in wavelength and are essentially reddening independent. The diagnostic diagrams only use the narrow components of the hydrogen recombination lines, because they are believed originated from the outer part of the AGN, while the broad lines originate closer to the black hole. The theoretical maximum starburst line from Kewley et al. (2006) (red solid line i.e Figure 3.9) and the star formation/demarcation line (green dashed line, i.e Figure 3.10) from Kauffmann et al. (2003) are also plotted, in order to define the upper limit that star forming galaxies can reach and the boundary between pure star forming galaxies from Seyfert-H II composites objects whose spectra contain contributions from both AGN and star formation, respectively. The maximum starburst line is determined by the upper limit of the theoretical pure stellar photoionization models and the galaxies lying above this line are dominated by an AGN. The first purely theoretical classification scheme to distinguish between AGN, LINERs and H II region-like objects was derived by Kewley et al. (2001), using a combination of stellar population synthesis, photoionization and shock models.

For the BPT diagnostic diagrams of our nearby sample, only the spectra with good quality were used. Therefore, 59 out of 89 HES spectra and 44 out of 59 6dFGS spectra were selected in order to derive the  $[\text{O III}]/\text{H}\beta$  versus  $[\text{N II}]/\text{H}\alpha$ . The  $[\text{S II}]$  and  $[\text{O I}]$  lines were not detectable at all in most HES spectra, thus only objects observed by 6dFGS were studied. In particular, 29 spectra were used for the  $[\text{S II}]$  line and 36 for the  $[\text{O I}]$  line out of 59 targets.

### 3.4.1 Classification using the BPT diagrams

The quality of the spectra which was obtained from the 6dFGS was good enough to allow us the clear detection of the seven optical emission lines. Figures 3.9 and 3.10a illustrate the  $[\text{O III}]/\text{H}\beta$  versus  $[\text{N II}]/\text{H}\alpha$  the standard optical diagnostic diagram for our nearby sample from the 6dFG survey and HE survey, respectively, comparing them with the sample selection of thousand SDSS galaxies (illustrated as a dark cloud in figures), which was used by Kewley et al. (2006). This sample contains also nearby galaxies with a redshift range  $0.04 < z < 0.1$  in order to ensure that the galaxy properties derived from the SDSS fibre spectra are not dominated by the small fixed-size aperture (see section 4.1). The red line is the 'theoretical maximum starburst' limit, galaxies with excitation above the line do not present star forming regions. Galaxies that lie below the star formation demarcation (green dashed line) are classified as pure H II regions-like galaxies. The galaxies that lie between the two classification lines are on the AGN-H II mixing sequence and are sorted as composite galaxies. The sources that classed above the dashed line are classified as AGNs. From Figures 3.10b and 3.10c, it is obvious that galaxies containing AGN lie on two branches. Seyfert galaxies are located at the upper part while LINERs are placed in the lower branch, which are also believed to be affected by shocks (Dopita & Sutherland 1995). The  $[\text{S II}]/\text{H}\alpha$  and the  $[\text{O I}]/\text{H}\alpha$  diagrams are the most suitable tools to separate Seyfert from LINER galaxies (Kewley et al. 2006). In these diagrams the 'theoretical maximum starburst' line provides the upper bound to the star forming sequence. The SDSS galaxy sample from Kewley et al. (2006) shows that galaxies that are classified as composite using the  $[\text{N II}]/\text{H}\alpha$  diagram located mostly within the star forming sequence on the  $[\text{S II}]/\text{H}\alpha$  diagram. This tendency seems to be followed for our sample as well. A yellow line is presented in our  $[\text{S II}]/\text{H}\alpha$  and the  $[\text{O I}]/\text{H}\alpha$  diagrams which provides an empirical division between Seyferts and LINERs. This line was suggested by Kewley et al. (2006) using the best fit through histogram minima for each of the two diagrams. The  $[\text{O I}]/\text{H}\alpha$  diagram is more sensitive and therefore a more reliable tracer of changes in ionization conditions due to fast shocks. The other diagrams are more sensitive to the star formation.

Figure 3.9 presents the  $[\text{N II}]/\text{H}\alpha$  diagram derived from the HES data. The classification of the galaxies using the three diagnostic diagrams for the optical spectroscopic observations from 6dFGS is presented in Figure 3.10.

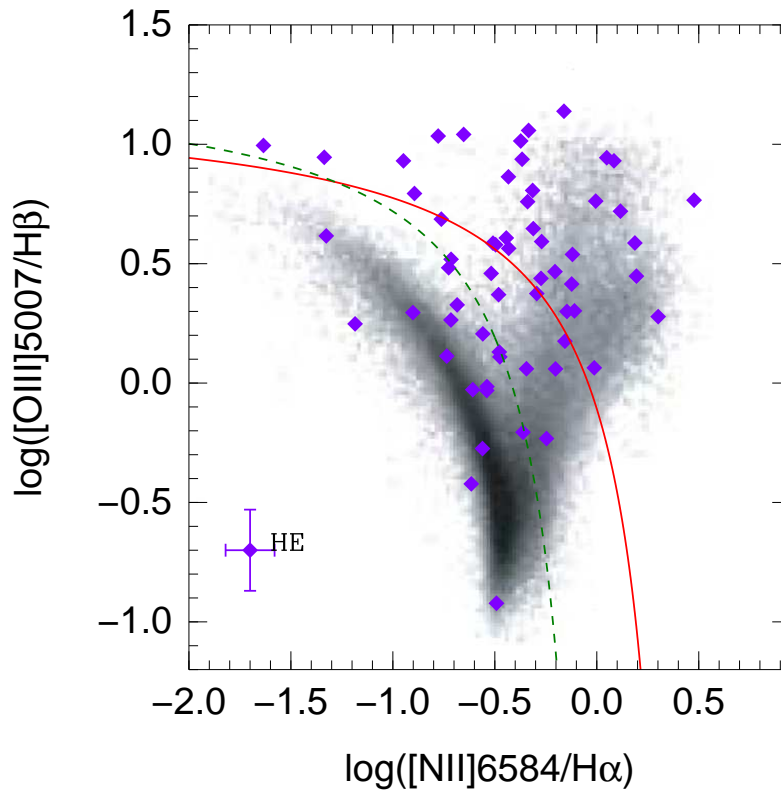


Figure 3.9:  $[N_{\text{II}}]/H\alpha$  versus  $[O_{\text{III}}]/H\beta$  diagnostic diagram for the HES data. The red line is the theoretical maximum starburst limit. Galaxies that lie below the star formation demarcation green dashed line are classified as  $H_{\text{II}}$  regions-like galaxies. The galaxies that lie between the two classification lines are on the AGN- $H_{\text{II}}$  mixing sequence and are sorted as composite galaxies. The sources above the dashed line are classified as AGNs. The dark cloud represents thousands of local SDSS galaxies from previous studies by Kewley et al. (2006).

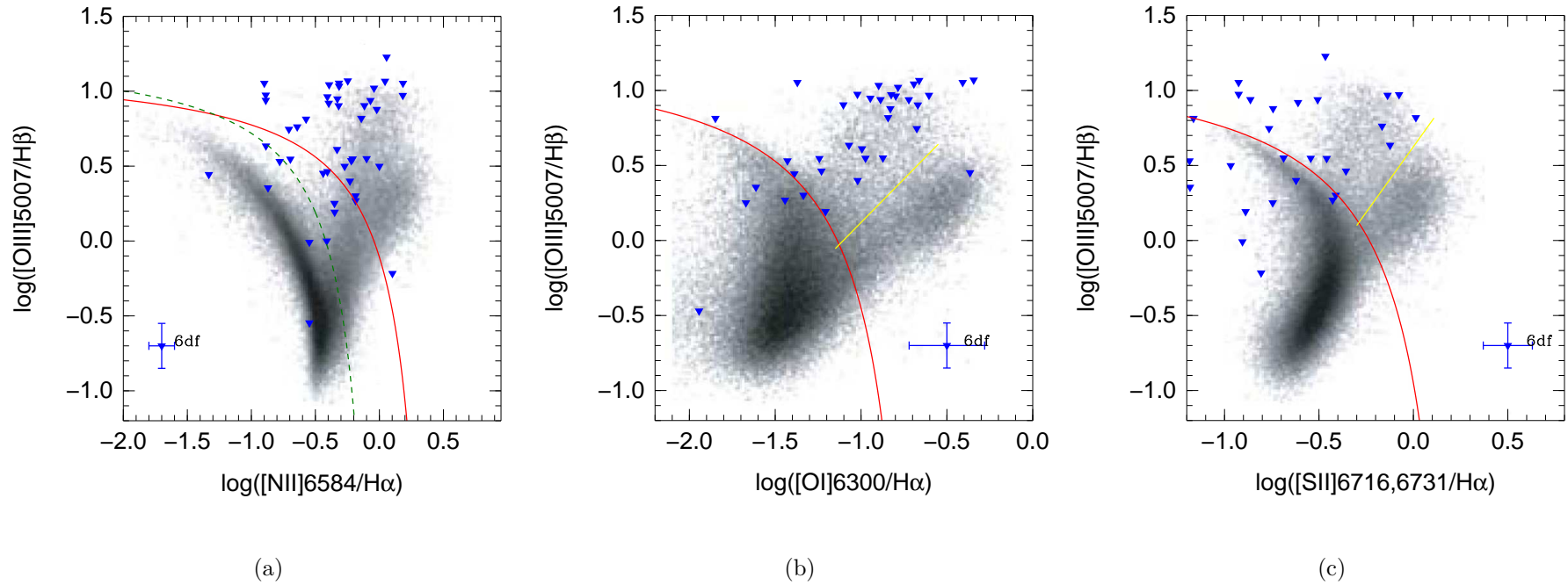


Figure 3.10: (a): The  $[NII]/H\alpha$  versus  $[OIII]/H\beta$  diagnostic diagram for the 6dFGS data. The red line is the theoretical maximum starburst limit. Galaxies that lie below the star formation demarcation green dashed line are classified as  $HII$  regions-like galaxies. The galaxies that lie between the two classification lines are on the AGN- $HII$  mixing sequence and are sorted as composite galaxies. The sources that classed above the dashed line are classified as AGNs. The dark cloud represents thousands of SDSS galaxies from previous studies by Kewley et al. (2006). (b): The  $[OI]/H\alpha$  versus  $[OIII]/H\beta$  diagnostic diagram. The yellow line represents the division between Seyferts and LINERs. (c): The  $[SII]/H\alpha$  versus  $[OIII]/H\beta$  diagnostic diagram.

	[O III]/H $\beta$ versus [N II]/H $\alpha$		[O III]/H $\beta$ versus [S II]/H $\alpha$	[O III]/H $\beta$ versus [O I]/H $\alpha$
	6dFGS	HES	6dFGS	6dFGS
No of targets	44	59	29	36
No of Seyfert	32	33	16	30
No of Starburst	5	18	12	5
No of LINERs	1	0	1	1
No of Composites	6	8	0	0

*Table 3.2: Statistics of the sample using both data sets (6dFGS, HES) in order to justify the differences in classifications.*

All these diagrams show that the LLQSOs sample need to populate the [O III]/H $\beta$  high excitation region of the diagram, and do not have a significant contamination to the most populated regions of the H II and LINER branches. Table 3.2 details the number of the studied sources and their classification. In terms of the 6dFGS [O III]/H $\beta$  versus [N II]/H $\alpha$  diagram 72.7% of the galaxies are classified as AGN, 11.3% as starburst galaxies, 2.3% as LINERs and 13.7% of the sources are lying in the composite part of the diagram (see Figure 3.10). According to the HES results the percentages are the following: 56% AGN, 30.5% starburst galaxies and 13.5% composite galaxies. Interesting feature is the fact that no galaxy was classified as LINER in the HES results (see also Figure 3.9).

The number of the galaxies with H II classification (about 11.3% and 30% in 6dFGS and HES, respectively) is remarkably high, especially according that the sources were selected to be Seyfert type - 1. This implies that 18 sources will have to be re - classified in the catalog, as most of these sources were not showing broad component, which is confirmed by their spectral profiles.

It is also interesting to note how poor is the LINER contribution of the sample. Only one source is classified as such, base on the 6dFGS spectra. This indicates two main facts: first, that there are no AGN with low ionization parameter  $U = \text{ionizing photon flux per unit area} / (\text{hydrogen density} * c)$  (Ho et al. 1993; Rupke et al. 2007); and the fast shocks, which are also believed to be responsible for the LINER activity (Dopita & Sutherland 1995) are not important in the sample.

On the other hand, the LINER - H II transition may be explained with a Wolf - Rayet starburst phase with high density gas and metallicity above solar (Barth & Shields 2000).

The classification derived (in %) by the [S II]/H $\alpha$  and [O I]/H $\alpha$  diagrams of the 6dFGS sample is different with respect to that of the [N II]/H $\alpha$ . This can be explained on two different reasons. First, the total number of galaxies classified on each diagram is different, as the sources with weak emission lines were neglected. Second, the three BPT diagrams are not equally sensitive to the physical processes taking place here. For instance, the [N II]/H $\alpha$  and [S II]/H $\alpha$  diagrams are more sensitive to star formation then the [O I]/H $\alpha$  one, which is proved to be more sensitive to shocks.

### Cross - matching sources

The comparison between the two data sets justified some differences on the taxonomy of the objects. In particular, some galaxies, whose spectra were taken from HE survey, lie on the composite branch of the standard optical diagnostic diagram. On the other hand, the 6dFGS classes them as either as Seyfert galaxies or as star forming regions. The objects analyzed in both surveys were selected to be over plotted in a common



diagnostic diagram for each of the three line ratios ( $[\text{N II}]/\text{H}\alpha$  versus  $[\text{O III}]/\text{H}\beta$ ,  $[\text{O I}]/\text{H}\alpha$  versus  $[\text{O III}]/\text{H}\beta$ ,  $[\text{S II}]/\text{H}\alpha$  versus  $[\text{O III}]/\text{H}\beta$ ) aiming to diagnose the differences in their taxonomy. Furthermore, another criterion for this selection was the clear detection of the lines in both surveys. The results are presented in Table 3.3 and in Figure 3.11. The  $[\text{N II}]/\text{H}\alpha$  versus  $[\text{O III}]/\text{H}\beta$  diagram is dominated by 65.6% of AGNs accordingly to the 6dFGS observations and 59.4% accordingly to the HES observations. In this diagram the percentage of the starburst galaxies is 18.8% for the 6dFGS and 25% for the HES while the composite galaxies are 12.5% for 6dFGS and 15.6% for the HES. One galaxy is classified as LINER for the 6dFGS while the HES results no LINERs. Some small differences in the classification between both catalogs could be explained by the uncertainties. However, in some cases, the same object show large differences in the excitation degree (up to  $\sim 0.5$  dex in  $[\text{N II}]/\text{H}\alpha$ ), which could only be explained by an observational effect (see section 4.1). Thus, key result drove our studies in to another project which is described in next section 4.1.

	[O III]/H $\beta$ versus [N II]/H $\alpha$	
	6dFGS	HES
No of targets	32	32
No of Seyfert	21	19
No of Starburst	6	8
No of LINERs	1	0
No of Composites	4	5

Table 3.3: Statistics of the cross-matching sources. They are classified differently depending on the survey.

### 3.4.2 Analysis of the broad component

Broad emission lines are one of the main feature of many AGN spectra. As it is already mentioned in the chapter 2.2.2 the BLR plays an important role in our understanding of AGNs due to the fact that it comes from the central source. The widths of AGN broad lines range from a minimum of  $\text{FWHM} \approx 500$  km/s to  $\text{FWHM} \approx 10^4$  km/s, with typical values  $\text{FWHM} \approx 5000$  km/s. The distributions of the  $\text{H}\alpha$  and  $\text{H}\beta$  broad components for both surveys are shown in Figures 3.12 and 3.13 for HES and 6dFGS, respectively. Both lines trace the rotating material around the central machine of an AGN, but their relative strength differs. In the majority of our sample, the objects were detected with an average FWHM of  $\sim 500$  km/s in the narrow components ( $\text{H}\alpha$  and  $\text{H}\beta$ ) in both surveys, while the  $\text{H}\beta$  component appear to be broader than  $\text{H}\alpha$  component in both cases. This is consistent with previous studies i.e (Colina et al. 1991). The  $\text{H}\alpha$  broad component of both surveys and  $\text{H}\beta$  broad component of HES appears to have a Gaussian distribution profile. Most of the sources have a  $\text{FWHM} > 2000$  km/s which is a solid probe for their classification since they were selected to be Seyfert type 1. Comparing the  $\text{H}\alpha$  broad components between the two data sets, the peak in the histogram of the HES is at 4000 km/s, in contrast to 6dFGS distribution where most of the sources have a  $\text{FWHM} \sim 2000$  km/s (see also Figure 3.12a and 3.13a). The FWHM of the  $\text{H}\beta$  broad components ranges from 2000 km/s up to 10000 km/s, but they do not show a clear peak in the statistics of both surveys. Interesting seems to be the fact that a significant number of the sources (4

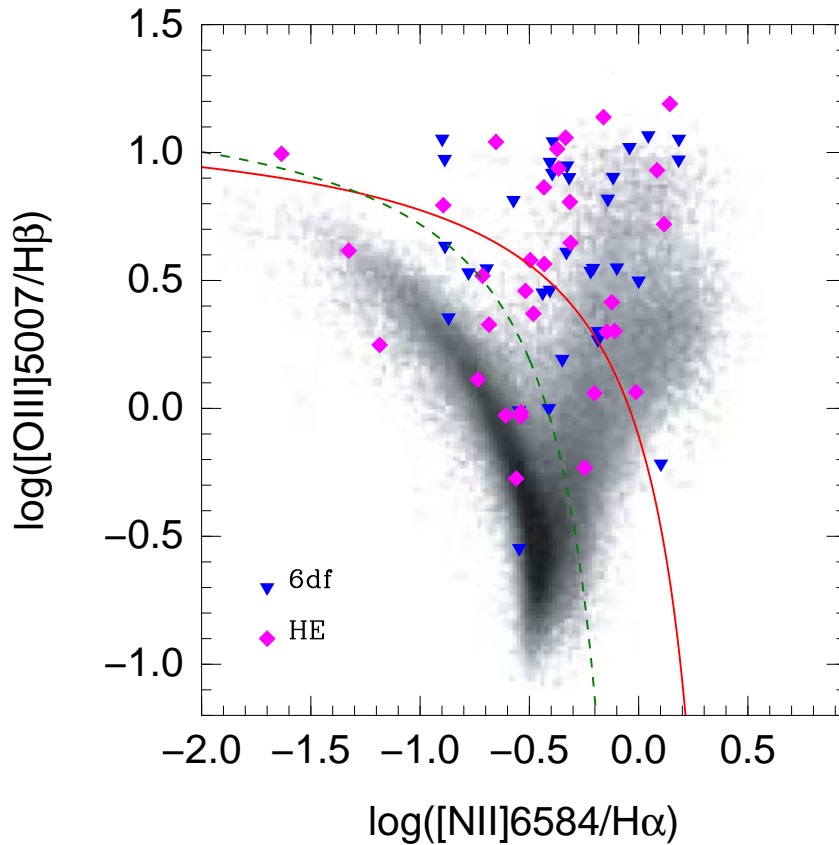


Figure 3.11: The  $[N_{II}]/H\alpha$  versus  $[O_{III}]/H\beta$  diagnostic diagram for the cross-matching sources. The red line is the theoretical maximum starburst limit. Galaxies that lie below the star formation demarcation green dashed line are classified as  $H_{II}$  regions-like galaxies. The galaxies that lie between the two classification lines are on the AGN- $H_{II}$  mixing sequence and are defined as composite galaxies. The sources that are located above the dashed line are classified as AGNs. The dark cloud represents thousands of SDSS galaxies from previous studies by Kewley et al. (2006).

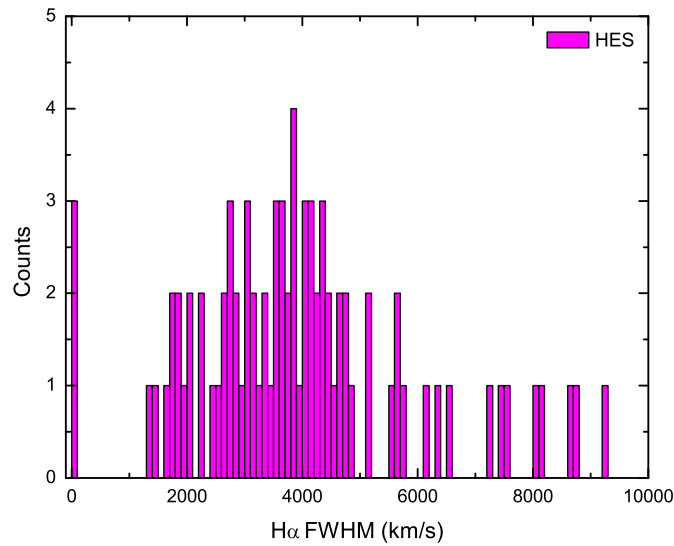
objects from HES and 7 from 6dFGS) appear to have  $FWHM \sim 500$  km/s in their broad components which is comparable to the average of the narrow components.

A feature key result for the analysis of the broad component is the fact that four objects of the LLQSOs sample show a double broad component. Representative examples are presented for the HE 0236-3101 and HE 0203-0031 sources (see Figures 3.14 and 3.15) for the  $H\beta$  and  $H\alpha$  line, respectively. Earlier studies about the HE 0236-3101 show that this galaxy is an accretion disk candidate among luminous galaxies (Colina et al. 1991). These kind of broad Balmer emission - line profiles are consistent with models of inclined small relativistic accretion disks around a massive black hole (Perez et al. 1988; Chen & Halpern 1989; Halpern 1990). Recent studies on our LLQSOs sample (Schulze et al. 2009) have shown that the average of the SMBHs of the sample corresponds to  $\log M_{BH} \sim 7.50 M_{\odot}$ .

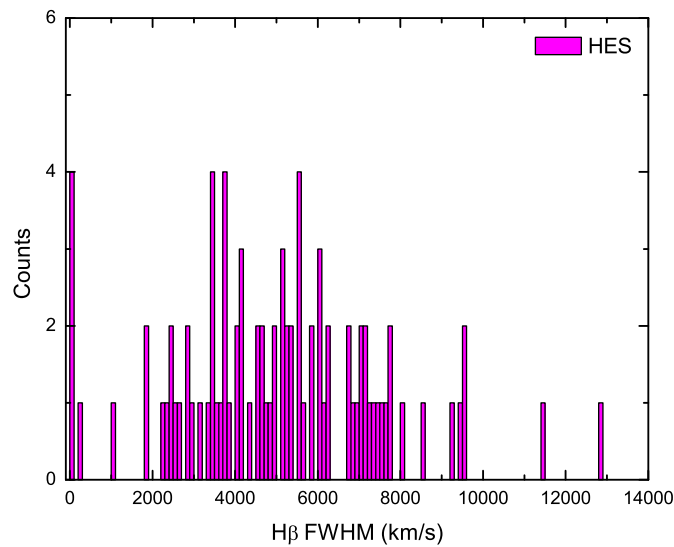
Previous X-ray studies (Strateva et al. 2006) about the the double-peaked emitters (Balmer lines) such as HE 0203-0031 (see Figure 3.15) show that the illumination of the accretion disk requires an external power to produce lines of this strength due to the insuf-

---

ficient local power. However, the fact that the X-ray emission of double-peaked emitters as a class does not differ from that of normal AGNs with similar properties suggests that a peculiarity of the X-ray emission structure and mechanism is not responsible for the occurrence of double-peaked Balmer lines in AGNs. HE 0203-0031 source shows one broad component and double narrow (see Figure 3.15b). The presence of double narrow components may be an indicator for superwinds.

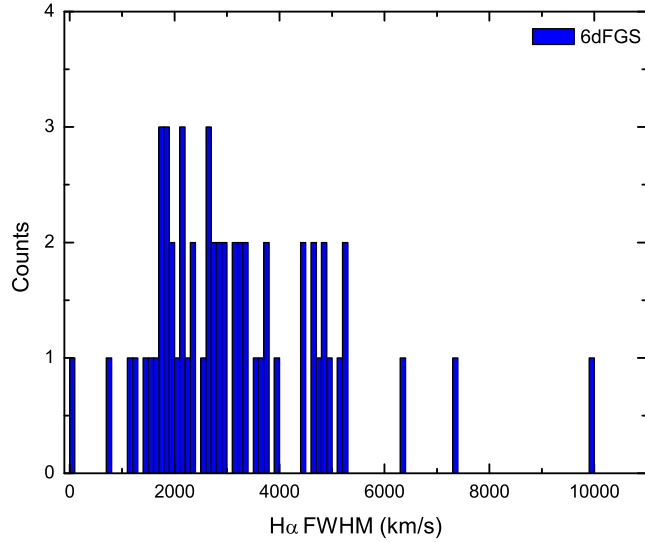


(a)

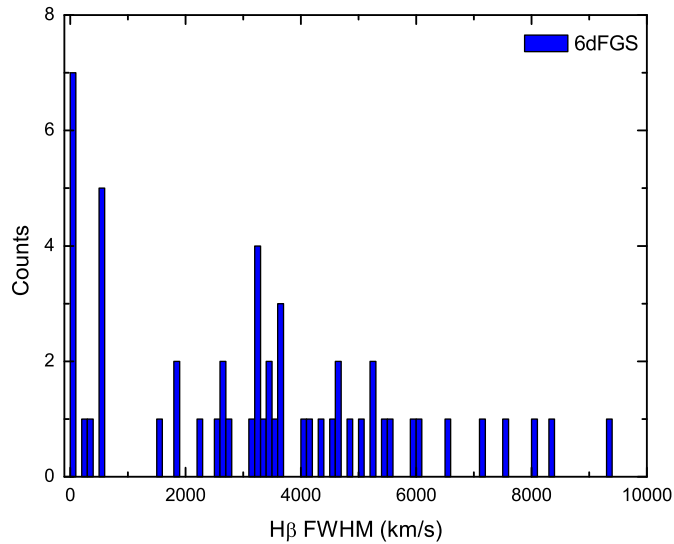


(b)

Figure 3.12: (a) The distribution of  $H\alpha$  broad component and (b) the distribution of  $H\beta$  broad component of HES. The  $H\alpha$  component show a Gaussian shape distribution with a mean  $\sim 4000$  km/s. Unlike, the  $H\beta$  component which does not show a clear peak, while the FWHM range is  $\sim 500 - 9000$  km/s.



(a)



(b)

Figure 3.13: (a) The distribution of  $H\alpha$  broad component and (b) the distribution of  $H\beta$  broad component of 6dFGS. The peak of the Gaussian shape distribution of the  $H\alpha$  component is at FWHM  $\sim 2000$  km/s. The FWHM of the  $H\beta$  broad component shows a spread distribution with seven objects to have  $\sim 500$  km/s, value comparable to the one of the narrow component.

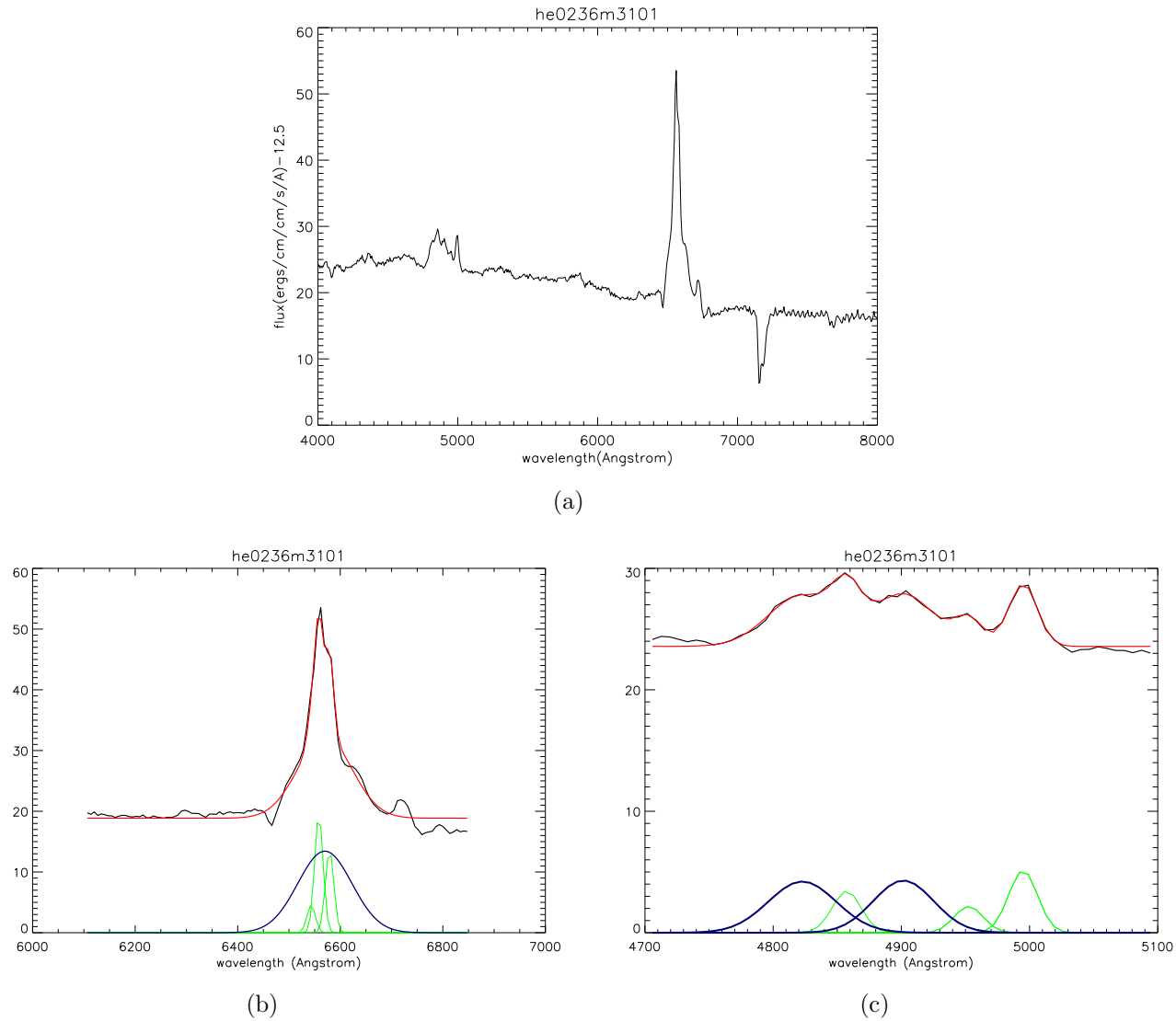


Figure 3.14: (a) The optical spectrum of HE0236-3101 source observed by HES and (b) Fitting of  $H\alpha$   $\lambda$  6562Å and  $[N_{II}]$ ,  $H\beta$   $\lambda$  4861Å and  $[O_{III}]$  lines. The  $H\beta$  component consists of two broad components with FWHM  $\sim$  3500 km/s.

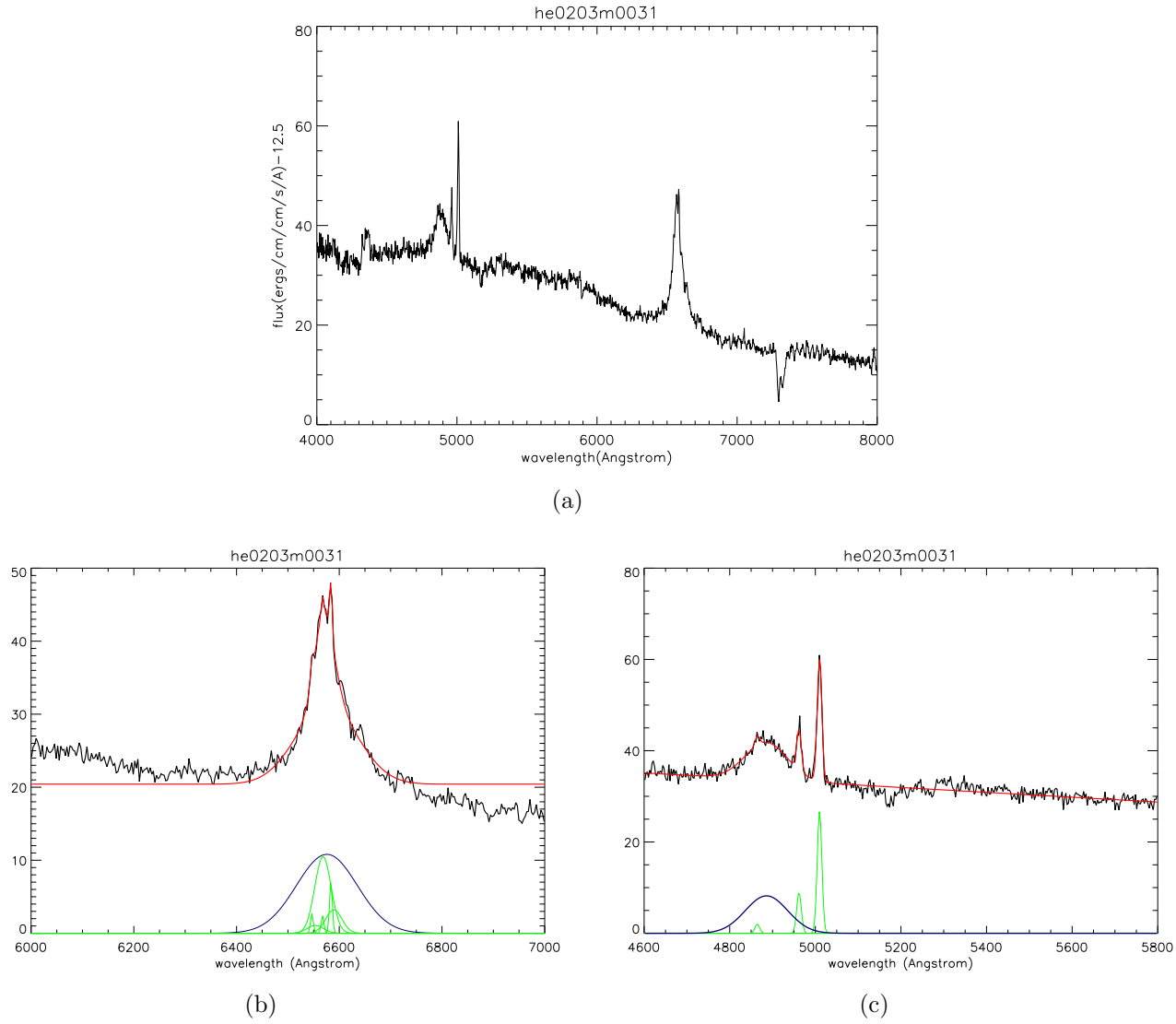


Figure 3.15: (a) The optical spectrum of HE0203m0031 source observed by HES, (b) Fitting of  $H\alpha$   $\lambda$  6562Å and (b)  $[N\text{II}]$ ,  $H\beta$   $\lambda$  4861Å and  $[O\text{II}]$  lines. The  $H\alpha$  line consists of one broad and two narrow components with FWHM  $\sim$  1500 km/s.

### 3.4.3 Electron density analysis

The average electron density can be calculated by comparing the intensities of two lines of the same ion. When the ions emit with almost same excitation energy, the relative excitation rates depend only on the ratio of the relative strengths (Rogers 1989). When they have different radiative transition probabilities, the emission depends on the density and the ratio of intensities of the lines they emit will likewise depend on the density. As an example for our nearby LLQSO sample we use the [S II]  $\lambda\lambda$  6717Å, 6731Å lines ratio to estimate the electron density, assuming a temperature of  $10^4$  K (Osterbrock 1989) (see also Table 3.4). The electron density,  $N_e$ , was defined in 17 objects of the 6dFGS, and the majority of these objects have an electron density of order  $N_e \sim 10^1 cm^{-3}$ , which is close to the typical densities of several H II regions. This result can explain the number of the galaxies that are classified as star forming galaxies. Also, some of the objects have an electron density  $N_e \sim 10^3 cm^{-3}$ , which represents the typical order of the Narrow Line Region of Seyfert galaxies and QSOs (Blandford et al. 1990).

Source Name	[S II] $\frac{\lambda_{6717}}{\lambda_{6731}}$	Electron Density $N_e (cm^{-3})$
g0039159-511702	0.61113799441991	$10^{3.5}$
g0042369-104922	1.44400742412934	$10^1$
g0111097-472735	1.15427947918893	$10^{2.5}$
g0111143-161555	1.38399991302038	$10^2$
g0259305-242254	1.28807255113882	$10^{2.2}$
g0334245-151340	1.29043317500074	$10^{2.2}$
g0400407-370506	0.66658514170377	$10^{3.2}$
g0401462-383320	1.21158686916084	$10^{2.3}$
g0436223-102234	0.86340554979787	$10^3$
g0856178-013807	1.1734054626975	$10^{2.5}$
g1031573-184633	1.32188609105656	$10^2$
g1110480-283004	1.44154783384269	$10^1$
g1251324-141316	1.06940607867028	$10^{2.8}$
g1331138-252410	1.39382549354895	$10^1$
g1351295-181347	0.97458113811883	$10^{2.9}$
g2130499-020814	0.78862039060731	$10^{3.1}$
g2234409-370644	1.40510354292447	$10^1$

Table 3.4: The electron density estimation using the [S II]  $\frac{\lambda_{6717}}{\lambda_{6731}}$  ratio (Osterbrock 1989).

## 3.5 Concluding Remarks

In this chapter, the analysis of the optical spectra of the Hamburg/ESO LLQSOs has been presented. The main aim was to fully characterize their excitation state, and derive all possible parameters that could enhance previous studies based on these sources. The main conclusions can be summarized as:

- A significant number of the LLQSOs sample members show strong star forming activity, despite the fact that they were initially selected to be Seyfert type - 1. In



particular, 18 sources out of 87 need to be re - classified in the catalogs, since most of them did not show broad component, according to their spectra profiles (see also [A.1](#)).

- LINER contribution is apparently not present in the LLQSOs sample, but this statement requires further observations in order to be confirmed. The  $[\text{O I}]/\text{H}\alpha$  line ratio is more sensitive and therefore a more reliable tracer of changes in ionization conditions due to fast shocks, but it was not clearly measured due to the weakness of the  $[\text{O I}] \lambda 6300\text{\AA}$  line.
- Most of the sources have a  $\text{FWHM} > 2000 \text{ km/s}$  which is a solid statement for their classification since they were selected to be Seyfert type 1. Comparing the  $\text{H}\alpha$  broad components between the two data sets, the peak in the histogram of the HES is at  $4000 \text{ km/s}$ , in contrast to 6dFGS distribution where most of the sources have a  $\text{FWHM} \sim 2000 \text{ km/s}$ . The  $\text{FWHM}$  of the  $\text{H}\beta$  broad components ranges from  $2000 \text{ km/s}$  up to  $10000 \text{ km/s}$ , but they do not show a clear peak in the statistics of both surveys. A significant number of sources (4 objects from HES and 7 from 6dFGS) appear to have  $\text{FWHM} \sim 500 \text{ km/s}$  in their broad components which is comparable to the average of the narrow components.
- The HE 0203-0031 galaxy shows a spectral profile, with two broad components. This result verifies, previous studies report on this source as an accretion disk candidate galaxy. Its broad Balmer emission line profile is consistent with models of relativistic accretion disks around a SMBH.
- Four galaxies (see also [A.1](#)) were detected with a double narrow component in their spectral profile, indicating the possible existence of 'superwinds'.
- The electron density,  $N_e(\text{cm}^{-3})$ , of 17 galaxies was calculated, using the  $[\text{S II}] \lambda\lambda 6717\text{\AA}, 6731\text{\AA}$  line ratio.  $N_e(\text{cm}^{-3})$  values of the typical order of H II regions ( $N_e \sim 10^1 \text{cm}^{-3}$ ) and typical order of the Narrow Line Region of Seyfert galaxies ( $N_e \sim 10^3 \text{cm}^{-3}$ ), confirm the taxonomy results.



# 4. Simulating the Aperture Effect

*Simulations of nearby and distant galaxies observed with different spectroscopic techniques are laid out through this chapter. First, the observational results that motivated the present study on the aperture effect are presented along with an overview of the current topic. The simulations carried out cover not only galaxies with different excitation degrees, but also sample a variety of cosmological distances. The impact of the aperture effect at high redshift galaxies is studied and compared with the local universe. The results illustrate their taxonomy under given conditions.*

## 4.1 Motivation

As described in subsection 2.2.1, conventional spectrographs employ a telescope focal plane mask that contains an entrance aperture or slit to admit the light from an isolated astronomical source. The major principle of operation of the mask is to conceal the night sky background that would otherwise arrive to the detector. Some of the light of the astronomical target is lost at the entrance aperture, due to the larger projected size of the aperture than the width of the PSF. Moreover, at the slit the amount of the light that is lost depends on the surface brightness distribution of the observed source, the aperture geometry, and the PSF. In these cases, flux calibration of ground-based optical spectra of variable AGNs is most often done by assuming a narrow-line flux constant with time. The lines arise in the narrow-line region (NLR) which has much larger dimensions ( $\geq 100$  light years) and much lower electron density ( $N_e \approx 10^{3-6} \text{cm}^{-3}$ ) than the

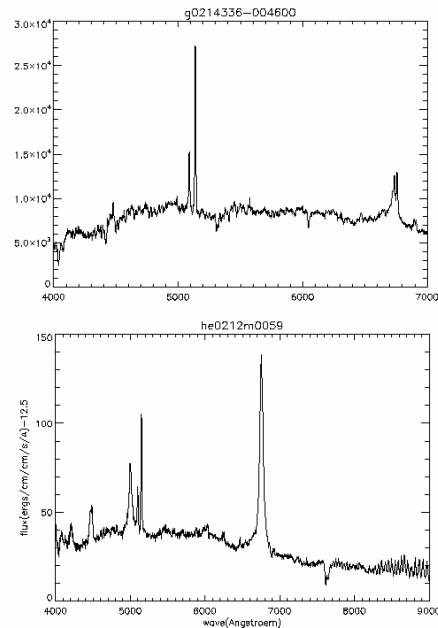


*Figure 4.1: The optical spectrum profile of the source HE0212-0059. The horizontal axis represents the wavelength in Angstrom and the vertical one, the flux in  $\text{erg cm}^{-2} \text{s}^{-1}$  and in arbitrary units for the 6dFGS. In the upper part, the image shows the spectrum obtained with the 6 arcsec fibre from 6dFGS while in the lower part the optical spectroscopic observations taken with ESO telescope with a 2 arcs long slit are shown.*

broad-line region (BLR). Both BLR and NLR are photoionized by the central continuum source, but variations in the photoionized flux are spread out in the NLR due to the large light travel (Clavel et al. 1990; Maoz et al. 1991; Peterson et al. 1991; Wanders et al. 1992). The narrow emission lines arise in a high surface brightness region, in some cases partially resolved, where the ratio of narrow line to broad line flux becomes a strong function of the aperture geometry.

In the analysis of our sample we had to deal with two different data sets from two different instruments. One set of observations was taken with a long slit spectroscopy technique (HES) and the other one a six arcsec fiber (6dFGS) was used. This implies that for several galaxies we end up with two very different optical spectra (see Figure 4.1). In one of them the  $H\alpha + [N II]$  complex clearly dominates, where in the other, the  $[O III] \lambda 5006.843\text{\AA}$  line shows a strong peaks above the hydrogen recombination lines. The obvious dissimilarity in spectra resulted a completely different classification of that particular source in our BPT diagnostic diagrams (see Figure 4.2), and implies that both spectra are coming from different regions of the galaxy. This is one of the cases which drove our studies to a more detail analysis of the simulations on the aperture effect, and how it does affect the classification of the sources depending on the cosmological distance and also the morphology of the astronomical objects.

#### 4.1.1 Previous Investigations

A powerful and unique tool for the study of the geometry and the structure of the spatially unresolved nuclear regions in AGNs is indubitably the observations of the continuum and the emission lines variability. Previous studies (Peterson et al. 1995) on the topic have shown the way to determine the point spread function taking into account seeing and aperture effects, including the surface brightness distributions for both NLR and starlight component of the host galaxy. On the angular scales achievable in ground based astronomy the BLR and the AGN continuum source are considered as point sources.

The PSF ( $\sigma$ ) can be mainly characterized by its full width half maximum (FWHM,  $s$ ) in arcseconds. The integral of the PSF ( $\Phi(R, s)$ ) over the projected aperture  $\mathbf{R}$  is given by :

$$\Phi(\mathbf{R}, s) = \int_{\mathbf{R}} \sigma(\mathbf{R}', s) d\mathbf{R}', \quad (4.1.1)$$

where the integral boundaries are specified by  $\mathbf{R}$ . For a symmetric PSF, the integral over a circular aperture with radius  $R$  centered ( $r=0$ ) on the source the integral becomes:

$$\Phi(\mathbf{R}, s) = 2\pi \int_0^R \sigma(r, s) r dr. \quad (4.1.2)$$

In order to calculate the total narrow line flux measured from the same PSF, the observed NLR surface brightness distribution  $\sum_{NL}$  is needed :

$$F_{NL}(\mathbf{R}, s) = \int_{\mathbf{R}} \sum_{NL}(\mathbf{R}', s) d\mathbf{R}'. \quad (4.1.3)$$

A *point source correction factor*  $\phi$  is required for the case that the NLR is more extended than the PSF, because the small entrance aperture receives a larger fraction of

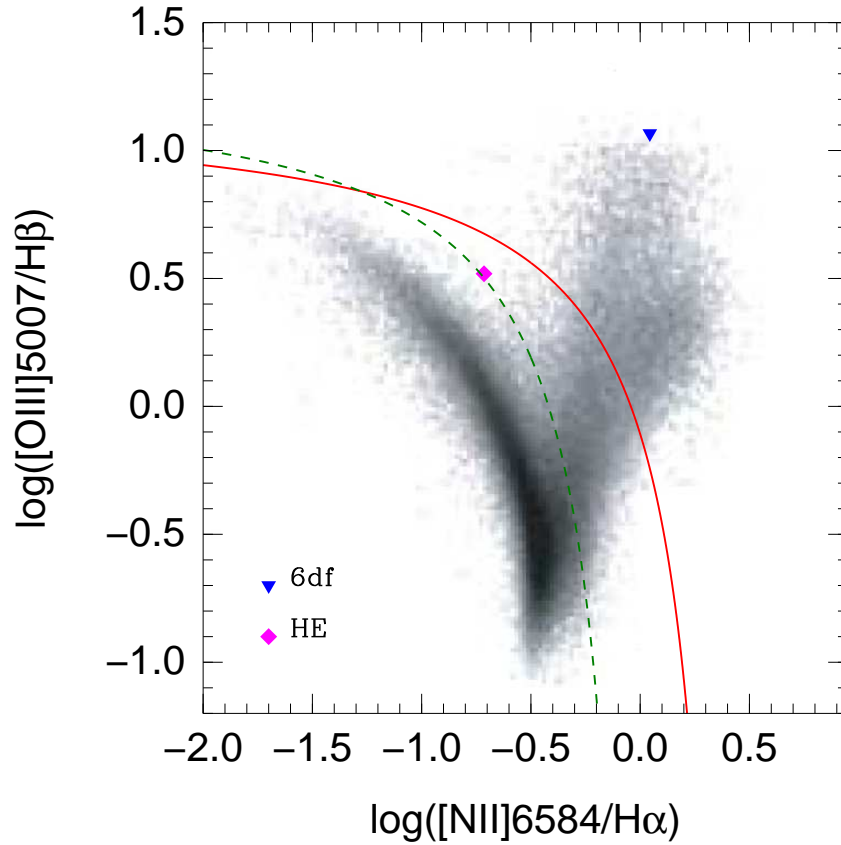


Figure 4.2: The difference in classification of the source HE0212-0059 which was observed with different instruments. The source is from our nearby sample and its cosmological distance is  $z = 0.02$ . In the case of the 6dFGS the galaxy is located in the Seyfert galaxies' part (upper left), while it is classified as a composite galaxy with data obtained via long slit spectroscopy. The dark cloud represents thousands of SDSS galaxies from previous studies by [Kewley et al. \(2006\)](#).

light from the PSF than from the NLR. The *point source correction factor*  $\Phi$  is derived by the ratio :

$$\phi(\mathbf{R}, s) = \frac{F_{NL}(\mathbf{R}, s)}{\Phi(\mathbf{R}, s)}. \quad (4.1.4)$$

The correction factor  $\phi$  is normalized to some standard aperture geometry and seeing. The correct AGN continuum flux  $A$  and the correct broad line flux  $L$  is given by equations 4.1.5 and 4.1.8 in terms of the measured fluxes  $A_{obs}$  and  $L_{obs}$  respectively.

$$A = \phi(\mathbf{R}, s)A_{obs}, \quad (4.1.5)$$

$$L = \phi(\mathbf{R}, s)L_{obs}. \quad (4.1.6)$$

Regarding the fact that the continuum  $C$  consists of two components, the point like

AGN component A and an extended starlight component G, it can be expressed by :

$$C = A + G. \quad (4.1.7)$$

Of course, the same situation is valid for the observed continuum flux since the two components have different surface brightness distributions.

$$C_{obs} = A_{obs} + G_{obs}. \quad (4.1.8)$$

The surface brightness distribution of the host galaxy is different from the NLR, therefore the galaxy flux should be adjusted by a correction factor similar to the equation 4.1.9 :

$$\psi(\mathbf{R}, s) = \frac{F_{NL}(\mathbf{R}, s)}{G_{obs}(\mathbf{R}, s)}, \quad (4.1.9)$$

where,  $G_{obs}$  stands for the integral of the observed starlight surface brightness distribution,  $\sum_g$ , over the aperture  $\mathbf{R}$  :

$$G_{obs}(\mathbf{R}, s) = \int_{\mathbf{R}} \sum_g(\mathbf{R}', s) d\mathbf{R}'. \quad (4.1.10)$$

Hence, the corrected starlight distribution with  $\psi$  to be normalized to standard geometry and PSF width is given by the equation:

$$G = \psi(\mathbf{R}, s)G_{obs}. \quad (4.1.11)$$

At this moment, the real AGN flux A can be isolated in terms of the observed total flux  $C_{obs}$  combining the equations 4.1.5, 4.1.8, 4.1.11 :

$$A = \phi(\mathbf{R}, s)A_{obs} = \phi[C_{obs} - G_{obs}] = \phi C_{obs} - \phi \frac{G}{\psi}. \quad (4.1.12)$$

A starlight correction factor :

$$\phi_g(\mathbf{R}, s) = \frac{\phi(\mathbf{R}, s)}{\psi(\mathbf{R}, s)} = \left( \frac{F_{NL}(\mathbf{R}, s)}{\Phi(\mathbf{R}, s)} \right) \left( \frac{G_{obs}(\mathbf{R}, s)}{F_{NL}(\mathbf{R}, s)} \right) = \frac{G_{obs}(\mathbf{R}, s)}{\Phi(\mathbf{R}, s)} \quad (4.1.13)$$

is needed in order to simplify the final flux. Consequently, the pure AGN flux , corrected for aperture effects, and in terms of the observed continuum flux  $C_{obs}$  is described by the following equation :

$$A = \phi(\mathbf{R}, s)C_{obs} - \phi_g(\mathbf{R}, s)G. \quad (4.1.14)$$

It is worth to mentioning that the correction factors  $\phi$  and  $\phi_g$  should be normalized through some standard aperture geometry under specific seeing conditions. The factors are determined empirically by simulated aperture photometry of images of the narrow line emission and the host galaxy starlight distribution.

Summarizing, it is obvious that aperture effects can change the continuum and the broad emission line fluxes obtained from an AGN. Estimations have proven that the smaller apertures are much more affected than large ones. The magnitude of these effects comprises an important topic in the science and it is further discussed in next section 4.2.

## 4.2 Studies on the Aperture Effect

The optical spectroscopic analysis of the sources in both surveys (Hamburg/ESO & 6dFGS) produced challenging results about the classification of the targets. A relevant shift in the plotted points of the diagnostic diagrams was noticed (see Figure 3.11). In other words, some individual sources are classified as different galaxy type due to the observations with different instruments (spectrographs). Furthermore, the comparison between the BPT diagrams of our sample and the SDSS indicated that some of the objects lied in the "not densely populated regions" of SDSS. As it has already been mentioned, the nearby LLQSOs sample has been selected to be Seyfert type galaxies but the results showed a significant number of sources to be classified as starburst or composite galaxies. Looking at the statistics of the two data sets, less than 10 sources appear to have a width  $\leq 2000$  km/sec (see Figure 3.6c).

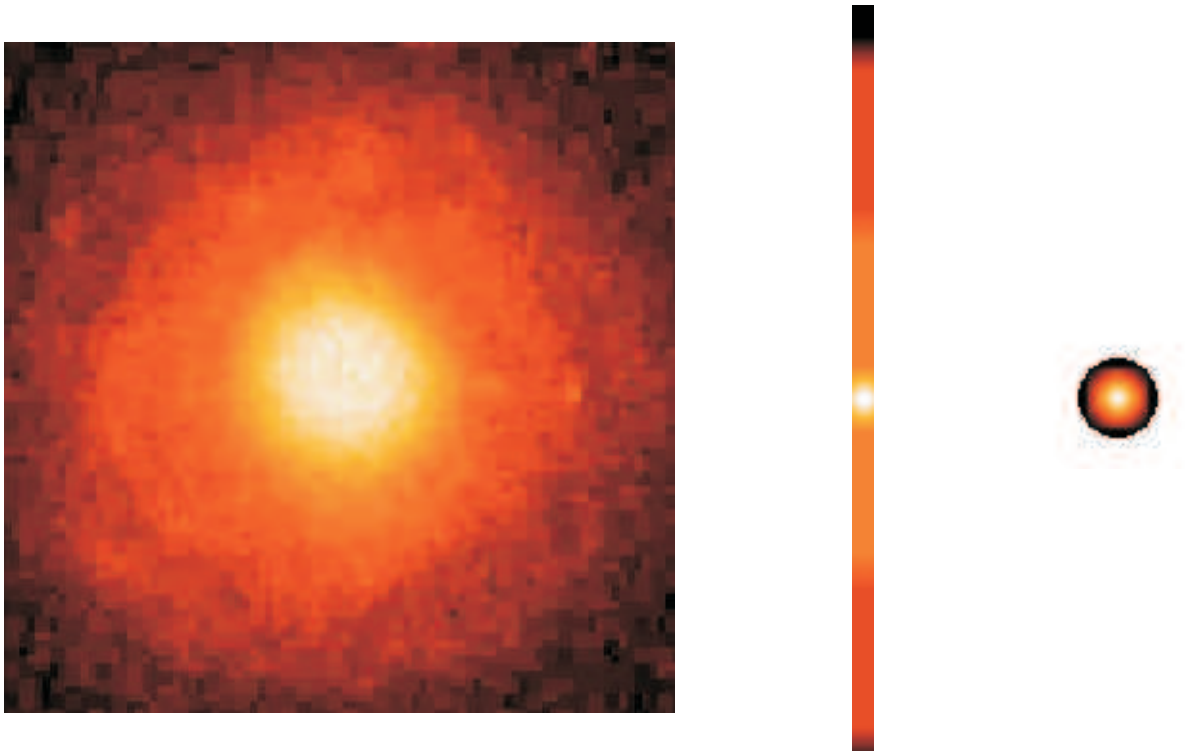


Figure 4.3: The HE0212-0059 galaxy (left) observed with Two Micron All Sky Survey (2MASS), H-Band and simulated with a slit 2 arcsec (middle) like HES and a fibre 6 arcsec (right) like 6dFGS.

The difference in the classification between the same galaxies coming from two different observational techniques, can be explained as an aperture effect. For the spectroscopic data coming from the Hamburg/ESO survey the width of the slit is less than the aperture size of the 6dF fibre. It is obvious then that the information which is admitted to the detector is coming from different parts of the galaxy. So, the question that arises is how much the science observations can be affected by the aperture of the instrument used. The cosmological distance  $z$ , the morphology of the galaxies, and the excitation conditions appear to be the most significant factors in sorting out the galaxies. For this reason, we have extended our studies by simulating galaxies with different morphologies in different cosmological distances under different excitation conditions. In these simulations

we assume observations with different spectroscopy techniques such as fibre (6 arcsec like 6dFGS and 3 arcsec like SDSS) and slit spectroscopy (2 arcsec like HES see Figure 4.3). The effect of the aperture is obvious, but the fundamental question is how this affect to the final results. Not only the implications on local galaxies but also the high redshift observations monopolize the interest of the discussion in the following sections.

#### 4.2.1 Nearby galaxies at high redshifts

One fundamental step in the simulations was to produce distant galaxies as the instruments would have observed them at optical wavelengths (Giavalisco et al. 1996). It is of high importance to mention that no evolutionary effects on the galaxies have been taken into account during this process.

In a generic curved spacetime, there is no preferred notion of the distance between two objects, but in Robertson - Walker spacetimes is possible to define sensible notions of the distance between co - moving objects. Hence, the coordinate distance to another comoving object is independent on time. However, intervals along spacelike slices are not accessible to observation, so it is typically more convenient to use distance measures which can be extracted from observable quantities (Carroll et al. 1992). These include the luminosity distance,

$$d_L \equiv \sqrt{\frac{L}{4\pi F}}, \quad (4.2.1)$$

where L is the intrinsic luminosity and F the measured flux. The proper motion distance is given by :

$$d_M \equiv \frac{u}{\dot{\theta}}, \quad (4.2.2)$$

where u is the transverse proper velocity and  $\dot{\theta}$  the observed angular velocity. The angular diameter distance depends on the proper size of the object, D, which is a known (or assumed) value and its apparent angular size  $\theta$  :

$$d_A \equiv \frac{D}{\theta}. \quad (4.2.3)$$

In an Euclidean space, all of these definitions are the usual notion of distance. In a RobertsonWalker universe, the proper-motion distance turns out to be equal to the physical distance:

$$d_M = R_0 r^1. \quad (4.2.4)$$

In particular,  $d_L$ ,  $d_M$ , and  $d_A$  are not independent but related by:

$$d_L = (1 + z)d_M = (1 + z)^2 d_A, \quad (4.2.5)$$

---

<sup>1</sup>From Lightman et al. (1975)  $(1 + z) = R_0/R_1$ ,  $d_A = R_1 r_1$ ,  $d_M = R_0 r_1$ ,  $d_L = (R_0)^2 r_1 / R_1$ , where r = 0 our self defined position to observe some object at coordinate value  $r_1$ , we are also looking back in time to some time  $t_1 < t_0$  and back to some expansion factor  $R_1 = R(t_1)$



independently of the dynamics  $R(t)$ . So any object can be converted to any other for sources of known redshift. The integral formula for the distance measures at redshift  $z_1$  is :

$$H_0 d_M = \frac{1}{(\Omega_k)^{1/2}} \operatorname{sinn} \left\{ (\Omega_k)^{1/2} \int_1^0 [(1+z)^2(1+\Omega_M z) - z(2+z)\Omega_\Lambda]^{-1/2} dz \right\} \quad (4.2.6)$$

The distance measure will generally increase at small redshifts, but decrease at redshifts higher than some particular value (see also Figure 4.4).

The Ned Wright's calculator<sup>2</sup> has been used in order to obtain the scale, and then to adjust it for the angular sizes calculations. Throughout this process we assume a Hubble constant of  $H_0 = 70 \text{ km s}^{-1} \text{ Mpc}^{-1}$  and cosmological density parameters  $\Omega_m = 0.3$  and  $\Omega_\Lambda = 0.7$  (Hamilton 1998).

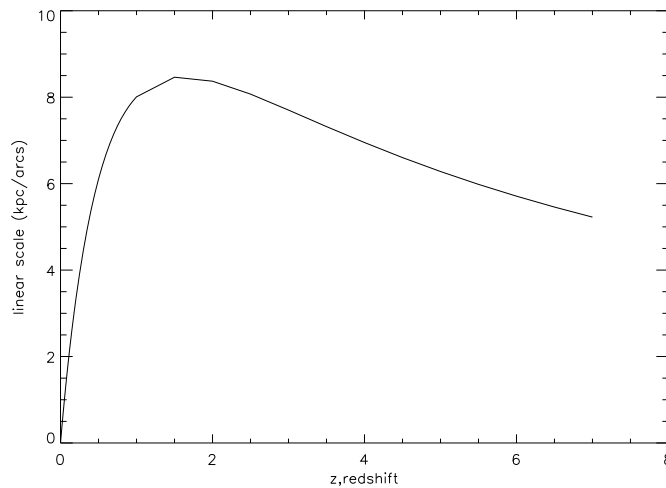


Figure 4.4: Linear scale size of the galaxies as a function of redshift. Due to gravitational lensing the linear scale increases till a certain redshift  $z \sim 1$  and then decreases for higher cosmological distances.

For the present simulations, the angular resolution of the wide field camera (WFPC2) of the Hubble telescope 0.1 arcsec/pixel (Hutchings & Morris 1995) has been assumed. The typical galaxy size has been estimated using 2MASS (Two Micron All Sky Survey) images. The plate scale of a telescope depends on the characteristics of the all its optical elements and can be described as the number of arcseconds, corresponding to a number millimeters at the focal plane.

$$PlateScale = \frac{206265}{D * f} (\text{arcsec/mm}), \quad (4.2.7)$$

where 1 radian = 206265 arcsec, D stands for the telescope mirror diameter and f is the focal length of the telescope.

The calculated angular sizes for some galaxies within a range of redshift are presented in Table 4.1. In Figure 4.4 the relation between the linear scale size of the galaxies versus the cosmological distance (Carroll et al. 1992) is plotted as it has been calculated from

<sup>2</sup>Ned Wright's calculator webpage: <http://www.astro.ucla.edu/wright/CosmoCalc.html>

the Ned Wright's calculator. Due to gravitational effects (lensing), the linear scale is increased till a certain redshift  $z \sim 1$  and then it is decreased for higher cosmological distances.

z	kpc/''	galaxy radius (pixel)	extended radius(pixel)	nucleus radius(pixel)	circumnuclear radius(pixel)
0.001	0.0021	10238.6	3839.48	153.579	1126.25
0.003	0.0062	3467.9	1300.46	52.0185	381.469
0.005	0.0103	2087.48	782.805	31.3122	229.623
0.007	0.0144	1493.12	559.92	22.3968	164.243
0.009	0.0185	1162.22	435.832	17.4333	127.844
0.011	0.0225	955.6	358.35	14.334	105.116
0.013	0.0266	808.308	303.115	12.1246	88.9139
0.015	0.0306	702.647	263.493	10.5397	77.2912
0.017	0.0346	621.416	233.031	9.32124	68.3558
0.019	0.0385	558.468	209.426	8.37702	61.4315
0.021	0.0425	505.906	189.715	7.58859	55.6497
0.023	0.0464	463.384	173.769	6.95076	50.9722
0.025	0.0504	426.607	159.978	6.39911	46.9268
0.03	0.0601	357.754	134.158	5.36631	39.3529
0.035	0.0697	308.479	115.68	4.62718	33.9327
0.04	0.0791	271.82	101.933	4.0773	29.9002
0.045	0.0885	242.949	91.1059	3.64424	26.7244
0.05	0.0977	220.072	82.527	3.30108	24.2079
0.055	0.1069	201.132	75.4245	3.01698	22.1245
0.06	0.1159	185.513	69.5674	2.7827	20.4064
0.065	0.1248	172.284	64.6065	2.58426	18.9512
0.07	0.1337	160.815	60.3056	2.41223	17.6897
0.075	0.1424	150.99	56.6213	2.26485	16.6089
0.08	0.151	142.391	53.3966	2.13587	15.663
0.085	0.1595	134.803	50.5511	2.02204	14.8283
0.09	0.1679	128.058	48.0217	1.92087	14.0864
0.095	0.1762	122.026	45.7598	1.83039	13.4229
0.1	0.1844	116.6	43.725	1.749	12.826
0.11	0.2006	107.183	40.1936	1.60775	11.7901
0.12	0.2163	99.4036	37.2764	1.49105	10.9344
0.13	0.2317	92.7967	34.7988	1.39195	10.2076
0.14	0.2468	87.1191	32.6697	1.30679	9.5831
0.15	0.2614	82.2532	30.8449	1.2338	9.04785
0.16	0.2758	77.9587	29.2345	1.16938	8.57546
0.17	0.2898	74.1926	27.8222	1.11289	8.16119
0.18	0.3035	70.8435	26.5663	1.06265	7.79279
0.19	0.3169	67.8479	25.443	1.01772	7.46327
0.2	0.33	65.1545	24.4329	0.977318	7.167
0.25	0.391	54.9898	20.6212	0.824847	6.04888
0.3	0.4454	48.2735	18.1026	0.724102	5.31008
0.35	0.494	43.5243	16.3216	0.652865	4.78767
0.4	0.5373	40.0168	15.0063	0.600252	4.40185
0.45	0.5759	37.3346	14.0005	0.560019	4.10681
0.5	0.6104	35.2244	13.2092	0.528366	3.87468
0.55	0.6411	33.5377	12.5766	0.503065	3.68915
0.6	0.6685	32.1631	12.0612	0.482447	3.53794
0.65	0.6929	31.0305	11.6364	0.465457	3.41336
0.7	0.7146	30.0882	11.2831	0.451323	3.3097
0.75	0.7338	29.3009	10.9878	0.439513	3.2231
0.8	0.7508	28.6375	10.7391	0.429563	3.15013
0.85	0.7658	28.0765	10.5287	0.421147	3.08841
0.9	0.7791	27.5972	10.349	0.413958	3.03569
0.95	0.7907	27.1924	10.1972	0.407886	2.99116
1	0.8008	26.8494	10.0685	0.402741	2.95343
1.5	0.8462	25.4089	9.52834	0.381133	2.79498
2	0.837	25.6882	9.63307	0.385323	2.8257
2.5	0.8071	26.6398	9.98993	0.399597	2.93038
3	0.7702	27.9161	10.4685	0.418741	3.07077
3.5	0.732	29.3729	11.0148	0.440593	3.23102
4	0.6951	30.9322	11.5996	0.463983	3.40254
4.5	0.6603	32.5625	12.2109	0.488438	3.58188
5	0.6281	34.2318	12.8369	0.513477	3.7655
5.5	0.5983	35.9368	13.4763	0.539052	3.95305
6	0.571	37.655	14.1206	0.564825	4.14205
6.5	0.5458	39.3936	14.7726	0.590904	4.3333
7	0.5226	41.1424	15.4284	0.617136	4.52566

Table 4.1: Angular diameter sizes of the simulated galaxies for a redshift range  $0.001 < z < 7$ . The pixel values of each part of the galaxy are also presented. The average size of 21.5 kpc for the entire galaxy was used.

### 4.2.2 Software algorithm for the simulations

The philosophy of the studies on the aperture effect can be described by the applied algorithm. The initial studies were performed using a galaxy with circular symmetry. The galaxy consists of three emission line regions (see Figure 4.5). The nucleus located on the central region of the galaxy, the circumnuclear region (bulge) and the extended region (disk). As it has been already described in section 2.2.2, the **nuclear optical continuum emission** is visible whenever we have a direct view of the accretion disc. Jets can also contribute to this component of the AGN emission. The optical emission has a roughly power-law dependence on wavelength. The **broad optical emission lines** come from cold material close to the central black hole. The lines are broad because the emitting material is revolving around the black hole with high speeds, emitting photons at varying Doppler shifts. Also, the **narrow optical emission lines** come from more distant cold material, and so are narrower than the broad lines.

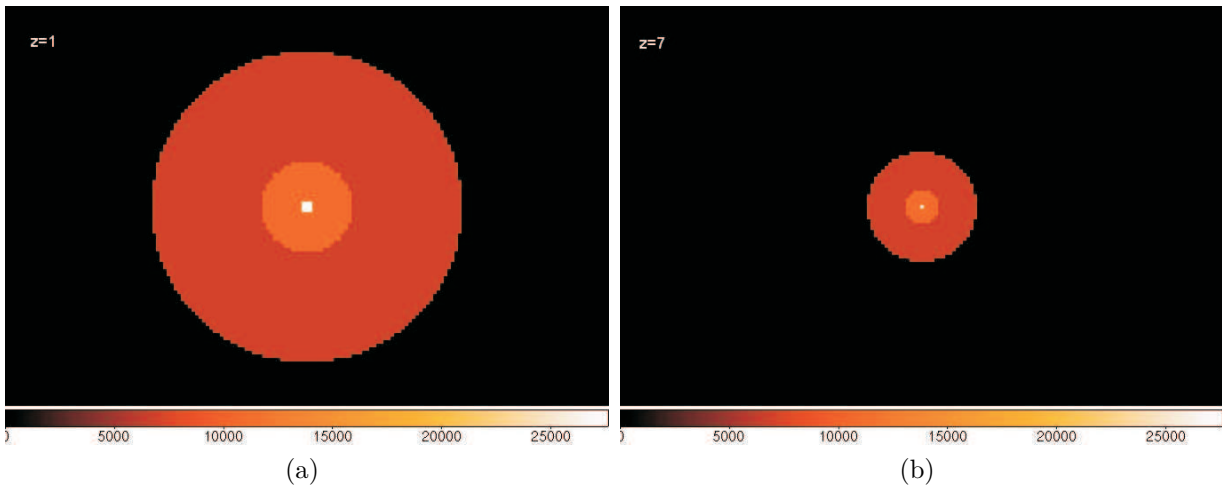


*Figure 4.5: Images of a local and a distant galaxy, as an example, produced by the simulations program (before smoothing), (a) local galaxy in redshift  $z=1$ , (b) distant galaxy in redshift  $z = 7$ . The simulated galaxies consist of three emission line regions, the central nucleus region, the circum nuclear environment (bulge) and the extended part (disk). The angular sizes of the galaxies strongly depend on their cosmological distance.*

Each part of the galaxy emits line fluxes at different percentages. Initial flux values were obtained from the fitting analysis of the sample. As the main objective of these simulations was to derive the BPT diagrams, the cosmological distance was not applied to the fluxes, since it equally affects all lines. Given that its effect would be canceled. Percentages of all detected emission lines were used according to the astrophysical background of the objects. Moreover, apart from the flux values, every region of the circular galaxy has a different radius (see Table 4.1). The extended region (disk) of the galaxy dominates the largest part of the galaxy, whereas the nucleus of the galaxy is almost point like and the rest of the galaxy is dominated by the circum nuclear environment (bulge). For these calculations, the NED Wright's angular sizes of the galaxies (section 4.2.1) were used, while an average size  $\sim 21.5$  kpc was applied. The values were also useful for the next steps of the simulation process where we place the nearby galaxies at higher cosmological distances (see also Figure 4.5).

The algorithm applies different slits and aperture sizes of fibers on the galaxy, in order to figure out in which way the instrument used affects the BPT classification. The initial simulation conditions were:

- Circular symmetry.
- Pixel scale: 0.1 " per pixel, like wide field camera of the Hubble Space Telescope.
- 3 concentric emission line regions, nucleus (3% of the galaxy size,  $\sim 0.6$  kpc), circum nuclear (22% of the galaxy size,  $\sim 4.7$  kpc) and extended (75% of the galaxy size,  $\sim 16.1$  kpc).
- The emitted line flux of each galaxy was defined as a constant. The relation between the flux and the region size was also considered. The line ratio between the hydrogen recombination lines were defined to respect to atomic parameters (i.e  $H\alpha / H\beta > 3$ ).<sup>3</sup>
- The slit size is 2" (see Figure 4.6a) like the one of the HE survey, the fibre sizes are 6.7" (see Figure 4.6b) as that of the 6dFGS, and 3" like the one of the SDSS survey (see Figure 4.6c).

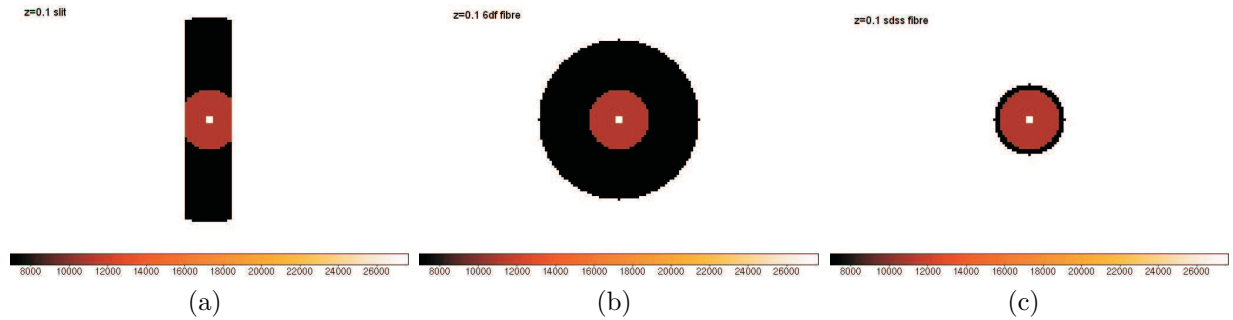


Figure 4.6: Simulation view of a galaxy in cosmological distant  $z = 0.1$ , observed with: (a) HES slit 2arcsec, (b) 6dFGS fiber 6 arcsec, and (c) SDSS fiber 3 arcsec.

Subsequently, the excitation conditions of the galaxies were changed and we finally run simulations for different redshifts. In order to investigate the aperture effect in the whole range of the classical diagnostic diagram, exotic conditions were assumed for some galaxies.

The spectroscopic techniques that were applied were similar to our observational data (slit 2 arcsec and fiber 6 arcsec) and they were also compared to the SDSS survey (3 arcs fiber). In addition, instead of the slit spectroscopy technique of the HES survey, we applied a long slit to complete our studies. The option for a different galaxy morphology, such as elliptical, is also provided by the simulations, in order to investigate any possible effect due to the galaxy's shape. The following sections present and discuss the simulation results.

<sup>3</sup>Only the  $H\beta$   $\lambda$  4861Å,  $[O\text{III}]$   $\lambda$  5006.843Å,  $H\alpha$   $\lambda$  6562Å,  $[N\text{II}]$   $\lambda$  6583.41Å emission lines were used due to the challenging quality of the observational data.

### 4.2.3 The aperture effect in the local universe

In chapter 3 differences in the classification of the HES sample were presented. There are cases with large differences in the classification (see Figure 4.1) and many others with different degrees of dissimilarities. This section presents the results of local universe ( $z \leq 0.1$ ) simulations. Several redshifts have been used, but for simplicity we present here the results for  $z = 0.02$ , like that of the source HE0212-0059 (see Figure 4.1). Galaxies with elliptical symmetry were also simulated and compared to circular one, but no strong difference was detected. Also, most members of the LLQSOs sample have circular morphology (see also Figure 4.3), therefore, hereafter we discuss the case of circular symmetry. In order to investigate the aperture effect in local universe, we design a galaxy which is representative of our sample and of the observations. The galaxy is dominated by the disk (extended part). The aim was to have different galaxy regions, traveling the BPT diagram, which is required in order to study the different possible types of galaxies and their properties. Therefore, four different models of galaxies were created.

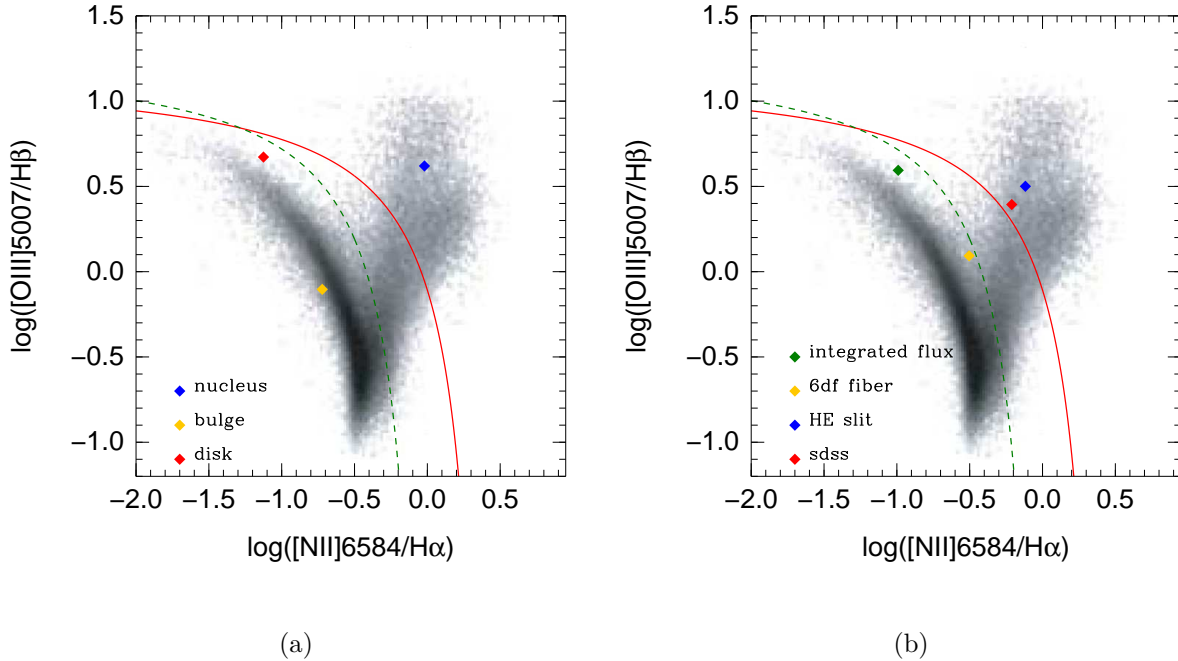


Figure 4.7: The classification diagram of a simulated local galaxy ( $z = 0.02$ ) consisting of three emission regions, nucleus, bulge and disk. (a) The initial conditions for the nucleus of the galaxy were selected to classify it in the AGN part of the optical diagnostic diagram. The bulge of the present galaxy is located in the pure star forming branch, while the disk was chosen to be dominated by star formation. (b) The classification of the integrated galaxy (green point) according to HES (blue point), 6dFGS (yellow point) and SDSS (red point) observations. The red line is the theoretical maximum starburst limit. Galaxies that lie below the star formation demarcation green dashed line are classified as  $H_{II}$  regions-like galaxies. The galaxies that lie between the two classification lines are on the AGN- $H_{II}$  mixing sequence and are sorted as composite galaxies. The sources that classed above the red line are classified as AGNs. The dark cloud represents thousands of galaxies from previous studies by Kewley et al. (2006) observed by SDSS (3 arcsec fiber). See also Table 4.2.

Figure 4.7a shows the classification diagram for the first case. The initial conditions for the nucleus of the galaxy were selected to classify it in the AGN part of the optical

<i>Pixel to Pixel</i>	Nucleus	Bulge	Disk	<i>Integrated</i>	Nucleus	Bulge	Disk
[N II]	94 %	5 %	1%	[N II]	1.5 %	4.5 %	94%
H $\alpha$	71.5%	19%	9.5%	H $\alpha$	0.2%	1.8%	98%
[O III]	83%	5%	12%	[O III]	0.1%	0.4%	99.5%
H $\beta$	68%	23%	9%	H $\beta$	0.1%	2.4%	97.5%

(a)
(b)

**Table 4.2:** *The emission line contribution on each region of the galaxy. (a) The pixel to pixel galaxy where the nucleus has the maximum percentage in all four lines. (b) The integrated galaxy, dominated by the disk.*

diagnostic diagram. The bulge of the present galaxy is located in the pure star forming branch, while the disk was chosen to be dominated by star formation, but it also lies close to the star formation demarcation line (green dashed line, see Figure 4.7). The classification of such an object is shown in Figure 4.7b, where techniques like HES, 6dFGS and SDSS were used for the simulated observations. The green data point (see Figure 4.7b) represents the classification of the simulated integrated galaxy, and it is quite similar to the initial classification of the disk. This implies that this source is totally dominated by its disk (see Table 4.2). The slit (HES) observations using only the seeing disk ( $\sim 2''$ ) classify the galaxy as an AGN, while fiber (6 arcsec, 6dFGS) observations result a star forming contaminated galaxy, close to the composite branch of the diagram. This model explains several classification cases of our nearby LLQSOs sample, where the same source was classified as an AGN with the data from HES and as a star forming galaxy with 6dFGS observations. The simulations with a similar to SDSS instrument (3 arcsec fiber) result in an AGN similar to HES (since their apertures are close to the size), but it is notable that the galaxy with the SDSS observations is approaching the composite region of the diagram. Essentially, the smallest the aperture, the more we are dominated by the nucleus.

Table 4.2 provides information about the contribution of each region of the galaxy according to the percentage of each emission line. In particular, Table 4.2a gives the percentages per emission line ([N II], H $\alpha$ , [O III], H $\beta$ ) of each region (nucleus, bulge, disk) in pixel to pixel scale, while Table 4.2b gives the percentages of the integrated galaxy. A comparison between these sub - tables shows that the nucleus dominates in pixel to pixel scale, unlike to the integrated galaxy, where either the disk dominates the galaxy. This implies that the relative flux which corresponds to the nucleus is the highest one in comparison to the bulge and disk, but since the area occupied by the disk or the bulge is larger than the nuclear one, the integrated galaxy is dominated in total by the disk.

Figure 4.8 illustrates the classification of a galaxy with more exotic conditions. The nucleus and the disk of the galaxy are located in the 'extreme' and not populated pure star forming region, while the bulge is placed in the AGN population of the optical diagnostic diagram (see Figure 4.8a). The combination of these three regions, results of an integrated galaxy, classified as a starburst (see green data point in Figure 4.8b). Observing this object with a big aperture size like the one of 6dFGS (6 arcsec), we end up with an Active galaxy (AGN part). In comparison, the same object is classified as a composite galaxy and as star forming galaxy, assuming HES (2 arcsec slit) and SDSS (3 arcsec fiber) observations, respectively. The current model is remarkable interesting, not only due to

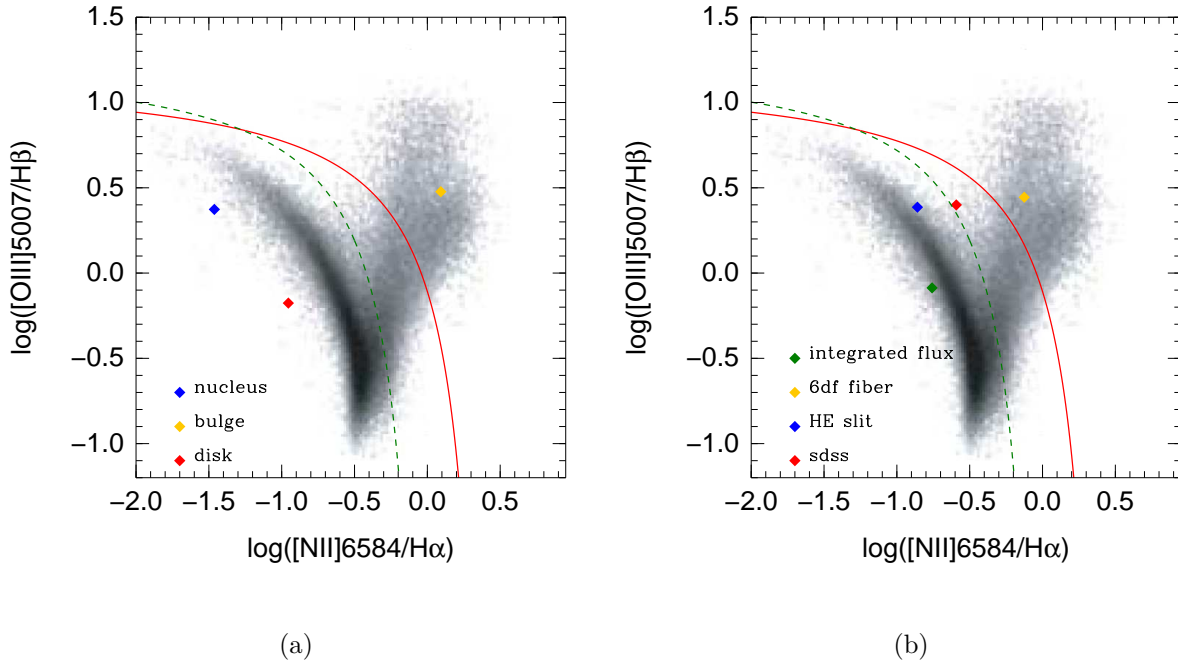


Figure 4.8: The classification diagram of a simulated local galaxy ( $z = 0.02$ ) consisting of three emission regions, nucleus, bulge and disk. (a) The initial conditions for the nucleus of the galaxy were selected to classify it in the  $H\text{II}$  of the optical diagnostic diagram. The bulge of the present galaxy is located in the pure star forming branch, while the disk was chosen to be dominated by star formation. (b) The classification of the integrated galaxy (green point) according to HES (blue point), 6dFGS (yellow point) and SDSS (red point) observations. The red line is the theoretical maximum starburst limit. Galaxies that lie below the star formation demarcation green dashed line are classified as  $H\text{II}$  regions-like galaxies. The galaxies that lie between the two classification lines are on the AGN- $H\text{II}$  mixing sequence and are sorted as composite galaxies. The sources that classed above the red line are classified as AGNs. The dark cloud represents thousands of galaxies from previous studies by Kewley et al. (2006) observed by SDSS (3 arcsec fiber). See also Table 4.3.

the initial exotic conditions of the three regions were chosen, but also because of the dissimilar classification outcome (AGN, composite, Starburst) for all three instruments. This model could be representative of galaxies with an extra nuclear ionization cone and a dusty nucleus. The contribution of each emission line is presented in Table 4.3 for both pixel to pixel and integrated galaxy. In Table 4.3a, we can conclude from the percentages that the nucleus is dominated in the three emission lines ( $H\alpha$ ,  $[\text{O III}]$ ,  $H\beta$ ), but in  $[\text{N II}]$  line the bulge is dominated. Concerning the integrated galaxy, the disk dominates all galaxy emission (consistently with the results shown in Figure 4.8).

Another good example of a simulated galaxy is presented in Figure 4.9. In this case the nucleus of the model galaxy dominated by Seyfert/AGN activity, the disk is dominated by  $H\text{II}$  regions, while the conditions of the bulge are described by composite activity (see also Figure 4.9a). The classification of such a galaxy is given in Figure 4.9b, where the integrated galaxy shows starburst activity. However, observations with all three instruments (HES, 6dFGS, SDSS) lead to an AGN galaxy, with the largest aperture (6 arcsec, 6dFGS) to be close to the maximum starburst limit (see red line in Figure 4.9b). Also, the percentages of each emission lines input are given in Table 4.4. The relative pixel to



<i>Pixel to Pixel</i>	Nucleus	Bulge	Disk	<i>Integrated</i>	Nucleus	Bulge	Disk
[N II]	25%	66%	9%	[N II]	0.1%	6.6%	93.4 %
H $\alpha$	84%	6%	10%	H $\alpha$	0.2%	0.6%	99.2%
[O III]	85%	11%	4%	[O III]	0.4%	2.6%	97%
H $\beta$	80%	8%	12%	H $\beta$	0.1%	0.6%	99.3%

(a) (b)

*Table 4.3: The emission line contribution on each region of the galaxy. (a) The pixel to pixel galaxy where the nucleus has the maximum percentage in all four lines. (b) The integrated galaxy, dominated by the disk.*

pixel flux of the nucleus is the highest one, since the contribution of all emission lines is much more than the bulge' s and disk' s one (see Table 4.4a). In the integrated galaxy (see Table 4.4b) the bulge has the highest relative flux in comparison to the nucleus and the disk, but as we can see in Figure 4.9, the galaxy is dominated by the disk, because of its large area.

<i>Pixel to Pixel</i>	Nucleus	Bulge	Disk	<i>Integrated</i>	Nucleus	Bulge	Disk
[N II]	83%	14%	3%	[N II]	0.5%	4.3%	95.2%
H $\alpha$	72%	14%	14%	H $\alpha$	0.4%	4.3%	95.6%
[O III]	94%	4%	2%	[O III]	0.8%	1.9%	97.3%
H $\beta$	67%	16.5%	16.5%	H $\beta$	0.0003%	0.95%	99.05%

(a) (b)

*Table 4.4: The emission line contribution on each region of the galaxy. (a) The pixel to pixel galaxy where the nucleus has the maximum percentage in all four lines. (b) The integrated galaxy, dominated by the disk.*

In the previous sections, we have mentioned that the HES data were taken with a slit 2 arcsec, while the spectra has been extracted in the seeing disk aperture size (2"  $\times$  2" slit), in order to avoid any contamination of neighboring sources. In this simulation, instead of this, a long slit covering all galaxy (2 arcsec) was applied and the result is presented in Figure 4.10. Figure 4.10b shows the classification of a model galaxy with a nucleus which has Seyfert activity and starburst activity in its bulge and disk (see also Figure 4.10a). The integrated galaxy is dominated by ionized gas (hot stars, H II) like its disk. Similar conditions are observed with a long slit technique in contrast to HES technique where the galaxy would be classified as Seyfert. This is due to the H II contribution of the bulge and disk along slit. Since they use fibers centered in the nucleus the SDSS observations result in an AGN activity and the 6dFGS taxonomy the galaxy as a composite. In particular, Table 4.5 shows the presence of each emission line in each region of the galaxy. The pixel to pixel flux is higher in the nucleus and in the integrated flux galaxy, apart from [N II] line, the rest of the lines (H $\alpha$ , [O III], and H $\beta$ ) are dominates by the disk.

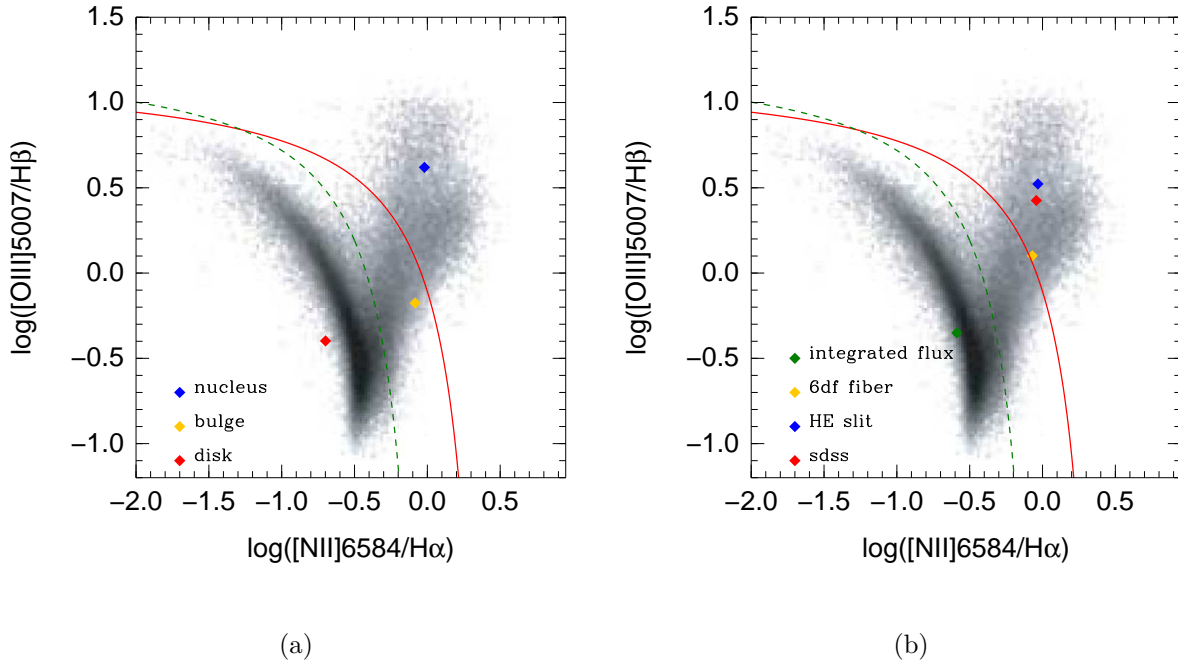


Figure 4.9: The classification diagram of a simulated local galaxy ( $z = 0.02$ ) consisting of three emission regions, nucleus, bulge and disk. (a) The initial conditions for the nucleus of the galaxy were selected to classify it in the AGN part of the optical diagnostic diagram. The bulge of the present galaxy is located in the pure star forming branch, while the disk was chosen to be dominated by star formation. (b) The classification of the integrated galaxy (green point) according to HES (blue point), 6dFGS (yellow point) and SDSS (red point) observations. The red line is the theoretical maximum starburst limit. Galaxies that lie below the star formation demarcation green dashed line are classified as  $H_{II}$  regions-like galaxies. The galaxies that lie between the two classification lines are on the AGN- $H_{II}$  mixing sequence and are sorted as composite galaxies. The sources that classed above the red line are classified as AGNs. The dark cloud represents thousands of galaxies from previous studies by Kewley et al. (2006) observed by SDSS (3 arcsec fiber). See also Table 4.4.

#### 4.2.4 Aperture effect at high redshift: Cosmological implications

Despite the fact that our LLQSOs sample consists only of nearby galaxies ( $z < 0.06$ ), the observations of high redshift galaxies are of high importance in astronomy. Galaxies at high redshift like  $z=8.5$  have already been observed these days. The understanding of the possible impact of the aperture effect while studying galaxies at redshifts higher than 0.1 is the topic of the current section.

The results of high redshift galaxies ( $0.1 < z \leq 7$ ) are directly compared to those of local galaxies ( $z \leq 0.1$ ). The symmetry of the galaxies that is applied in this section is circular (Figure 4.11). According to the studies of Kewley et al. (2006), the majority of the local galaxies included in the SDSS sample, do not present extreme behaviors in the diagnostic diagrams, hence this study is focused on 'normal' excitation conditions.

In this section we deal with a model of a representative galaxy of our nearby LLQSOs sample almost similar to the case of Figure 4.7, placing it at higher redshifts without any consideration of evolution. The standard optical diagnostics diagrams for each observational technique similar to HES (seeing disk aperture size), SDSS, and 6dFGS are presented in Figures 4.11a, 4.11b, 4.11c, respectively. In the optical diagnostic diagrams

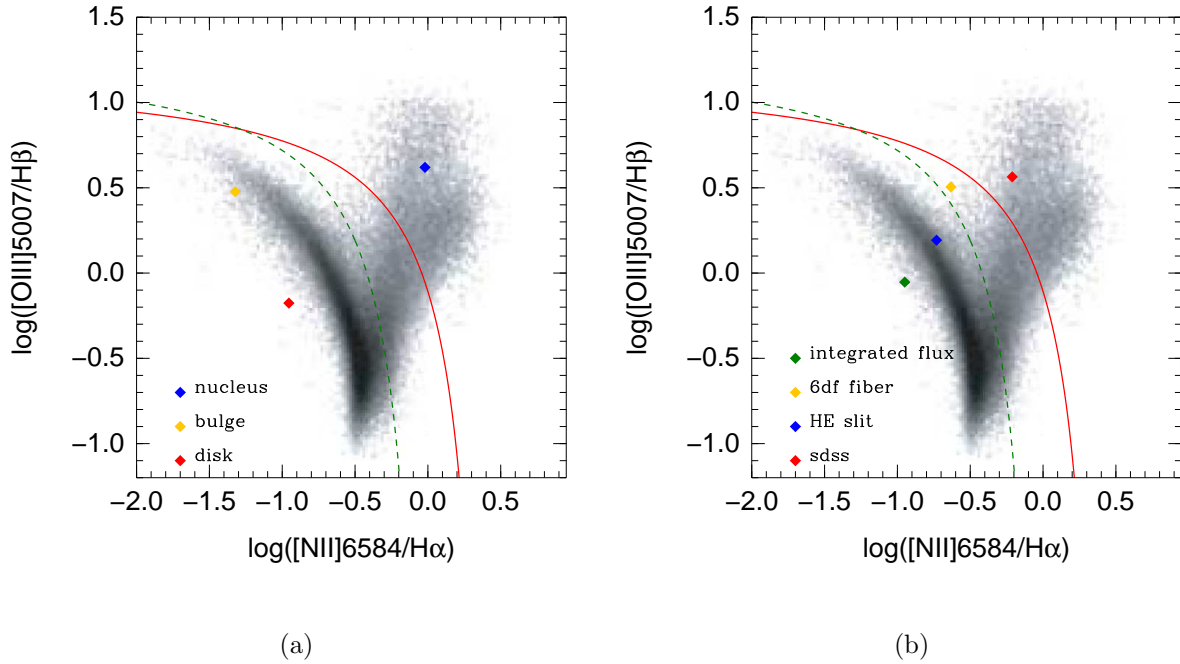


Figure 4.10: The classification diagram of a simulated local galaxy ( $z = 0.02$ ) consisting of three emission regions, nucleus, bulge and disk. (a) The initial conditions for the nucleus of the galaxy were selected to classify it in the AGN part of the optical diagnostic diagram. The bulge of the present galaxy is located in the pure star forming branch, while the disk was chosen to be dominated by star formation. (b) The classification of the integrated galaxy (green point) according to HES (blue point), 6dFGS (yellow point) and SDSS (red point) observations. The red line is the theoretical maximum starburst limit. Galaxies that lie below the star formation demarcation green dashed line are classified as  $H_{II}$  regions-like galaxies. The galaxies that lie between the two classification lines are on the AGN- $H_{II}$  mixing sequence and are sorted as composite galaxies. The sources that classed above the red line are classified as AGNs. The dark cloud represents thousands of galaxies from previous studies by Kewley et al. (2006) observed by SDSS (3 arcsec fiber). See also Table 4.5

In Figure 4.11, the plotted points correspond to galaxies with a variety of cosmological distances ( $0.1 < z \leq 7$ ) and their distribution in the range of the diagram is correlated with the spectroscopic technique. The largest distribution takes place in the BPT diagram for galaxies observed with an instrument similar to HES (2 arcsec slit), so the smallest the aperture size of the instrument the smallest the area occupied by the data points. Furthermore, the galaxies with the smallest cosmological distant of this subsample of high  $z$  galaxies, correspond to the higher value of the Y axis,  $[O III]/H\beta$ . The difference in this case is that the galaxy with the highest redshift is not located in the lower value of the Y axis, but somewhere in between. Due to the gravitational lensing (see also Figure 4.4), the linear scale of the galaxy increases until  $z \approx 1$  and then decreases again. Therefore, in the diagnostic diagrams the galaxy that is located in the lower value of the Y axis is the one with redshift  $z \approx 1$ . The most local galaxy of this sub - sample is located in higher value of the X axis ( $[N II]/H\alpha$ ). This galaxy is dominated by Seyfert activity in the HES observations, but in the SDSS it is located in the composite part of the diagram and especially it lies exactly on the pure star formation demarcation line (green dashed line), while in the 6dFGS sample the galaxy shows starburst contamination. In particular, the

<i>Pixel to Pixel</i>	Nucleus	Bulge	Disk	<i>Integrated</i>	Nucleus	Bulge	Disk
[N II]	96.5%	1%	2.5%	[N II]	0.7%	0.4%	98.9%
H $\alpha$	71%	14.5%	14.5%	H $\alpha$	0.1%	0.9%	99%
[O III]	82.5%	14.3%	3.2%	[O III]	0.4%	4.1%	95.5%
H $\beta$	66%	17%	17%	H $\beta$	0.07%	0.95%	98.98%

(a) (b)

*Table 4.5: The emission line contribution on each region of the galaxy. (a) The pixel to pixel galaxy where the nucleus has the maximum percentage in all four lines. (b) The integrated galaxy, dominated by the disk.*

shift from the SDSS observations is approximately 0.5 dex for the HES and 0.3 dex for the 6dFGS. In Y axis ( $[\text{O III}]/\text{H}\beta$ ), the shift is less in all three techniques ( $\sim 0.3$  dex for HES and  $\sim 0.1$  for 6dFGS, having as reference the SDSS observations).

The results indicates that at high redshift the aperture effect loses importance. The galaxies occupy smaller area of the sky, and they are likely to be integrated by most instruments.

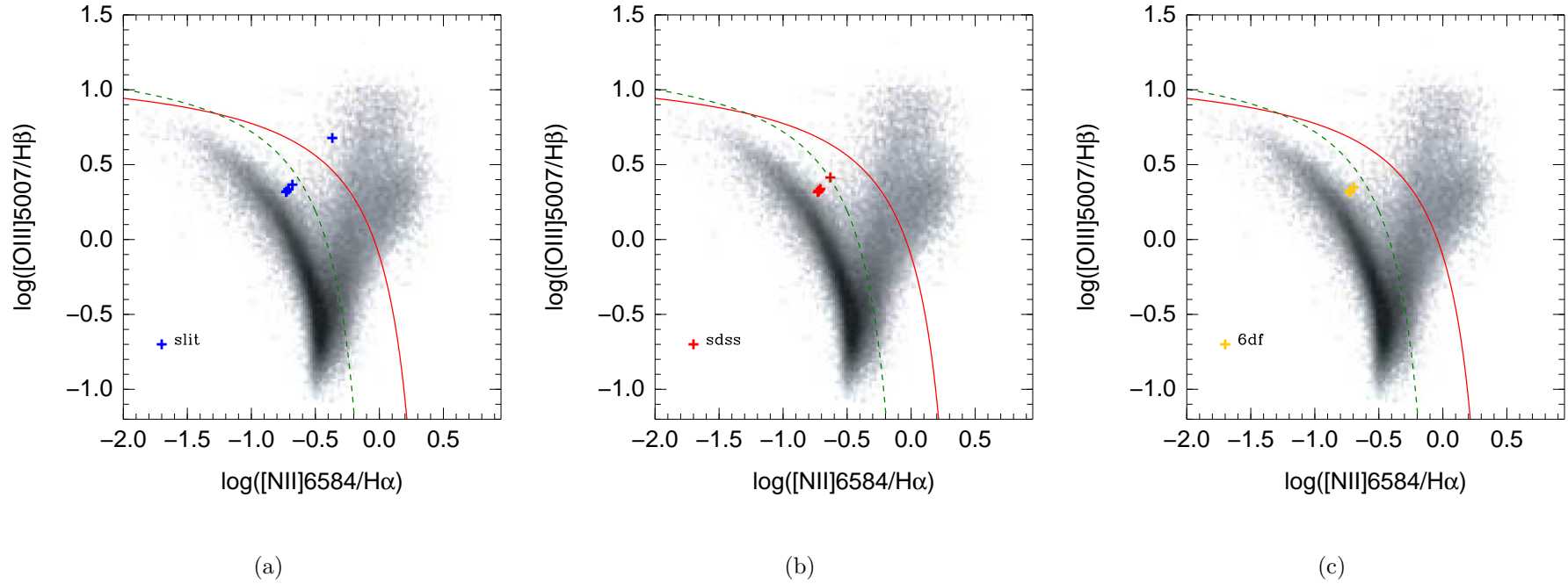


Figure 4.11: The classification diagrams for high redshift objects  $0.1 \leq z \leq 7$ , observed with three different instruments, (a) slit 2 arcsec like HES observations (spectra extracted in the seeing disk aperture size), (b) 3 arcsec fiber like SDSS observations, (c) 6 arcsec fiber like 6dFGS observations. The symmetry of the galaxies is circular, similar to the case of Figure 4.7, placing it at higher redshifts without any consideration of evolution. The dark cloud represents thousands of galaxies from previous studies by Kewley et al. (2006) observed by SDSS (3 arcsec fiber). The red line is the theoretical maximum starburst limit and the green dashed represents the pure star formation demarcation line.

A more detailed attention was given in the slit observations depending on the way that the spectra is extracted. An attempt to simulate high redshift galaxies observed with long slit spectroscopy is presented in Figure 4.12. In contrast to the simulations where the slit extraction minimizes the contamination of nearby sources (see also Figure 4.11a), the point distribution is not so spread in the long slit and the source with the smallest cosmological distant of this subsample lies exactly in the green dashed line, which represents the pure star formation demarcation line and is comparable to the SDSS (see also Figure 4.11b).

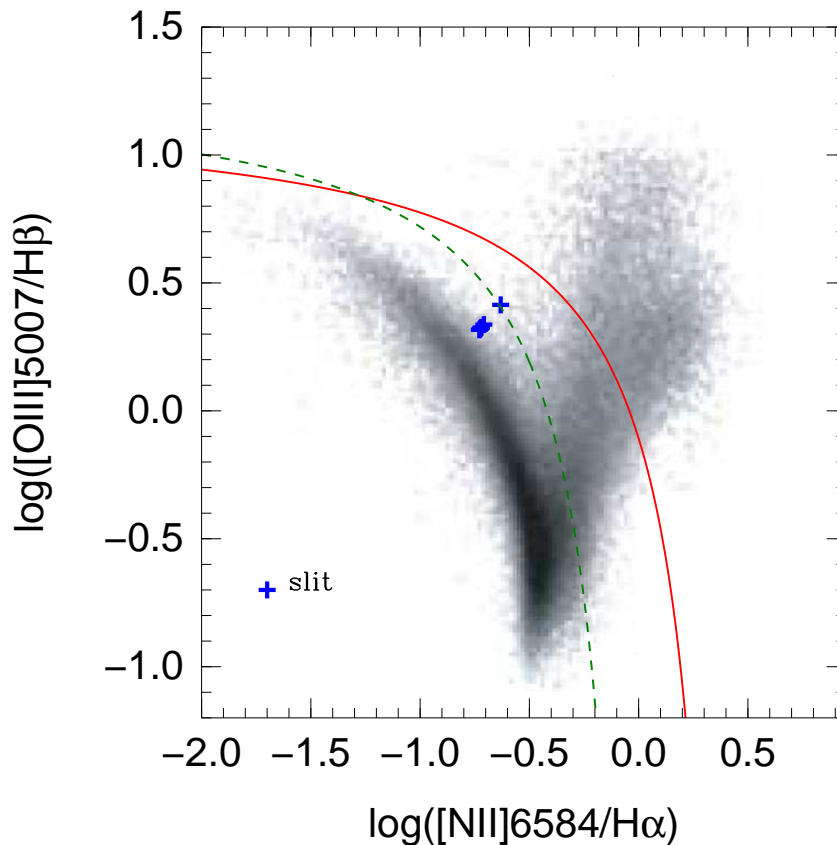


Figure 4.12: The classification diagrams for high redshift objects  $0.1 \leq z \leq 7$ , observed with long slit spectroscopy. The symmetry of the galaxies is circular, similar to the case of Figure 4.7, placing it at higher redshifts without any consideration of evolution. The dark cloud represents thousands of galaxies from previous studies by Kewley et al. (2006) observed by SDSS (3 arcsec fiber). The red line is the theoretical maximum starburst limit and the green dashed represents the pure star formation demarcation line.

The SDSS diagram (dark cloud in the BPT) represents mostly the nuclei and the bulge of the observed galaxies. All contribution coming from (but may be excited) regions is likely not there. Also, each individual point is slightly different affected by the aperture effect. So an ideal SDSS diagram would slightly shift each observation and would probably be not so spiral. If compared with a high redshift population, the BPT diagram would look different, as there are likely to integrate the entire galaxy.

### 4.3 Concluding Remarks

In order to investigate the aperture effect, several simulations have been presented and discussed in detail. The different techniques that can be used in order to obtain spectroscopic observations apply different aperture sizes, and this issue can play a critical role in the classification of observed objects. Local galaxies ( $z < 0.1$ ) with different ionizing sources were modeled and compared with distant ones, in order to provide a solid explanation about the effect of the aperture size. The LLQSOs sample members, generally, they do not show exotic galaxy morphologies but mainly circular and elliptical symmetries. Examples with circular symmetry were provided, while elliptical galaxy models resulted in no relevant differences. The main results of this chapter can be summarized as follows:

- The simulations can explain dex variations up to  $\sim 0.6$  in  $[\text{N II}]/\text{H}\alpha$  and up to  $\sim 0.4$  in  $[\text{O III}]/\text{H}\beta$ . Several 'tendencies' of the aperture effect have been proven. From small to large apertures, galaxies classified from H II to Seyfert, Seyfert to H II; and Seyfert to composite have been shown. These differences in the classification explain the shifts measured in Chapter 3.
- The aperture effect has a much larger impact on the local universe than at high redshift. This is of course expected, since at high redshifts the instruments are likely to observe almost all the galaxy structure.
- The importance of the individual classification of the galaxy region, as well as its effective area have been shown. These two parameters are ultimately related and are needed to understand how an instrument configuration affects the final galaxy classification.
- The SDSS classification must be affected by the aperture effect. Each point, depending on the redshift, carries a small shift that may have an impact in the broadness and peak of the diagram. At higher redshifts the SDSS distribution would be affected by selection effects. Some regions could be not so densely populated to the weakness of the galaxies.
- Further investigations on this topic are necessary. To create more galaxy models, which include nuclear dominated and bulge dominated galaxies or galaxies with a broad range of observations.

It is remarkable, that the simulations are ideal cases and in real observations there are several other factors (i.e detector errors, S/N ratio) that could affect the result 'negative'.





# 5. Optical/Infrared Interferometry - LINC NIRVANA

*The historical breakthroughs consequence of the great efforts to achieve high spatial resolution are described in the first section of this chapter. Furthermore, the Large Binocular Telescope, its instruments, and particularly the LINC NIRVANA instrument, and the main components built at I. Physics Department of the University of Cologne, are described.*

## 5.1 Interferometry retrospection

The development of optical interferometry extends over more than 300 years and is closely linked with the history of wave optics. The starting point of optical interferometry can be defined when Boyle and independently Hooke first described the commonly known Newtons rings in the latter half of the 17th century. In 1868, Fizeau proposed an arrangement consisting of two slits placed in front of a telescope with the aim to measure the angular dimensions of a star. The separation when the interference fringes crossing the image of the star disappeared could then be used to calculate the angle subtended by the star. Due to the small aperture of the telescope, this experiment failed. However, in 1890, Michelson's attempt to apply this interference idea in order to measure the diameters of Jupiters satellites was successful. Michelson also tried to extend this technique to longer baselines but problems such as mechanical stability and the atmospheric turbulence were obvious obstacles.

However, the idea of measuring the degree of correlation of the intensity fluctuations at two points in the field ([Brown & Twiss 1957](#)) represents a completely different approach. This new method was used in the intensity interferometer ([Brown 1964](#)) to make measurements on 32 stars with angular diameters down to 0.4 mas (milliarcsec). Some ideas were based on heterodyne techniques ([Johnson et al. 1974](#)) followed by the development of lasers. In this method, the light from the star is mixed with light from a laser at two photodetectors, and the resulting heterodyne signals are multiplied in a correlator. The output from this correlator is a measure of the degree of coherence of the wave fields at the two photodetectors.

Because of Fraunhofer diffraction, the resolution limit of a telescope is a function of the size of the main mirror. When field waves are passing through an aperture or slit, the size of the observed aperture image changes. That happens because of the far -field location of the observation and the two dimensional nature of the outgoing diffracted waves passing through the aperture. The Airy disk is the result of these images of the

distant objects (see also section 1.2) and the image (PSF) is the Fourier transform of the pupil.

When the aperture of a telescope  $D$  is greater than the Fried's parameter  $r_0$  (Fried 1966), light waves reaching an image from various parts of the aperture have random phase and so on average do not interfere constructively, and do not contribute to making a sharper image. The resolution limit of such a telescope for exposures longer than the atmospheric coherence time is about  $\lambda/r_0$ , while the angular resolution of an interferometer is given by  $\lambda/B$ , where  $B$  is the length of the maximum physical separation of the telescopes in the array, called the baseline. The only advantage arising from increasing the aperture is to collect more photons.

The astronomical imaging is not the only one that is directly affected by the atmosphere. Interferometry is also limited by atmospheric distortion of the wavefront incident on the subapertures. If the subaperture diameters are smaller than  $r_0$ , they do not need wavefront correction within each one. The only correction necessary is to the relative phases of the subapertures, which are usually separated by more than  $r_0$ ; this is called piston correction and corresponds to an adjustment of the path-length compensation between the interfering waves so as to stabilize the fringes. However, if the subaperture diameters each are larger than  $r_0$ , their full benefit of their diameters will contribute to improving the sensitivity and limiting magnitude of the interferometer only if they are adaptively corrected. The correction must of course be completed within a time shorter than  $t_0$ , which is of the order of ms, in order to be useful. For many years telescope performance was limited by this effect, until the introduction of speckle interferometry (Labeyrie 1970) and adaptive optics provided ways to remove this limitation.

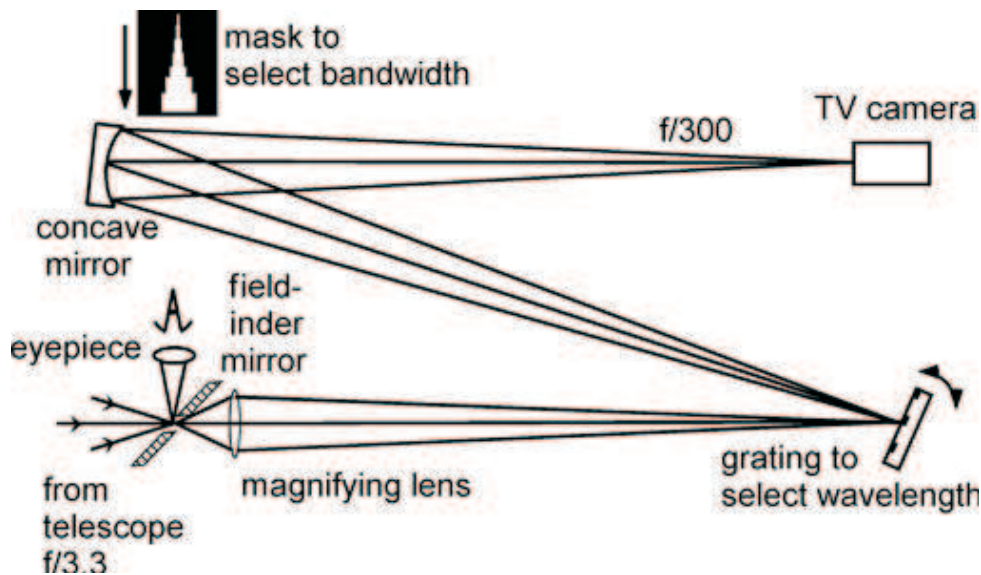


Figure 5.1: Optics originally used by Labeyrie, Stachnik and Gezari for speckle interferometry. Atmospheric dispersion was compensated by translating the TV camera axially, the entire instrument being rotary and oriented so that the grating dispersion was in the direction of the zenith. Analogue Fourier analysis of the recorded images used Fraunhofer diffraction. Image Credit: Haniff (2007).

The principle of speckle interferometry was introduced for first time by the French astronomer Antoine Labeyrie, in 1970, (Labeyrie 1970). The speckle interferometry (see Figure 5.1) is a technique aiming to increase the angular resolution of telescopes which is

impeded by the atmospheric turbulence. The term 'speckles' is based on the explanation when imaging the pictures from long exposures consist of a large number of instantaneous images, they together form the seeing disc. Labeyrie (1970) found that using Fourier analysis on the speckle patterns which are produced by the mutual interference of a set of wavefronts, the actual resolution of the telescope can nearly be reached. Several methods have been developed and they allow the interferometric reconstruction of hundred short exposure images from these speckle patterns.

### 5.1.1 Adaptive Optics

The idea of adaptive optics (AO) was proposed by H. W. Babcock in 1953 (Babcock 1953) to correct for the effects of the atmospheric turbulence. The idea behind the AO is the compensation of the wavefront distortions introduced by the turbulent atmosphere. The relative phases of the waves from the various parts of the aperture could interfere and improve the angular resolution (Babcock 1990). The resolution could be improved in principle to the diffraction limit,  $1.22\lambda/D$ ,  $D$  being the telescope diameter. The distortions in the images of astronomical objects due to the turbulence in the earth's atmosphere (Beckers 1993) can be measured by a Wavefront Sensor (WFS) coupled to a Guide Star (GS), for instance a point source reference. A Deformable Mirror (DM) can correct the incoming wavefront in real time (Roddier & Roddier 1993).

The aberrations of the science target differ from those of the guide star's due to the different path and the high altitude layers, resulting the commonly known effect of angular anisoplanatism. Therefore, the selection criteria for the guide star are to be close in distance to the astronomical source, and being bright enough to be detected by the WFS. In case that a Laser Guide Stars (LGS) (see Figure 5.2) is used there is no limitation in the sky coverage, since the GS should not be in same isoplanatic region as the reference star. Though, the laser beacon takes a different path through the atmosphere, since it is not at infinite conjugated.

The earliest adaptive optical systems used a lenslet array and a set of position sensitive detectors (a Hartmann-Shack sensor) to measure distortions of the incoming wavefront, and a deformable mirror driven by an array of actuators to which correction signals could be applied (Tyson 1991). The principle operation of AO systems



Figure 5.2: Gemini North Laser Guide Star from Canada. France Hawaii Telescope.  
Image credit: Gemini Observatory.

is illustrated in Figure 5.3.

The beam from a telescope is collimated and reflects off a deformable mirror that eliminates high frequency wavefront errors. A beam-splitter splits the beam into two parts; one is directed to the wavefront sensor and the other is going to produce an image. The former measures the residual error in the wavefront and provides information to the actuator control computer to compute the deformable mirror actuator voltages. This process should be at speeds commensurate with the rate of change of the corrugated wavefront phase errors.

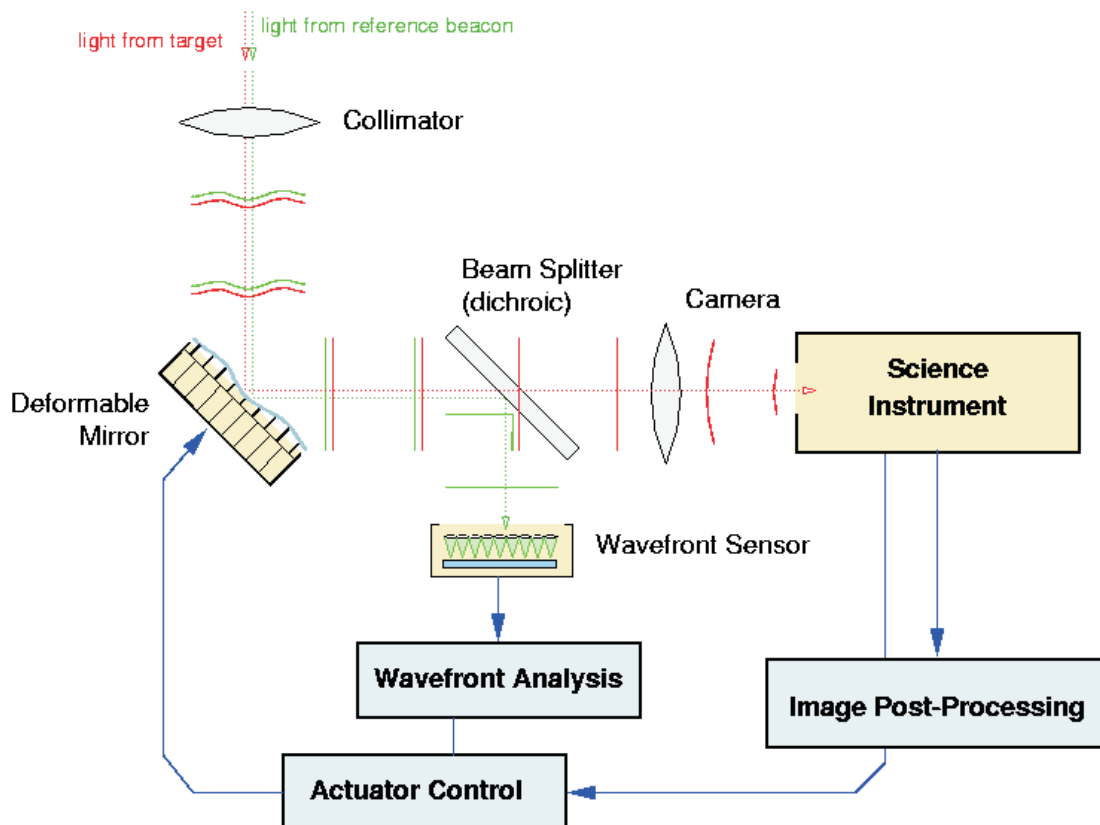


Figure 5.3: Scheme represents the principle of operation of Adaptive Optics system. The main required components for implementing an AO system are an image stabilization device that is a combination of deformable reflecting surfaces, a device that measures the distortions in the incoming wavefront of starlight, called wavefront sensor, wavefront phase error computation (Roggemann et al. 1997), and post-detection image restoration (Roddiier 1999). In addition, a laser guide star (beacon) may also be needed to improve the signal-to-noise (S/N) ratio for the wavefront signal since the natural guide stars are not always available within an iso-planatic patch. Image credit: CFAO.

AO system is currently used primarily at NIR wavelength domain, for instance a dichroic filter separates the visible light for the wavefront sensor from the NIR light that is used for scientific observations. AO system is also useful for spectroscopic observations, low light level imaging with very large telescopes, and ground-based long baseline optical interferometers.

### 5.1.2 Multi-Conjugate Adaptive Optics

Multi-Conjugate Adaptive Optics (MCAO) (see Figure 5.4) is a technique described for the first time by (Beckers & Merkle 1989) to overcome the isoplanatic patch limitations and obtain a more uniform correction over a wide field of view. In this technique, the atmospheric turbulence is measured at various elevations and in different directions, and it is corrected in three-dimensions with more than one DM (Tallon & Foy 1990; Ragazzoni et al. 1999). Each deformable mirror is conjugated optically to a certain layer above the telescope.

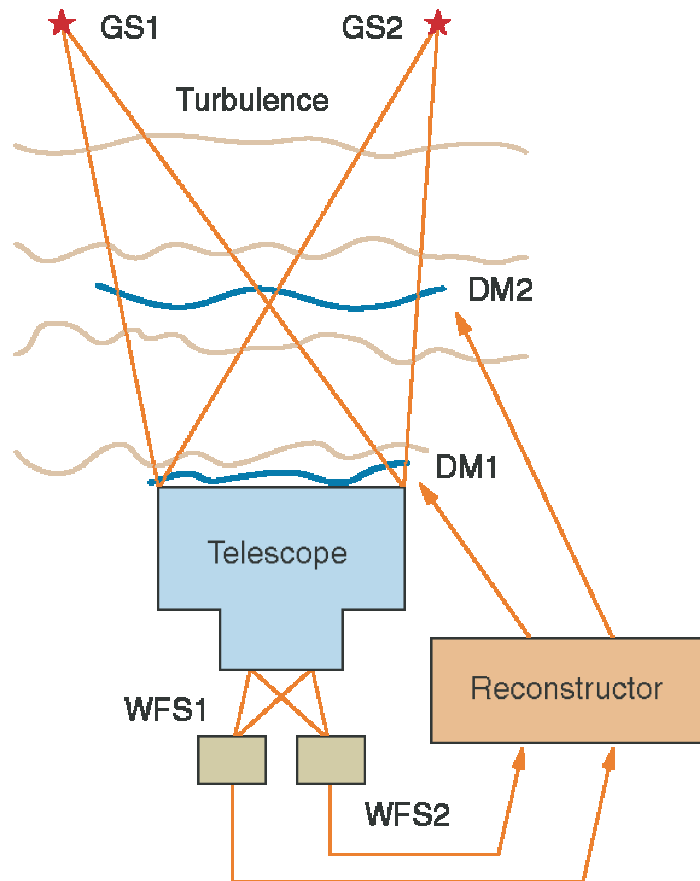


Figure 5.4: Scheme represents the principle of operation of Multi-Conjugate Adaptive Optics. The Multi-Conjugate Adaptive Optics system under development at European Southern Observatory uses multiple guide stars and multiple wavefront sensors to reconstruct atmospheric turbulence in three dimensions, referred to as turbulence tomography due to its theoretical similarity to medical tomography. Image credit: OptIQ.

The functioning of the system depends on the quality of the wavefront sensing of the individual atmospheric layers. The WFSs are not coupled to the GSs but are conjugated with specific layers in the atmosphere so called layer-oriented proposed by Ragazzoni (2000). The DMs are conjugated with the same layers as the WFSs and each of them applies a correction proportional to what the corresponding WFS measures, optically combining the light from the GSs. This optical combination ensures a very efficient use of the incoming photons and it has been speculated that a more uniform sky coverage is possible even with Natural Guide Stars (NGS). Each DM coupled to a WFS and produce

an independent loop, being possible to optimize the sampling of this loop according to the statistical properties of the corresponding conjugated layer. This technique will be useful for the extremely large telescopes such as the Extremely Large Telescopes (ELTs) (Diolaiti et al. 2010). However, the limitations are mainly related to the finite number of actuators in a DM, wavefront sensors, and guide stars.

## 5.2 The Large Binocular Telescope

The Large Binocular Telescope (LBT) (Hill et al. 2010) is one of the first ELTs and takes the first place in the table of optical telescope historically progression. The LBT is an optical/infrared telescope that utilizes two 8.4 meter diameter mirrors side-by-side on a common altitude-azimuth mounting, resulting in a combined collecting area of  $110m^2$  equivalent to a single 11.8 m telescope. The center-to-center distance of the two primary mirrors is 14.4 m providing an interferometric baseline of 22.8 m edge-to-edge with F/1.14 focal ratio (see Figure 5.5). The two individual 8.4 m telescopes can be pointed either to the same position on the sky or to neighboring fields up to a few arcminutes apart. An unequaled characteristic of the LBT is that the light from the two primary mirrors can be combined optically in the center of the telescope to produce phased-array imaging of an extended field. The operation of active and adaptive optics increases the telescope performance from visible to mid-infrared wavelengths. The main wavefront correctors are the two F/15 Gregorian adaptive secondary mirrors. The interferometric focus combining the light from the two 8.4 m primaries will re image the two folded Gregorian focal planes in a central location.

Several of the instruments will implement an additional wavefront corrector at a higher conjugate after the initial Gregorian focus. This cophased imaging gives the telescope the diffraction-limited resolution of a 22.65 m telescope in one spatial direction producing high resolution images of the order of 5 milliarcsec at visible wavelength (4000 - 7000 Å) and 20 milliarcsec in the near-infrared (7000 Å - 50000 Å).

The Large Binocular Telescope Observatory (LBTO) is located in southeastern Arizona near Safford in the Pinaleno Mountains on Mt. Graham, at an altitude of 3191 m. The LBT is an international collaboration of the University of Arizona, Italy (INAF: Istituto Nazionale di Astrofisica), Germany (LBTB: LBT Beteiligungsgesellschaft), the Ohio State University, and the Tucson-based Research Corporation.

### 5.2.1 The LBT Instruments

The unique design of the telescope gives the benefit of 12 focal stations, where instruments can be accommodated. The first generation instruments and their capabilities are presented in Table (5.1) which are foreseen for the LBT. At this time, some of them are already operational and some others under development.

The LBC (Speziali et al. 2008) is a pair of blue - red optimized prime focus imagers with a field of view of almost  $0.5^\circ$ . MODS (Pogge et al. 2010) is a pair of dual - beam, blue - red optimized, optical spectrographs incorporating long slit, custom multi slit, and direct imaging modes. LUCIFER (Mandel et al. 2008) is a pair of near-infrared (NIR) imagers and spectrographs that can be used in both seeing- and diffraction- limited modes by virtue of interchangeable cameras for direct imaging, long - slit spectroscopy, and customized multi-slit spectroscopy. In addition, both  $1 - 2.5\mu m$  (LINC-NIRVANA)



*Figure 5.5: The Large Binocular Telescope uses an elevation over an azimuth mounting. The two 8.4 meter diameter primary mirrors are mounted with a 14.4 m center-center separation. By using swing arms to rotate the secondary mirrors and their supports, it is possible to switch the telescope from one mode of observation to another very quickly. The short focal length of the primary mirrors ( $F/1.142$ ) permits a compact, and therefore quite stiff telescope structure. Its construction began at July 1996 and the first light was on October 2005. Updates about the telescope and its instruments can be found in the official webpage: [http://lbtwww.arcetri.astro.it/observatory\\_status.htm](http://lbtwww.arcetri.astro.it/observatory_status.htm)*

(Herbst et al. 2010) and  $3 - 25\mu m$  (LBTI) (Skrutskie et al. 2010) interferometers are under development and construction. PEPSI (Strassmeier et al. 2008) is a fiber-fed echelle spectrograph for ultra-high resolution optical spectroscopy and spectropolarimetry. The locations of these instruments on a rendering of the LBT at the various foci are shown in Figure 5.6.

The LBC is mounted at the prime focus on swingarm spiders just inside the location of the Gregorian secondary mirror. MODS is attached at the direct  $F/15$  Gregorian focus and is accessed by swinging the LBC out of the beam and inserting the secondary into the beam. LUCIFER, LBTI, and LINC - NIRVANA are mounted at the front, center, and back bent  $F/15$  focal stations respectively and are accessed by a rotating tertiary mirror. The PEPSI spectrograph is located in the base of the LBT pier in an environmentally controlled chamber. Optical fibers running from a fixed location behind LINC/NIRVANA for integral light spectroscopy and from polarimeters mounted in place of MODS at the direct  $F/15$  foci for spectropolarimetry are connected to the spectrograph. In addition, a separate solarfeed telescope directs integrated sunlight through an optical fiber to the PEPSI spectrograph for daily ultrahigh resolution solar spectroscopy investigations and the solarstellar connection.

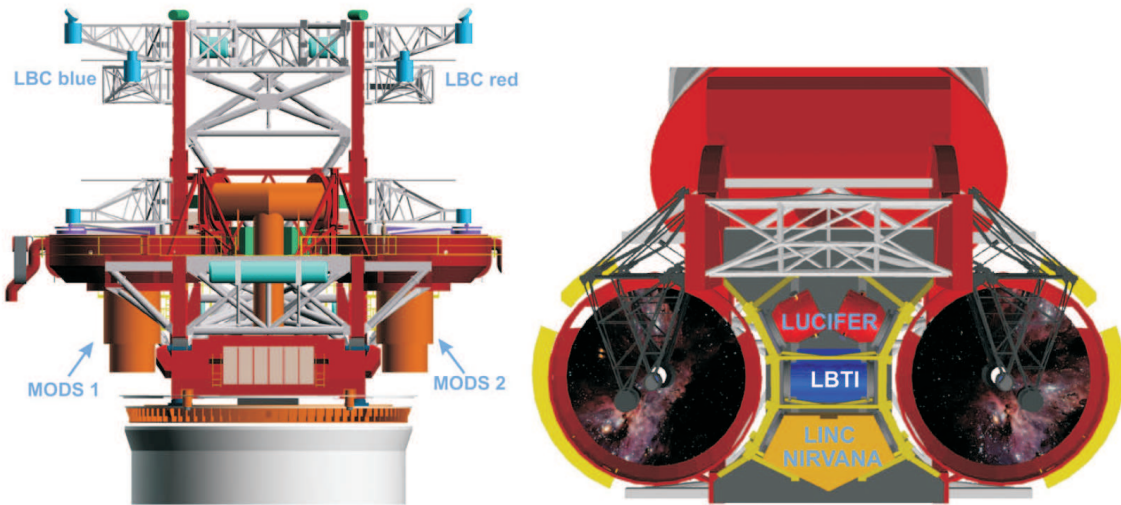


Figure 5.6: Overview of the instruments to be installed at the LBT. There are 6 single-eye cameras and two interferometric cameras. LBTI will provide imaging and nulling interferometry at longer wavelength. LINC-NIRVANA is a NIR homothetic imager with large FoV. The PEPSI spectrograph and polarimeter is not shown, as it is a fibre-fed instrument. Image taken from [Rost et al. \(2008\)](#)

Instrument	Focal Station	Modes	Spectral Coverage	Spectral Resolution $\mu\text{m}$	FoV	Pixel scale	status
LBC-Blue LBC-Red	prime	Direct CCD	U,B,V,g,r V,R,I,r,i,z	4- 50	$27' \times 27'$	0.28"	operational
LUCIFER	Front-Bent	Imager, Longslit, MOS AO	z, J, H, K, Ks J, H, K, Ks	2000-8500 30,000	$4' \times 4'$ $30'' \times 30''$	0.12" - 0.25" 0.015"	operational
MODS-Blue MODS-Red	Direct F/15	Imager, Longslit, MOS	0.32-0.65 0.55-1.1	100-1540 100 -1730	$6' \times 6'$	0.125"	operational
LBTI	Center-Bent	Nulling/Fizeau Interf Fizeau Interf	7-25 3-5	1-100 350	7" 10"	0.030 0.010	under development
LINC NIRVANA	Rear-Bent	Fizeau Interferometer	J, H, Ks	5-20	$10''$ - $20''$	0.006	under development
PEPSI	Rear-Bent Direct F/15	Spectroscopy Spectropolarimetry	0.39-1.1	40,000 to 300,000	$0.5''$ - $1.4''$	0.165	under development

Table 5.1: Main characteristics and status of the LBT Instruments

### 5.3 The LINC-NIRVANA Instrument

LINC-NIRVANA ([Herbst et al. 2004](#)) instrument is an adaptive optics aided near-infrared Fizeau imaging interferometer that will combine the beams from the two telescopes of the LBT ([Ashby et al. 2008](#)). It will be mounted at the bent rear focal station on the central platform of the Large Binocular Telescope (see Figure 5.6) and is the largest instrument to be deployed at the LBT consisting of an optical bench 6 m wide  $\times$  4.5 m deep by 4.5 m high. The instrument combines two ambiguous technologies in ground-based instrumentation in one instrument: cophased imaging and Multi Conjugate Adaptive Optics (MCAO) ([Ragazzoni 2000](#)). The difference between the two phases of implementation are the capabilities (and the complexity) of the adaptive optics systems. LINC incorporates a single on-axis wavefront sensor per telescope while NIRVANA provides full MCAO capabilities.

In its initial implementation phase the instrument will be operated in the so-called LINC-mode which provides interferometric near-infrared (NIR) imaging with a single on-axis natural guide star AO correction. With this implementation the telescope will produce interferometric images with the sensitivity of a 12 m telescope but with the



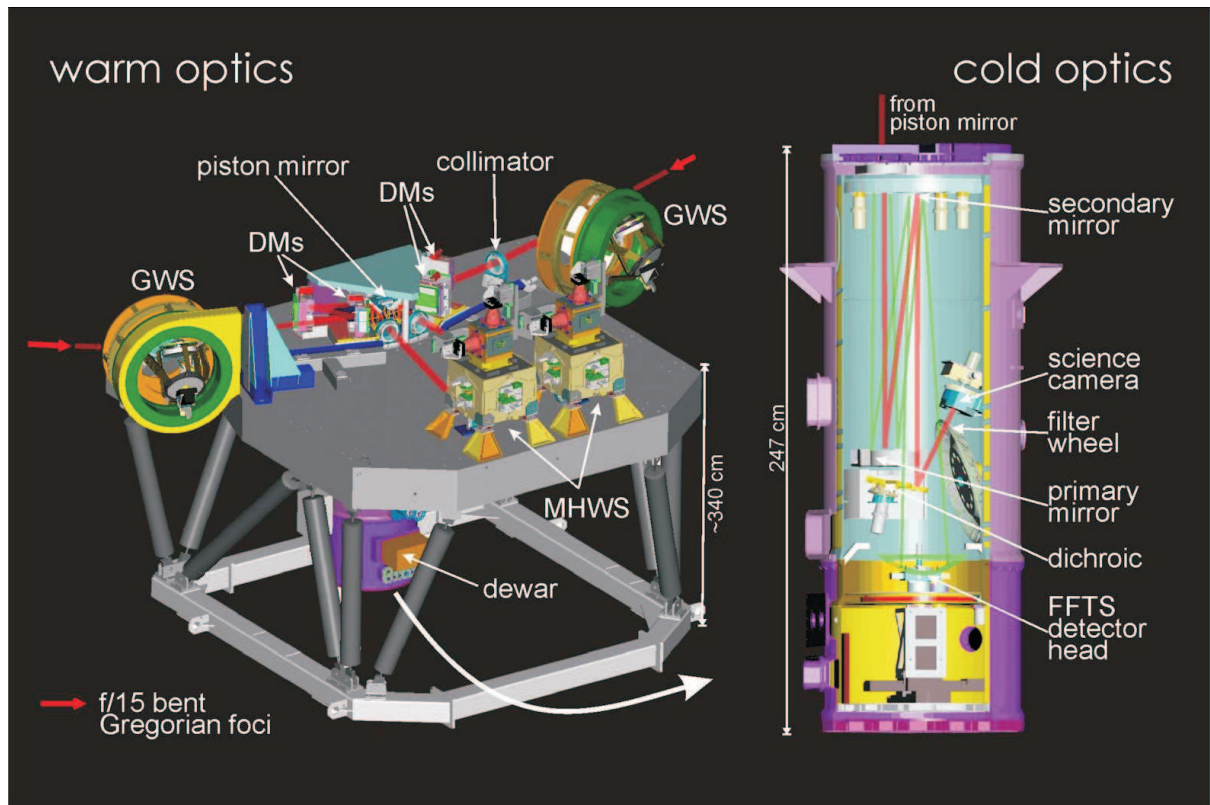


Figure 5.7: LINC-NIRVANA cold and warm optics. The left and right arm of the interferometer are symmetrical. The warm optics are mainly assigned to the single-eye adaptive optics systems. Stellar light sources in an annulus of 20- 60 around the optical axis of the telescopes are used by the ground-layer wavefront sensor (GWS). The light passing through in the center is collimated and reflected on DMs. A dichroic beamsplitter directs the visible light to the mid/high-layer wavefront sensor (MHWS) while the NIR light is reflected by the piston mirror to the Cassegrain beam combiner telescope in the cryostat. A dichroic wheel in the cryostat allows to chose the band that is reflected to the science detector. The remaining light is available to the Fringe and Flexure Tracking System (FFTS), taken from T. Bertram PhD thesis (Bertram et al. 2008).

spatial resolution of a 23 m telescope ( $\sim 9$  mas at J and  $\sim 20$  mas at K) over a science field of view of  $10''$ . Due to the finite isoplanatic patch size, this implies that the AO performance degrades with increasing separation between AO star and scientific target. Generally, this on-axis guide star will also be used as the reference star for the fringe and flexure tracking system (FFTS), and a similar performance degradation occurs with increasing separation from the guide star due to the related finite isoplanatic patch size. To be able to integrate on the science detector for longer than fractions of a second without losing fringe contrast (Bertram et al. 2005) and the respective gain in spatial resolution, fringe tracking is mandatory. The FFTS, therefore, is the adaptive optics system that is inherently necessary to operate LINC-NIRVANA as a cophased imaging camera. The NIRVANA-mode will finally provide a layer-oriented (two-layer) MCAO correction whose detailed performance will depend not only on the atmospheric conditions (as does classical AO), but strongly also on the detailed asterism of guide stars available, i.e. the number of stars, their spatial distribution, and their magnitudes. A maximum of eight stars will be accessible for the two mid-high-layer wavefront sensors (MHWS), and a maximum of 12 stars for the two ground-layer wavefront sensors (GWS). In both

cases these maximum numbers of stars can only be achieved when certain conditions on the geometrical distribution of the stars are met. The performance of LINC-NIRVANA suggests that reconstructed point sources as faint as  $\sim 26$  mag with a S/N ratio of 5 can be detected in one hour in the K-band.

### 5.3.1 Principle of operation

As it is illustrated in the drawing view of the instrument (see Figure 5.7), it consists of cold and warm optics. The warm optics are mainly assigned to single on-axis natural guide star AO systems. The stellar light which is collected by the two LBT mirrors directed by the annual mirrors near each telescope focal plane in order to reach the GWS. The GWS measures the wavefront using up to 12 natural guide stars and corrects this component using the LBT adaptive secondary mirrors. The light which enters the instrument is collimated and reflected on the Deformable Mirror (DM). The visible wavelengths go to the MHWS with the help of a dichroic beam splitter. The NIR light is reflected by the piston mirror in the cryostat, where a dichroic wheel allows to choose the band that is reflected to the science detector. The remaining light is available to the FFTS which is described in detail in the next paragraphs. For more information about the LINC NIRVANA and its current status see [Herbst et al. \(2004\)](#), and [Herbst et al. \(2010\)](#), respectively.

## 5.4 The Fringe and Flexure Tracking System

One of the major contributions of the I. Physikalisches Institut of the University of Cologne to this project is the development of the Fringe and Flexure Tracking System (FFTS) ([Straubmeier et al. 2004](#)). The FFTS is an integral part of the LINC NIRVANA instrument and it is located at the bottom of the cold optics part of the instrument (see Figure 5.8 and [Bertram et al. \(2006\)](#)).

The FFTS itself is comprised of three main components (see Figure 5.8) such as the detector head with detector fanout board and filter wheel ([Zuther et al. 2010](#)), the moving baffle, and the detector positioning unit (DPU). The support structure stands for the mechanical outer skeleton of FFTS and contains the moving baffle and the DPU. Some parts of the FFTS hardware placed in an ambient temperature environment and other parts have to be in within the cryogenic environment. The demarcation between the ambient temperature where the DPU is located and the cryogenic environment is defined by the moving baffle (see Figure 5.8). The role of the interlock protection part is to prevent the system of any possible mechanical damage of the system in case of asynchronous motion of both DPU and moving baffle. The DPU is discussed extensively in the next chapter since its tests are part of the current thesis.

In close cooperation with the Adaptive Optics systems of LINC-NIRVANA the FFTS is a fundamental component to ensure a complete and time-stable wavefront correction at the position of the science detector in order to allow for long integration times at interferometric angular resolutions. By fitting a parameterized theoretical model PSF to the preprocessed image-data the FFTS determines the amount of piston phase difference and the amount of an angular misalignment between the wavefronts of the two optical paths of LINC-NIRVANA ([Rost et al. 2010](#); [Horrobin et al. 2010](#)). For every exposure the correcting parameters are derived in real-time and transmitted to the control electronics

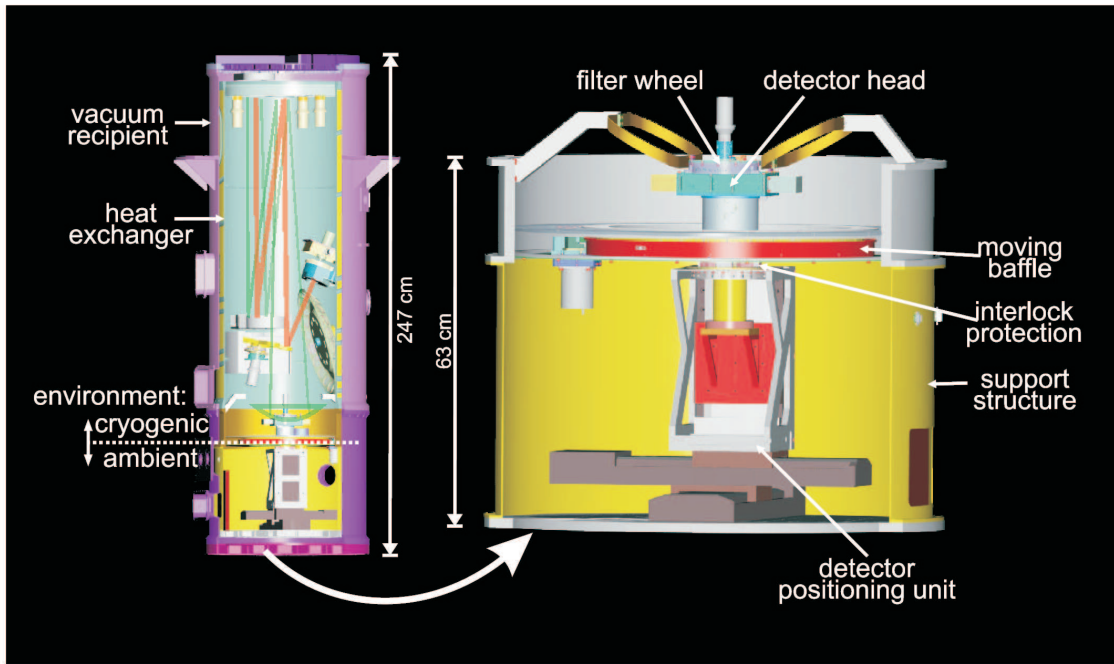


Figure 5.8: Main components of the FFTS hardware. With the exception of the piston mirror, FFTS computer and additional electronics, all hardware related to the FFTS is located in the bottom part of the LINC-NIRVANA vacuum recipient. Part of the hardware is located in an ambient temperature environment, other components have to be within the cryogenic environment of the beam combining camera. A moving baffle comprises the boundary between these two environments. Image credit: [Bertram et al. \(2006\)](#).

of the opto - mechanical elements in closed loop operation (several hundred Hz up to 1kHz). In other words, the FFTS uses a bright reference source which is in the FoV and analyzes the Point Spread Function (PSF) of the reference star. The PSF is sampled by the FFTS detector resulting in a time stable fringe pattern and a time varying residual piston<sup>1</sup> of less than  $\lambda/10$ .

In particular in order to compensate the measured differential piston, a piston mirror is moved according to the actuating variable and introduces controlled path-length variations. A filter wheel in front of the FFTS detector allows to select the NIR band that is used for fringe tracking and allows to switch between broadband filters with a small coherence length or narrowband filters with a longer coherence length.

In general, the fringe tracking can be employed with three different modes, but this depends on the interferometer and its purpose. The detection of the fringes requires the differential piston to be limited to the coherence length,  $\ell_c$ :

$$\ell_c = \frac{\bar{\lambda}^2}{\Delta\lambda}, \quad (5.4.1)$$

where,  $\bar{\lambda}$  is the mean wavelength and the  $\Delta\lambda$  the width of the observed band. The **Coherencing** mode of fringe tracking keeps the fringes by controlling the OPD within the

<sup>1</sup>In optics, piston is the mean value of a wavefront or phase profile across the pupil of an optical system. The piston coefficient is typically expressed in wavelengths of light at a particular wavelength. Its main use is in curve-fitting wavefronts with Cartesian polynomials or Zernike polynomials.

coherence length in order to ensure their detection, since the time for their measurement is comparable to the fringe motion scale. Unlike, the **Phase Tracking** concept 'freezes' the motion of the fringes over periods much longer than the timescale of the differential piston variation. In the **Cophasing** mode the differential piston is always controlled to remain at zero by continuously tracking the central fringe.

## 6. Laboratory Tests of FFTS-DPU

*In this chapter, I present the design and the realization of some fundamental FFTS laboratory tests, taking into account the system requirements (see Table 6.1). We have to sample the large Field of View and to follow the reference source during science observations to an accuracy of less than 2 microns. In particular, important tests such as tip - tilt test (the repeatability and the precision under the different inclinations) are presented. The system parameters such as internal flexure and precision are also discussed.*

### 6.1 The Detector Positioning Unit

The Detector Positioning Unit DPU ([Bertram et al. 2008](#)) occupies the largest part of the FFTS volume. This integral part of the FFTS consists of three vacuum qualified micro positioning stages (see Figure 6.1) from Physik Instrumente (PI) company. The most important features of the linear stages are presented in Table 6.2.

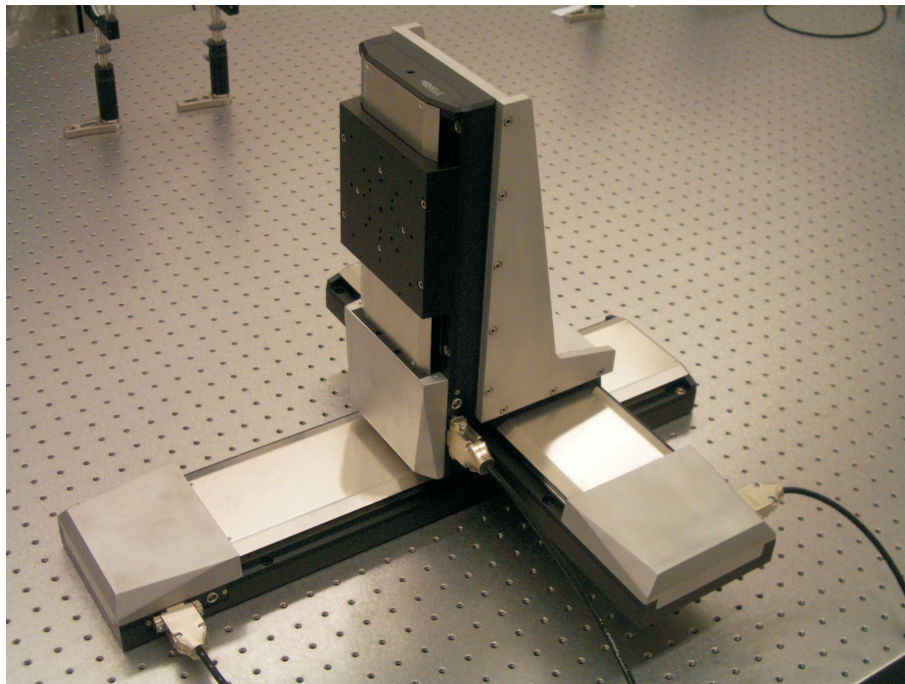


*Figure 6.1: The X, Y, Z linear stages represent a 3D coordinate system. The 3 micro positioning stages are manufactured by the Physik Instrumente (PI) company.*

FFTS field-of-view	60x90 arcec <sup>2</sup>
Sensitivity	$\leq 1$ pixel = 18.5 $\mu\text{m}$
Unambiguity (minimum Airy separation)	30mm
Frequency	$\sim 1\text{Hz}$
Positioning accuracy of the detector	$\sim 1$ subpixel
Maximum velocity for guide star tracking	2.6 mm/sec <sup>2</sup>
Position reproducibility	$\pm 4 \mu\text{m}$ for psf trajectory tracking
Maximum time for repositioning (reference target)	90 sec
Distance between target and reference star	up to 45 arcec = 150 mm
Operation in vacuum conditions	$10^{-6}$ mbar

Table 6.1: The high level requirements of the FFTS component.

Characteristics	X - stage Model: M-531K037	Y - stage Model: M-521K048	Z - stage Model: M-511K056
Maximum Velocity (mm/s)	3	1.5	1.5
Travel Range (mm)	306	204	102
Encoder (counts/rev)	2048	2048	2048
Design Resolution ( $\mu\text{m}/\text{counts}$ )	0.33	0.014	0.014
Translation Ratio (counts/ $\mu\text{m}$ )	30.3533	71.4285	71.4285
Repeatability ( $\mu\text{m}$ )	0.2	0.2	0.2

Table 6.2: The main characteristics of the 3 micro positioning stages.

The scope of the DPU is the movement of the detector head in the curved focal plane of the FFTS in order to follow the Point Spread Function (PSF) trajectory of the reference target during the science observations. That particular part of the instrument can be defined as a three dimensional (3D) coordinate system which is able to be moved within the volume of the support structure, sample the large FoV, and follow the curved focal plane. Inevitably, the selection criteria of the characteristics of the linear stages should correspond to the entire FFTS requirements (see Table 6.1). The accuracy that should be achieved should be less than the detector's pixel size (1 detector pixel  $\sim 18\mu\text{m}$ ) in order to get as result the desired quality of the fringe tracking. The DPU is located in the ambient temperature environment at the bottom of the dewar. A vertical fiberglass tube mounted to the Z-stage (Z coordinate of the 3D coordinate system) points through the moving hole in the baffle and carries the detector head (see Figure 5.8).

Due to the altitude - azimuth mounting of the LBT, it is obvious that the field rotates with the time. The parallactic angle is a function of the hour angle and for every hour angle describes the orientation of the field. In order to keep a constant orientation with respect to equatorial coordinate system (see Figure 6.2), we should calculate how the parallactic angle changes (see Figure 6.2). Within a few degrees of the zenith, the azimuth tracking rate is almost equal to the rate of change of the parallactic angle.

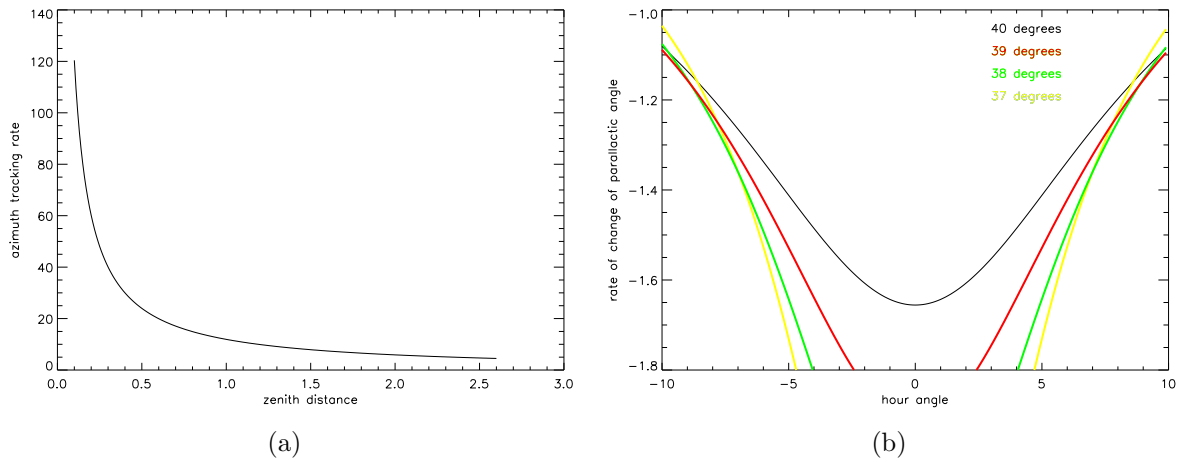


Figure 6.2: The origin of the field rotation in an altitude over azimuth mount is due to the fact that the coordinate system of the mount is not aligned to the earth's axis of rotation. (a) Azimuth tracking range versus zenith distance and (b) The rate of change of the parallactic angle. Within a few degrees of the zenith, the azimuth tracking rate is almost equal to the rate of change of the parallactic angle.

### Symbols:

$$\alpha = 90 - z = \text{altitude}$$

$$A = \text{azimuth}$$

$$h = \text{hour angle}$$

$$\phi = 32^{\circ}42' = \text{LBT latitude}$$

$$\delta = \text{declination}$$

$$p = \text{parallactic angle}$$

$$z = \text{zenith distance}$$

$$S = \text{source}$$

$$\dot{h} = 0.25^{\circ}/\text{min} = \text{sidereal rate}$$

### Equations from spherical trigonometry:

$$\sin z * \sin A = \cos \delta * \sin h \quad (6.1.1)$$

$$\sin \delta = \cos z * \sin \phi + \sin z * \cos \phi * \cos A \quad (6.1.2)$$

$$\cos z = \sin \delta * \sin \phi + \cos \phi * \cos \delta * \cos h \quad (6.1.3)$$

$$\tan p = \sin h \div (\tan \phi * \cos \delta - \sin \delta * \cos h) \quad (6.1.4)$$

For a celestial source S,  $\delta$ ,  $\phi$  are constants, and  $h$  increases at the sidereal rate of  $0.25^\circ/\text{minute}$ . The rate of change the parallactic angle and the rate of change the azimuth are given by:

$$dp/dh = 0.25(x * \cos h - \sin^2 h * \sin \delta)/(x^2 + \sin^2 h) \quad (6.1.5)$$

in degrees/min and where

$$x = \cos \delta * \tan \phi - \sin \delta * \cos h \quad (6.1.6)$$

$$dA/dh = 0.25(\cot z * \cos A * \cos \phi - \sin \phi) \quad (6.1.7)$$

in degrees/min.

When an altitude azimuth mounted telescope is tracking, there is a zone of avoidance near the zenith set by the maximum azimuth tracking rate. In order to find this zone of avoidance for a given azimuth tracking speed ( $dA / dH$ ), we can set  $A = 0$  in equation 6.1.7 and solving for  $z$  we have:

$$z = \tan^{-1}[\cos \phi / (4(dA/dh) + \sin \phi)] \quad (6.1.8)$$

$dA/dh$  in degrees/min. Hence, the obvious limitations have to be taken into account for the control algorithm and to be corrected from the software.

## 6.2 Laboratory Tests of FFTS

Obtaining an overview of the entire FFTS part of the LINC NIRVANA instrument, we reach the most suitable moment that we are able to present and discuss some of the laboratory tests of the system. The tests handle not only the characterization of the linear stages, which is of great importance but also the check of the working order of the whole system under the proper conditions. The DPU has to be moved in the curved focal plane in order to sample the large FoV ( $60 \times 90 \text{ arcsec}^2$ ) of the FFTS and to follow the reference source during science observations to an accuracy of less than 2 microns (see Table 6.1). In particular, important tests (Tremou et al. 2010) such as the tip - tilt test (the repeatability and the precision under the different elevations) are presented. The system parameters such as internal flexure and precision are discussed.

### 6.2.1 Temperature and heat transfer tests of the linear stages

The investigation of every individual linear stage's behaviour comprises the initial step before proceeding to any other experiment. The purpose of this test was to measure the temperatures across the stage while the motor stage is moving. In order to check how the temperature changes and whether the heat transfer is significant or not, we set up eight thermal sensors in some critical positions on the motor stages and the linear stage was moving continuous for long time (24 h in the beginning and 30 min with the maximum velocity). Since the DPU is placed in the part of the cold optics of the instrument, the



experiment took place in vacuum, in order to achieve the realistic conditions. The pressure inside the dewar was  $1 \cdot 10^{-3}$  mbars. As it presented in Figure 6.3, the finest approaching was to get to covered most of the part of the surface of the linear stages. Moreover, having as scope to examine the case of any heat transfer between the motors each other, two heat sensors was placed on the top of the motor (sensors number 6 and 7).

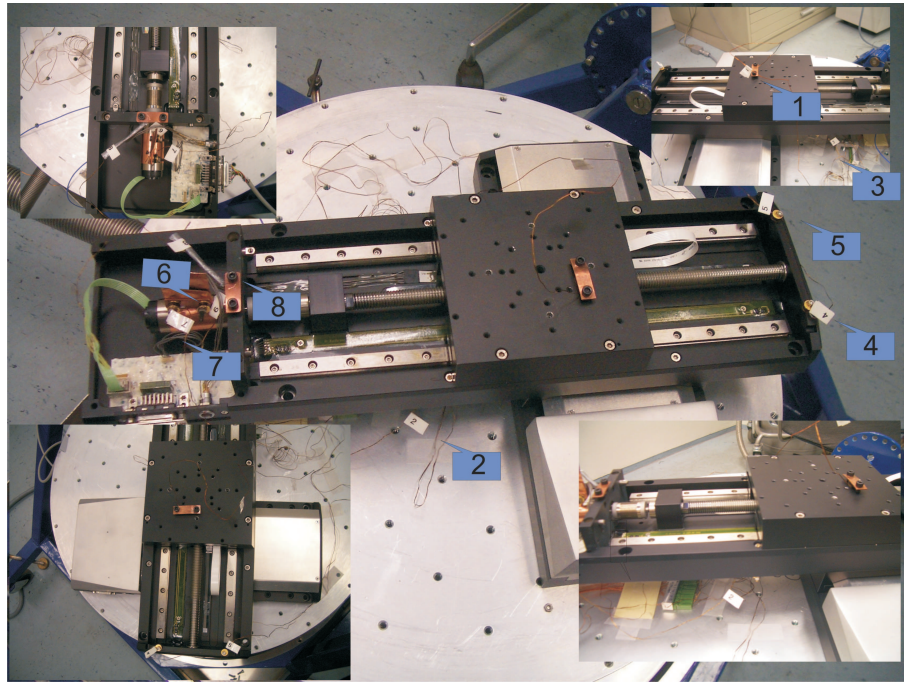


*Figure 6.3: The set up of the temperature test. 8 thermal sensors were set in the most critical positions of the linear stages. Sensors number 6 and 7 were particularly placed on the top of the motors for testing any possible heat transfer between them.*

It is worthwhile to mention that the maximum velocity requirement of every stage plays a major role in this part of the test. The first measurements were taken with the maximum velocity of the stage, which is used during the period that the stages follow the PSF trajectory of the reference source during the science observations. As already been discussed the closest distance to the zenith, requires the highest the tracking velocity. Furthermore, the velocity that corresponds to the repositioning (i.e: when the initial reference source is not anymore in the FoV, the reference target changes) differs from the tracking velocity. Afterwards, the extreme case of the maximum velocity that the linear stage is able to achieve was tested as well. Every 120 sec for a period of 24 hours temperature measurements were taken place. A pause of the whole movement was unavoidable to verify the exact time that is needed for the temperature of the linear stages to be dropped in the normal level. That happened after three hours. Then, the motor velocity was increased by a factor of four and the movement continued for 30 minutes.

The results are presented in Figure 6.4 and this demonstrates that the requirements are matched. During the first part of the test, while the motor was moving continuously for one day, there are no significant changes in the temperatures. Only in the two thermal sensors, number 6 and number 7, the temperatures were increased almost 3 degrees. The temperature in the other parts of the linear stages remain almost constant. The second part of the test allows a similar behaviour. Despite the fact, that we have tested the

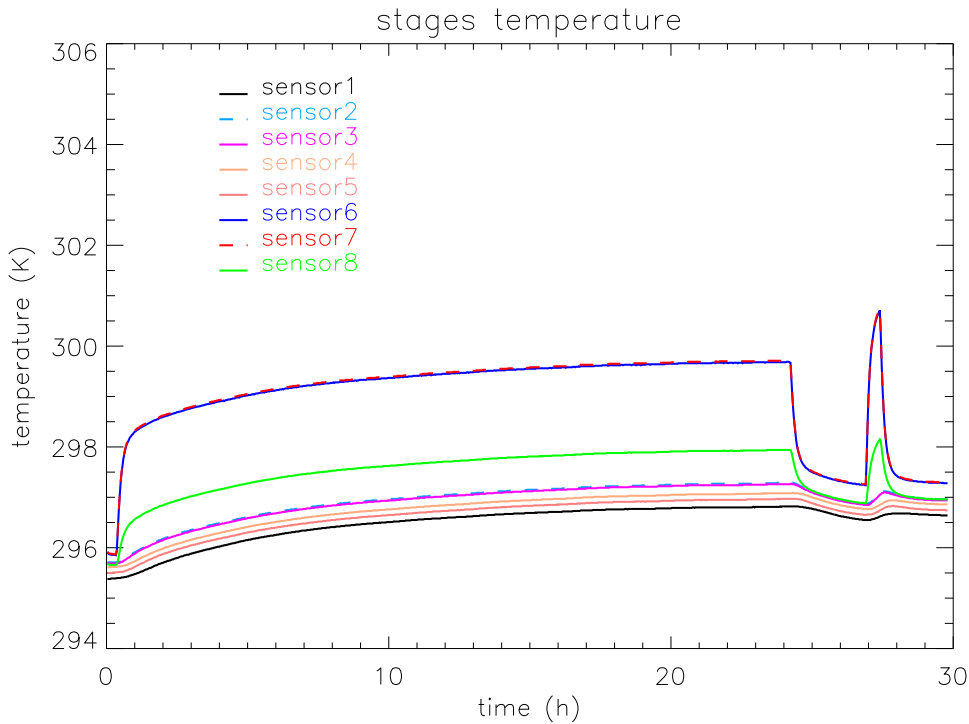


*Figure 6.4: The Results of the temperature measurements are plotted versus time. The stages were moving continuously with the intermediate velocity that they can achieve (see Table 6.2) for 24 h and no significant increase in their temperature was observed. Afterwards, there is a pause to cool them down to their initial temperature. After 2 h approximately, the desired temperature was achieved and the movement started again with the maximum velocity (see Table 6.2).*

extreme cases the system behaves politely in terms of temperature.

### 6.2.2 Tip-Tilt test

The main purpose of tip-tilt test is the measurement of repeatability and precision of the DPU at different degrees of elevation. The detector Position Unit consists of three linear PI (Physik Instrumente) stages, corresponding to three degrees of freedom. The FFTS should work under tilt angles following the movement of the telescope which is supported by an altitude-azimuth mounting. Hence, it is of high importance to test whether the high positional repeatability of the DPU is feasible under different degrees of elevations and generate the working order of the system under these conditions. Initially the design and then the building of the test set up (Figure 6.5) was mandatory, in order to achieve the aim of the laboratory test.

The setup is designed to hold the entire FFTS support structure and can be tilted up to 90 degrees in steps of 5 degrees of elevation. The support structure is the mechanical outer skeleton of the FFTS and consists of glass-fibre reinforced plastic (GRP). In the upper part, it supports the moving baffle, hence it forms the boundary between the cryogenic environment and the ambient temperature environment of the LINC NIRVANA dewar. Its

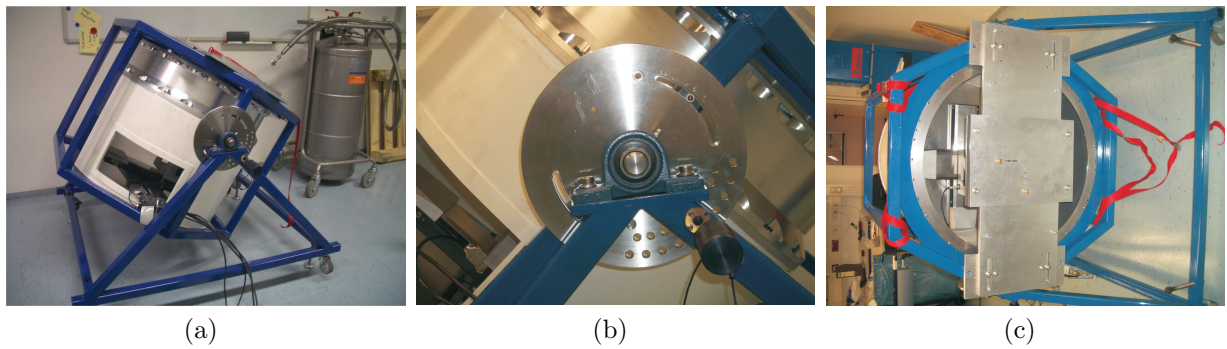


Figure 6.5: The Tip - Tilt test set up. (a) The building of a skeleton (blue skeleton) was needed which is able to accommodate the GPR support structure (white component) of the FFTS. (b) The blue skeleton supports an elevation control for giving access to an altitude - azimuth movement under different elevations ( $0^\circ$  to  $90^\circ$ ). (c) A goniometer (silver metal part) was assembling as a key tool for the high accurate calibration of the Heidenhain equipment. It is located on top of the GPR structure and supported by the blue skeleton. The grid Heidenhain plate is placed below it (see also Figure 6.6a).

design has to include thermal insulation between these two environments. Additionally, it includes the mounting and thermal interface to the LINC NIRVANA heat exchanger. The support structure consists of an aluminium ring at the top, cold part, fibre glass ring in the warm, bottom part and a base plate. The break test of the support structure was the most critical one and was carried out without any problem. More than the expected force was applied in order to figure out whether the structure can tolerate this weight.

The procedure of measuring the precision of the DPU is not straight forward. First of all, we should make clear that the use of an almost perfect device, which is able to measure position with high precision, is required. The instrument that was used comes from the Heidenhain manufacturer and the model is the KGM182 encoder (see Table 6.3) and the IKK220 counter card (see Figure 6.6).

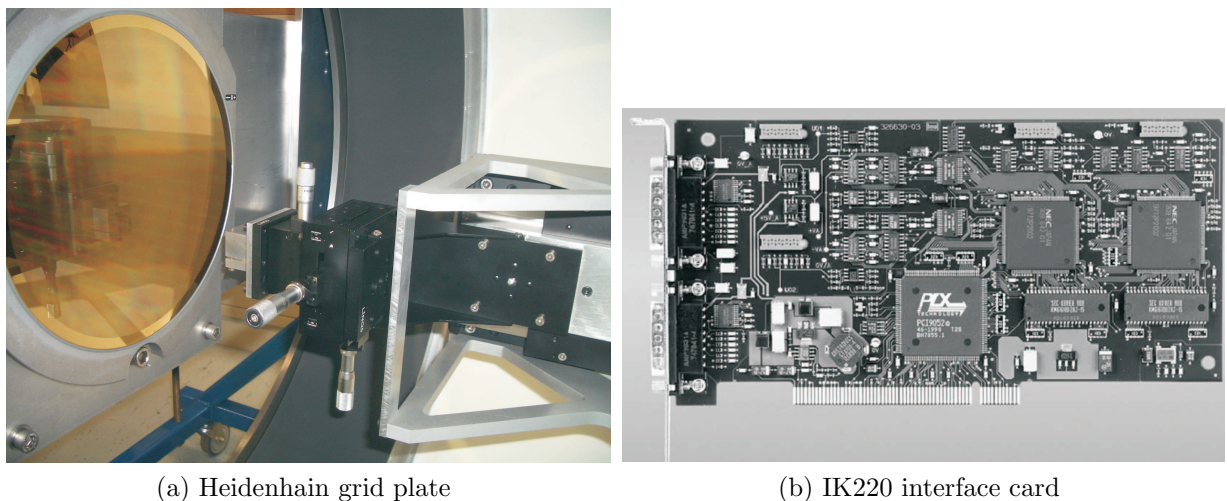


Figure 6.6: The KGM 182 Heidenhain equipment consists of 3 components. (a) The detector head is mounted on top of the 3D coordinate system of the stages and scans the interferential plate (yellow grid plate) while the stages are moved. (b) Its interface IKK220 card is required for the communication with the FFTS computer system.

Measuring Standard	2 Coordinate TITANID phase grating
Accuracy Grade	2 $\mu\text{m}$
Measuring Range	230 mm
Incremental Signals	$\sim 1 V_{pp}$
Signal Period	4 $\mu\text{m}$
Measuring Step	$\geq 0.001 \mu\text{m}$ with IK220

Table 6.3: The main characteristics of KGM 182 Heidenhain grid plate.

The KGM182 encoder consists of two parts. The detector head and the interferential plate (grid plate). The interferential scanning principle exploits the diffraction and interference of light on a fine graduation to produce signals used to measure displacement. A step grating is used as the measuring standard: reflective lines  $0.2 \mu\text{m}$  high are applied to a flat, reflective surface. In front of that is the scanning reticle, a transparent phase grating with the same grating period as the scale. The scanning head of the KGM182 encoder has been mounted on the top of the Z stage without having any contact between each other in order to be able to detect, measure and record every single movement of the linear stages of the DPU (see Figure 6.6).

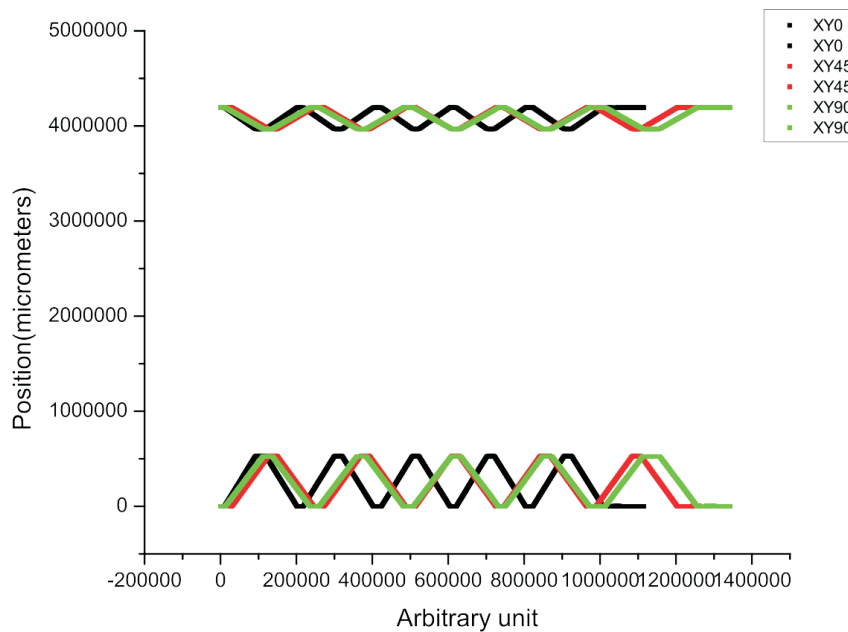
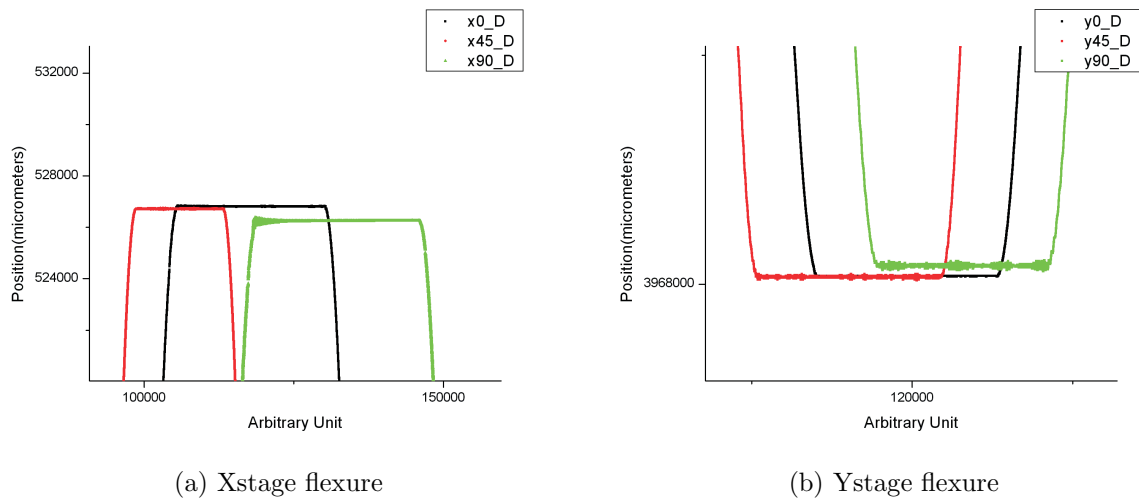


Figure 6.7: The forth and back movement of X and Y stages with constant velocity under 0, 45 and 90 degrees of elevation. The X - axis is proportional to time steps, while the Y - axis represents the position shift in  $\mu\text{m}$ . The linear stages were moving for a certain distance forth and back several times (5). The start point is compared with the end point in order to test the repeatability of the system.

Taking measurements of the position for every stage (X,Y individually) while they move with constant velocity (2400 rev/min) comprises the first step of the tip-tilt test. The resolution was 2048 counts /rev. As starting point the degree of elevation was set at zero degrees and in the continue the movement was tested in all different possible elevations (elevation step = 5 degrees).

The linear stages were moving for several times, forth and back (see Figure 6.7) for 999999 steps ( $30.35 \text{ counts}/\mu\text{m}$ ) having as reference position the home position that it



*Figure 6.8: The flexure of X and Y stage. The position in  $\mu\text{m}$  of the (a) X linear stage and (b) the Y linear stage are plotted versus an arbitrary unit for different elevations ( $0^\circ$ ,  $45^\circ$ ,  $90^\circ$ ). The horizontal lines in the plots represent the end points of the movement and thus their difference correspond to the flexure of the system.*

was defined in the beginning. In the mean time, the coordinates of the relative position (values in counts) are detected and recorded from the Heidenhain detector head. Some of the results of this effort to examine the behaviour of the system are discussed in subsection 6.2.4 that follows.

### 6.2.3 Software

TwiceAsNice (Gaessler et al. 2004) is a new and flexible framework, which was developed at the Max Planck Institute for Astronomy in Heidelberg/Germany within the scope of the LBT interferometer LINC-NIRVANA control software, but may also be used, in respect of its flexibility, for other astronomical instruments. The systems architecture was designed to decrease the development time of large service-oriented architecture (SOA) based systems like astronomical instrument control software. The advantages of this new framework are the combination of online instrument data handling, validation and the ability to integrate user defined data manipulation, which can be executed during instrument operation. This way the developer/astronomer may include just-in-time data pipelining functionalities into the system. More detailed information about the common software for the LINC-NIRVANA instrument can be found in the its webpage, <https://svn.mpia.de/trac/gulli/TwiceAsNice>.

### Dr. Greenthumb

In particular, the graphical interface Dr. Greenthumb (see Figure 6.9) which belongs to TwiceAsNice was used for testing the precision and the repeatability of the linear stages and the flexure of the system as well. Dr. Greenthumb is a tool, that can manage and control remotely multiple servers, which provide several services. The application can not only manipulate and supervise the status of those services, but can also be setup to provide complex gui application encapsulated within Dr. Greenthumb. The configuration

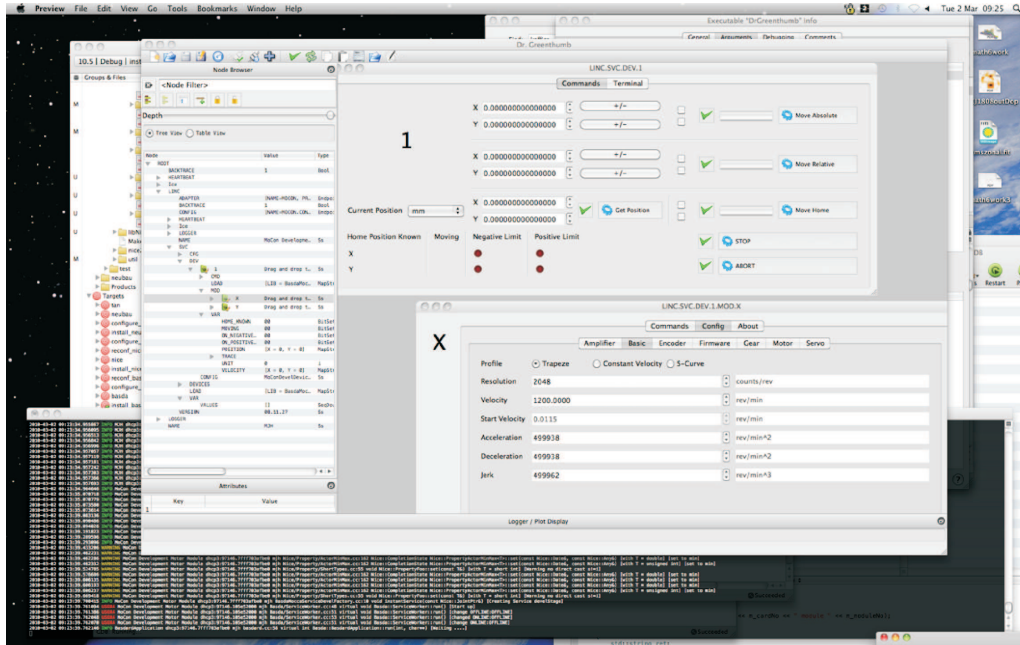


Figure 6.9: Screen shot of Dr. Greenthumb graphical interface. Dr. Greenthumb is a routine of the common LINC - NIRVANA software called 'TwiceAsNice', for controlling the stages' movement. Parameters such as velocity, acceleration, resolution etc of the linear stages can be set by the graphical interface. The routine provides also the possibility for scripting and hence the definition of certain trajectory that the stages can follow.

data of each config service is arranged in a so called hierarchical tree structure. To each node or leaf of the tree, data can be attached. The data type can be one out off a variety of data types provided by the TwiceAsNice framework. Each data type provides a defined gui element with which the data can be visually represented.

#### 6.2.4 DPU Repeatability and Flexure

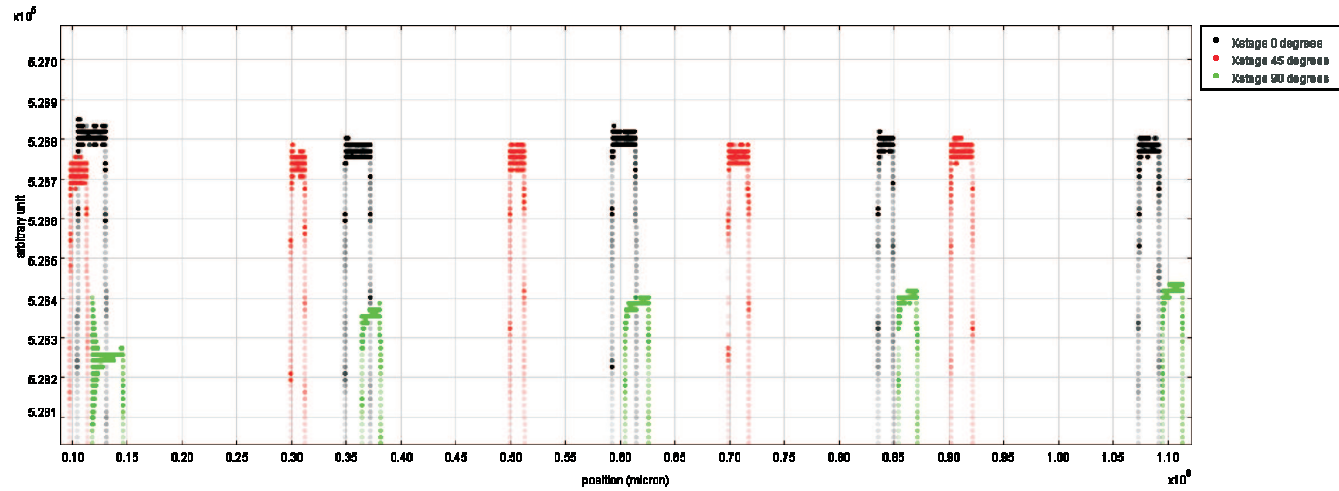
The data analysis on the measurements obtained from the tip-tilt test, holds critical information about the repeatability and the flexure of the entire FFTS due to the change of the elevation. The scope is to make well known and defined the expected flexure in order to be fully controlled and corrected by the FFTS software.

The values that recorded by the Heidenhain scanning head were converted in micrometers and plotted versus the time. An example that illustrates clearly the flexure of the system under different degrees of elevation is shown in Figure 6.8. For the accomplishment of the initial aim of the test a big amount of measurements are needed since the flexure phenomenon can be better described by statistical methods. Hence, more measurements should be done in the near future adding also the other parts of the FFTS such as the pin (interlock protection). Certainly, another parameter that we should to consider for the flexure estimations is the weight of the FFTS detector which is not included in this particular flexure test.

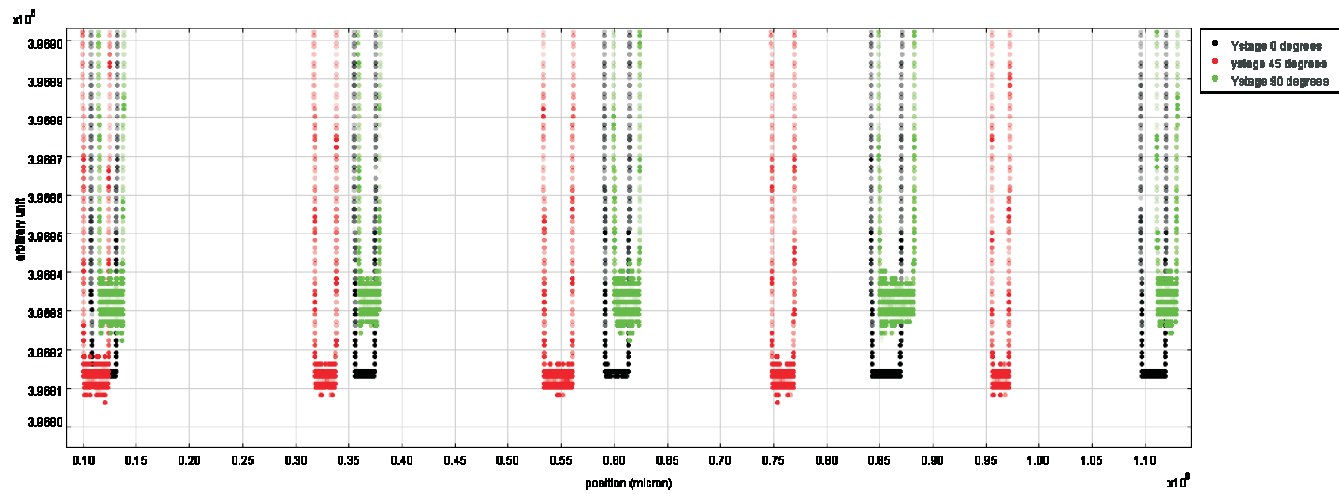
The repeatability of every linear stage can be checked while plotting the different times that every individual linear stage did the forth and back movement and comparing them with the reference-home position (see Figure 6.10). The Y linear stage seems to be more accurate than the X linear stage. The Y stage (see Figure 6.10b) comes back almost at

---

the same position in all the times in which the procedure was repeated. Although, the points of the positions of the X stage (see Figure 6.10a) appear to be in different places.



(a)



(b)

Figure 6.10: The repeatability of the X and Y stage. The position of (a) the X stage and (b) the Y stage in  $\mu\text{m}$  under different elevations ( $0^\circ$ ,  $45^\circ$ ,  $90^\circ$ ) is illustrated. Focusing on the end positions of each linear stage and comparing them each time of the movement, an estimation about the repeatability can be achieved. The Y stage seems to be more accurate in comparison to the X linear stage, since the end positions of the latter are different in some  $\mu\text{m}$ .



The explanation of this issue can be found on the different direction that every linear stage is mounted within the supported structure. The gravitational force that is applied on the X stage is higher than the Y linear stage due to the fact that the latter is located parallel to the orientation of the tilting. Hence the motors of the X stage are overloaded during the tilting procedure, therefore the algorithm of the FFTS software should apply a specific correction on each linear stage.

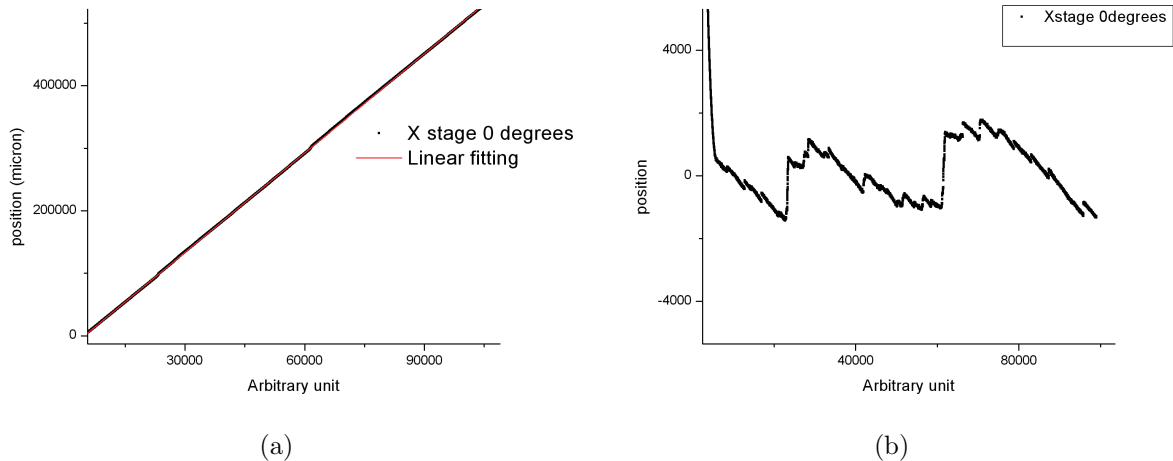


Figure 6.11: The precision of X linear stage movement. (a) A theoretical fitting is applied in the trajectory of the X stage. (b) The difference between the theoretical values and the ones that were measured illustrates the error coming from the motor of the linear stage.

Furthermore, this issue affects also the ability of the linear stages to follow the trajectory precisely. For a simple trajectory of the linear stage from a position with known coordinates traveling to another known coordinates position, a theoretical linear fitting was applied (see Figure 6.11). The theoretical values, assuming constant velocity, were subtracted from the measured ones and the error (see Figure 6.11) was not random. The error seems to have a certain behaviour. This error is related to the motor itself of the linear stage which has to be taken into account for the future implementations. Figures 6.12 and 6.13 show the distribution of the motor error for the X and Y micro positioning stages for different elevations ( $0^\circ$ ,  $45^\circ$ ,  $90^\circ$ ), respectively. If we assume that there is not an error of the motor, the histograms would show a Gaussian (normal) distribution, where the random variables tend to cluster around a single mean value (zero). This assumption tends to be confirmed only in the  $90^\circ$  elevation (see Figures 6.12c and 6.13c) for both linear stages which can probably be excused due to the gravity.

Further tests on the DPU, using a mass dummy or the real setup, have already been planned for the near future in order to quantify the positional errors and the flexure. The collection of the data will drive to the creation of look - up tables for both flexure and positional errors in all possible elevations, which will be used, later, during the operation of the instrument. The look - up tables will provide corrections in order to allow the detector move to the desired position within the focal plane, therefore the system coordinates require to be translated into sky coordinates. A software algorithm is developed to control and correct these impacts of flexure and errors.

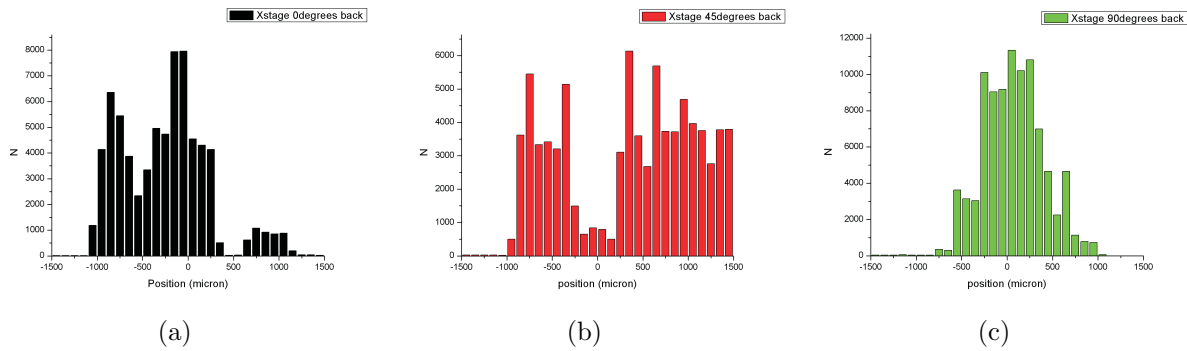


Figure 6.12: The motor error distribution of the X micro positioning stage under different elevations, (a)  $0^\circ$ , (b)  $45^\circ$ , and (c)  $90^\circ$ . Under  $90^\circ$  elevation, the error of the motor show a Gaussian distribution, unlike to  $0^\circ$  and  $45^\circ$  of elevation.

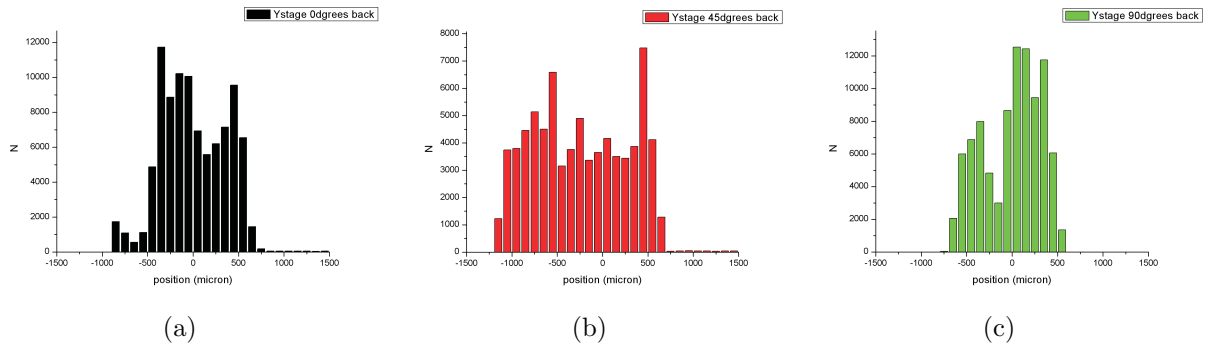


Figure 6.13: The motor error distribution of the Y micro positioning stage under different elevations, (a)  $0^\circ$ , (b)  $45^\circ$ , and (c)  $90^\circ$ . Under  $90^\circ$  elevation, the error of the motor show a Gaussian distribution, unlike to  $0^\circ$  and  $45^\circ$  of elevation.

## 6.3 Concluding Remarks

In this chapter, I have described and discussed the most fundamental tests, in order to fully characterize the DPU part of the FFTS. In particular, the components (three vacuum qualified micro positioning stages) of the DPU were tested. The design and the accomplishment of heat transfer and tilting tests were presented in detail. First measurements about the flexure, the precision, and the repeatability of the DPU system were introduced, while a comprehensive discussion about the high importance of the corrections, that should be applied in these parameters comprises the major topic of the current chapter.

### 6.3.1 Outlook through High Angular Resolution Interferometry

The high spatial resolution of LINC-NIRVANA will allow us to tackle several crucial questions, which follow after an extensive study of AGNs. The power of interferometric instruments in the field of AGN will allow to resolve its structure, test the unified model and handle a lot of key questions such as :

- What is the geometry of the dust and gas distribution?

- How is the mass transported through the torus towards the AGN?
- What is the chemical composition of the torus?

With LINC-NIRVANA and its high spatial resolution, we will achieve 10 pc angular diameter distance, which corresponds to the torus of an AGN.



# A. Appendix

## A.1 The optical spectra of 6dFGS

The optical spectrum (4000 Å - 7000Å) of 58 sources of LLQSOs sample is presented. Also, the fitting of the  $H\beta$   $\lambda$  4861Å and  $[O\text{III}]$   $\lambda$  5006.843Å,  $H\alpha$   $\lambda$  6562Å and  $[N\text{II}]$   $\lambda$  6583.41Å lines of each source is attached. The blue line represents the broad components, while the green one indicates the narrow components.

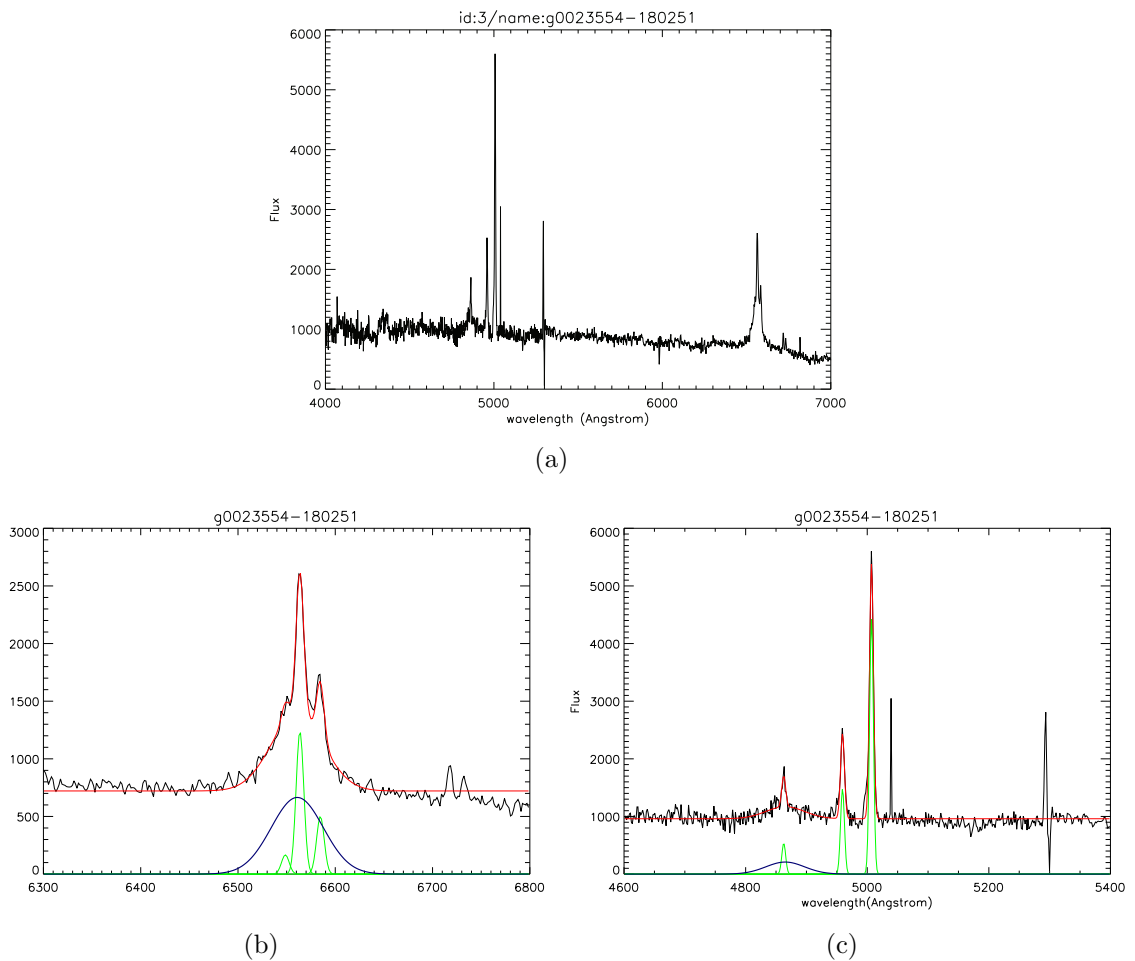


Figure A.1: (a) The optical spectrum of g0023554-180251 source observed by 6dFGS and (b) Fitting of lines  $H\alpha$   $\lambda$  6562Å and  $[N\text{II}]$ , (c)  $H\beta$   $\lambda$  4861Å and  $[O\text{III}]$ .

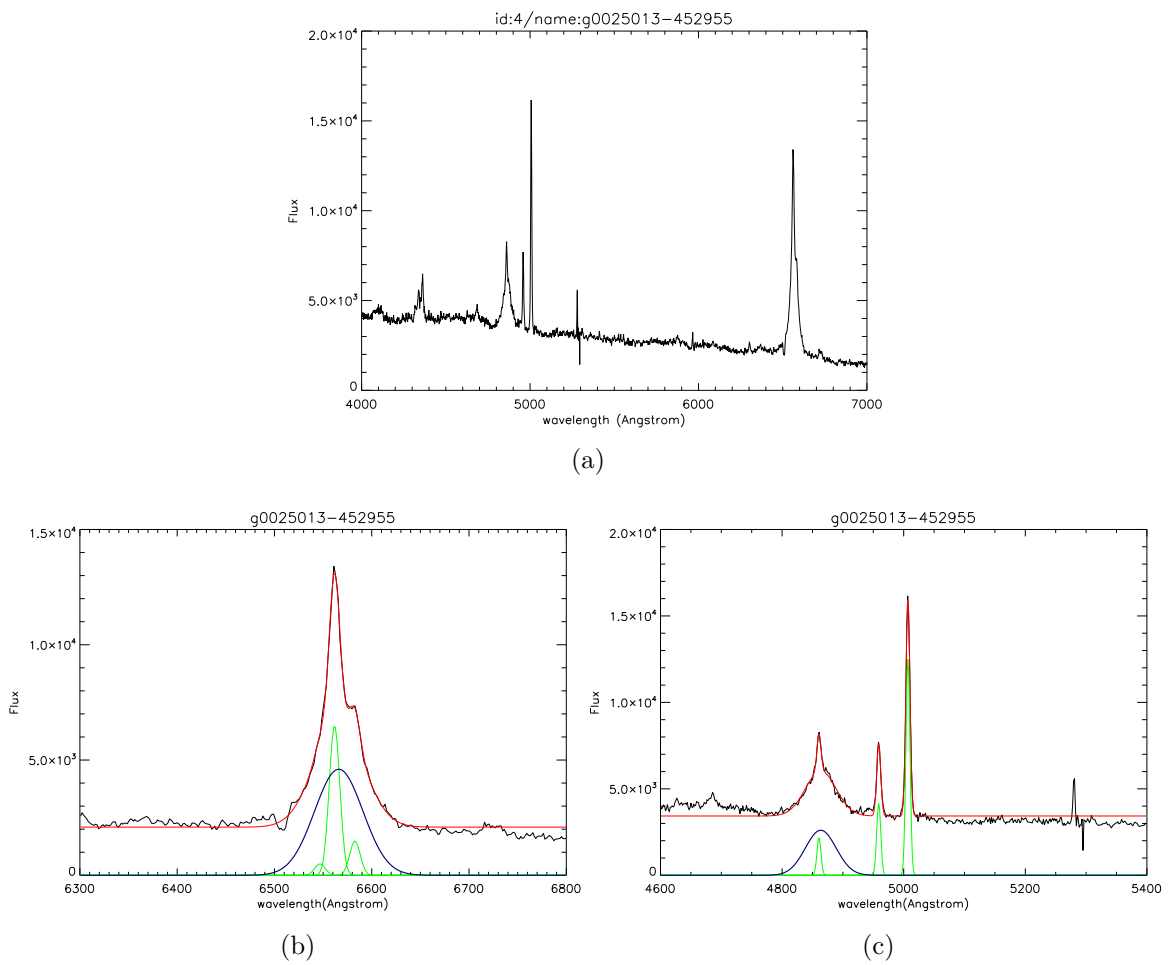


Figure A.2: (a) The optical spectrum of g0025013-452955 source observed by 6dFGS and (b) Fitting of lines H $\alpha$   $\lambda$  6562 $\text{\AA}$  and [N II], (c) H $\beta$   $\lambda$  4861 $\text{\AA}$  and [O III].

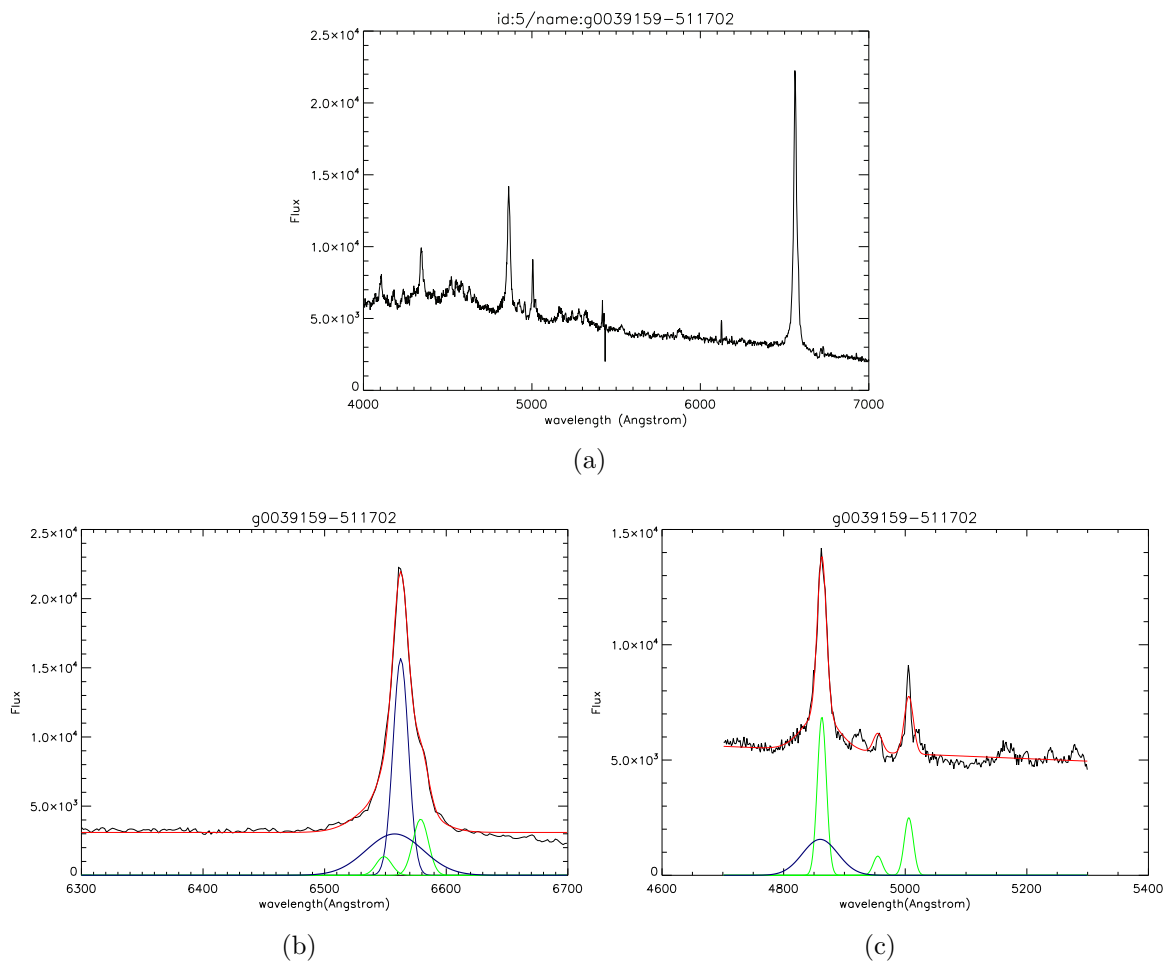


Figure A.3: (a) The optical spectrum of g0039159-511702 source observed by 6dFGS and (b) Fitting of lines H $\alpha$   $\lambda$  6562 $\text{\AA}$  and [N II], (c) H $\beta$   $\lambda$  4861 $\text{\AA}$  and [O III].

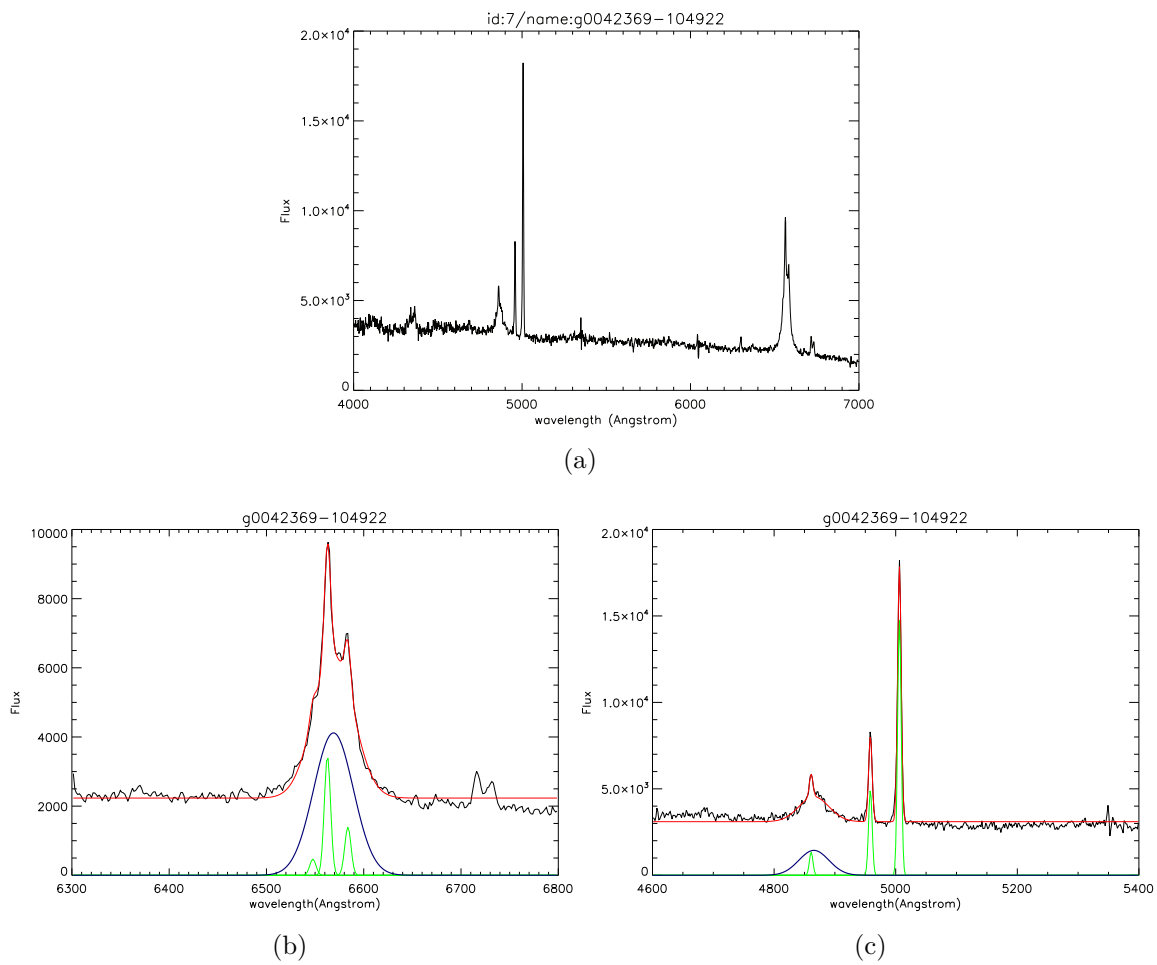


Figure A.4: (a) The optical spectrum of g0042369-104922 source observed by 6dFGS and (b) Fitting of lines H $\alpha$   $\lambda$  6562 $\text{\AA}$  and [N II], (c) H $\beta$   $\lambda$  4861 $\text{\AA}$  and [O III].



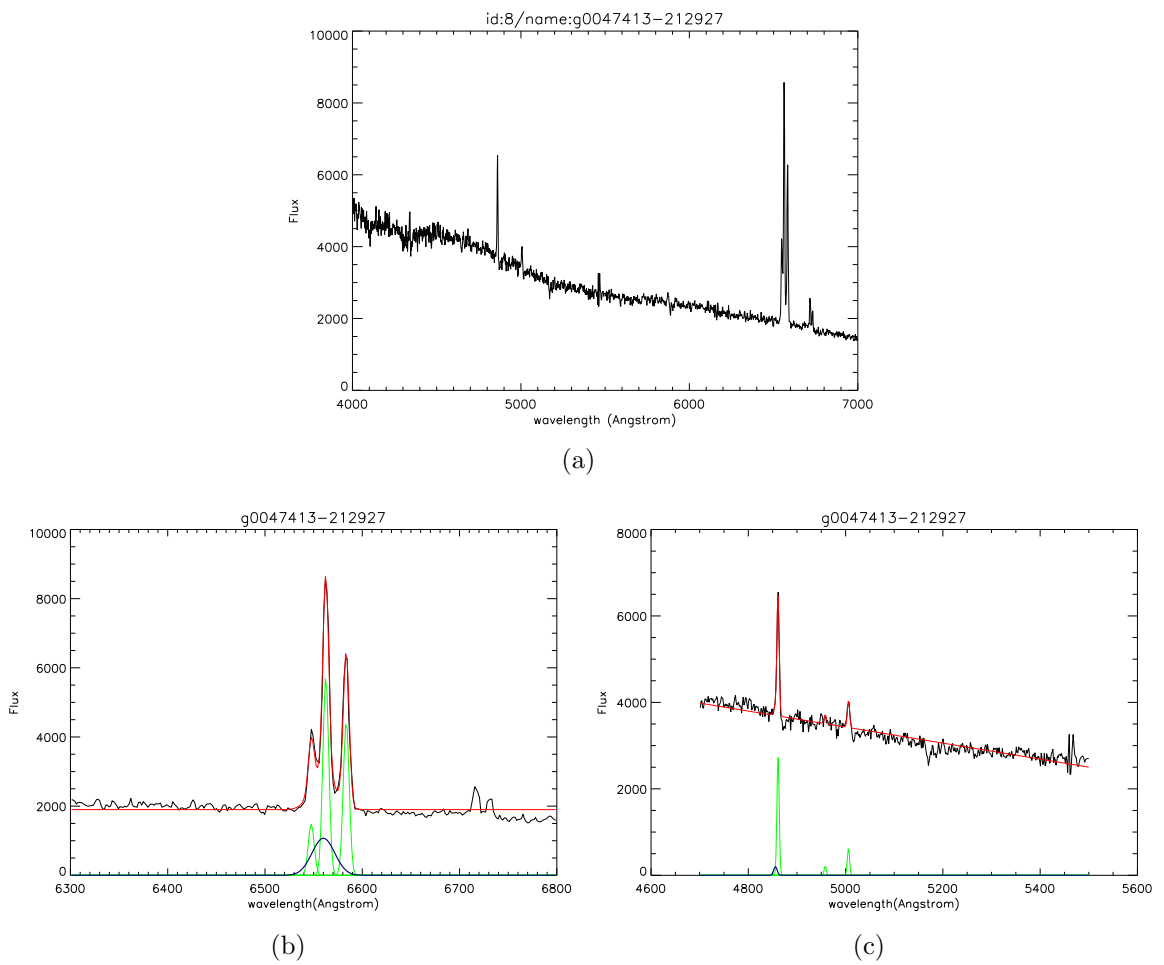


Figure A.5: (a) The optical spectrum of g0047413-212927 source observed by 6dFGS and (b) Fitting of lines H $\alpha$   $\lambda$  6562 $\text{\AA}$  and [N II], (c) H $\beta$   $\lambda$  4861 $\text{\AA}$  and [O III].

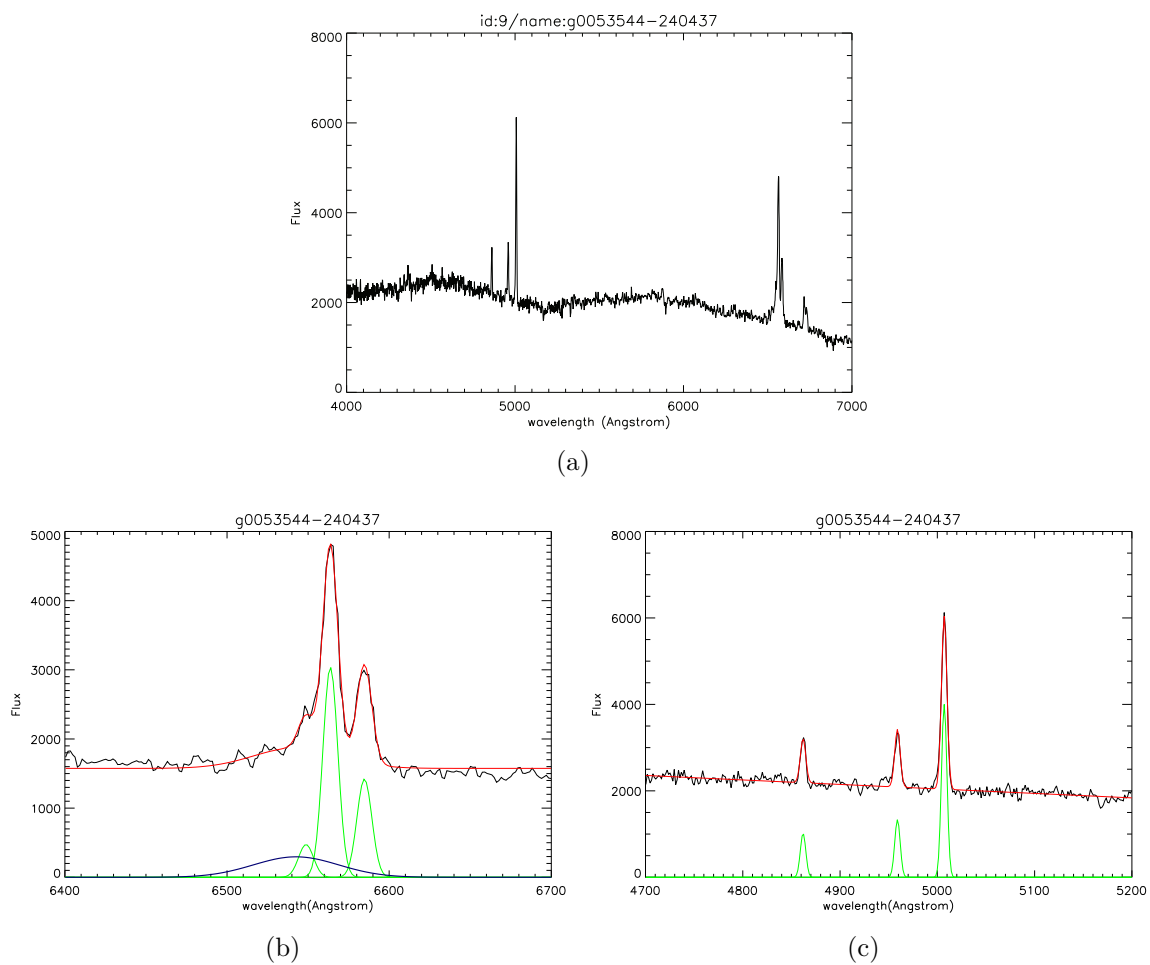


Figure A.6: (a) The optical spectrum of g0053544-240437 source observed by 6dFGS and (b) Fitting of lines H $\alpha$   $\lambda$  6562Å and [N II], (c) H $\beta$   $\lambda$  4861Å and [O III].

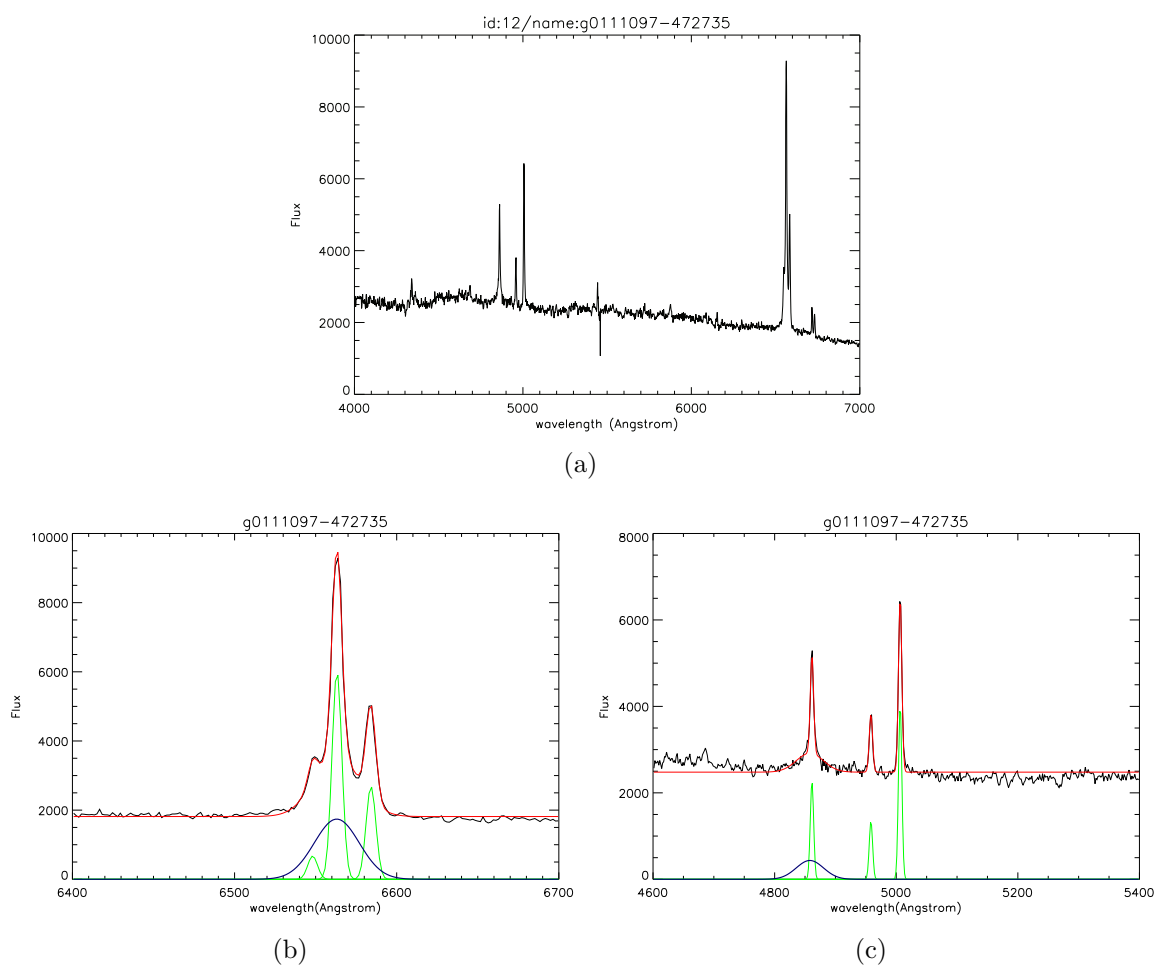


Figure A.7: (a) The optical spectrum of g0111097-472735 source observed by 6dFGS and (b) Fitting of lines H $\alpha$   $\lambda$  6562 $\text{\AA}$  and [N II], (c) H $\beta$   $\lambda$  4861 $\text{\AA}$  and [O III].

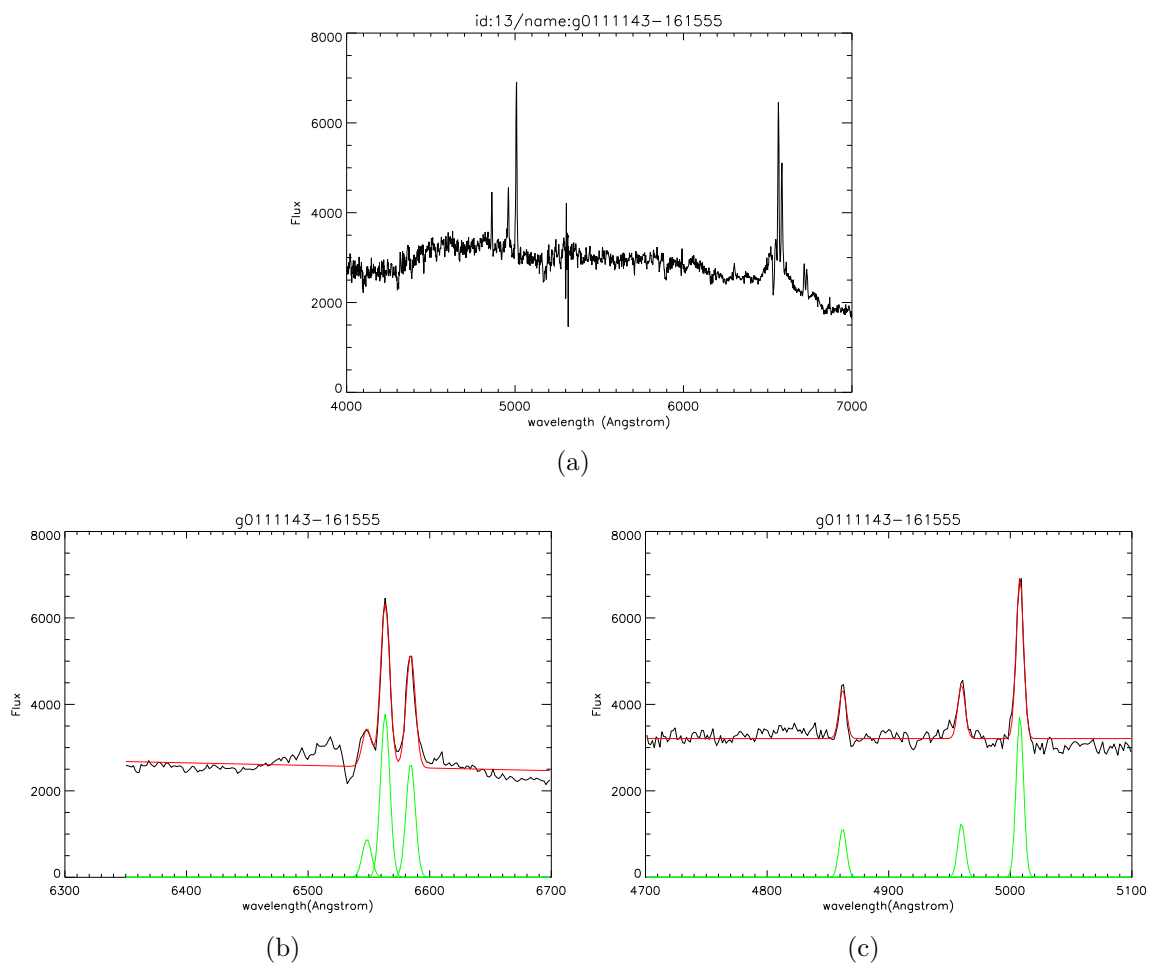


Figure A.8: (a) The optical spectrum of g0111143-161555 source observed by 6dFGS and (b) Fitting of lines H $\alpha$   $\lambda$  6562 $\text{\AA}$  and [N II], (c) H $\beta$   $\lambda$  4861 $\text{\AA}$  and [O III].

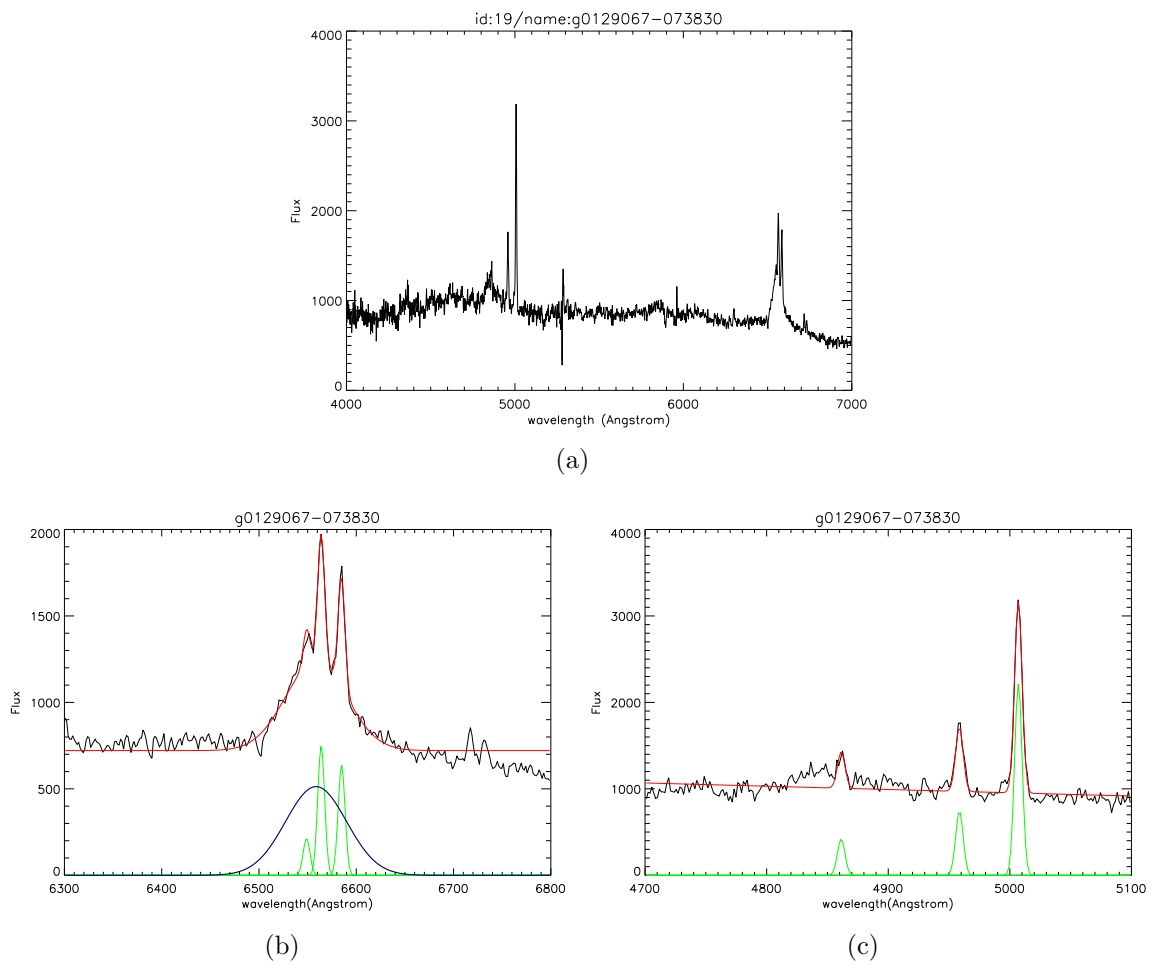


Figure A.9: (a) The optical spectrum of g0129067-073830 source observed by 6dFGS and (b) Fitting of lines H $\alpha$   $\lambda$  6562 $\text{\AA}$  and [N II], (c) H $\beta$   $\lambda$  4861 $\text{\AA}$  and [O III].

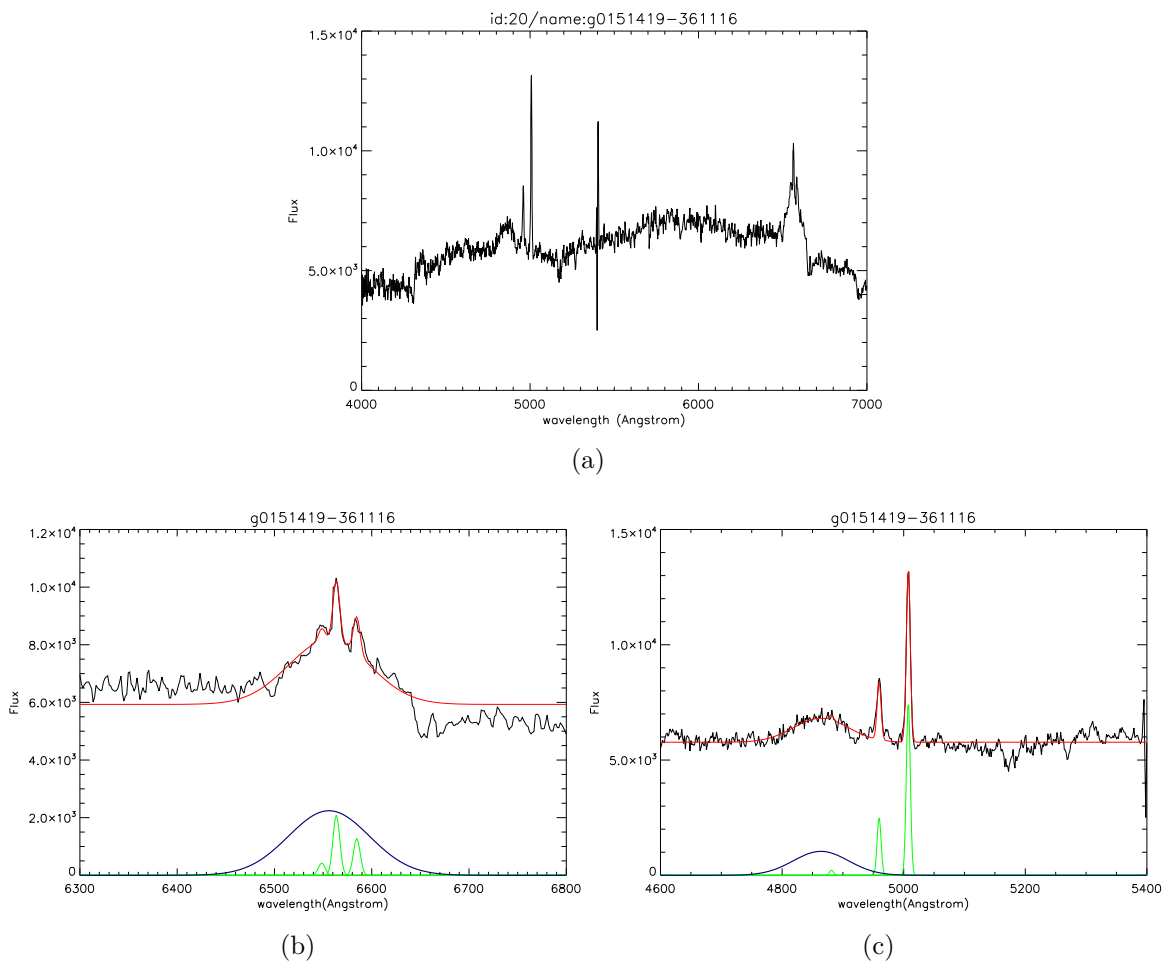


Figure A.10: (a) The optical spectrum of g0151419-361116 source observed by 6dFGS and (b) Fitting of lines  $H\alpha$   $\lambda$  6562 $\text{\AA}$  and  $[NII]$ , (c)  $H\beta$   $\lambda$  4861 $\text{\AA}$  and  $[OIII]$ .

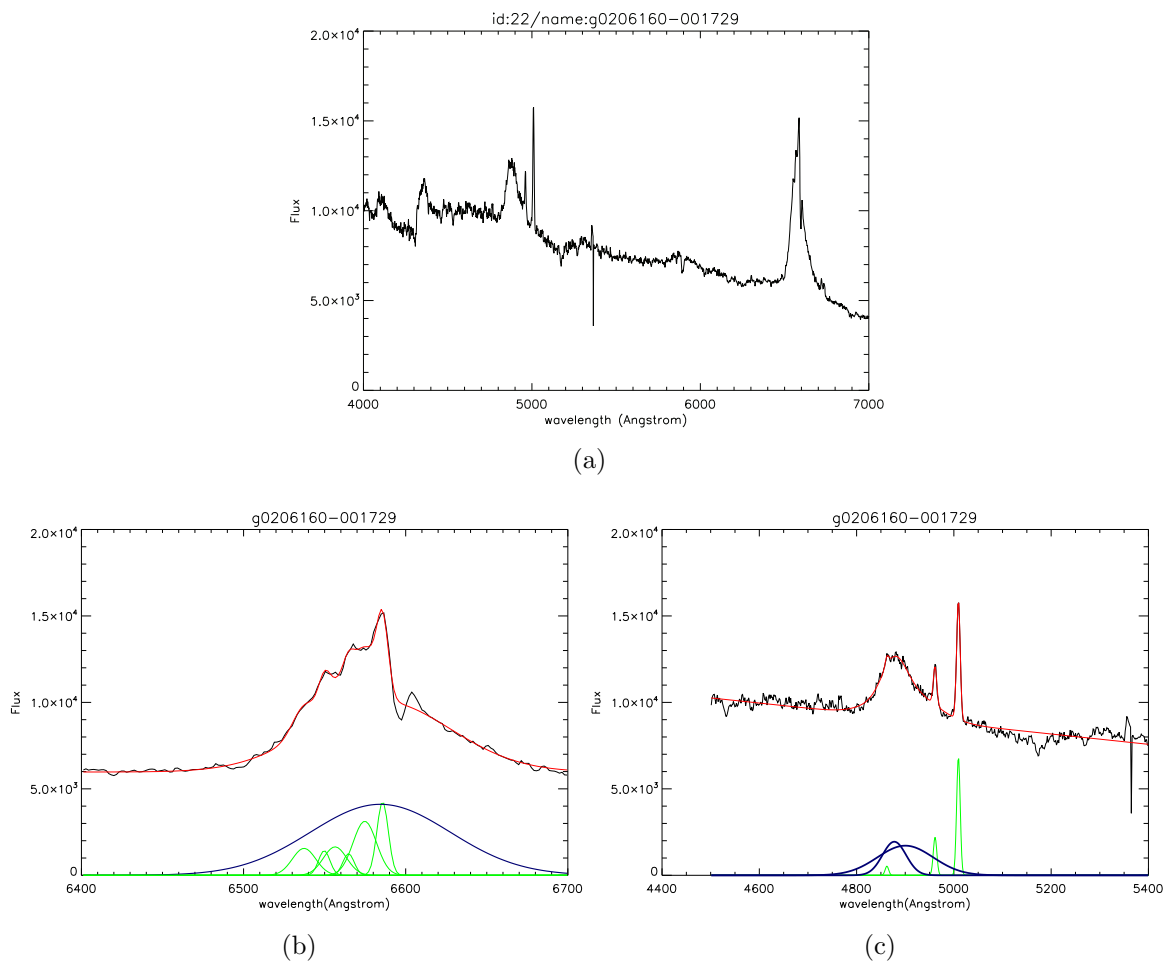


Figure A.11: (a) The optical spectrum of g0206160-001729 source observed by 6dFGS and (b) Fitting of lines  $H\alpha$   $\lambda$   $6562 \text{ \AA}$  and  $[N II]$ , (c)  $H\beta$   $\lambda$   $4861 \text{ \AA}$  and  $[O III]$ .

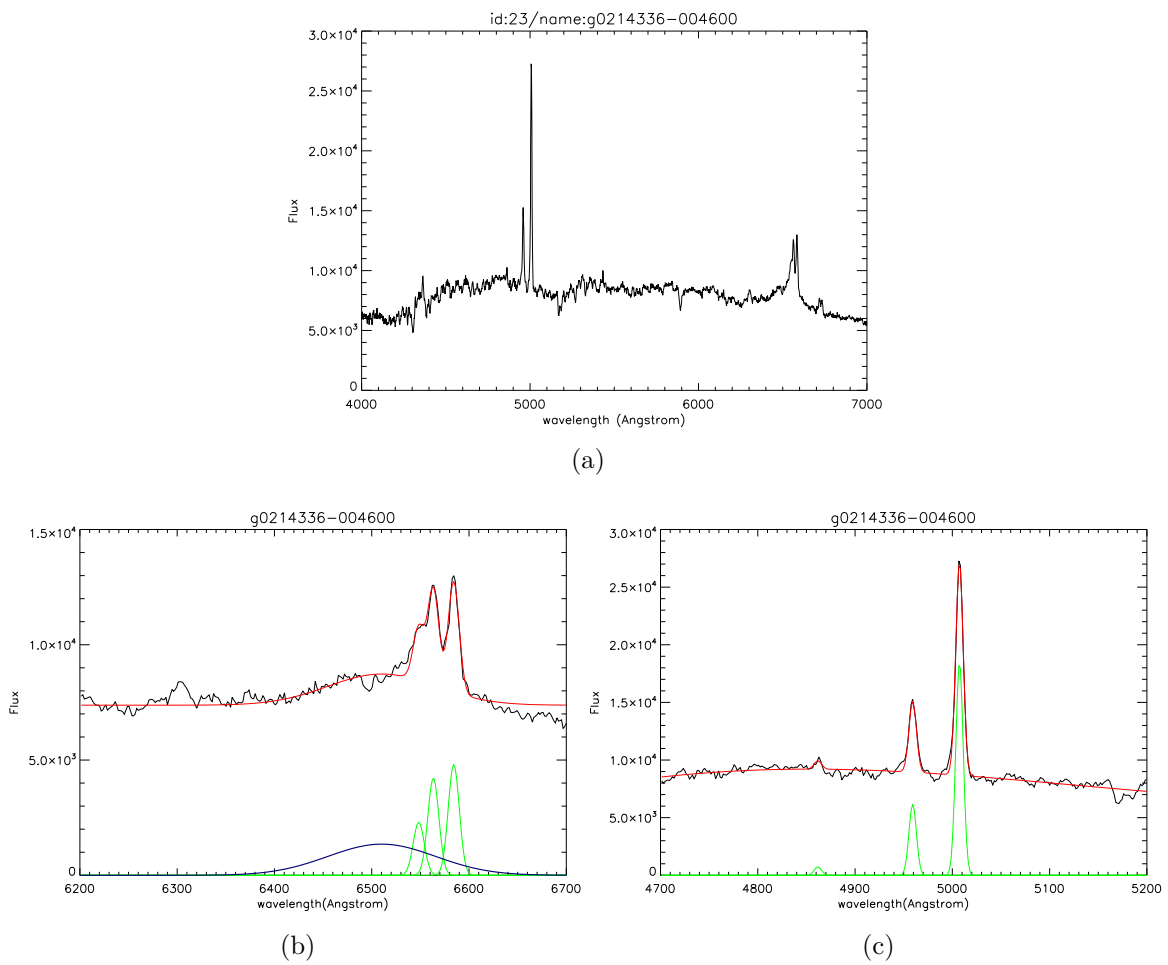


Figure A.12: (a) The optical spectrum of g0214336-004600 source observed by 6dFGS and (b) Fitting of lines  $H\alpha$   $\lambda$  6562 $\text{\AA}$  and  $[N II]$ , (c)  $H\beta$   $\lambda$  4861 $\text{\AA}$  and  $[O III]$ .



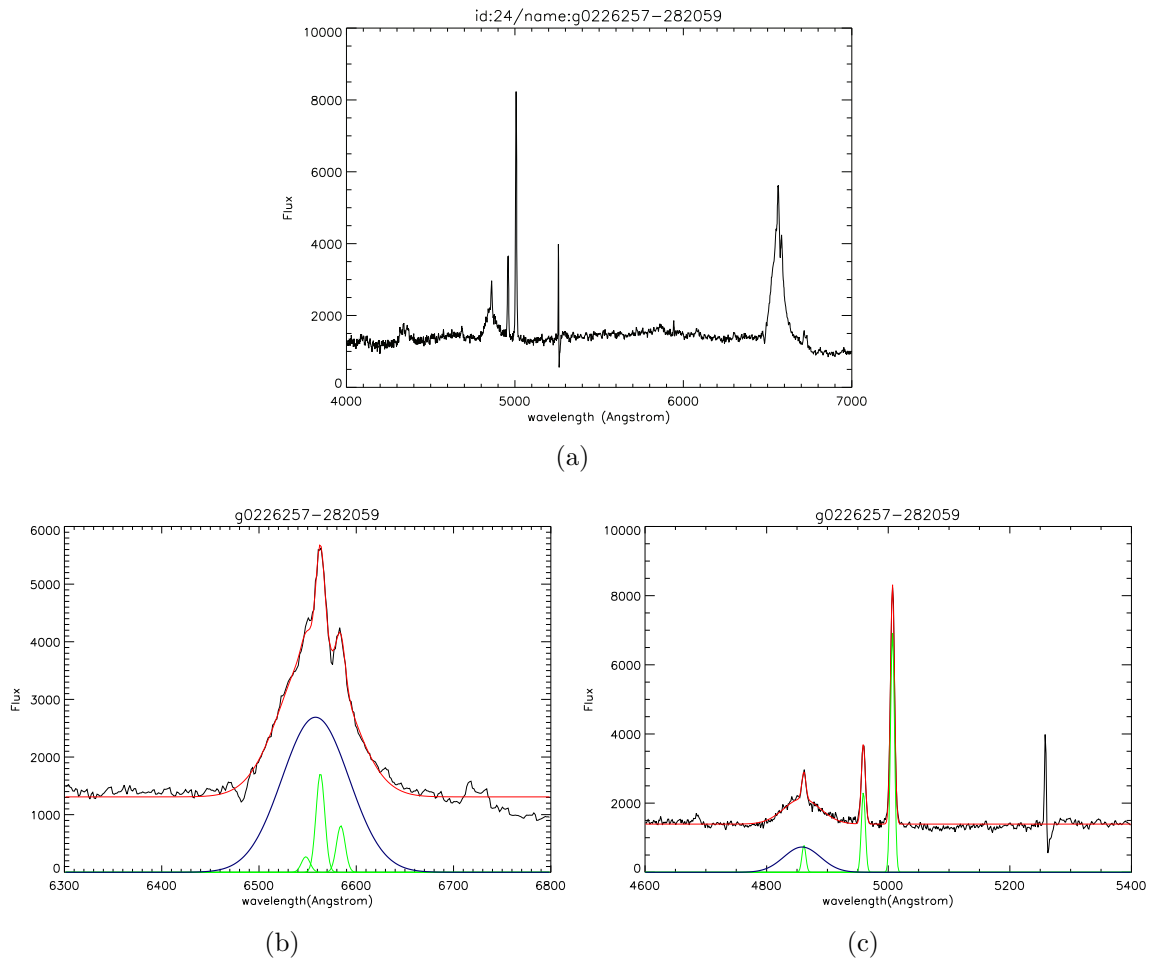


Figure A.13: (a) The optical spectrum of g0226257-282059 source observed by 6dFGS and (b) Fitting of lines H $\alpha$   $\lambda$  6562 $\text{\AA}$  and [N II], (c) H $\beta$   $\lambda$  4861 $\text{\AA}$  and [O III].

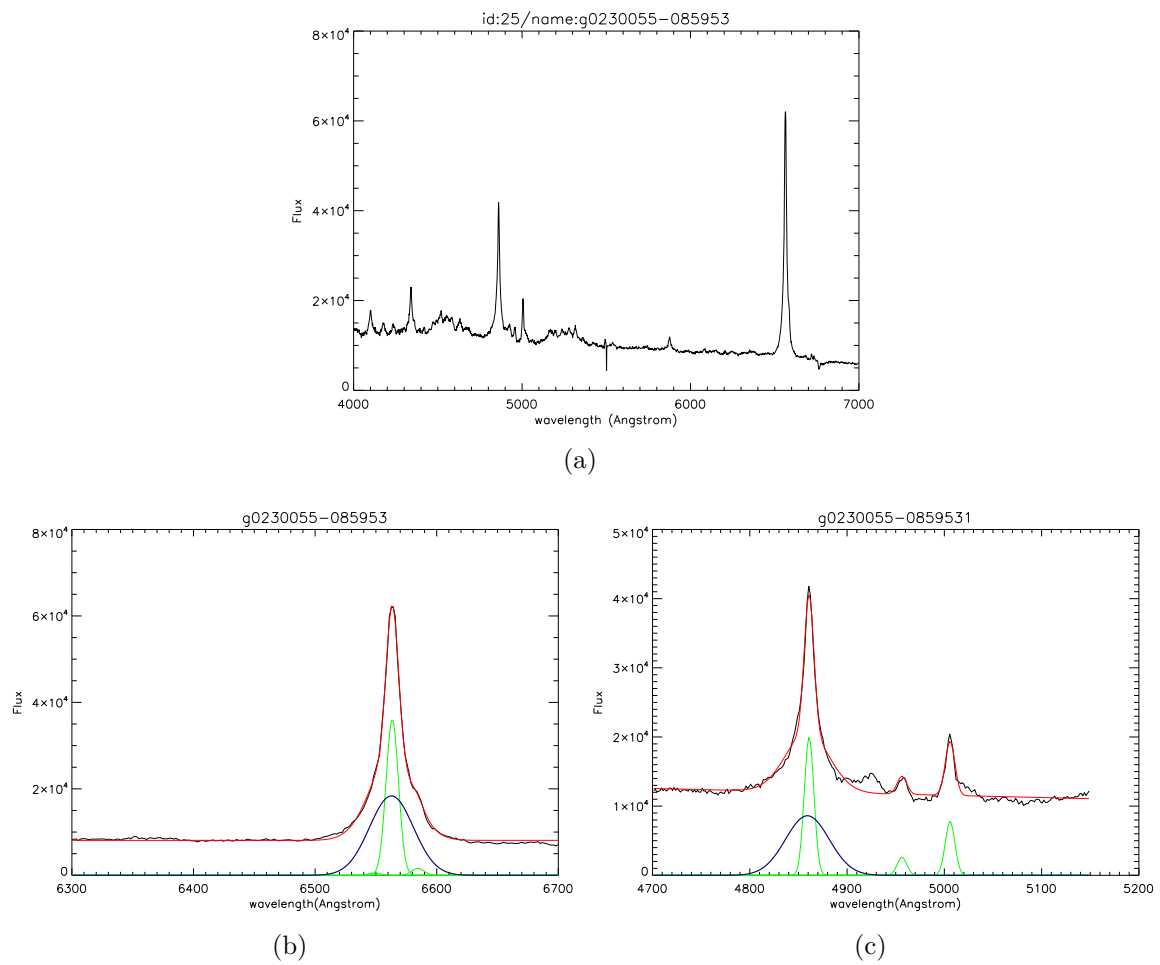


Figure A.14: (a) The optical spectrum of g0230055-085953 source observed by 6dFGS and (b) Fitting of lines H $\alpha$   $\lambda$  6562Å and [NII], (c) H $\beta$   $\lambda$  4861Å and [OIII].

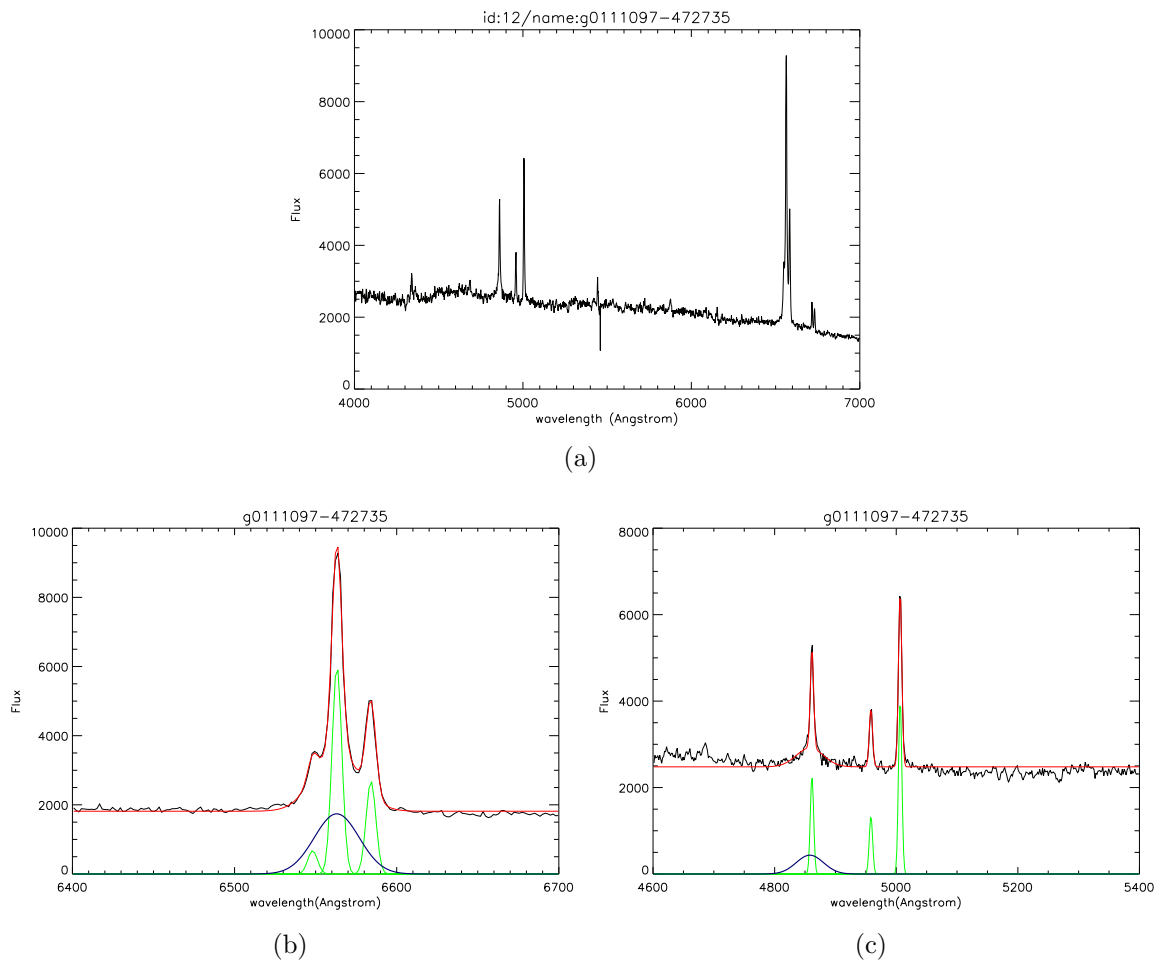


Figure A.15: (a) The optical spectrum of g0111097-472735 source observed by 6dFGS and (b) Fitting of lines H $\alpha$   $\lambda$  6562Å and [N II], (c) H $\beta$   $\lambda$  4861Å and [O III].

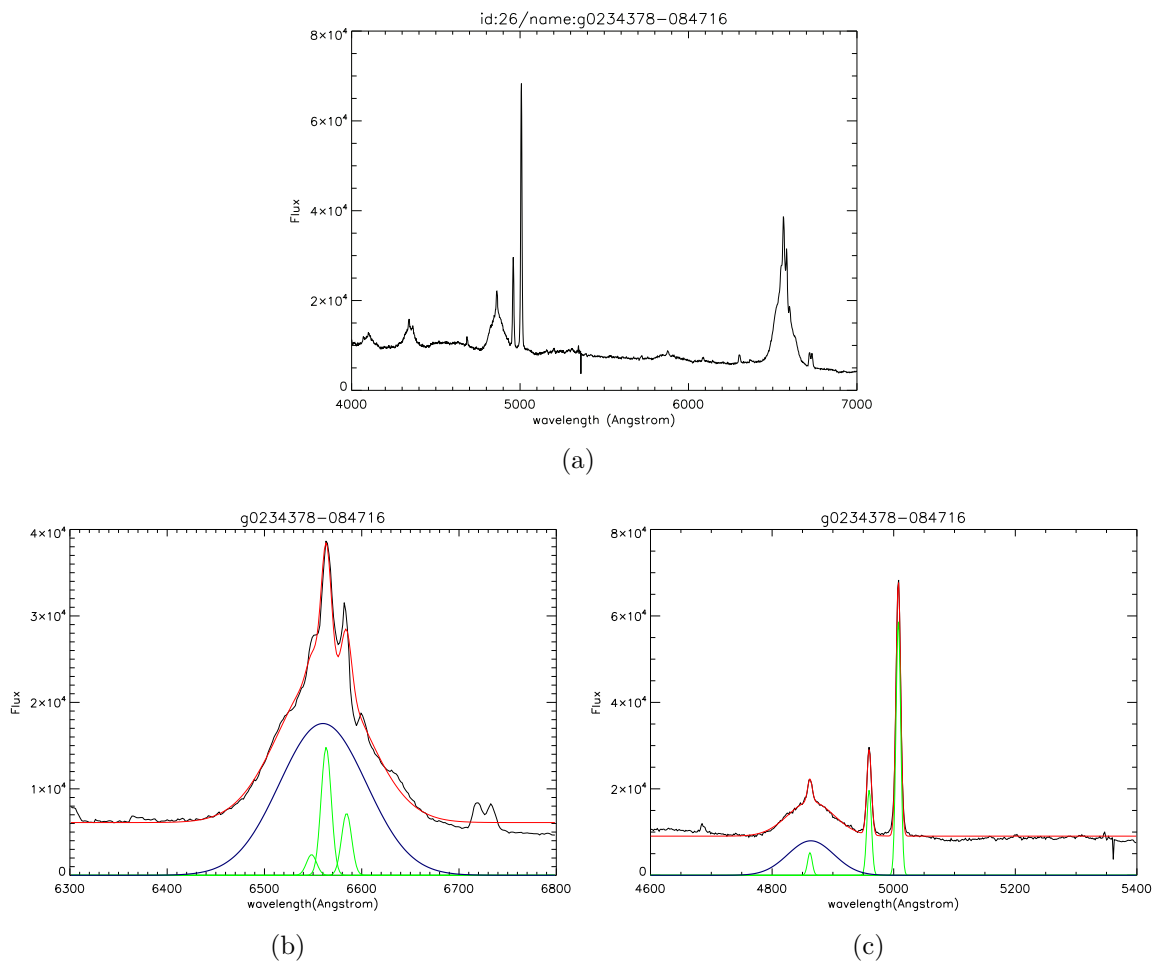


Figure A.16: (a) The optical spectrum of g0234378-084716 source observed by 6dFGS and (b) Fitting of lines H $\alpha$   $\lambda$  6562Å and [N II], (c) H $\beta$   $\lambda$  4861Å and [O III].

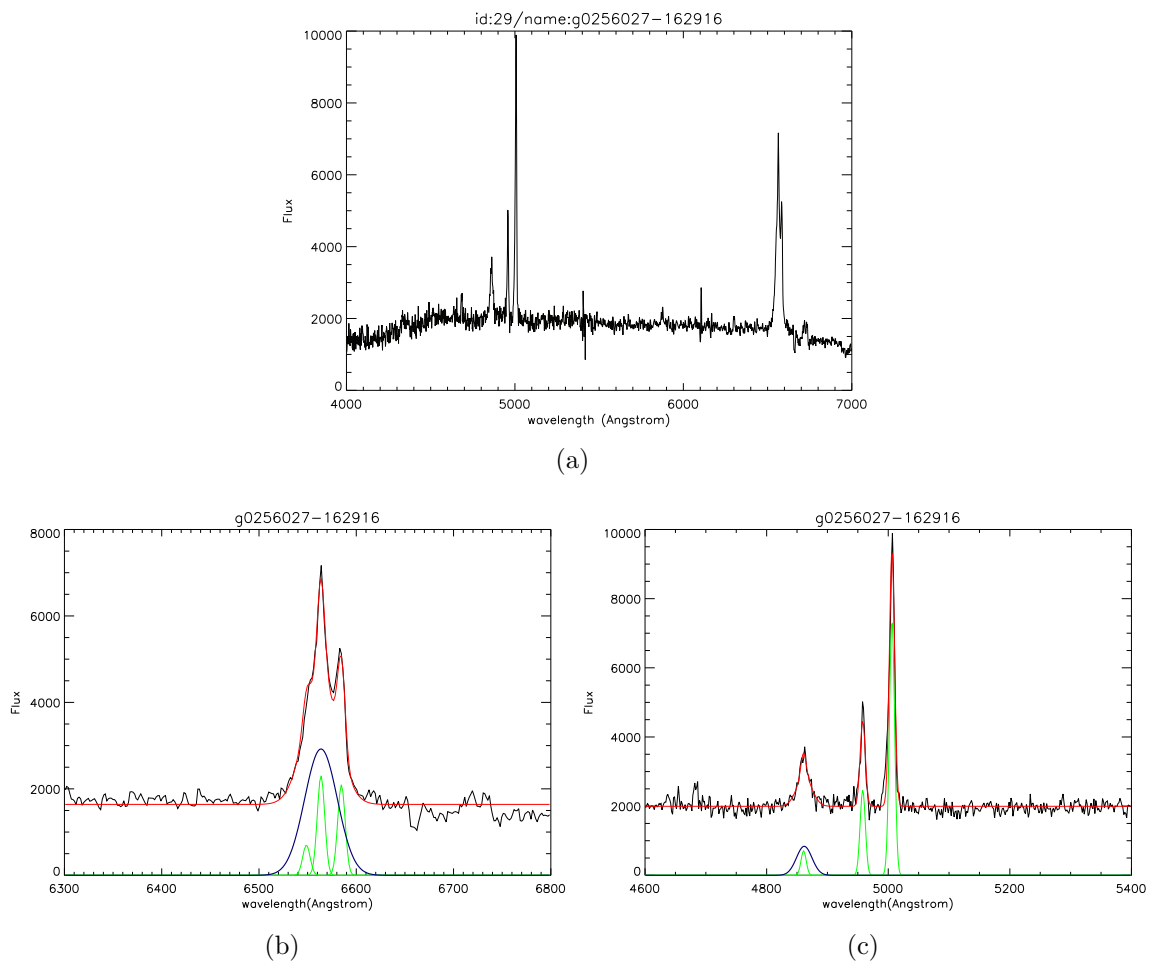


Figure A.17: (a) The optical spectrum of g0256027-162916 source observed by 6dFGS and (b) Fitting of lines H $\alpha$   $\lambda$  6562Å and [N II], (c) H $\beta$   $\lambda$  4861Å and [O III].

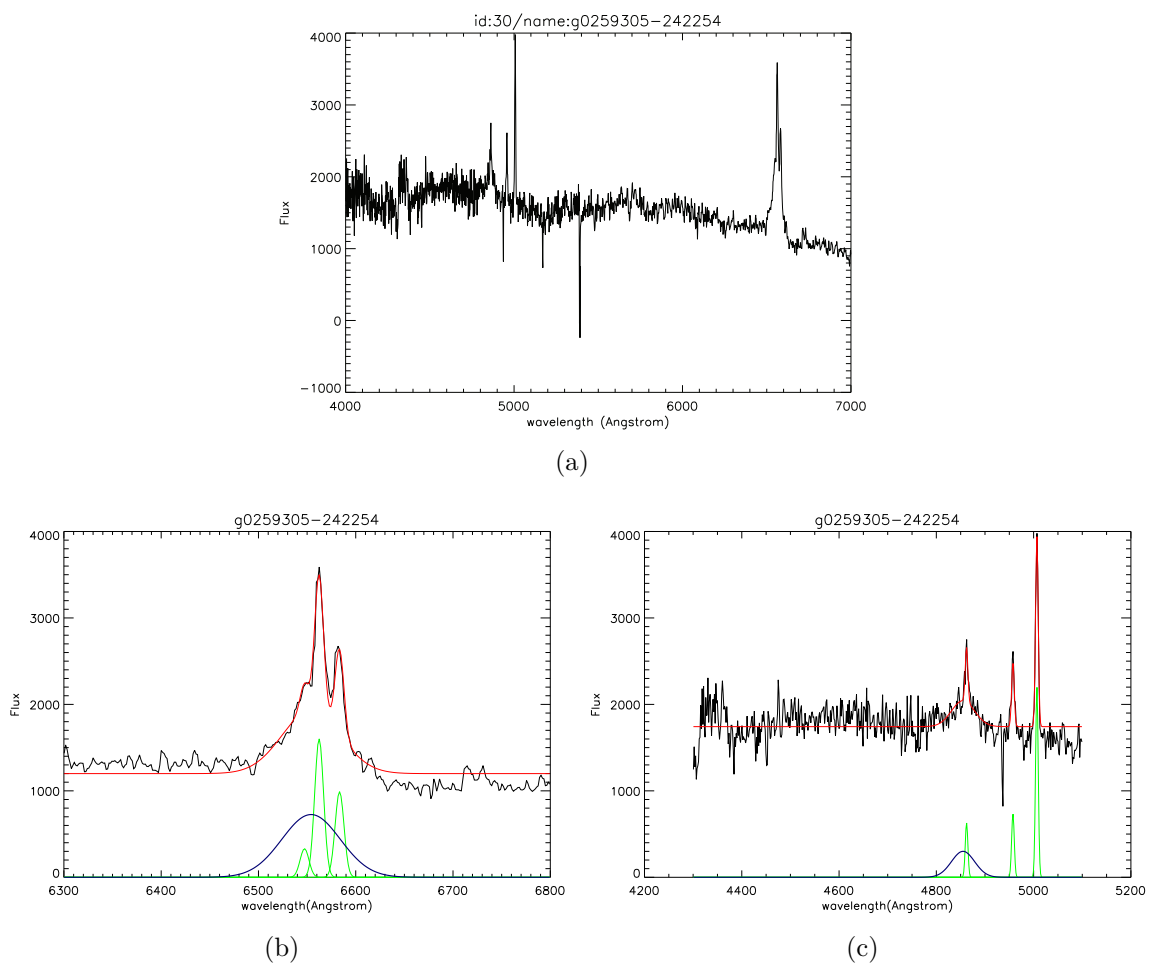


Figure A.18: (a) The optical spectrum of g0259305-242254 source observed by 6dFGS and (b) Fitting of lines H $\alpha$   $\lambda$  6562Å and [N II], (c) H $\beta$   $\lambda$  4861Å and [O III].

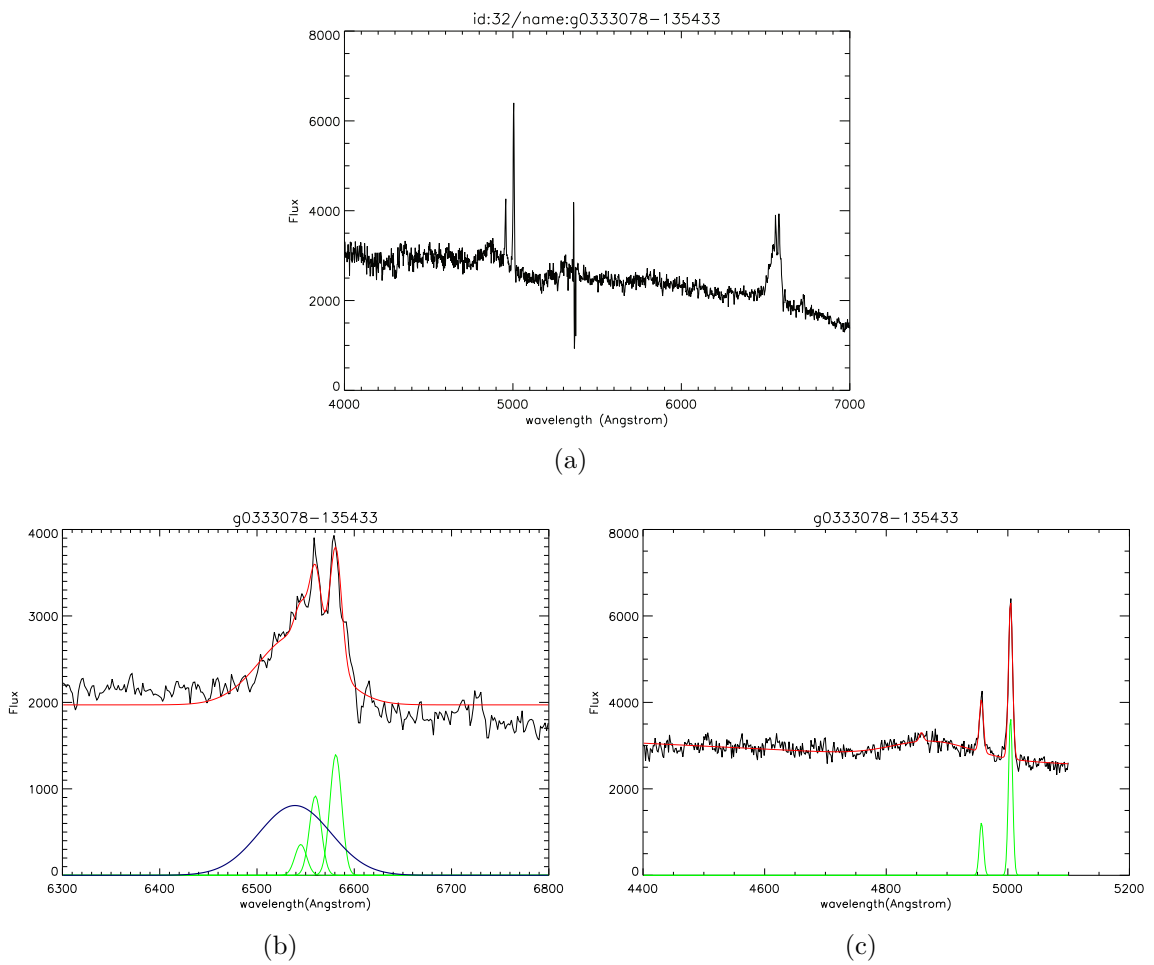


Figure A.19: (a) The optical spectrum of g0333078-135433 source observed by 6dFGS and (b) Fitting of lines H $\alpha$   $\lambda$  6562 $\text{\AA}$  and [N II], (c) H $\beta$   $\lambda$  4861 $\text{\AA}$  and [O III].

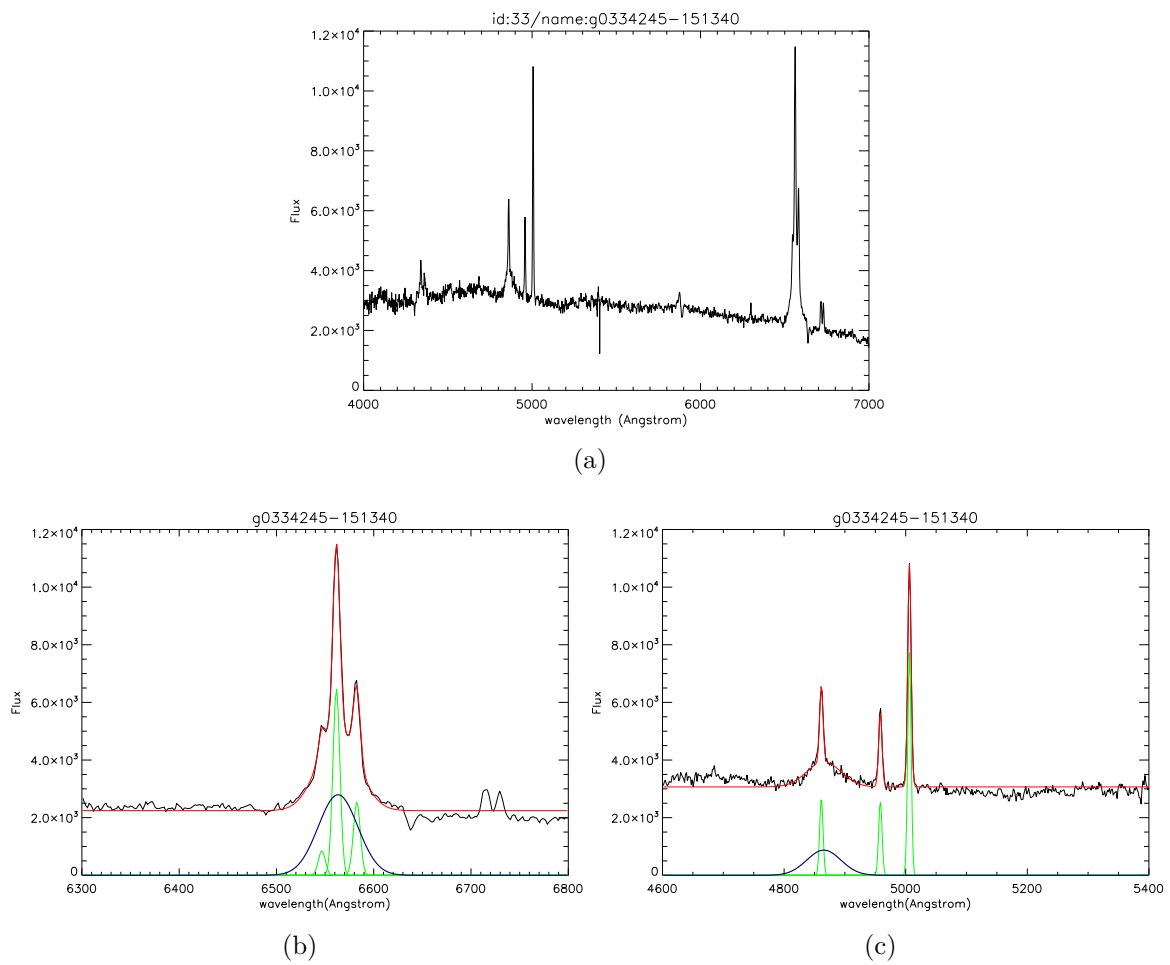


Figure A.20: (a) The optical spectrum of g0334245-151340 source observed by 6dFGS and (b) Fitting of lines  $H\alpha$   $\lambda$  6562 $\text{\AA}$  and  $[N II]$ , (c)  $H\beta$   $\lambda$  4861 $\text{\AA}$  and  $[O III]$ .



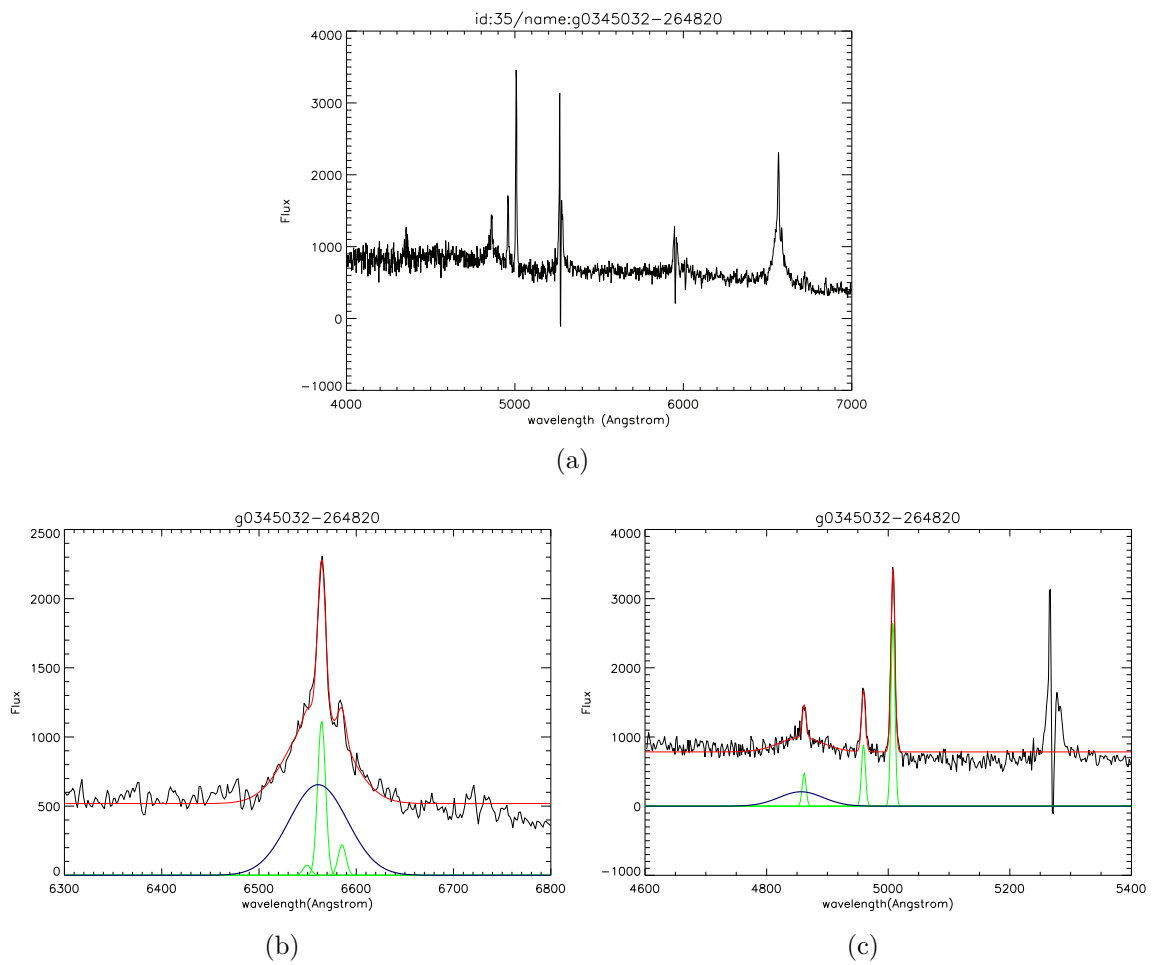


Figure A.21: (a) The optical spectrum of g0345032-264820 source observed by 6dFGS and (b) Fitting of lines H $\alpha$   $\lambda$  6562 $\text{\AA}$  and [N II], (c) H $\beta$   $\lambda$  4861 $\text{\AA}$  and [O III].

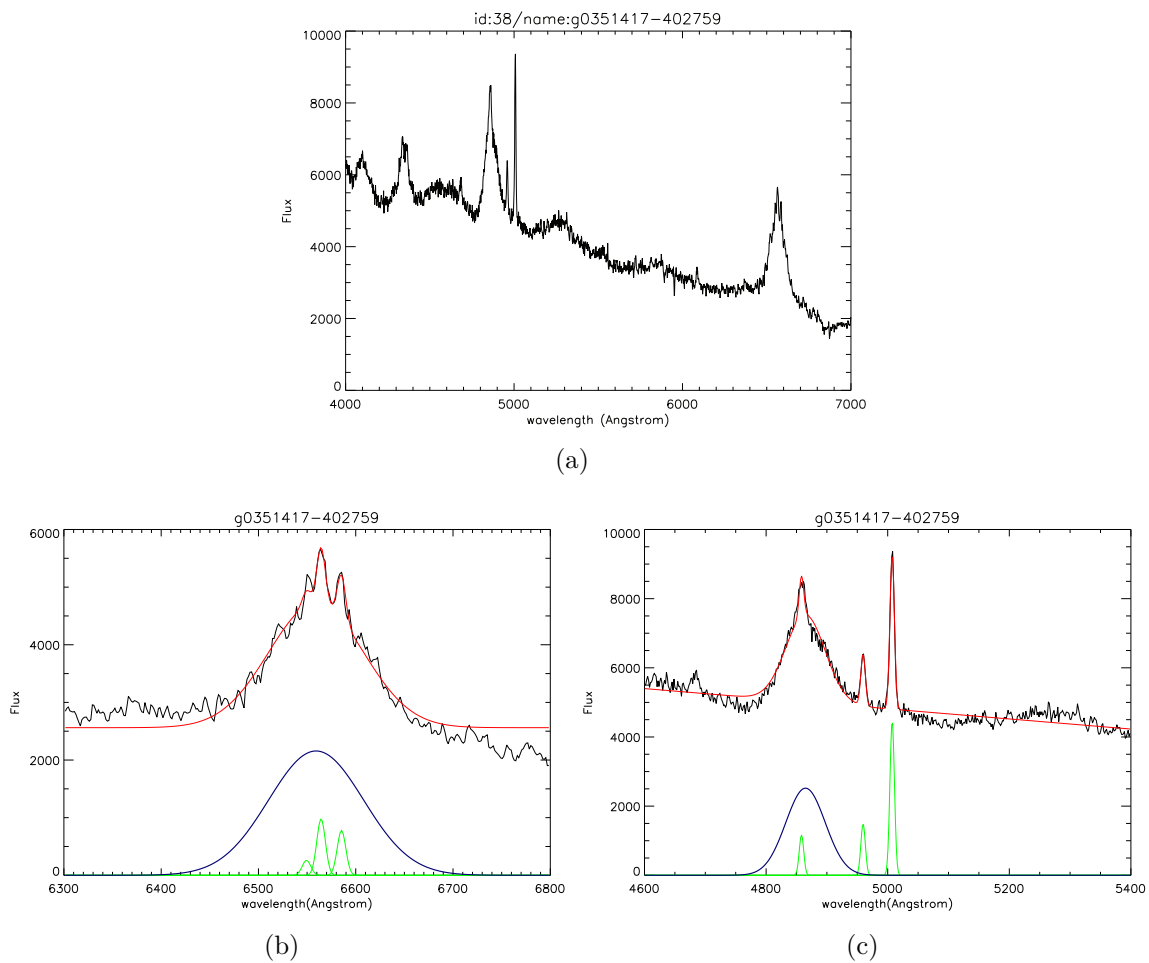


Figure A.22: (a) The optical spectrum of g0351417-402759 source observed by 6dFGS and (b) Fitting of lines H $\alpha$   $\lambda$  6562 $\text{\AA}$  and [N II], (c) H $\beta$   $\lambda$  4861 $\text{\AA}$  and [O III].

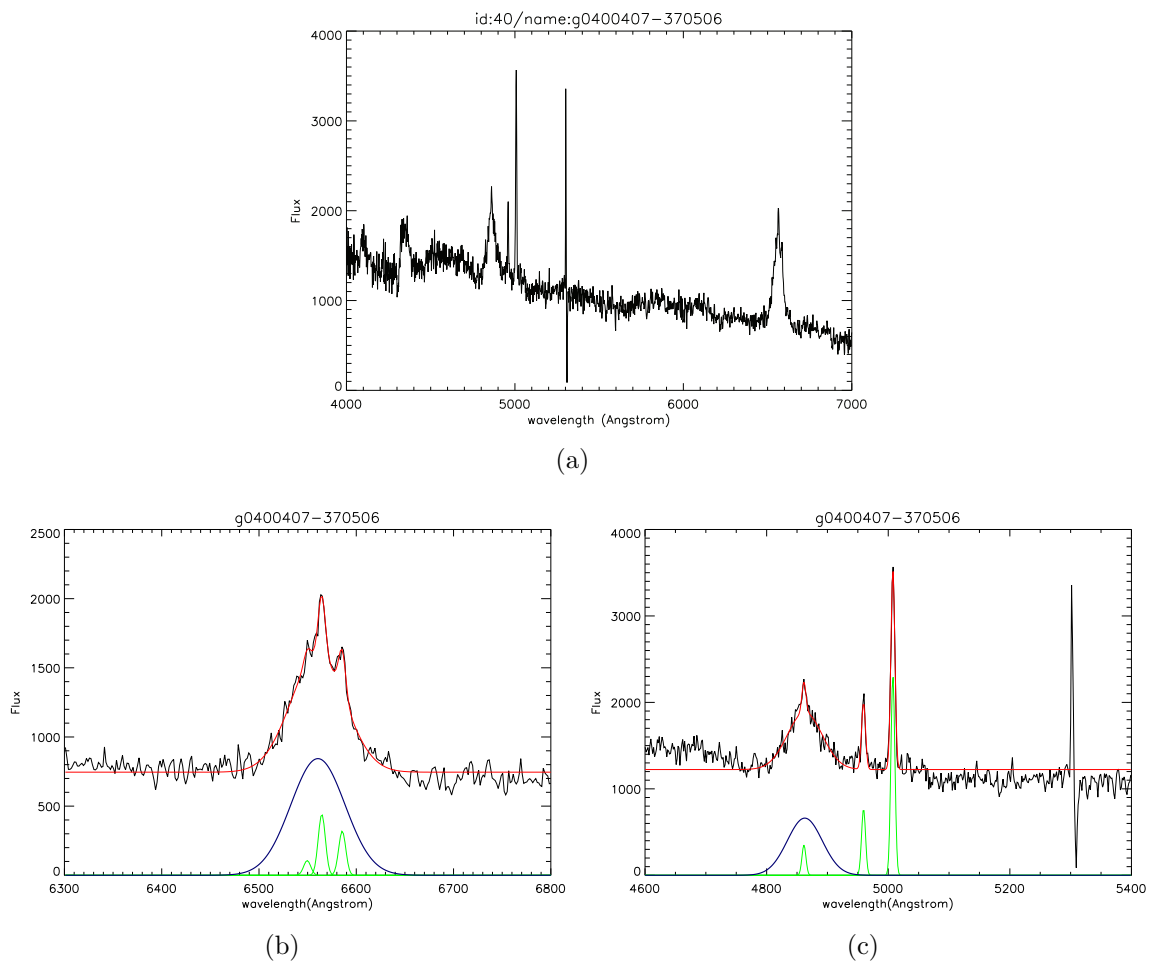


Figure A.23: (a) The optical spectrum of g0400407-370506 source observed by 6dFGS and (b) Fitting of lines H $\alpha$   $\lambda$  6562 $\text{\AA}$  and [N II], (c) H $\beta$   $\lambda$  4861 $\text{\AA}$  and [O III].

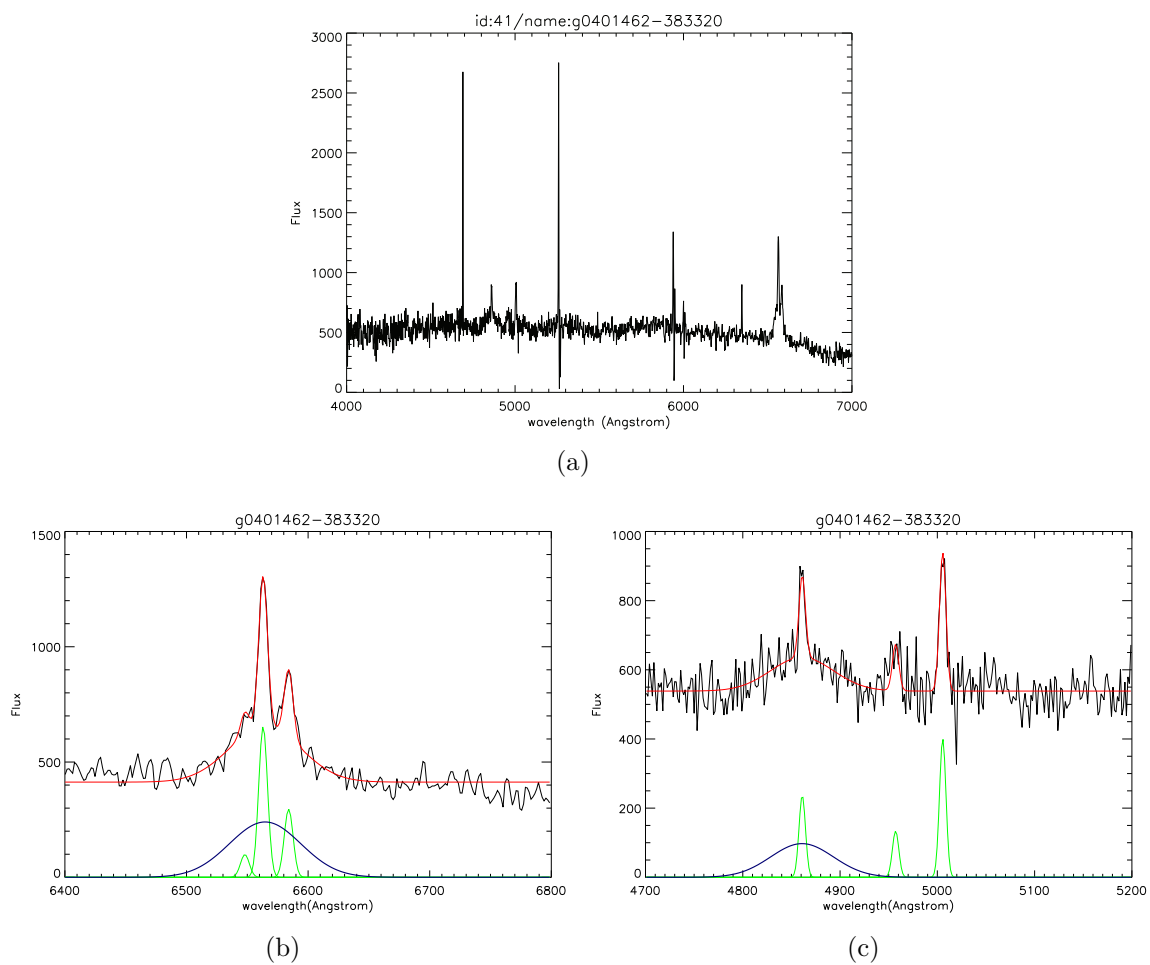


Figure A.24: (a) The optical spectrum of g0401462-383320 source observed by 6dFGS and (b) Fitting of lines H $\alpha$   $\lambda$  6562Å and [N II], (c) H $\beta$   $\lambda$  4861Å and [O III].

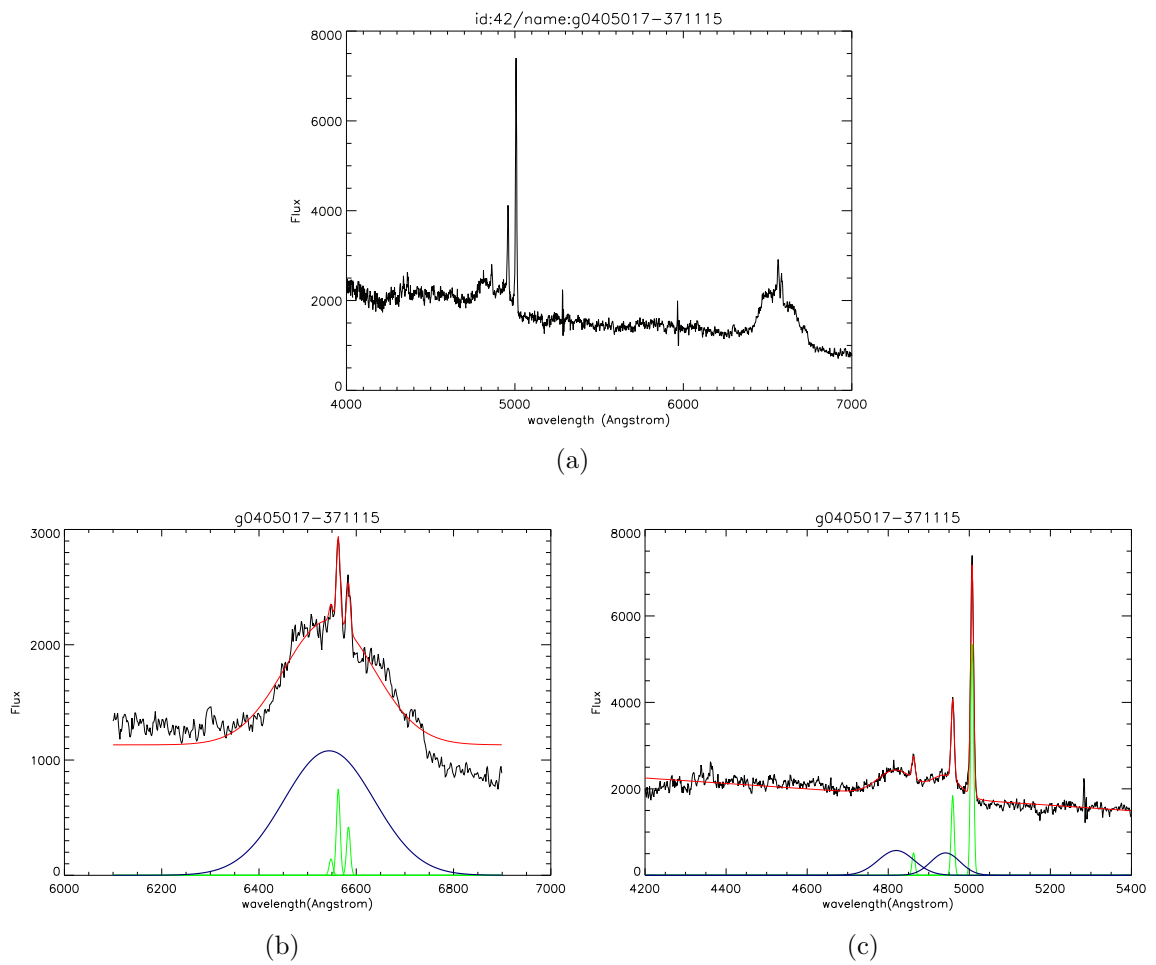


Figure A.25: (a) The optical spectrum of g0405017-371115 source observed by 6dFGS and (b) Fitting of lines H $\alpha$   $\lambda$  6562 $\text{\AA}$  and [N II], (c) H $\beta$   $\lambda$  4861 $\text{\AA}$  and [O III].

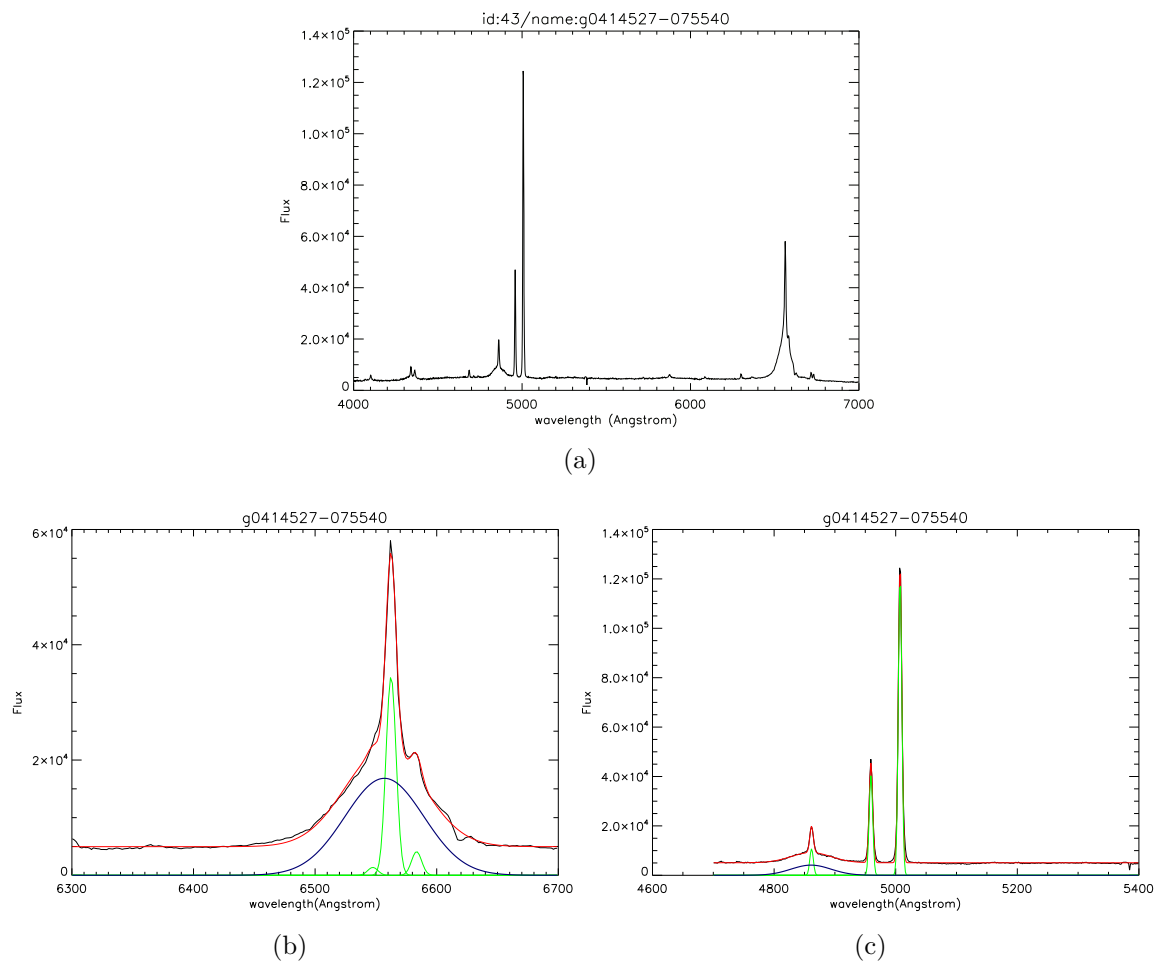


Figure A.26: (a) The optical spectrum of g0414527-075540 source observed by 6dFGS and (b) Fitting of lines H $\alpha$   $\lambda$  6562 $\text{\AA}$  and [N II], (c) H $\beta$   $\lambda$  4861 $\text{\AA}$  and [O III].

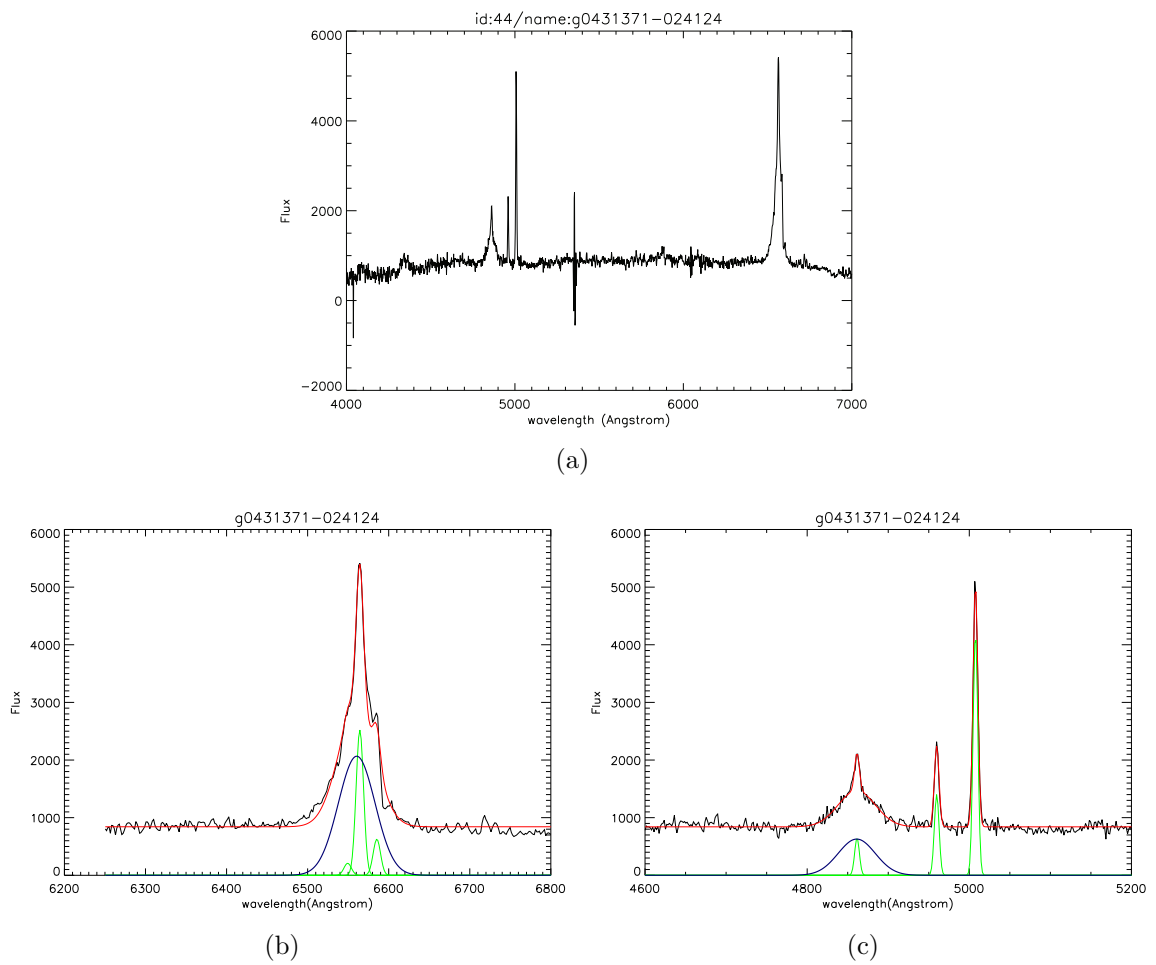


Figure A.27: (a) The optical spectrum of g0431371-024124 source observed by 6dFGS and (b) Fitting of lines H $\alpha$   $\lambda$  6562Å and [N II], (c) H $\beta$   $\lambda$  4861Å and [O III].

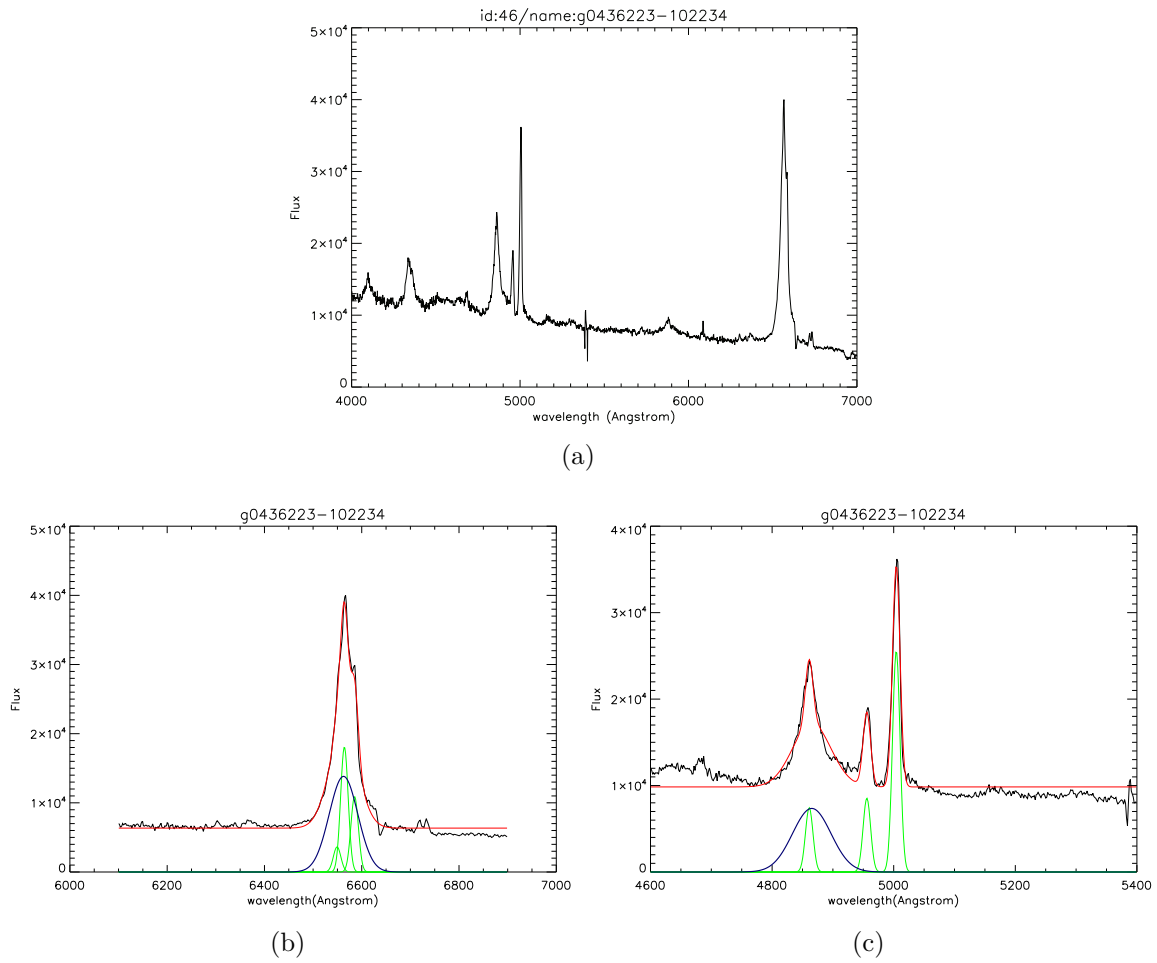


Figure A.28: (a) The optical spectrum of g0436223-102234 source observed by 6dFGS and (b) Fitting of lines H $\alpha$   $\lambda$  6562Å and [N II], (c) H $\beta$   $\lambda$  4861Å and [O III].



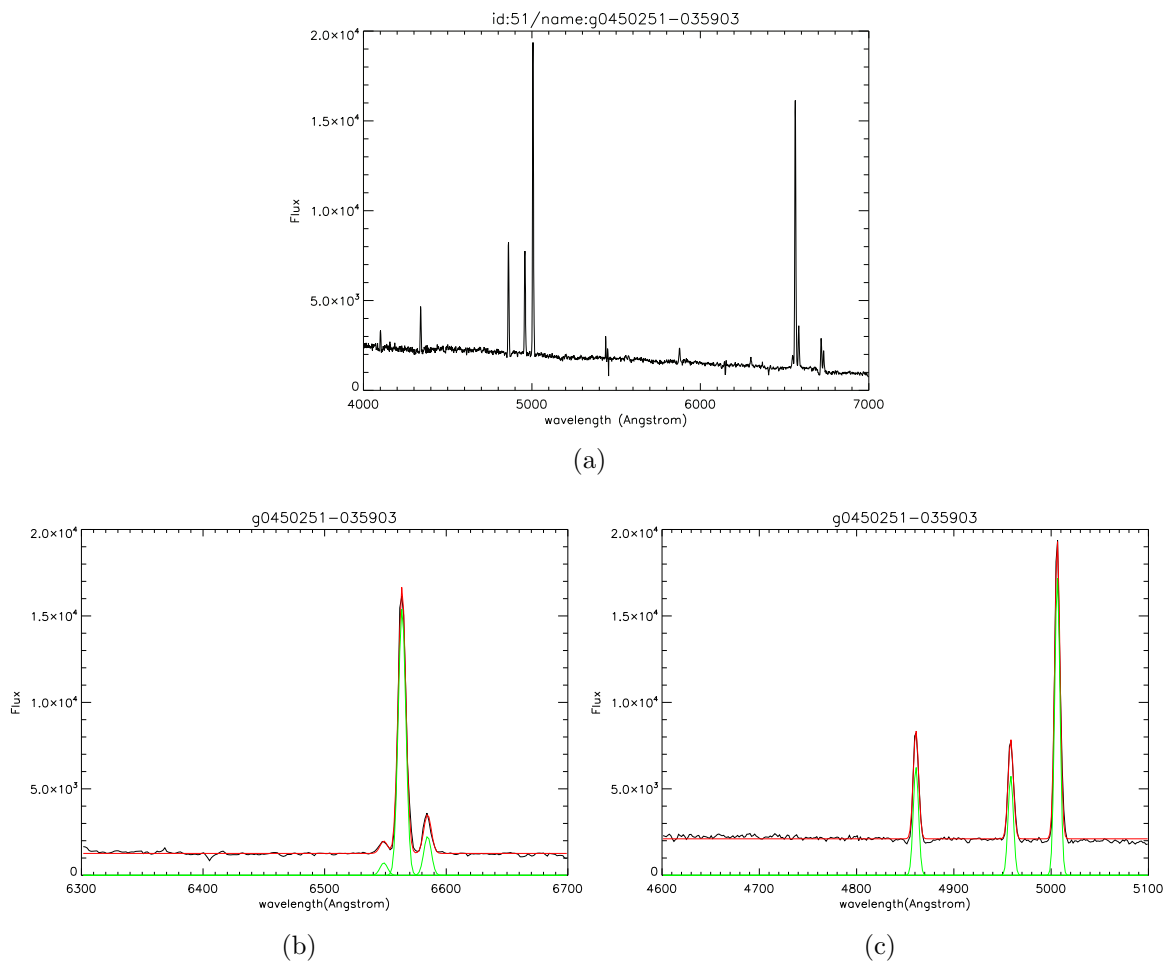


Figure A.29: (a) The optical spectrum of g0450251-035903 source observed by 6dFGS and (b) Fitting of lines H $\alpha$   $\lambda$  6562 Å and [N II], (c) H $\beta$   $\lambda$  4861 Å and [O III].

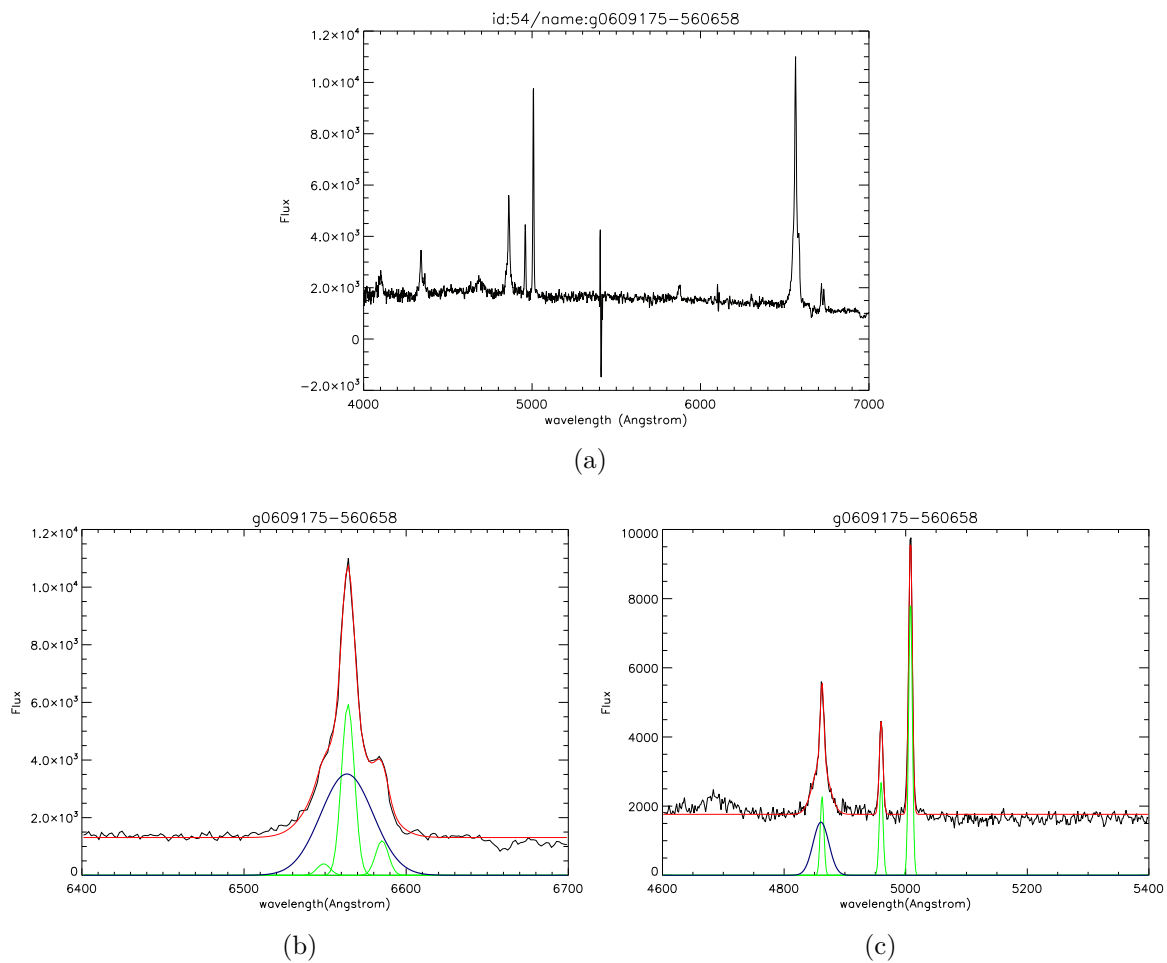


Figure A.30: (a) The optical spectrum of g0609175-560658 source observed by 6dFGS and (b) Fitting of lines  $H\alpha$   $\lambda$  6562 $\text{\AA}$  and  $[N II]$ , (c)  $H\beta$   $\lambda$  4861 $\text{\AA}$  and  $[O III]$ .

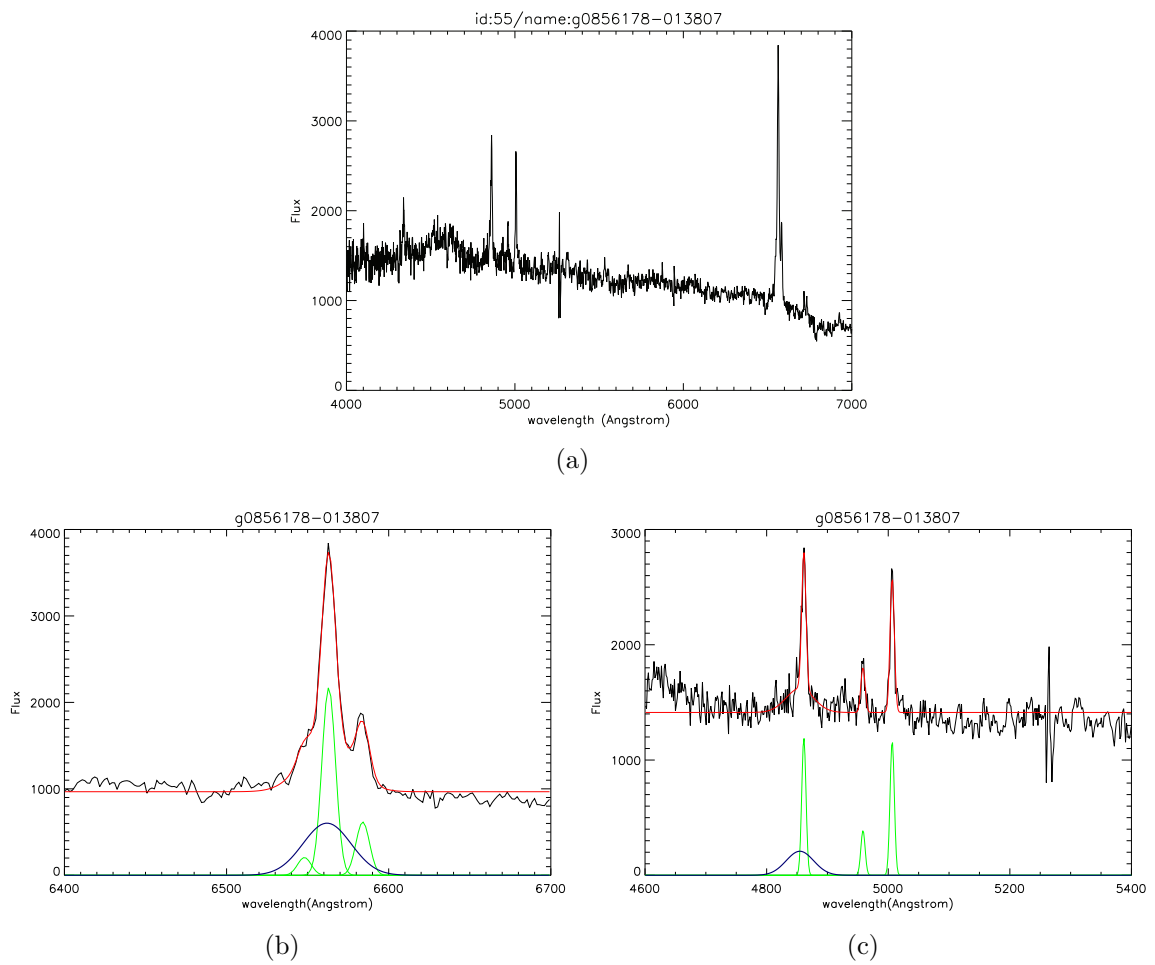


Figure A.31: (a) The optical spectrum of g0856178-013807 source observed by 6dFGS and (b) Fitting of lines H $\alpha$   $\lambda$  6562 $\text{\AA}$  and [N II], (c) H $\beta$   $\lambda$  4861 $\text{\AA}$  and [O III].

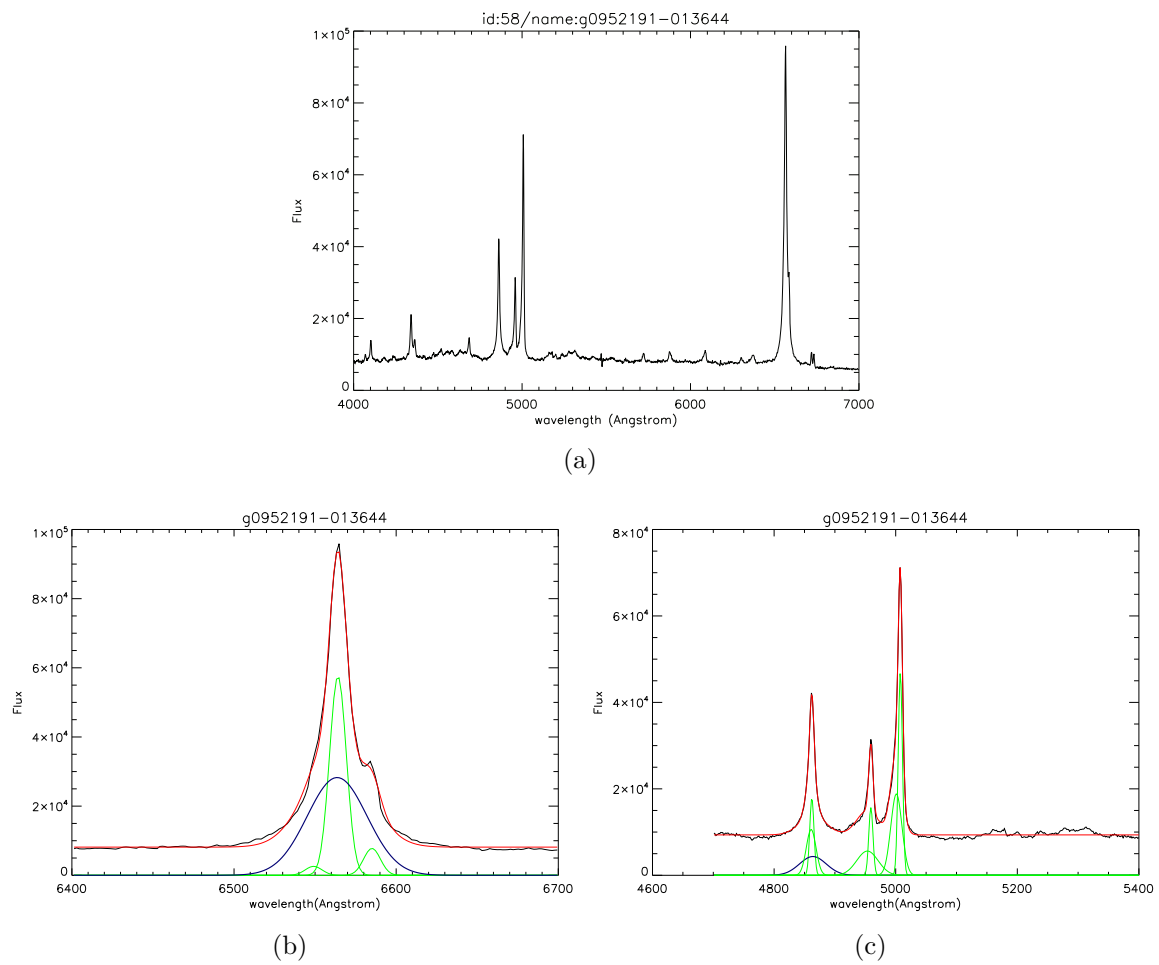


Figure A.32: (a) The optical spectrum of g0952191-013644 source observed by 6dFGS and (b) Fitting of lines  $H\alpha$   $\lambda$  6562 $\text{\AA}$  and  $[N II]$ , (c)  $H\beta$   $\lambda$  4861 $\text{\AA}$  and  $[O III]$ .

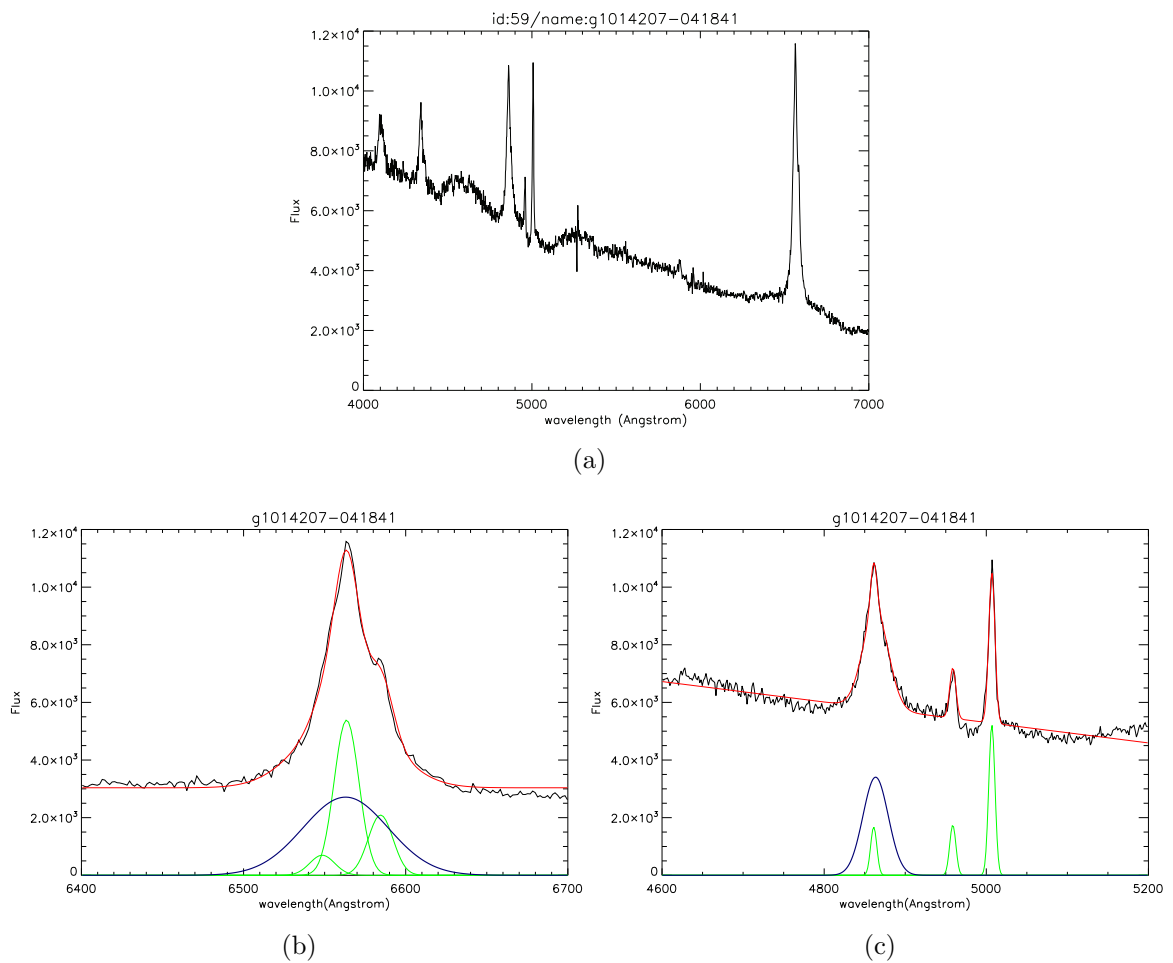


Figure A.33: (a) The optical spectrum of g1014207-041841 source observed by 6dFGS and (b) Fitting of lines  $H\alpha$   $\lambda$   $6562 \text{ \AA}$  and  $[N II]$ , (c)  $H\beta$   $\lambda$   $4861 \text{ \AA}$  and  $[O III]$ .

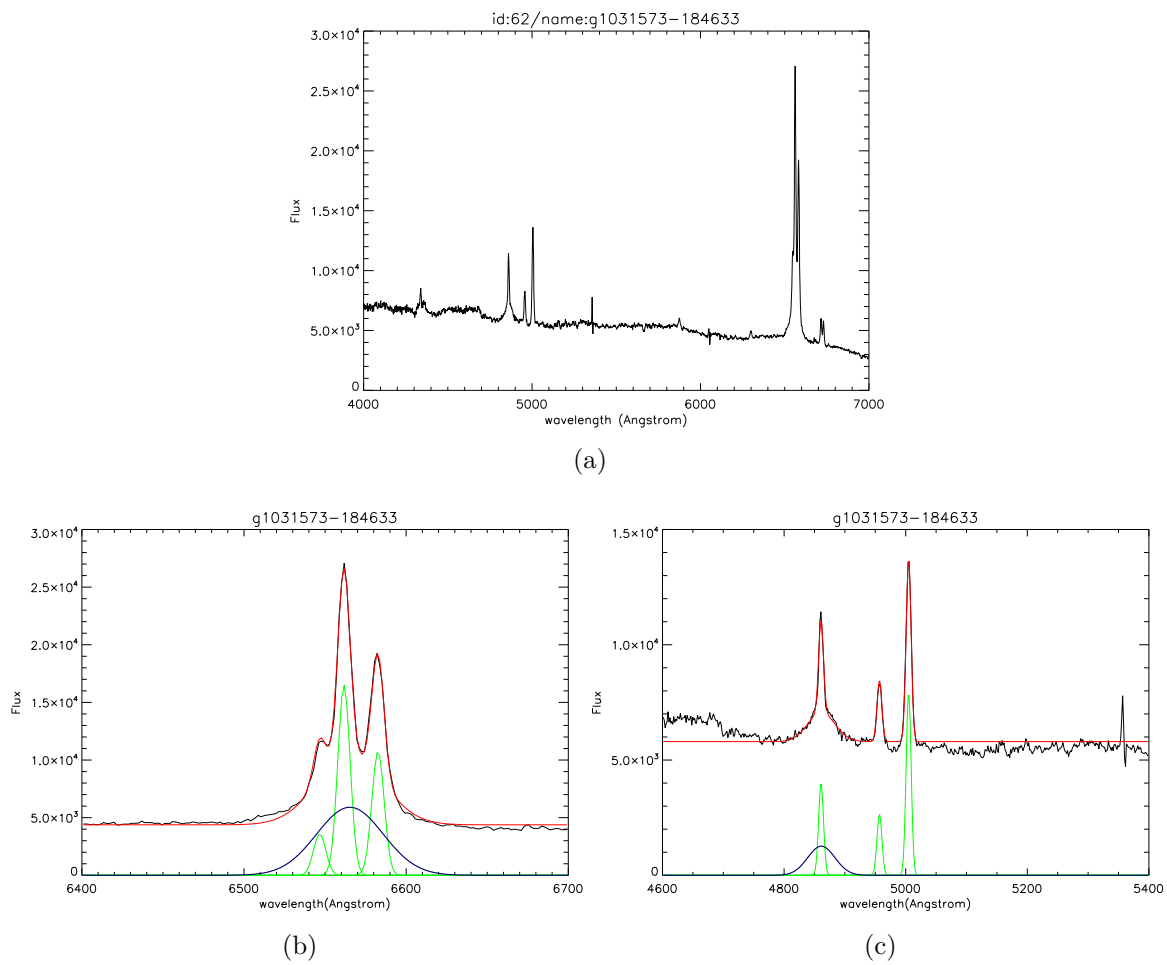


Figure A.34: (a) The optical spectrum of g1031573-184633 source observed by 6dFGS and (b) Fitting of lines  $H\alpha$   $\lambda$  6562 $\text{\AA}$  and  $[NII]$ , (c)  $H\beta$   $\lambda$  4861 $\text{\AA}$  and  $[OIII]$ .

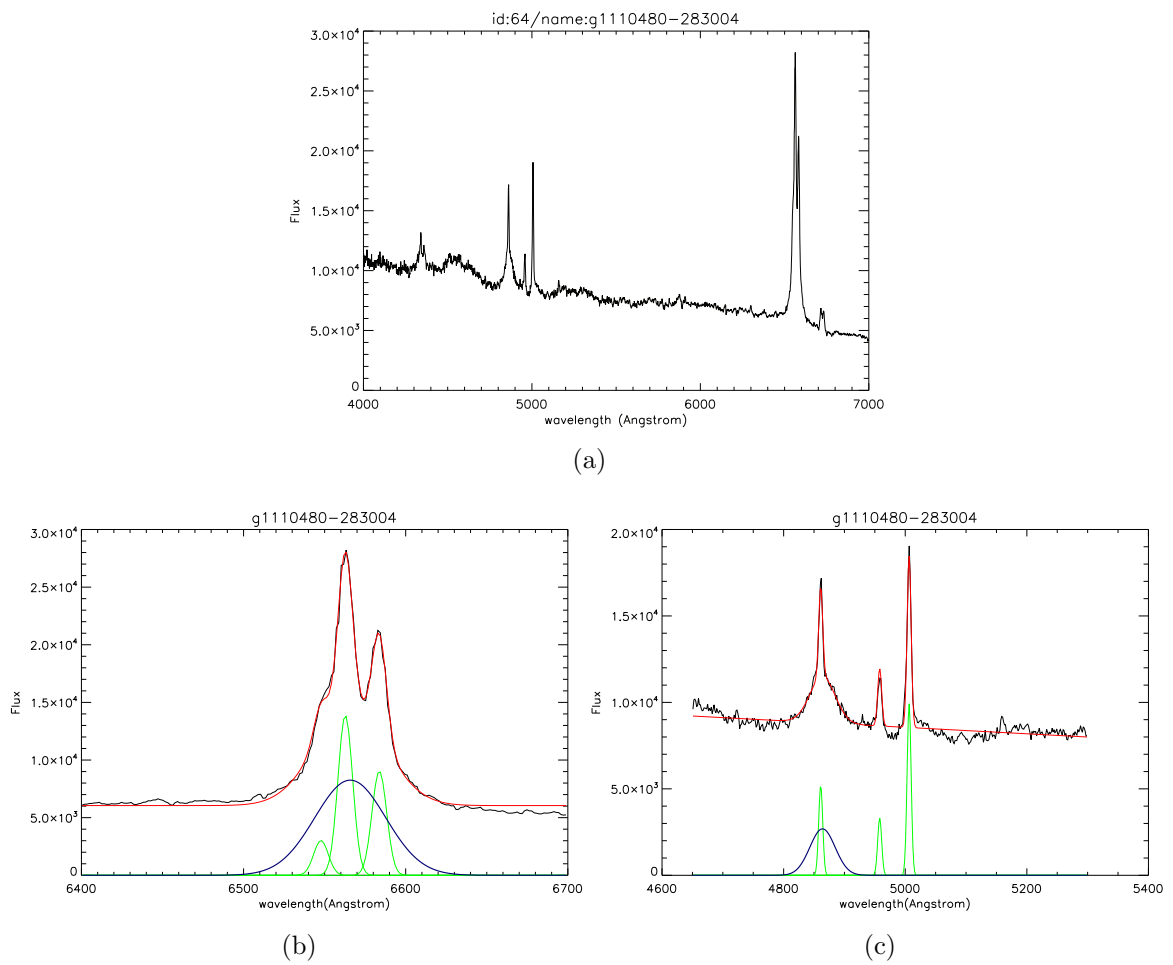


Figure A.35: (a) The optical spectrum of g1110480-283004 source observed by 6dFGS and (b) Fitting of lines  $H\alpha$   $\lambda$   $6562 \text{ \AA}$  and  $[N II]$ , (c)  $H\beta$   $\lambda$   $4861 \text{ \AA}$  and  $[O III]$ .

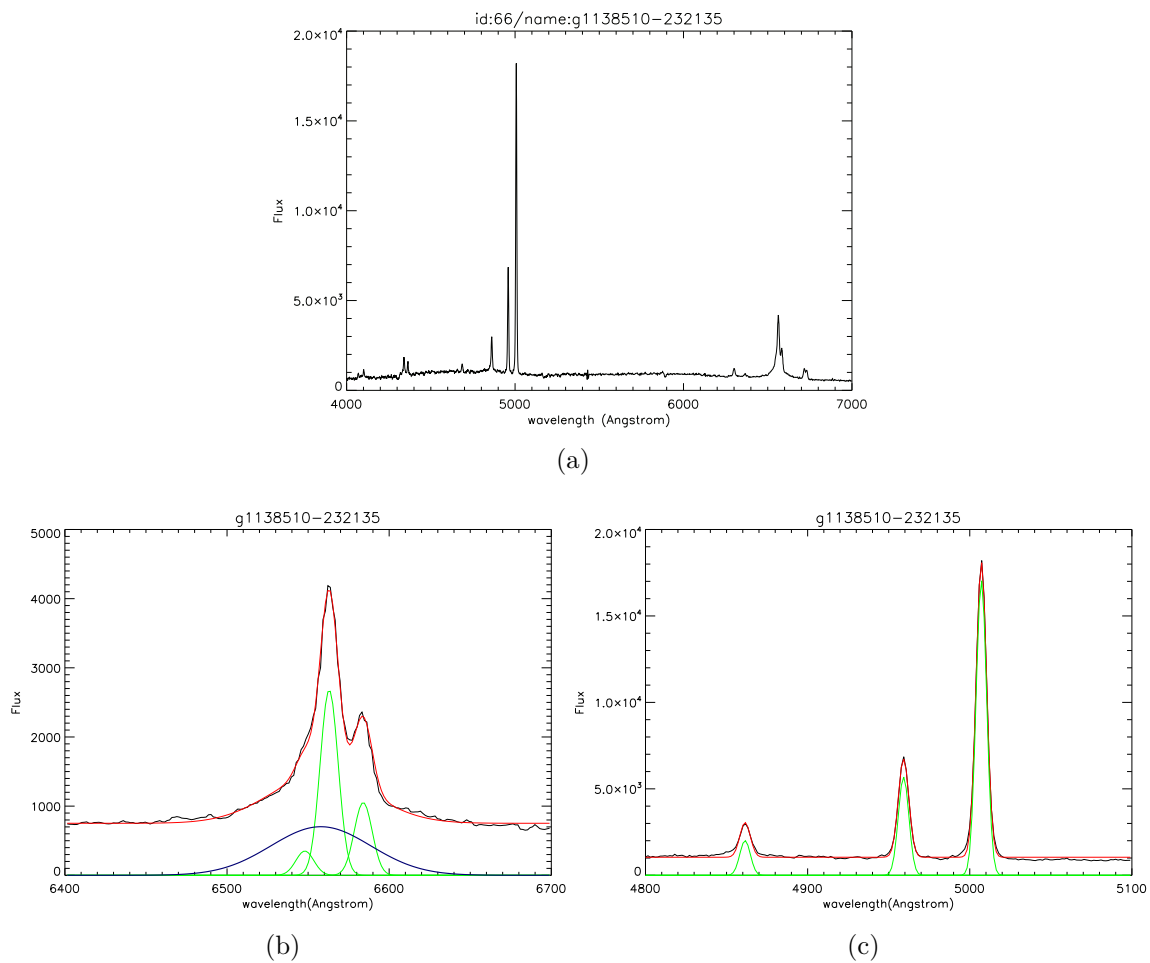


Figure A.36: (a) The optical spectrum of g1138510-232135 source observed by 6dFGS and (b) Fitting of lines H $\alpha$   $\lambda$  6562Å and [N II], (c) H $\beta$   $\lambda$  4861Å and [O III].



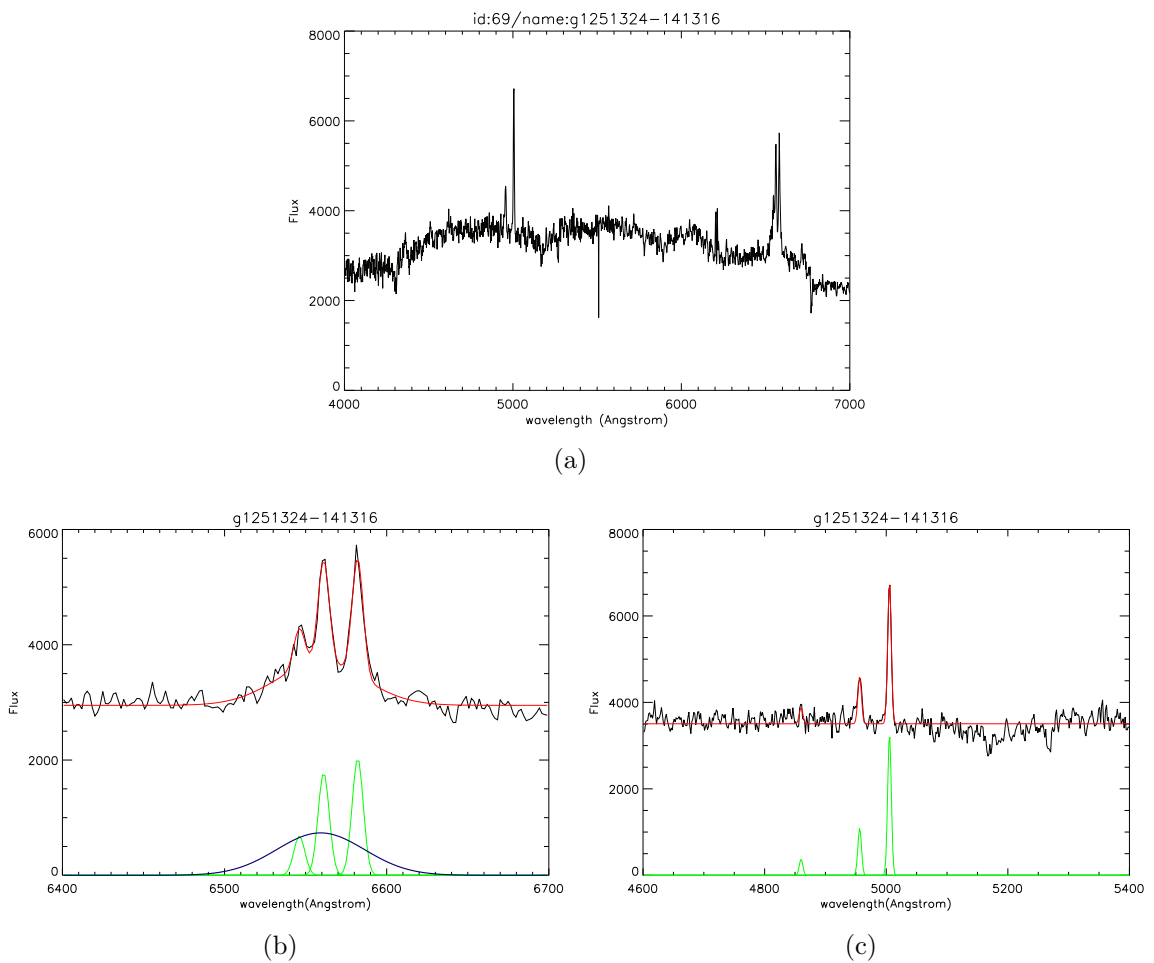


Figure A.37: (a) The optical spectrum of g1251324-141316 source observed by 6dFGS and (b) Fitting of lines H $\alpha$   $\lambda$  6562 $\text{\AA}$  and [N II], (c) H $\beta$   $\lambda$  4861 $\text{\AA}$  and [O III].

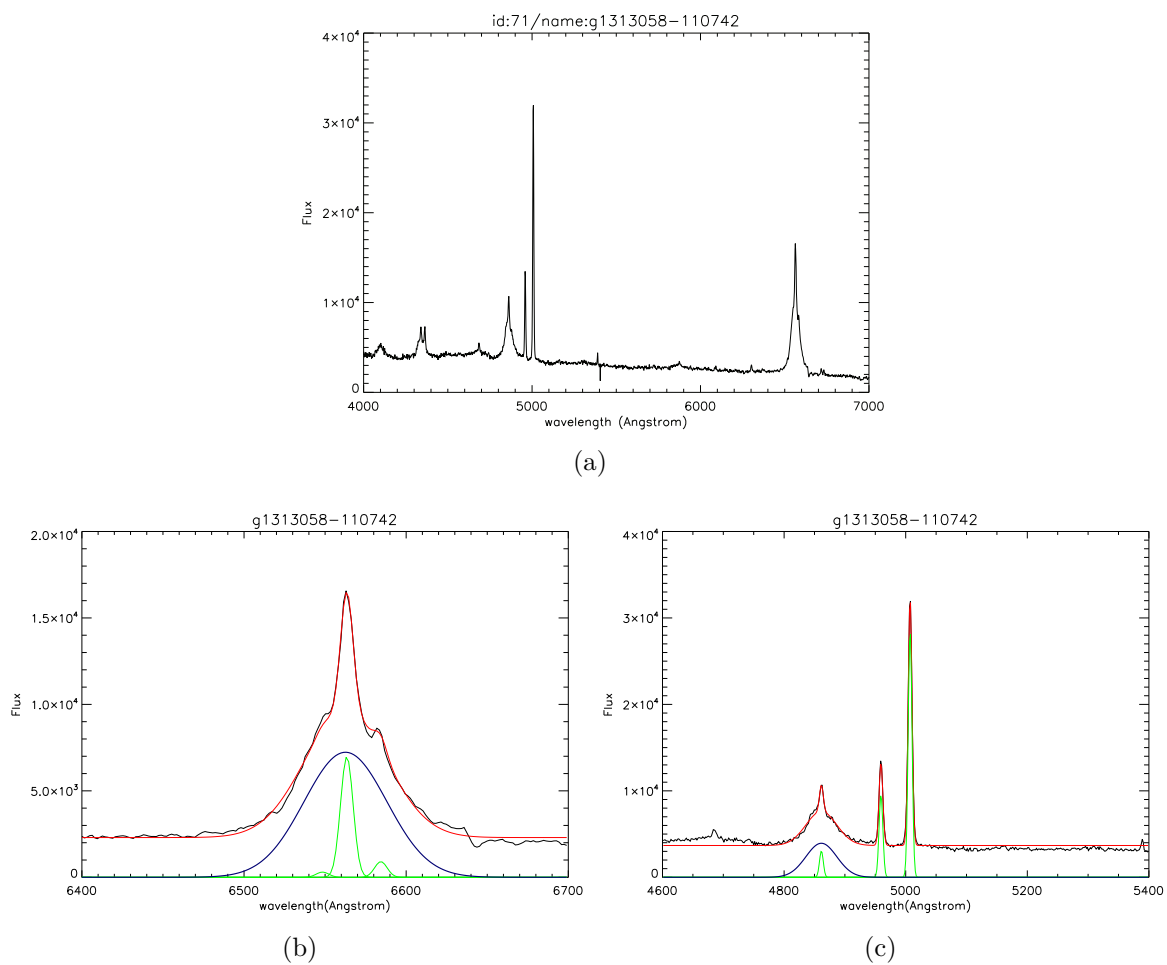


Figure A.38: (a) The optical spectrum of g1313058-110742 source observed by 6dFGS and (b) Fitting of lines  $H\alpha$   $\lambda$  6562Å and  $[N_{II}]$ , (c)  $H\beta$   $\lambda$  4861Å and  $[O_{III}]$ .

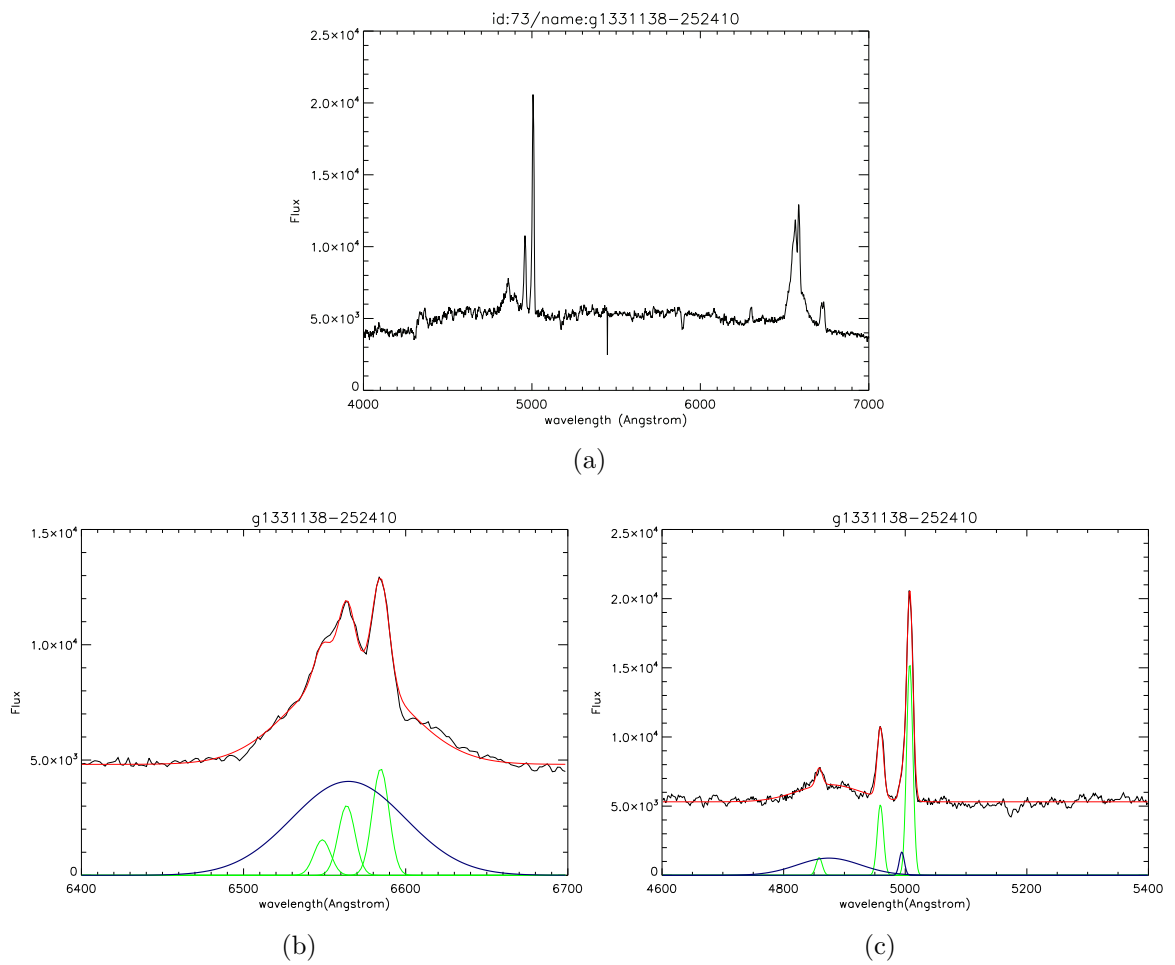


Figure A.39: (a) The optical spectrum of g1331138-252410 source observed by 6dFGS and (b) Fitting of lines  $H\alpha$   $\lambda$  6562Å and  $[N\text{II}]$ , (c)  $H\beta$   $\lambda$  4861Å and  $[O\text{III}]$ .

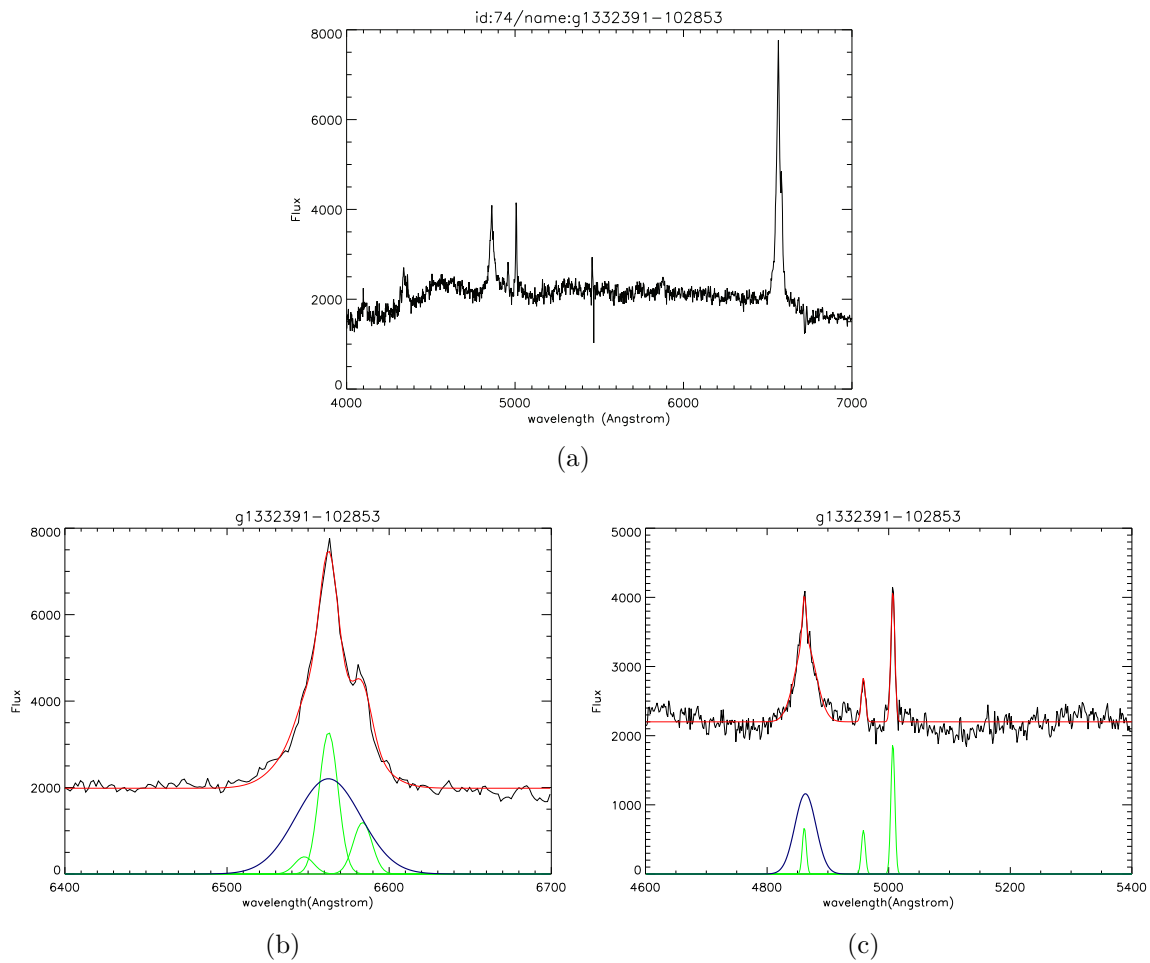


Figure A.40: (a) The optical spectrum of g1332391-102853 source observed by 6dFGS and (b) Fitting of lines  $H\alpha$   $\lambda$  6562Å and [N II], (c)  $H\beta$   $\lambda$  4861Å and [O III].

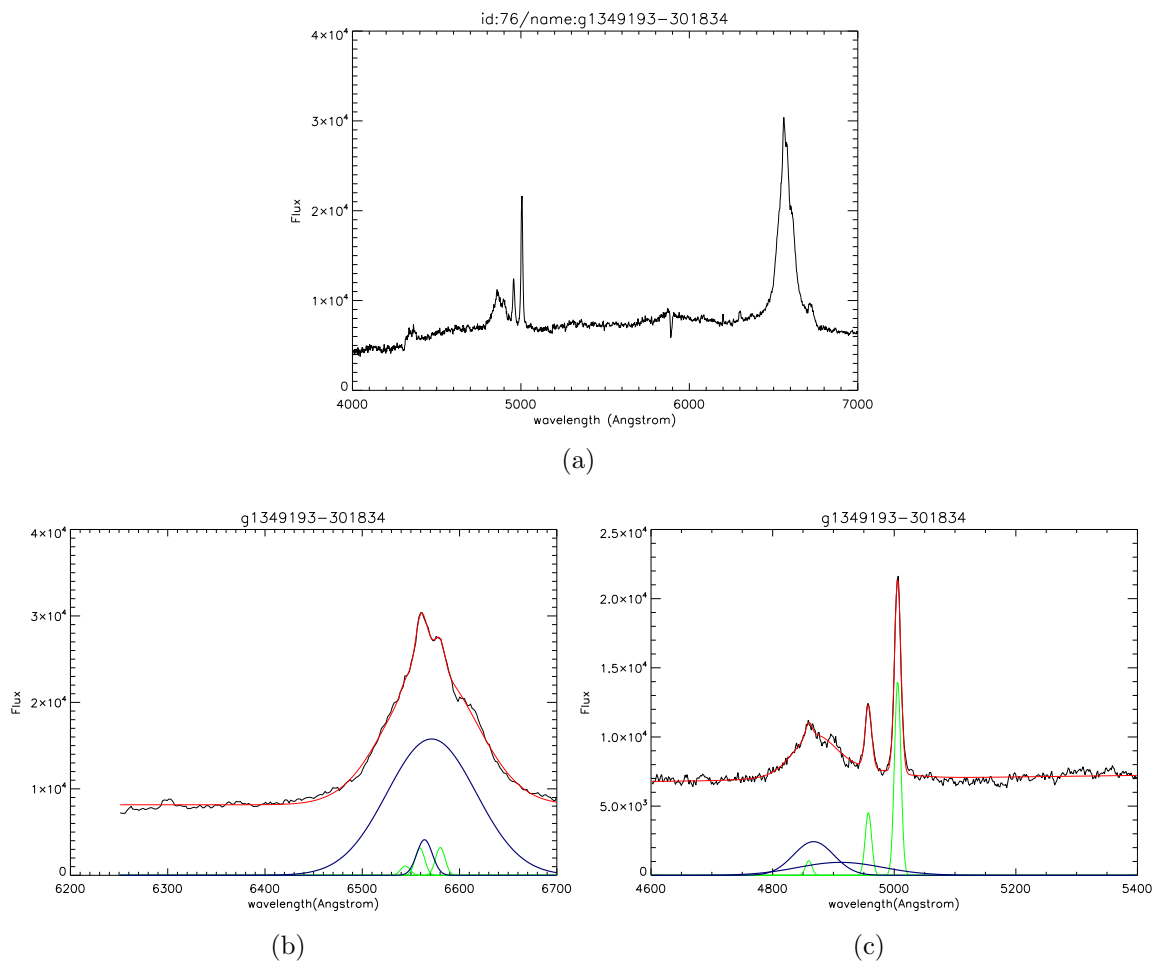


Figure A.41: (a) The optical spectrum of g1349193-301834 source observed by 6dFGS and (b) Fitting of lines H $\alpha$   $\lambda$  6562 $\text{\AA}$  and [N II], (c) H $\beta$   $\lambda$  4861 $\text{\AA}$  and [O III].

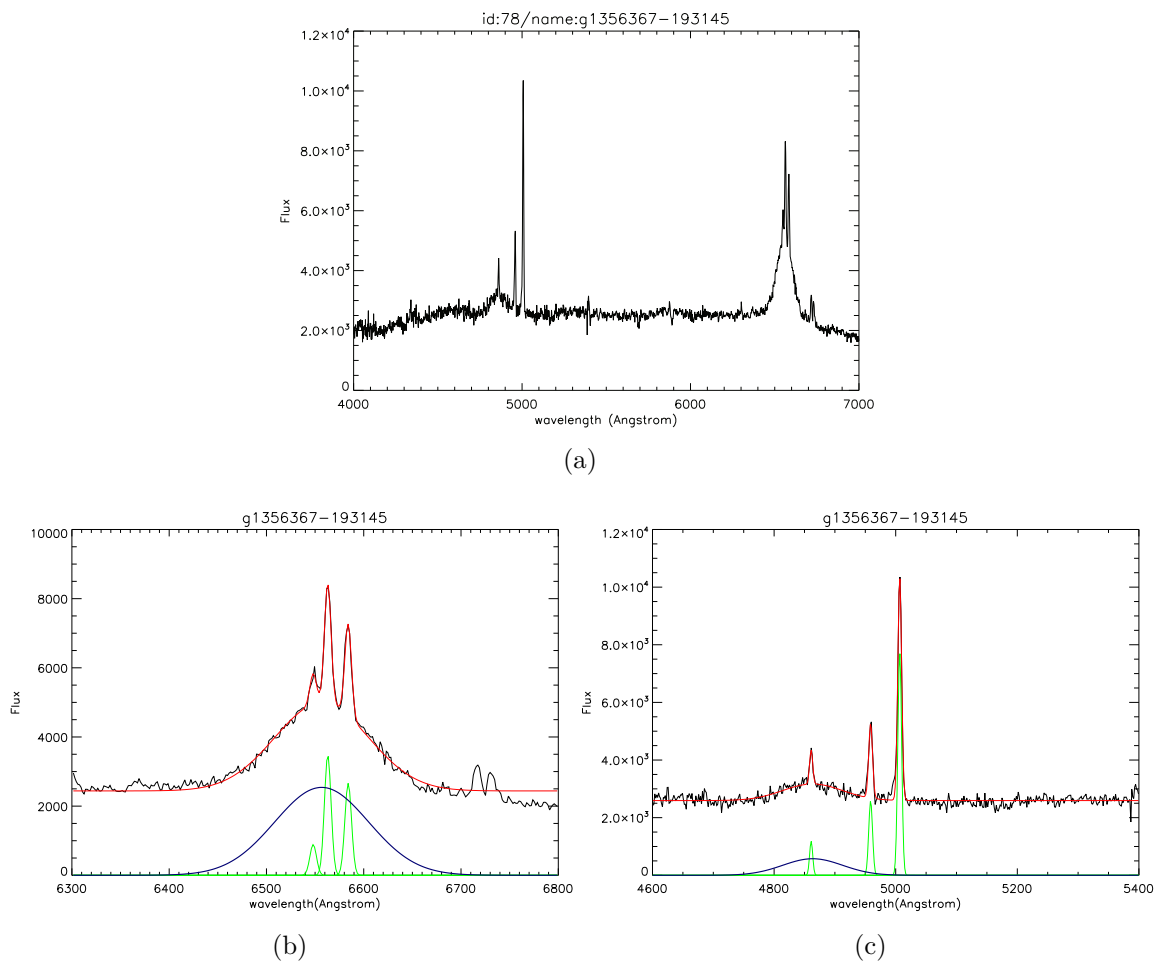


Figure A.42: (a) The optical spectrum of g1356367-193145 source observed by 6dFGS and (b) Fitting of lines  $H\alpha$   $\lambda$  6562Å and  $[N_{II}]$ , (c)  $H\beta$   $\lambda$  4861Å and  $[O_{III}]$ .

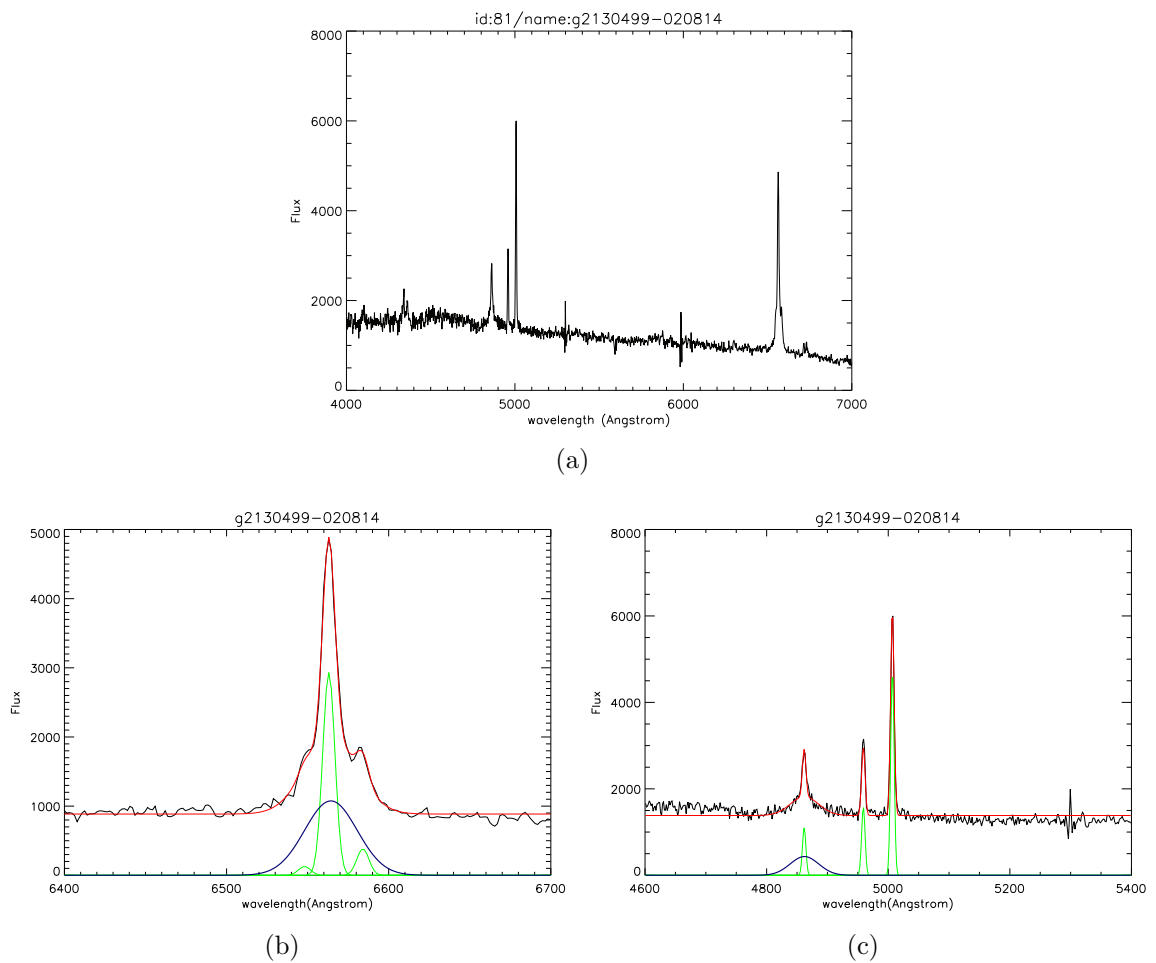


Figure A.43: (a) The optical spectrum of g2130499-020814 source observed by 6dFGS and (b) Fitting of lines H $\alpha$   $\lambda$  6562Å and [N II], (c) H $\beta$   $\lambda$  4861Å and [O III].

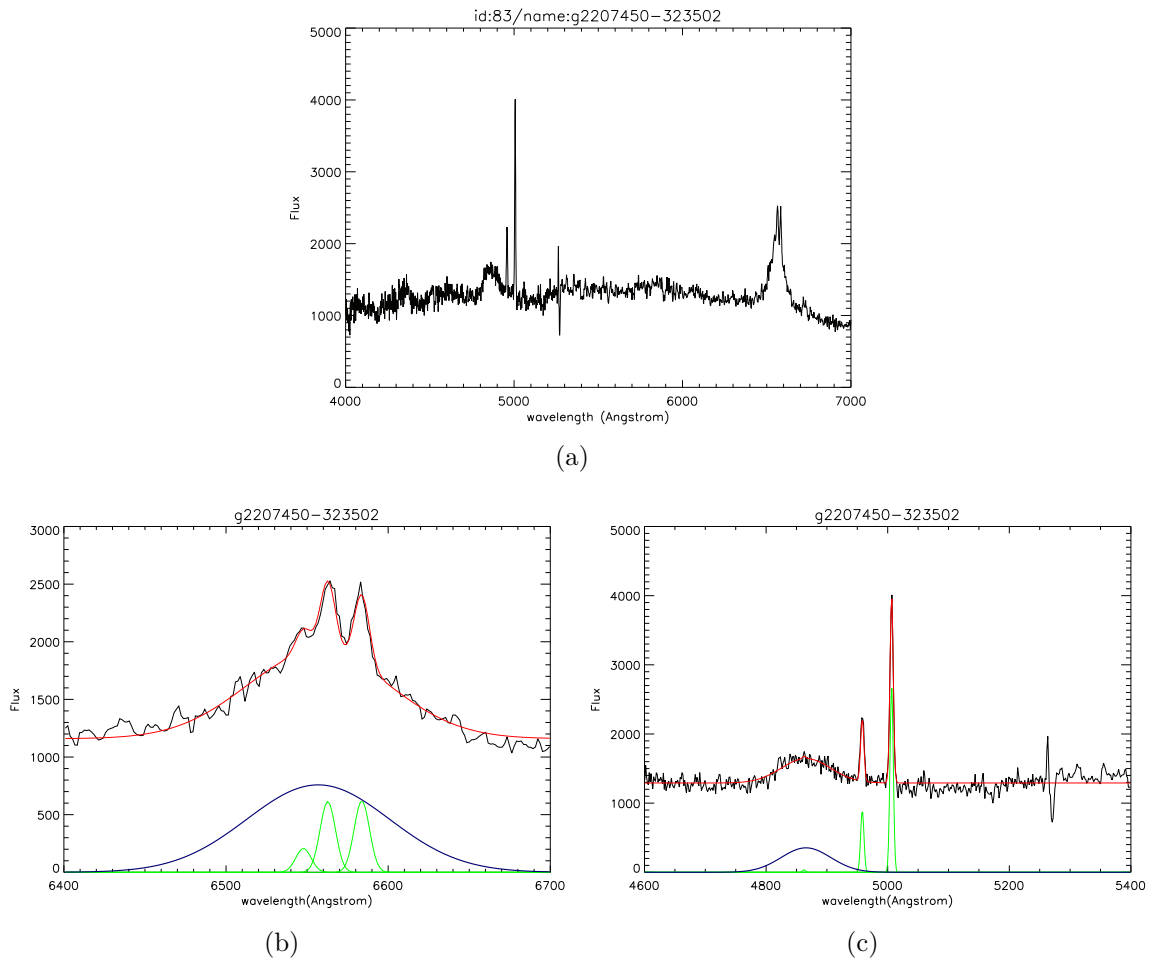


Figure A.44: (a) The optical spectrum of g2207450-323502 source observed by 6dFGS and (b) Fitting of lines H $\alpha$   $\lambda$  6562 $\text{\AA}$  and [NII], (c) H $\beta$   $\lambda$  4861 $\text{\AA}$  and [OIII].



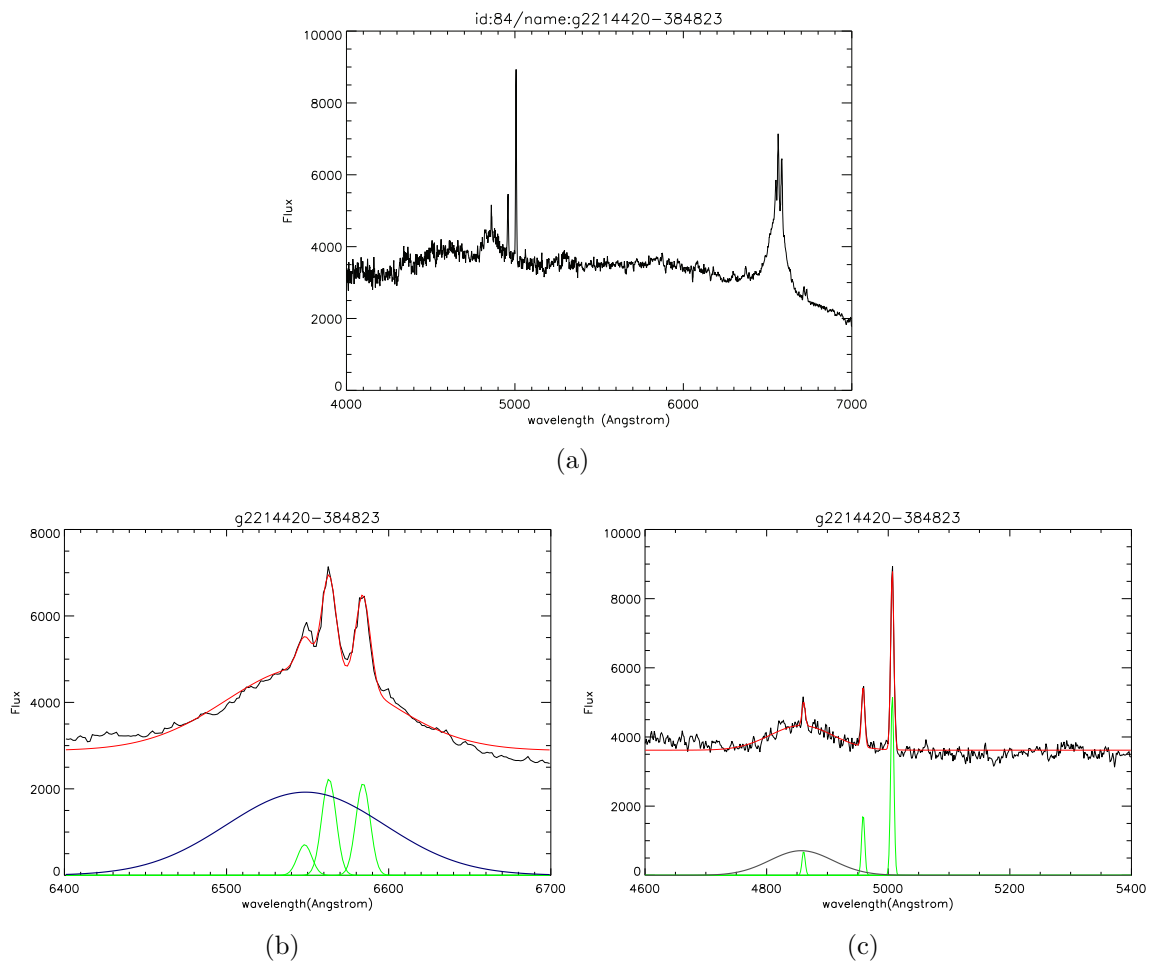
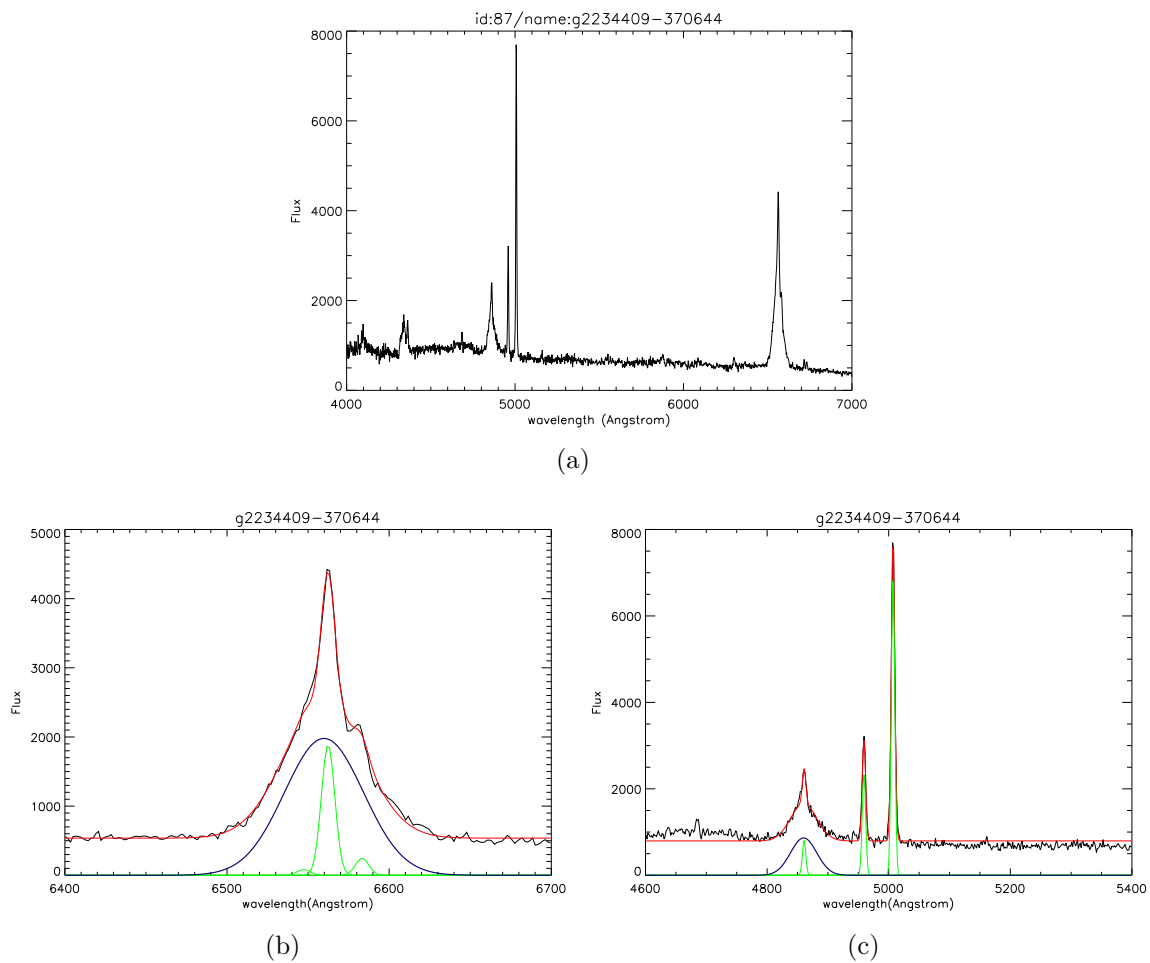


Figure A.45: (a) The optical spectrum of g2214420-384823 source observed by 6dFGS and (b) Fitting of lines  $H\alpha \lambda 6562\text{\AA}$  and  $[N\text{II}]$ , (c)  $H\beta \lambda 4861\text{\AA}$  and  $[O\text{III}]$ .



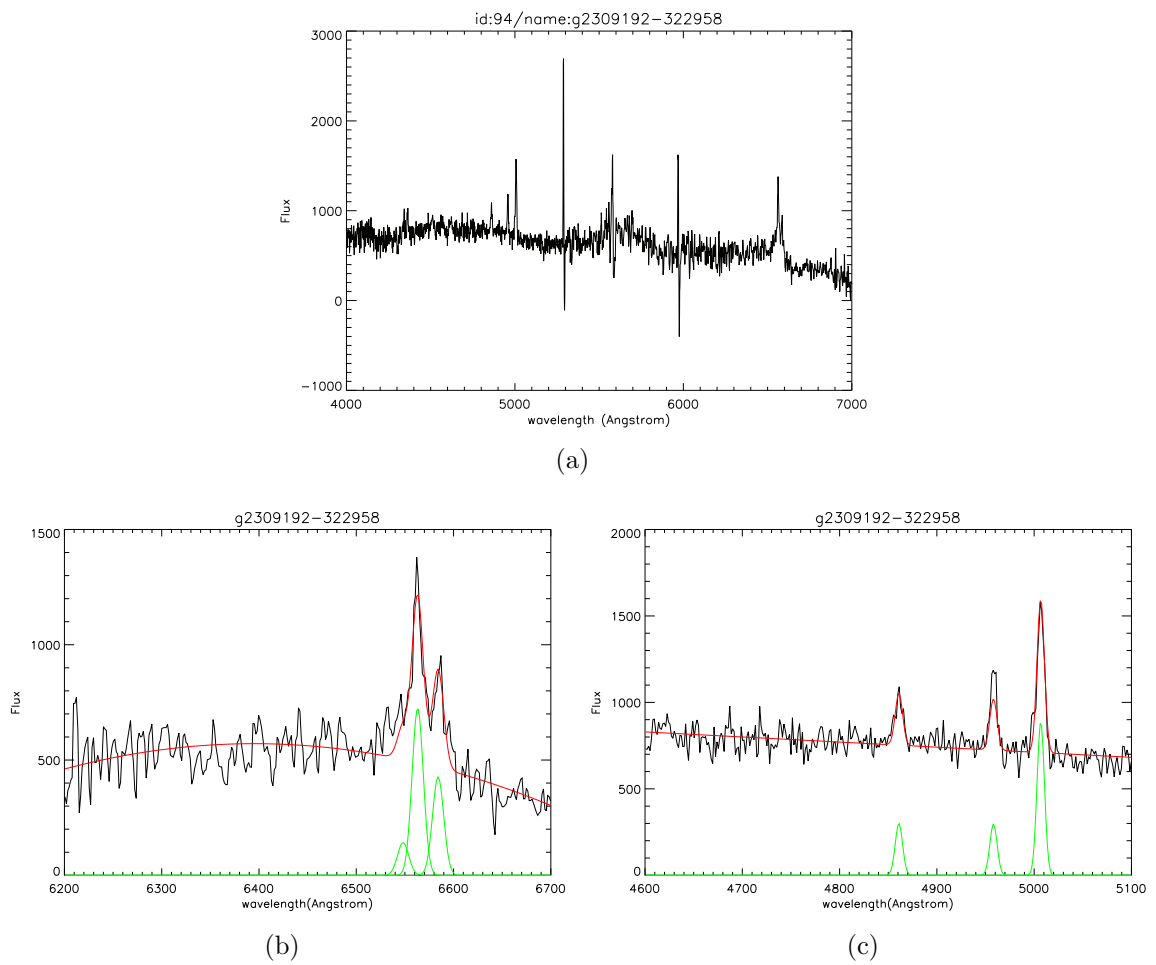


Figure A.47: (a) The optical spectrum of g2309192-322958 source observed by 6dFGS and (b) Fitting of lines H $\alpha$   $\lambda$  6562 $\text{\AA}$  and [N II], (c) H $\beta$   $\lambda$  4861 $\text{\AA}$  and [O III].

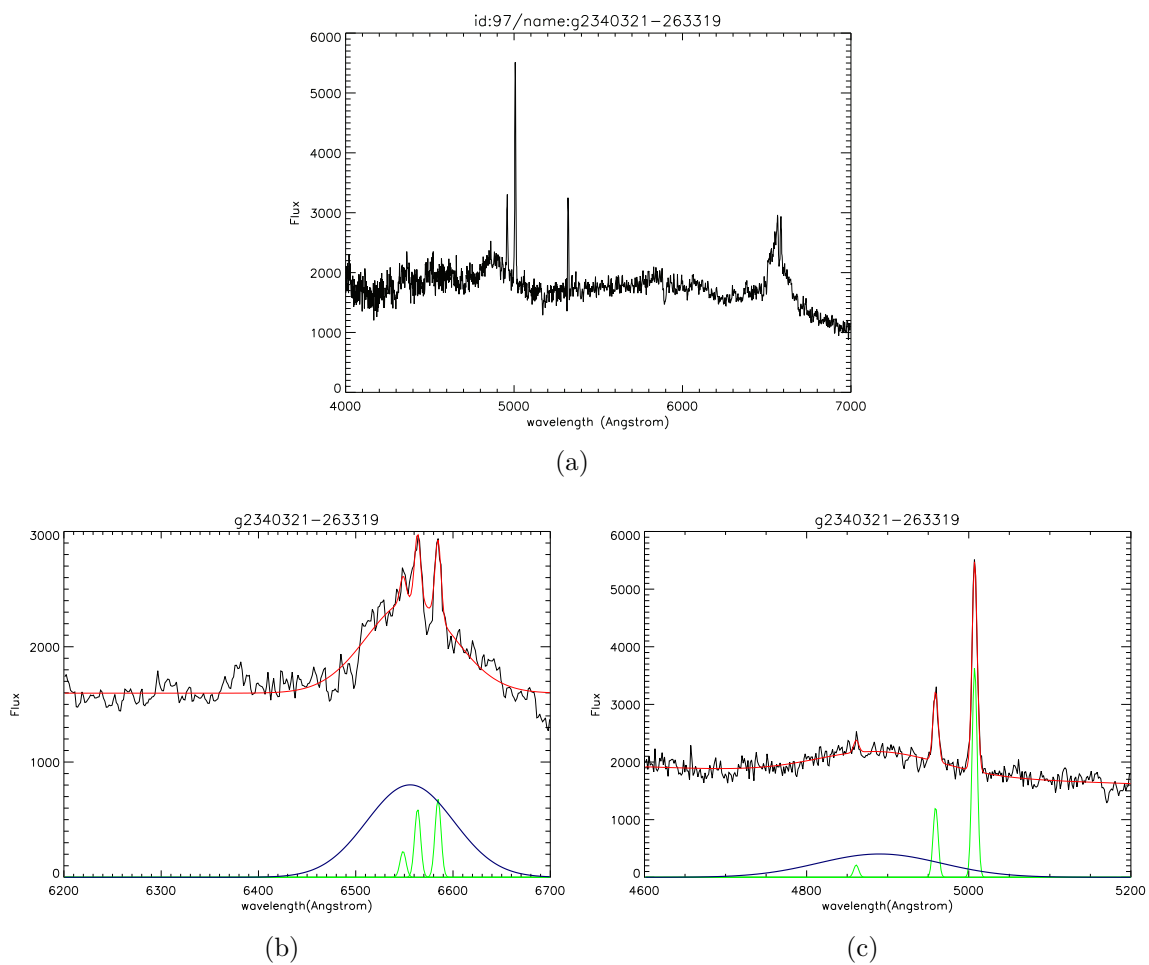


Figure A.48: (a) The optical spectrum of g2340321-263319 source observed by 6dFGS and (b) Fitting of lines H $\alpha$   $\lambda$  6562 $\text{\AA}$  and [N II], (c) H $\beta$   $\lambda$  4861 $\text{\AA}$  and [O III].

# Bibliography

- Allington-Smith, J. & Content, R. 1998, PASP, 110, 1216
- Allington-Smith, J. R., Content, R., Haynes, R., & Lewis, I. J. 1997, in Society of Photo-Optical Instrumentation Engineers (SPIE) Conference Series, Vol. 2871, Society of Photo-Optical Instrumentation Engineers (SPIE) Conference Series, ed. A. L. Ardeberg, 1284–1294
- Antonucci, R. 1993, ARA&A, 31, 473
- Ashby, D. S., Kern, J., Hill, J. M., et al. 2008, in Presented at the Society of Photo-Optical Instrumentation Engineers (SPIE) Conference, Vol. 7018, Society of Photo-Optical Instrumentation Engineers (SPIE) Conference Series
- Babcock, H. D. 1924, Nature, 114, 276
- Babcock, H. W. 1953, PASP, 65, 229
- Babcock, H. W. 1990, Science, 249, 253
- Bacon, R., Adam, G., Baranne, A., et al. 1995, A&AS, 113, 347
- Baldwin, J. A., Phillips, M. M., & Terlevich, R. 1981, PASP, 93, 5
- Baldwin, J. E., Beckett, M. G., Boysen, R. C., et al. 1996, A&A, 306, L13+
- Banse, K., Crane, P., Grosbol, P., et al. 1983, The Messenger, 31, 26
- Barth, A. J. & Shields, J. C. 2000, PASP, 112, 753
- Beckers, J. M. 1993, ARA&A, 31, 13
- Beckers, J. M. & Merkle, F. 1989, Ap&SS, 160, 345
- Bertram, T., Baumeister, H., Laun, W., et al. 2006, in Presented at the Society of Photo-Optical Instrumentation Engineers (SPIE) Conference, Vol. 6268, Society of Photo-Optical Instrumentation Engineers (SPIE) Conference Series
- Bertram, T., Eckart, A., Fischer, S., et al. 2007, A&A, 470, 571
- Bertram, T., Eckart, A., Lindhorst, B., et al. 2008, in Presented at the Society of Photo-Optical Instrumentation Engineers (SPIE) Conference, Vol. 7013, Society of Photo-Optical Instrumentation Engineers (SPIE) Conference Series
- Bertram, T., Straubmeier, C., Rost, S., & Eckart, A. 2005, Astronomische Nachrichten, 326, 560

- Binney, J. & Merrifield, M. 1998, Galactic astronomy, ed. Binney, J. & Merrifield, M.
- Blandford, R. D., Netzer, H., Woltjer, L., Courvoisier, T., & Mayor, M., eds. 1990, Active Galactic Nuclei
- Brown, R. H. 1964, *Nature*, 201, 1111
- Brown, R. H. & Twiss, R. Q. 1957, *Royal Society of London Proceedings Series A*, 242, 300
- Burki, G., Rufener, F., Burnet, M., et al. 1995, *The Messenger*, 80, 34
- Buscher, D. 1988, *MNRAS*, 235, 1203
- Buscher, D. F., Baldwin, J. E., Warner, P. J., & Haniff, C. A. 1990, *MNRAS*, 245, 7P
- Carroll, S. M., Press, W. H., & Turner, E. L. 1992, *ARA&A*, 30, 499
- Chen, K. & Halpern, J. 1989, *News Letter of the Astronomical Society of New York*, 3, 19
- Clavel, J., Boksenberg, A., Bromage, G. E., et al. 1990, *MNRAS*, 246, 668
- Colina, L., Borne, K., Bushouse, H., et al. 2001, *ApJ*, 563, 546
- Colina, L., Lipari, S., & Macchetto, F. 1991, *ApJ*, 382, L63
- Colless, M., Dalton, G., Maddox, S., et al. 2007, *VizieR Online Data Catalog*, 7250, 0
- Colless, M., The 2DF Galaxy Redshift Survey Team, Ellis, R., et al. 1999, in *Looking Deep in the Southern Sky*, ed. R. Morganti & W. J. Couch, 9–+
- Content, R. 1997, in *Society of Photo-Optical Instrumentation Engineers (SPIE) Conference Series*, Vol. 2871, Society of Photo-Optical Instrumentation Engineers (SPIE) Conference Series, ed. A. L. Ardeberg, 1295–1305
- Cox, A. N. 2000, *Allen’s astrophysical quantities*, ed. Cox, A. N.
- Dekker, H., D’Odorico, S., Kaufer, A., Delabre, B., & Kotzlowski, H. 2000, in *Society of Photo-Optical Instrumentation Engineers (SPIE) Conference Series*, Vol. 4008, Society of Photo-Optical Instrumentation Engineers (SPIE) Conference Series, ed. M. Iye & A. F. Moorwood, 534–545
- Dierickx, P., Enard, D., Merkle, F., Noethe, L., & Wilson, R. N. 1988, in *Very Large Telescopes and their Instrumentation*, Vol. 1, Vol. 1, 487–493
- Dimitrijević, M. S., Popović, L. Č., Kovačević, J., Dačić, M., & Ilić, D. 2007, *MNRAS*, 374, 1181
- Diolaiti, E., Conan, J., Foppiani, I., et al. 2010, in *SF2A-2010: Proceedings of the Annual meeting of the French Society of Astronomy and Astrophysics*. Eds.: S. Boissier, M. Heydari-Malayeri, R. Samadi and D. Valls-Gabaud, p.63, ed. S. Boissier, M. Heydari-Malayeri, R. Samadi, & D. Valls-Gabaud, 63–+
- Dopita, M. 1997, *PASA*, 14, 230
- Dopita, M. A. & Sutherland, R. S. 1995, *ApJ*, 455, 468

- Emsellem, E. 2001, in *Astronomical Society of the Pacific Conference Series*, Vol. 249, *The Central Kiloparsec of Starbursts and AGN: The La Palma Connection*, ed. J. H. Knapen, J. E. Beckman, I. Shlosman, & T. J. Mahoney, 91–+
- Englmaier, P. & Shlosman, I. 2000, *ApJ*, 528, 677
- Fabricant, D., Fata, R., Roll, J., et al. 2005, *PASP*, 117, 1411
- Fanaroff, B. L. & Riley, J. M. 1974, *MNRAS*, 167, 31P
- Fath, E. A. 1909, *Lick Observatory Bulletin*, 5, 71
- Filippenko, A. V. & Terlevich, R. 1992, *ApJ*, 397, L79
- Fried, D. L. 1966, *Journal of the Optical Society of America (1917-1983)*, 56, 1380
- Gaessler, W., Bertram, T., Briegel, F., et al. 2004, in , 10
- Gebhardt, K., Bender, R., Bower, G., et al. 2000, *ApJ*, 539, L13
- Genzel, R., Tacconi, L. J., Rigopoulou, D., Lutz, D., & Tecza, M. 2001, *ApJ*, 563, 527
- Giavalisco, M., Livio, M., Bohlin, R. C., Macchetto, F. D., & Stecher, T. P. 1996, *AJ*, 112, 369
- Grosbøl, P. & Ponz, D. 1990, in *Acquisition, Processing and Archiving of Astronomical Images*, ed. G. Longo & G. Sedmak, 111–123
- Hadden, D. E. 1895, *Popular Astronomy*, 3, 84
- Halpern, J. P. 1990, *ApJ*, 365, L51
- Hamilton, A. J. S. 1998, in *Astrophysics and Space Science Library*, Vol. 231, *The Evolving Universe*, ed. D. Hamilton, 185–+
- Haniff, C. 2007, *The Observatory*, 127, 140
- Hardy, J. W. 1998, *Adaptive Optics for Astronomical Telescopes*, ed. Hardy, J. W.
- Häring, N. & Rix, H. 2004, *ApJ*, 604, L89
- Heckman, T. M. 1980, *A&A*, 87, 152
- Heckman, T. M., Miley, G. K., van Breugel, W. J. M., & Butcher, H. R. 1980, in *Bulletin of the American Astronomical Society*, Vol. 12, *Bulletin of the American Astronomical Society*, 809–+
- Herbst, T. M., Ragazzoni, R., Eckart, A., & Weigelt, G. 2004, in , 1045–1052
- Herbst, T. M., Ragazzoni, R., Eckart, A., & Weigelt, G. 2010, in *Presented at the Society of Photo-Optical Instrumentation Engineers (SPIE) Conference*, Vol. 7734, *Society of Photo-Optical Instrumentation Engineers (SPIE) Conference Series*
- Hernandez, G. 1986, *S&T*, 72, 363

- Hill, J. M., Green, R. F., Ashby, D. S., et al. 2010, in Presented at the Society of Photo-Optical Instrumentation Engineers (SPIE) Conference, Vol. 7733, Society of Photo-Optical Instrumentation Engineers (SPIE) Conference Series
- Ho, L. C., Filippenko, A. V., & Sargent, W. L. W. 1993, *ApJ*, 417, 63
- Ho, L. C., Filippenko, A. V., & Sargent, W. L. W. 2003, *ApJ*, 583, 159
- Ho, L. C., Filippenko, A. V., Sargent, W. L. W., & Peng, C. Y. 1997, *ApJS*, 112, 391
- Hopkins, P. F., Hernquist, L., Martini, P., et al. 2005, *ApJ*, 625, L71
- Horne, K. 1986, *PASP*, 98, 609
- Horrobin, M., Eckart, A., Lindhorst, B., et al. 2010, in Presented at the Society of Photo-Optical Instrumentation Engineers (SPIE) Conference, Vol. 7734, Society of Photo-Optical Instrumentation Engineers (SPIE) Conference Series
- Huchra, J. P. 1977, *ApJ*, 217, 928
- Hutchings, J. B. & Morris, S. C. 1995, *AJ*, 109, 1541
- Johnson, M. A., Betz, A. L., & Townes, C. H. 1974, *Physical Review Letters*, 33, 1617
- Jones, D. H., Read, M. A., Saunders, W., et al. 2009, *MNRAS*, 399, 683
- Jones, D. H., Saunders, W., Colless, M., et al. 2004, *MNRAS*, 355, 747
- Karttunen, H., Krüger, P., Oja, H., Poutanen, M., & Donner, K. J., eds. 2007, *Fundamental Astronomy*
- Kauffmann, G., Heckman, T. M., Tremonti, C., et al. 2003, *MNRAS*, 346, 1055
- Kewley, L. J., Dopita, M. A., Sutherland, R. S., Heisler, C. A., & Trevena, J. 2001, *ApJ*, 556, 121
- Kewley, L. J., Groves, B., Kauffmann, G., & Heckman, T. 2006, *MNRAS*, 372, 961
- Khachikian, E. Y. & Weedman, D. W. 1974, *ApJ*, 192, 581
- Kitchin, C. R. 1996, *Astronomische Nachrichten*, 317, 422
- Knapen, J. H. 2005, in American Institute of Physics Conference Series, Vol. 783, *The Evolution of Starbursts*, ed. S. Hüttmeister, E. Manthey, D. Bomans, & K. Weis, 171–181
- Koehler, T., Groote, D., Reimers, D., & Wisotzki, L. 1997, *A&A*, 325, 502
- Kolmogorov, A. 1941, *Akademiia Nauk SSSR Doklady*, 30, 301
- König, S., Eckart, A., García-Marín, M., & Huchtmeier, W. K. 2009, *A&A*, 507, 757
- Kormendy, J. & Richstone, D. 1995, *ARA&A*, 33, 581
- Kormendy, J. & Sanders, D. B. 1992, *ApJ*, 390, L53
- Koski, A. T. 1978, *ApJ*, 223, 56



- Labeyrie, A. 1970, *A&A*, 6, 85
- Lehnert, M. D., Nesvadba, N. P. H., Cuby, J., et al. 2010, *Nature*, 467, 940
- Lightman, A. P., Press, W. H., Price, R. H., & Teukolsky, S. A. 1975, *Problem book in relativity and gravitation*, ed. Lightman, A. P., Press, W. H., Price, R. H., & Teukolsky, S. A.
- Lípari, S., Mediavilla, E., Garcia-Lorenzo, B., et al. 2004, *MNRAS*, 355, 641
- Llebaria, A. & Martinis, J. 1990, in *European Southern Observatory Conference and Workshop Proceedings*, Vol. 34, *European Southern Observatory Conference and Workshop Proceedings*, ed. D. Baade & P. J. Grosbol, 89–+
- Lutz, D., Veilleux, S., & Genzel, R. 1999, *ApJ*, 517, L13
- Maciejewski, W. 2004, in *IAU Symposium*, Vol. 222, *The Interplay Among Black Holes, Stars and ISM in Galactic Nuclei*, ed. T. Storchi-Bergmann, L. C. Ho, & H. R. Schmitt, 431–434
- Magorrian, J., Tremaine, S., Richstone, D., et al. 1998, *AJ*, 115, 2285
- Mandel, H., Seifert, W., Hofmann, R., et al. 2008, in *Presented at the Society of Photo-Optical Instrumentation Engineers (SPIE) Conference*, Vol. 7014, *Society of Photo-Optical Instrumentation Engineers (SPIE) Conference Series*
- Maoz, D., Koratkar, A., Shields, J. C., et al. 1998, *AJ*, 116, 55
- Maoz, D., Netzer, H., Mazeh, T., et al. 1991, *ApJ*, 367, 493
- Martini, P., Regan, M. W., Mulchaey, J. S., & Pogge, R. W. 2003, *ApJ*, 589, 774
- Matthews, T. A. & Sandage, A. R. 1963, *ApJ*, 138, 30
- Michelson, A. A. 1891, *PASP*, 3, 274
- Michelson, A. A. & Pease, F. G. 1921, *ApJ*, 53, 249
- Oke, J. B. 1990, *AJ*, 99, 1621
- Orr, M. J. L. & Browne, I. W. A. 1982, *MNRAS*, 200, 1067
- Osterbrock, D. E. 1981, *ApJ*, 249, 462
- Osterbrock, D. E. 1989, *Astrophysics of gaseous nebulae and active galactic nuclei*, ed. Osterbrock, D. E.
- Padovani, P. 1997, *Mem. Soc. Astron. Italiana*, 68, 47
- Parker, Q. A., Miziarski, S., & Watson, F. G. 1998, *IAU Commission on Instruments*, 10, 17
- Parker, Q. A. & Watson, F. 2000, *IAU Commission on Instruments*, 12, 5
- Perez, E., Mediavilla, E., Penston, M. V., Tadhunter, C., & Moles, M. 1988, *MNRAS*, 230, 353
- Peterson, B. M. 1997, *An Introduction to Active Galactic Nuclei*, ed. Peterson, B. M.
- Peterson, B. M., Balonek, T. J., Barker, E. S., et al. 1991, *ApJ*, 368, 119

- Peterson, B. M., Pogge, R. W., Wanders, I., Smith, S. M., & Romanishin, W. 1995, *PASP*, 107, 579
- Pogge, R. W., Atwood, B., Brewer, D. F., et al. 2010, in Presented at the Society of Photo-Optical Instrumentation Engineers (SPIE) Conference, Vol. 7735, Society of Photo-Optical Instrumentation Engineers (SPIE) Conference Series
- Ragazzoni, R. 2000, in European Southern Observatory Conference and Workshop Proceedings, Vol. 57, European Southern Observatory Conference and Workshop Proceedings, ed. T. Andersen, A. Ardeberg, & R. Gilmozzi, 175–+
- Ragazzoni, R., Marchetti, E., & Rigaut, F. 1999, *A&A*, 342, L53
- Rees, M. J. 1984, *ARA&A*, 22, 471
- Reimers, D., , T., & Wisotzki, L. 1996, *A&A*, 115, 235
- Ridgway, S. T. & Hinkle, K. H. 2010, in Society of Photo-Optical Instrumentation Engineers (SPIE) Conference Series, Vol. 7735, Society of Photo-Optical Instrumentation Engineers (SPIE) Conference Series
- Ritchey, G. W. 1928, *JRASC*, 22, 207
- Roddier, C. & Roddier, F. 1993, *Journal of the Optical Society of America A*, 10, 2277
- Roddier, F. 1999, *Adaptive optics in astronomy*, ed. Roddier, F.
- Rogers, C. 1989, *JRASC*, 83, 345
- Roggemann, M. C., Bright, V. M., Welsh, B. M., et al. 1997, in Presented at the Society of Photo-Optical Instrumentation Engineers (SPIE) Conference, Vol. 3126, Society of Photo-Optical Instrumentation Engineers (SPIE) Conference Series, ed. R. K. Tyson & R. Q. Fugate, 173–+
- Rost, S., Bertram, T., Lindhorst, B., et al. 2008, in Presented at the Society of Photo-Optical Instrumentation Engineers (SPIE) Conference, Vol. 7013, Society of Photo-Optical Instrumentation Engineers (SPIE) Conference Series
- Rost, S., Eckart, A., Horrobin, M., et al. 2010, in Presented at the Society of Photo-Optical Instrumentation Engineers (SPIE) Conference, Vol. 7734, Society of Photo-Optical Instrumentation Engineers (SPIE) Conference Series
- Rowan-Robinson, M. 1977, *ApJ*, 213, 635
- Rupke, D., Veilleux, S., Kim, D., et al. 2007, in *Astronomical Society of the Pacific Conference Series*, Vol. 373, *The Central Engine of Active Galactic Nuclei*, ed. L. C. Ho & J.-W. Wang, 525–+
- Sanders, D. B., Soifer, B. T., Elias, J. H., et al. 1988a, *ApJ*, 325, 74
- Sanders, D. B., Soifer, B. T., Elias, J. H., Neugebauer, G., & Matthews, K. 1988b, *ApJ*, 328, L35
- Sarazin, M. & Roddier, F. 1990, *A&A*, 227, 294

- Saunders, W., Parker, Q., Watson, F., et al. 2001, *Anglo-Australian Observatory Epping Newsletter*, 97, 14
- Scheuer, P. A. G. & Readhead, A. C. S. 1979, *Nature*, 277, 182
- Schinnerer, E., Eckart, A., Tacconi, L. J., Genzel, R., & Downes, D. 2000, *ApJ*, 533, 850
- Schmidt, M. 1969, *ARA&A*, 7, 527
- Schmidt, M. & Green, R. F. 1983, *ApJ*, 269, 352
- Schulze, A. & Wisotzki, L. 2010, *A&A*, 516, A87+
- Schulze, A., Wisotzki, L., & Husemann, B. 2009, *A&A*, 507, 781
- Seyfert, C. K. 1943, *ApJ*, 97, 28
- Shields, G. A. 1978, *Nature*, 272, 706
- Shields, J. C. 1992, *ApJ*, 399, L27
- Shlosman, I., Frank, J., & Begelman, M. C. 1989, *Nature*, 338, 45
- Skrutskie, M. F., Jones, T., Hinz, P., et al. 2010, in Presented at the Society of Photo-Optical Instrumentation Engineers (SPIE) Conference, Vol. 7735, Society of Photo-Optical Instrumentation Engineers (SPIE) Conference Series
- Speziali, R., Di Paola, A., Giallongo, E., et al. 2008, in Presented at the Society of Photo-Optical Instrumentation Engineers (SPIE) Conference, Vol. 7014, Society of Photo-Optical Instrumentation Engineers (SPIE) Conference Series
- Stasińska, G., Cid Fernandes, R., Mateus, A., Sodré, L., & Asari, N. V. 2006, *MNRAS*, 371, 972
- Strassmeier, K. G., Woche, M., Ilyin, I., et al. 2008, in Presented at the Society of Photo-Optical Instrumentation Engineers (SPIE) Conference, Vol. 7014, Society of Photo-Optical Instrumentation Engineers (SPIE) Conference Series
- Strateva, I. V., Brandt, W. N., Eracleous, M., Schneider, D. P., & Chartas, G. 2006, *ApJ*, 651, 749
- Straubmeier, C., Bertram, T., Eckart, A., et al. 2004, in Presented at the Society of Photo-Optical Instrumentation Engineers (SPIE) Conference, Vol. 5491, Society of Photo-Optical Instrumentation Engineers (SPIE) Conference Series, ed. W. A. Traub, 1486–+
- Tallon, M. & Foy, R. 1990, *A&A*, 235, 549
- Tatarskii, V. I. 1971, *The effects of the turbulent atmosphere on wave propagation*, ed. Tatarskii, V. I.
- Traub, W. A. 1986, *Appl. Opt.*, 25, 528
- Tremaine, S., Gebhardt, K., Bender, R., et al. 2002, *ApJ*, 574, 740
- Tremou, E., Eckart, A., Horrobin, M., et al. 2010, in Presented at the Society of Photo-Optical Instrumentation Engineers (SPIE) Conference, Vol. 7734, Society of Photo-Optical Instrumentation Engineers (SPIE) Conference Series

- Tyson, R. K. 1991, in Presented at the Society of Photo-Optical Instrumentation Engineers (SPIE) Conference, Vol. 1542, Society of Photo-Optical Instrumentation Engineers (SPIE) Conference Series, ed. M. A. Ealey, 62–+
- Urry, C. M. & Padovani, P. 1995, *PASP*, 107, 803
- Veilleux, S. & Osterbrock, D. E. 1987a, *ApJS*, 63, 295
- Veilleux, S. & Osterbrock, D. E. 1987b, in NASA Conference Publication, Vol. 2466, NASA Conference Publication, ed. C. J. Lonsdale Persson, 737–740
- Wanders, I., Peterson, B. M., Pogge, R. W., Derobertis, M. M., & van Groningen, E. 1992, *A&A*, 266, 72
- Wisotzki, L., Christlieb, N., Bade, N., et al. 2000, *A&A*, 358, 77
- Wright, E. L. 2006, *PASP*, 118, 1711
- Yu, Q. & Tremaine, S. 2002, *MNRAS*, 335, 965
- Zuther, J., Eckart, A., Bertram, T., et al. 2010, in Presented at the Society of Photo-Optical Instrumentation Engineers (SPIE) Conference, Vol. 7734, Society of Photo-Optical Instrumentation Engineers (SPIE) Conference Series

# List of Acronyms

2DFDR	Two-Degree Field Data Reduction
2dFGRS	Two-Degree Field Galaxy Redshift Survey
2MASS	Two Micron All Sky Survey
6dFGS	Six-Degree Field Galaxy Survey
AAO	Anglo-Australian Observatory
AGN	Active Galactic Nucleus
AO	Adaptive Optics
BH	Black Hole
BLRGs	Broad Line Radio Galaxies
CONICA	High Resolution IR Camera and Spectrometer
CCD	Charge-Coupled Device (detector)
DFOSC	Danish Faint Object Spectrograph and Camera
DM	Deformable Mirror
DPU	Detector Positioning Unit
ESO	European Southern Observatory
FFTS	Fringe Flexure Tracking System
FIR	Far-Infrared
FoV	Field of view
FR I	Fanaroff-Riley Type I
FR II	Fanaroff-Riley Type II
FWHM	Full Width at Half Maximum
GRP	Glass-fibre Reinforced Plastic
GS	Guide Star
GWS	Ground-Layer Wavefront Sensors
HE / HES	Hamburg/ESO survey
HST	Hubble Space Telescope
IDL	Interactive Data Language
IFU	Integral Field Unit
IMBH	Intermediate-mass black hole
ING	Isaac Newton Group of Telescopes
IMF	Initial mass function
IR	Infrared
IRAS	Infrared Astronomical Satellite
ISAAC	Infrared Spectrometer and Array Camera (at the VLT)
ISM	Interstellar medium
LBT	Large Binocular Telescope
LBTI	Large Binocular Telescope Interferometer
LBTO	Large Binocular Telescope Observatory
LGS	Laser Guide Star

---

LINC	LBT iNterferometric Camera
LINERs	Low Ionization Nuclear Emission-line Region
mas	mili-arcsecond
MCAO	Multi Conjugate Adaptive optics
MBH	Massive Black Hole
MHWS	Mid-High-layer Wavefront Sensors
MIR	Mid-Infrared
NACO	NAOS/CONICA adaptive optics device/near-infrared camera at the VLT
NAOS	Nasmyth Adaptive Optics System
NIFS	Near-Infrared Integral Field Spectrometer
NGS	Natural Guide Star
NICMOS	Near Infrared Camera and Multi-Object Spectrometer
NIR	Near-Infrared
NIRVANA	Near-IR/Visible Adaptive iNterferometer for Astronomy
NLRGs	Narrow Line Radio Galaxies
OPD	Optical Path Difference
OVV	Optically Violent Variables
OWL	Overwhelmingly Large
PG	Palomar-Green Bright Quasar Survey
PSF	Point Spread Function
SDSS	Sloan Digital Sky Survey
Sgr A*	Sagittarius A*
SMBH	Supermassive Black Hole
UKST	UK Schmidt Telescope
ULIRGS	Ultra Luminous Infrared Galaxy
UV	Ultraviolet
UVES	Ultraviolet and Visual Echelle Spectrograph
VLA	Very Large Array
VLBA	Very Long Baseline Array
VLT	Very Large Telescope
VISIR	VLT Spectrometer and Imager for the MidInfrared
WHT	William Herschel Telescope
WFS	Wavefront Sensor
WR	Wolf-Rayet

# Acknowledgements

I feel totally urged to acknowledge certain people for their valuable assistance and support during my PhD course. I hope I do not forget anybody and if I do I am sincerely sorry. However, even if somebody is not referred here they have my gratitude.

I begin with my gratitude to my supervisor Professor Dr. A. Eckart for giving me the opportunity to work under his supervision. It is my honour to work with him and be part of his 'aegroup'. Thanks to all members of the entire group.

I am grateful to Professor Dr. A. Zensus for being in my thesis committee and providing me always with constructive and essential comments and guidance. I would like to thank Professor A. Klein for being a member of my defense committee.

I want thank all LINC-NIRVANA Cologne team for the nice collaboration and for the amazing time we had during business trips. I would like to express my special thanks to Dr. T. Bertram, who introduced me to the LINC NIRVANA world. His guidance especially the first months of my PhD course is more than appreciative.

Special thanks and appreciation to Dr. J. Zuther for his constant help and advice all these years. Our endless discussions about both science and instrumentation were always valuable and conducive to me.

I am grateful to all Ph1 secretaries for their assistance to everything from the first days in Germany. Special thanks to Frau S. Krämer and Frau I. Wank for the refreshing breaks during the daily working life.

I should not forget to thank the IMPRS secretaries. The former secretary Frau G. Breuer, who made my life easier during the first days in Germany. Many thanks to the current IMPRS secretary Frau S. Pott for being always there to provide any kind of help.

I would also like to thank all my Cologne friends for the inspirational beers we had. Devy, Kora, Constanza, Nadeen, Momo, Monika, Silvia thank you all guys. Special thanks to Nadeen for reading my thesis and providing me with useful comments. Many thanks to Constanza for all technical discussions we had.

My thanks to the greek 'gang' of Cologne/Bonn for all the nice time we had keeping the greek spirit up. Despo, Kosmas, Jiannis A. and Jiannis N., thank you all mates.

Thanks to all my friends in Greece. Despite the distance, their faithful support is always more than enough. Nancy, Kostas, Vasso K., Thanos, Marietta, Vaios, I miss you all guys. Special thanks to my good friend Nancy for her encouragement and patience and of course many many thanks for her 'colourful' suggestions.

I feel forced to express my gratitude to my diploma supervisor and my mentor Professor J. H. Seiradakis, who is always available and open to any question/problem I face.

It is difficult to express my sincere thankfulness in a piece of paper to the IMPRS Coordinator and my good friend Dr. E. Angelakis, whose endless support, encouragement, guiding from the very beginning are more than appreciated. I cordially thank him for being always there, discussing all my concerns either in science or in daily life.

I am deeply thankful to my advisor and good friend Dr. M. Garcia Marin. First, I would like

to thank her for trusting me. She was always there and willing to help me with all my concerns. Her endless interest in my progress and her encouragement will be unforgettable. Despite the last stressful days, she managed to keep everything under control.

To conclude with, I would like to say thanks to my parents Efthimios and Eleni, for standing always by my side and provide their unconditional support with all possible ways. My appreciation to my brother Dimitris, his wife Maria, and my sister Vivi for their patience all these years. Especially, I want to thank my sister Vivi for solving any of my mathematical questions I encountered. I should not forget my grandparents for their constant encouragement. I love you all. Thanks from the bottom of my heart.

This work was financially supported by the International Max Planck Research School (IMPRS) for Astronomy and Astrophysics at the MPIfR and the Universities of Bonn and Cologne.

This thesis has made use of the Final Release of 6dFGS data ([Jones et al. 2004, 2009](#)). This research has also made use of the NASA/IPAC Extragalactic Database (NED) which is operated by the Jet Propulsion Laboratory, California Institute of Technology, under contract with the National Aeronautics and Space Administration. While studying the current thesis, Ned's Wright calculator was also used ([Wright 2006](#)).



# Erklärung

Ich versichere, daß ich die von mir vorgelegte Dissertation selbständig angefertigt, die benutzten Quellen und Hilfsmittel vollständig angegeben und die Stellen der Arbeit – einschließlich Tabellen, Karten und Abbildungen –, die anderen Werken im Wortlaut oder dem Sinn nach entnommen sind, in jedem Einzelfall als Entlehnung kenntlich gemacht habe; daß diese Dissertation noch keiner anderen Fakultät oder Universität zur Prüfung vorgelegen hat; daß sie – abgesehen von unten angegebenen Teilpublikationen – noch nicht veröffentlicht worden ist sowie, daß ich eine solche Veröffentlichung vor Abschluß des Promotionsverfahrens nicht vornehmen werde. Die Bestimmungen dieser Promotionsordnung sind mir bekannt. Die von mir vorgelegte Dissertation ist von Prof. Dr. Andreas Eckart betreut worden.

Köln, 14. 02. 2011

## Teilpublikationen

- **Tremou, Evangelia**, Eckart, Andreas; Horrobin, Matthew; Lindhorst, Bettina; Moser, Lydia; Rost, Steffen; Smajic, Semir; Straubmeier, Christian; Wank, Imke; Zuther, Jens; Bertram, Thomas:  
“*The LINC-NIRVANA fringe and flexure tracker: laboratory tests*”, Optical and Infrared Interferometry II. Proceedings of the SPIE, Volume 7734, pp. 773441-773441-8, 2010

## Weitere Publikationen

- Zuther, Jens; Eckart, Andreas; Bertram, Thomas; Horrobin, Matthew; Lindhorst, Bettina; Lindhorst, Uwe; Moser, Lydia; Rost, Steffen; Straubmeier, Christian; **Tremou, Evangelia**; Wank, Imke:  
“*The LINC-NIRVANA fringe and flexure tracker: an update of the opto-mechanical system*”, Optical and Infrared Interferometry II. Proceedings of the SPIE, Volume 7734, pp. 773448-773448-9, 2010
- Moser, L.; Eckart, A.; Horrobin, M.; Lindhorst, B.; Rost, S.; Straubmeier, C.; **Tremou, E.**; Wank, I.; Zuther, J.; Bertram, T:  
“*The LINC-NIRVANA fringe and flexure tracker: first measurements of the testbed interferometer*”, Optical and Infrared Interferometry II. Proceedings of the SPIE, Volume 7734, pp. 77342X-77342X-7, 2010

- Horrobin, Matthew; Eckart, Andreas; Lindhorst, Bettina; Lindhorst, Uwe; Moser, Lydia; Rost, Steffen; Smajic, Semir; Straubmeier, Christian; **Tremou, Evangelia**; Wank, Imke; Zuther, Jens; Bertram, Thomas; Arcidiacono, Carmelo:  
 “*Fringe detection and piston variability in LINC-NIRVANA*”, Optical and Infrared Interferometry II Proceedings of the SPIE, Volume 7734, pp. 77341X-77341X-10, 2010
  
- Rost, Steffen; Eckart, Andreas; Horrobin, Matthew; Lindhorst, Bettina; Lindhorst, Uwe; Moser, Lydia; Smajic, Semir; Straubmeier, Christian; **Tremou, Evangelia**; Wank, Imke; Zuther, Jens; Bertram, Thomas:  
 “*The LINC-NIRVANA fringe and flexure tracker: control design overview*”, Optical and Infrared Interferometry II. of the SPIE, Volume 7734, pp. 77341V-77341V-8, 2010
  
- Unda-Sanzana, E.; Marsh, T. R.; Gänsicke, B. T.; Maxted, P. F. L.; Morales-Rueda, L.; Dhillon, V. S.; Thoroughgood, T. D.; **Tremou, E.**; Watson, C. A.; Hinojosa-Goñi:  
 “*The not-so-extreme white dwarf of the CV GD 552*”, Journal of Physics: Conference Series, Volume 172, Issue 1, pp. 012041, 2009
  
- Rebassa-Mansergas, A.; Gänsicke, B. T.; Schreiber, M. R.; Southworth, J.; Schwöpe, A. D.; Nebot Gomez-Moran, A.; Aungwerojwit, A.; Rodriguez-Gil, P.; Karamanavis, V.; Krumpke, M.; **Tremou, E.**; Schwarz, R.; Staude, A.; Vogel, J.:  
 “*Post-common envelope binaries from SDSS - III. Seven new orbital periods*”, Monthly Notices of the Royal Astronomical Society, Volume 390, Issue 4, pp. 1635-1646, 2008
  
- Unda-Sanzana, E.; Marsh, T. R.; Gänsicke, B. T.; Maxted, P. F. L.; Morales-Rueda, L.; Dhillon, V. S.; Thoroughgood, T. D.; **Tremou, E.**; Watson, C. A.; Hinojosa-Goñi, R.:  
 “*GD 552: a cataclysmic variable with a brown dwarf companion?*”, Monthly Notices of the Royal Astronomical Society, Volume 388, Issue 2, pp. 889-897, 2008
  
- Eckart, Andreas; Witzel, Gunther; Kunneriath, Devaky; König, Sabine; Straubmeier, Christian; Bertram, Thomas; Zamaninasab, Mohammad; Schödel, Rainer; Muzic, Koraljka; **Tremou, Evangelia**; Meyer, Leonhard; Rost, Steffen; Vogel, Stuart; Wiesemeyer, Helmut; Sjouwerman, Lorant; Herbst, Tom:  
 “*Prospects for observing the Galactic Center: combining LBT LINC-NIRVANA observations in the near-infrared with observations in the mm/sub-mm wavelength domain*”, Optical and Infrared Interferometry. Proceedings of the SPIE, Volume 7013, pp. 70134L-70134L-12 , 2008

- Rost, Steffen; Bertram, Thomas; Lindhorst, Bettina; Straubmeier, Christian; **Tremou, Evangelia**; Wang, Yeping; Witzel, Gunther; Eckart, Andreas:  
“*The LINC-NIRVANA Fringe and Flexure Tracker: testing piston control performance*”, Optical and Infrared Interferometry. Proceedings of the SPIE, Volume 7013, pp. 701338-701338-12, 2008
- Bertram, Thomas; Lindhorst, Bettina; **Tremou, Evangelia**; Rost, Steffen; Wang, Yeping; Wank, Imke; Witzel, Gunther; Straubmeier, Christian; Eckart, Andreas:  
“*The LINC-NIRVANA Fringe and Flexure Tracker: the testbed interferometer*”, Optical and Infrared Interferometry. Proceedings of the SPIE, Volume 7013, pp. 701337-701337-9, 2008
- Bertram, Thomas; Eckart, Andreas; Lindhorst, Bettina; Rost, Steffen; Straubmeier, Christian; **Tremou, Evangelia**; Wang, Yeping; Wank, Imke; Witzel, Gunther; Beckmann, Udo; Brix, Mario; Egner, Sebastian; Herbst, Tom:  
“*The LINC-NIRVANA fringe and flexure tracking system*”, Optical and Infrared Interferometry. Proceedings of the SPIE, Volume 7013, pp. 701327-701327-12, 2008



# Lebenslauf

## Personalangaben

Name: Evangelia Tremou  
Anschrift: I Physikalisches Institut  
Zulpicher strasse 77, 50937 Koln  
E-mail: tremou@ph1.uni-koeln.de  
Geburtsdatum und -ort: 18.06.1983 in Trikala, Griechenland

## Ausbildung

Seit März 2008: Promotionstudentin an der Universität zu Köln und dem Max-Planck-Institut für Radioastronomie  
wiss. Betreuer: Prof. Dr. Anton J. Zensus,  
Prof. Dr. Andreas Eckart  
Titel: "High angular resolution in the NIR:  
The construction of an imaging beam combiner  
for the LBT and Spectroscopic studies on AGNs "

2002 - 2008: Diplom in Physik (Ptychion) an der Aristotle  
Universität zu Thessaloniki, Griechenland  
wiss. Betreuer: Prof. Dr. John H. Seiradakis  
Titel: "*H<sub>II</sub> REGION DETECTION IN  
LOCAL GROUP CENSUS*"

1999 - 2000: 2nd Gymnasium von Trikala, Griechenland

## Stipendium

Seit März 2008: Stipendium der *International Max Planck Research School (IMPRS) for Astronomy and Astrophysics*

